Université du Québec

INRS Institut national de la recherche scientifique

Centre Énergie, Matériaux et Télécommunications

STUDY OF ETHANOL OXIDATION REACTION ON Rh- AND SnO_2-BASED Pt CATALYSTS IN ACIDIC MEDIUM

Par

Haixia Wang

Thèse présentée pour l'obtention du grade de

Philosophiae Doctor (Ph.D.)

en sciences de l'énergie et des matériaux

Jury d'évaluation

Président du jury et examinateur interne	Kulbir Kaur Ghuman Professeure à l'INRS-ÉMT
Examinateur externe	Elena Baranova Professeure à l'Université d'Ottawa
Examinateur externe	Sasha Omanovic Professeur à l'Université de McGill
Directeur de recherche	Mohamed Mohamedi Professeur à l'INRS-ÉMT
Codirecteur de recherche	Shuhui Sun Professeur à l'INRS-ÉMT

ACKNOWLEDGEMENTS

This Ph.D. thesis has been carried out in Prof. Mohamedi's Electrochemistry and Micro Energy Sources Laboratory (EMESL) at the Institut National de la Recherche Scientifique (INRS), Québec, Canada. I would like to take this opportunity to express my sincere gratitude and appreciation to all those who made this Ph.D. thesis possible.

First and foremost, I would like to extend my profound gratitude to my advisor Prof. Mohamed Mohamedi for offering me the opportunity to work in his lab, for his continuous support and comprehensive help for my Ph.D. study. His guidance helped me in all the time of the research and writing of this thesis. I could not have imagined having a better advisor and mentor for my Ph.D. study.

Besides my advisor, I would also like to thank my co-supervisor Prof. Shuhui Sun for closely following the research progress and for his valuable contribution of accomplishing my Ph.D. project.

I thank the Jury members, Prof. Kulbir Kaur Ghuman, Prof. Elena Baranova and Prof. Sasha Omanovic for agreeing and taking the time to review and evaluate this work.

I would also like to express my sincere gratitude to the senior engineers Mr. Christophe Chabanier and Mr. Étienne Charette for their valuable suggestions and professional technical support.

I am also grateful to my kindly colleagues, Dr. Alonso Moreno Zuria, Juan Carlos Abrego Martínez, Chahrazed Benabid, Xin Tong, Naser Mohammadi, Xiaoying Zheng and Khawtar Hasan for the excellent atmosphere in the lab. Special thanks to Dr. Youling Wang, who provided me a warm welcome when I arrived in Canada and gave me training for Raman and CVD.

I thank the great friends from INRS. I owe my deepest gratitude towards my sincerely dear friends David, Rita and Gérard, for your eternal support during this challenging period.

I gratefully acknowledge the following funding sources that made my Ph.D. work possible. I was funded by the China Scholarship Council (CSC) and my work was supported by the Natural Sciences and Engineering Research Council of Canada (NSERC), Fonds de Recherche du Québec – Nature et technologies (FRQNT) and the Centre Québécois sur les Matériaux Fonctionnels (CQMF).

Last but not the least, a heartfelt thanks to my dear family for loving me unconditionally, supporting me financially and spiritually, believing in me and encouraging me to follow my dream. I love you, Mom and Dad.

RÉSUMÉ

Étude de la réaction d'oxydation de l'éthanol sur des catalyseurs Pt à base de Rh et SnO_2 en milieu acide

Avec la détérioration du climat mondial et la pénurie croissante de ressources pétrolières, l'exploration de sources d'énergie propres, renouvelables et durables est devenue la priorité absolue. On s'attend à ce que les piles à combustible à éthanol direct (DEFC) deviennent un combustible alternatif pour leurs applications potentielles en tant que sources d'énergie portables, car l'éthanol possède une haute densité d'énergie, une faible toxicité et peut-être produit à partir de la biomasse, ce qui en fait un combustible vert. Néanmoins, la commercialisation des DEFC est entravée par la faible sélectivité de la génération de CO_2 et la lente cinétique à l'anode. Il est très important de développer un catalyseur anodique avec une activité, une stabilité et une efficacité d'oxydation élevées.

Cette thèse débute par l'étude de l'effet de l'épaisseur de la couche de Rh (liée au nombre d'impulsions laser N_{lp}) sur la morphologie, la taille des particules et l'électrooxydation du CO. Afin d'améliorer l'efficacité de l'électrooxydation de l'éthanol, du SnO_2 est ajouté comme support. Une série d'électrocatalyseurs Pt/SnO_2, Rh_x/Pt et $Rh_x/Pt/SnO_2$ sur du papier carbone déposé couche par couche fabriquée en PLD sont étudiés pour l'électrooxydation du CO ainsi que de l'éthanol. Les résultats révèlent le rôle du promoteur du dioxyde d'étain et du rhodium dans l'amélioration de l'activité électrocatalytique envers la réaction d'oxydation de l'éthanol (ROE). Il concerne en particulier l'effet de la quantité de Rh ($N_{lp,\ Rh}$). On constate que le catalyseur ternaire $Rh_5/Pt/SnO_2$ ($N_{lp,\ Rh}$=5000) présente les meilleures performances, tandis que le catalyseur $Rh_{50}/Pt/SnO_2$ est le plus mauvais. En outre, un accent particulier est mis sur l'influence du substrat pour améliorer la surface électrochimique et l'activité catalytique. Les résultats montrent que les nanotubes de carbone supportés par les catalyseurs CNT sont supérieurs aux catalyseurs supportés par le papier carbone (PC). En outre, la disposition et la composition de Pt et Rh sont soigneusement prises en compte. Le rapport atomique optimal du Pt et du Rh est établi lors de la caractérisation électrochimique. Nos résultats suggèrent que les électocatalyseurs Pt_xRh_{100-x} supportés par le PC co-déposés par CBPLD, en particulier Pt_3Rh, surpassent le catalyseur déposé couche par couche Pt/Rh, voire $Rh_5/Pt/SnO_2$/CNT. Ces études fournissent des informations fondamentales sur l'électrooxydation de l'éthanol et sont propices à la conception de nouveaux électrocatalyseurs anodiques avec une activité et une sélectivité améliorée vis-à-vis de la ROE, ce qui est important pour d'ultérieures études sur les DEFC.

Mots-clés: Piles à combustible à éthanol direct, ablation laser, catalyseurs à plusieurs composants, empoisonnement au monoxyde de carbone, électrooxydation à l'éthanol

ABSTRACT

With the deterioration of global climate and the growing shortage of oil resources, exploring clean, renewable and sustainable energy sources has become the top priority. Direct ethanol fuel cells (DEFCs) have been expected to become an alternate fuel for their potential applications as portable power sources, because ethanol is in high energy density and low toxicity. Besides, ethanol can be produced from biomass, making it a green fuel. Nonetheless, the commercialization of DEFCs is hindered by the low selectivity of CO_2 generation and sluggish kinetics at the anode. It is of great significance to develop an anodic catalyst with high activity, stability and oxidation efficiency.

This thesis is started by investiging the effect of the Rh thickness layer (related to number of laser pulses N_{lp}) on the morphology, particle size and CO electrooxidation. In order to improve the efficiency of ethanol electrooxidation, SnO_2 is added as carrier. A series of PLD-made layer-by-layer structured carbon paper (CP) supported electrocatalysts Pt/SnO_2, Rh_x/Pt and $Rh_x/Pt/SnO_2$ are studied for ethanol electrooxidation. The results reveal the role of tin oxide and rhodium promoter in enhancing electrocatalystic activity towards ethanol oxidation reaction (EOR). It particulary concerns the effect of the Rh amount ($N_{lp,\ Rh}$) on EOR. It is found the ternary catalyst $Rh_5/Pt/SnO_2$ ($N_{lp,\ Rh}$ = 5000) has the best performance, while the catalyst $Rh_{50}/Pt/SnO_2$ is the worst. In addition, a special focus is on the the influence of substrate on improving the electrochemical surface area and catalystic activity. The results manifest the carbon nanotubes CNT supported catalysts are superior to the corresponding CP supported catalysts. Furthermore, the arrangement and composition of Pt and Rh are carefully taken into account. The optimal atomic ratio of Pt and Rh is established during the electrochemical characterization. Our findings suggest the CBPLD-syntheised co-deposited CP supported electocatalysts Pt_xRh_{100-x} alloy, especially Pt_3Rh, outperform the layer-by-layer depositied catalyst Pt/Rh, even $Rh_5/Pt/SnO_2$/CNT. These investigations provide fundamental insight on ethanol electrooxidation and conducive to designing novel anodic electrocatalysts with enhancing activity and selectivity toward EOR, which is important for further DEFCs study.

Keywords: Direct ethanol fuel cell, laser ablation, multicomponent catalysts, carbon monoxide poisoning, ethanol electrooxidation

TABLE OF CONTENTS

LIST OF FIGURES

LIST OF TABLES

LIST OF ABREVIATIONS

AA	Acetic Acid
AAL	Acetaldehyde
ACL	Anode Catalyst Layer
ADL	Anode Diffusion Layer
AFCs	Alkaline Fuels Cells
ASV	Anodic Stripping Voltammetry
BE	Binding Energy
BPs	Bipolar Plates
CA	Chronoamperometry
CBPLD	Cross-Beam Pulsed Laser Deposition
CCL	Cathode Catalyst Layer
CDL	Cathode Diffusion Layer
CE	Counter Electrode
CL	Catalyst Layer
CNFs	Carbon Nanofibers
CNTs	Carbon Nanotubes
CP	Carbon Paper
CV	Cyclic Voltammetry
CVD	Chemical Vapor Deposition

DAFCs	Direct Alcohol Fuel Cells
DEFCs	Direct Ethanol Fuel Cells
DEMS	Differential Electrochemical Mass Spectrometry
DFAFCs	Direct Formic Acid Fuel Cells
DFT	Density Functional Theory
DL	Double Layer
DMFCs	Direct Methanol Fuel Cells
EC-MS	Electrochemical Mass Spectrometry
ECSA	Electrochemical Active Surface Area
EDS	Energy Dispersive X-ray Spectroscopy
EMF	Electromotive Force
EOR	Ethanol Oxidation Reaction
ESA	Electroactive Surface Area
FC	Fuel Cells
FCEV	Fuel Cell Electric Vehicles
FFVs	Flex-Fuel Vehicles
FTIR	Fourier Transform Infrared Spectroscopy
FWHM	Full Width at Half Maximum
HPLC	High Performance Liquid Chromatography
HUPD	Hydrogen Underpotential Deposition

ICEs	Internal Combustion Engines
IRRAS	Infrared Reflection-Absorption Spectroscopy
KE	Kinetic Energy
LSV	Linear Sweep Voltammetry
MA	Mass Activity
MCFC	Molten Carbonate Fuel Cells
MCs	Mesoporous Carbons
MEA	Membrane Electrode Assembly
MWCNTs	Multi-Walled Carbon Nanotubes
NAA	Neutron Activation Analysis
N_{lp}	Number of the laser pulses
ORR	Oxygen Reduction Reaction
PAFCs	Phosphoric Acid Fuels Cells
PDF	Powder Diffraction File
PEM	Proton Exchange Membrane
PEMFC	Proton Exchange Membrane Fuels Cells
PLD	Pulsed Laser Deposition
RE	Reference Electrode
RF	Roughness Factor
SA	Specific Activity

SERS	Surface Enhanced Raman spectroscopy
SEM	Scanning Electron Microscopy
SMSI	Strong Metal Support Interaction
SOFCs	Solid Oxide Fuels Cells
TEM	Transmission Electron Microscopy
WE	Working Electrode
XPS	X-ray Photoelectron Spectroscopy
XRD	X-Ray Diffraction

1 INTRODUCTION

1.1 Background

Energy plays a crucial role in economic and social development. Nowadays global demand for energy is exponentially increasing due to the rapidly expanding economy and the continuous population growth. Whereas the current energy system is highly dependent on fossil fuels (coal, oil and natural gas), which dominate ca. 80% of the world energy consumption (Figure 1.1a and Figure 1.1b) [1]. It is reported that by 2050 oil and gas supplies will not likely be able to meet the global energy demand [2]. Besides, the combustion of fossil fuels causes serious environmental problems, especially the air pollution and climate change. Facing the depletion of fossil fuels, deterioration of the environment and the ever-rising energy demand, it is of paramount importance to explore the clean, renewable and sustainable energy sources to create a better future for generations to come. Many alternatives have been studied, such as solar, hydro, tide, wind power, nuclear power, terrestrial heat and fuel cells. Among these resources, fuel cells are regarded as the most promising energy and key strategies for sustainable energy development owning to their attractive features: high efficiency, free pollution and ambient operation condition.

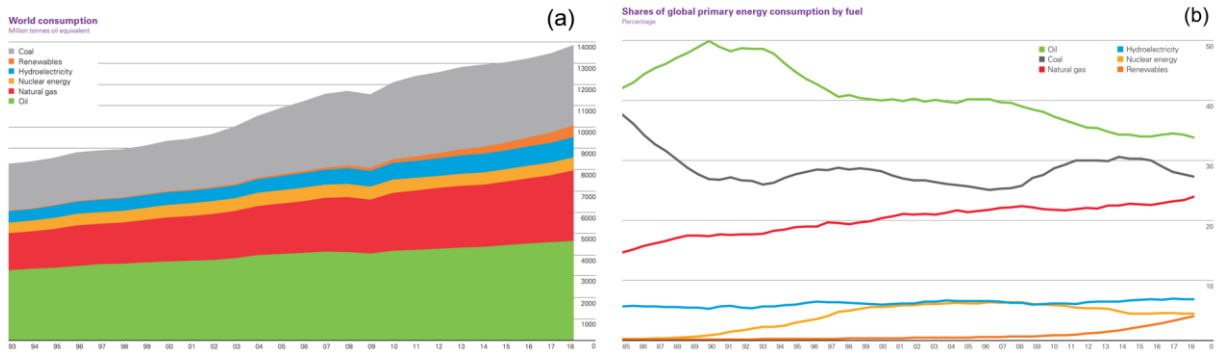

Figure 1.1 **(a) The global energy consumption by fuel in 2018 (b) Share of global primary energy consumption by fuel [1].**

1.2 Fuel cells

1.2.1 Fuel cell, battery and internal combustion engine (ICE)

A fuel cell is a static energy conversion device, which transforms the chemical energy from fuel oxidation directly into electrical energy [3]. Although there are various types of fuel cells, they all consist of an electrolyte sandwiched between an anode and a cathode. Fuel cell is akin to a

continuously recharging battery [2], both of fuel cell and battery belong to one class of devices-Galvanic cells. The biggest difference between them is that the battery (secondary cell) delivers power from a finite amount of stored energy, while fuel cell generates electricity and heat indefinitely and continuously as long as the fuel and oxidizer are supplied, which is similar to the internal combustion engines (ICEs). Unlike the conventional system ICEs or turbines, fuel cells do not involve multistep energy conversion (the flow path in grey as shown in Figure 1.2) but directly transfer chemical energy to electrical energy. Hence, fuel cells are not subject to the limitation of the Carnot cycle but with high-energy conversion efficiency.

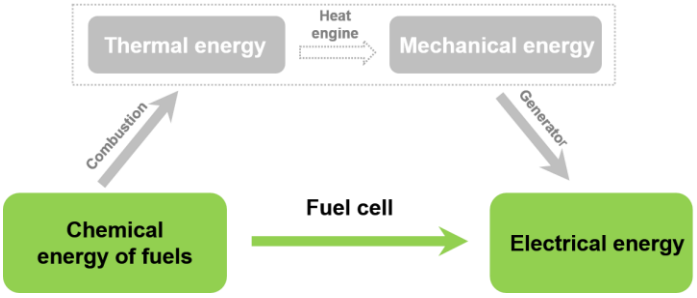

Figure 1.2 **Graphical illustration of the difference in energy conversion between fuel cells and the internal combustion engines (ICEs).**

1.2.2 Characteristics of fuel cells

Fuel cells are present as a highly efficient and environmentally friendly alternative technology for decentralized energy production. Fuel cells have the following features:

(i) **Clean**-the fuel is not combusted but reacts electrochemically instead. Therefore, fuel cells have virtually zero pollutant emission: the products are water, heat and CO_2. Heat can be used in cogeneration, and CO_2 can be absorbed by plants through photosynthesis. While the batteries are associated with waste disposal and non-renewable fossil fuels NO_X or SO_X exhaust.

(ii) **No noise**-more silent in operation alternative to the conventional sources of power generators. There are no moving parts in a fuel cell stack, making them quieter.

(iii) **Fuel flexibility**-fuels can be obtained from natural sources or organics with low carbon number, such as methanol, formic acid, ethanol, *etc*.

(iv) **Good reliability**-quality of power provided does not degrade over time.

(v) **High efficiency**-fuel cells are not constrained by Carnot cycle limit. The conversion efficiency of fuel cells can up to 80% *vs.* ICEs 40%.

(vi) **Wide range of applications**-the power the fuel cells provide can be from 1 W to 1 MW. Therefore, fuel cells have wide potential applications, such as portable devices, electric vehicles and power plants.

(vii) **Higher energy density and longer discharge time**-compared with other electrochemical power sources as illustrated in Ragone plot (Figure 1.3).

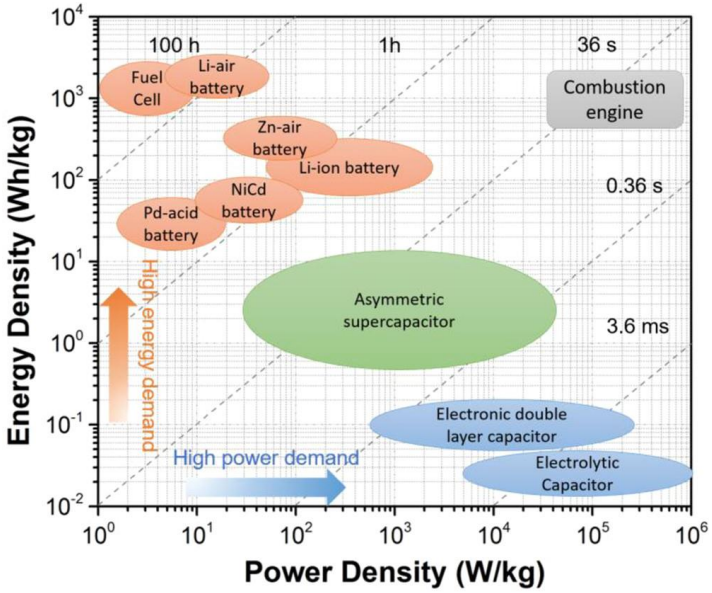

Figure 1.3 **Ragone plot illustrating the performances of specific power vs specific energy for different electrical energy-storage technologies. Times shown in the plot are the discharge time, obtained by dividing the energy density by the power density [4].**

1.2.3 Historical overview of fuel cells

Fuel cells are not new technology. In 1801, Sir Humphrey Davy created a simple fuel cell ($C|H_2O$, $HNO_3|O_2|C$) with which he could give himself a feeble electric shock. Christian Friedrich Schönbein discovered the principle of the fuel cell in 1838 and published it in 1839 [5]. In the same year, the Welsh lawyer and physical scientist Sir William Robert Grove (who is often referred to as the founder of the fuel cell) was the first to demonstrate the concept of fuel cell [6]. He argued that by reversing this process electricity could be generated by the reaction of hydrogen and oxygen together.

The term “fuel cell” was first used in 1889 by two chemists Ludwig Mond and Charles Langer [7], who tried to develop a practical fuel cell which ran on air and coal gas. But they did not succeed due to the catalyst poisoning problem. In 1899, Nernst observed the conduction in stabilized zirconia solid oxide electrolytes [8] and forty years later the ceramic fuel cells were

presented [9]. However, fuel cell lost its glamor in the early 20th century since the high-power internal combustion engines were utilized in industries despite their low efficiencies.

Though the development of fuel cells towards practical application was relatively slow, the research on exploring novel fuel cell technologies never stopped. In 1932, English mechanical engineer Francis Thomas Bacon developed the first alkali electrolyte fuel cell by modification of Mond-Langer fuel cell, using nickel electrode in alkaline instead of platinum electrode in acid solution. He and his coworkers eventually developed a workable fuel cell-5 kW welding machinery in 1959 [10]. In 1937, Baur and Preis operated the first ceramic fuel cell (solid oxide fuel cell SOFC prototype) based on zirconia at 1000 ℃ [9]. While the technology problem still plagued the fuel cell until 1955 when the General Electric engineer Willard Thomas Grub modified fuel cell concept and developed the first polymer exchange membrane fuel cell (PEMFC) [11].

Alkaline fuel cells (AFC) stepped into a rapid development stage in the 1960s, partly driven by the fund from NASA, which spent tens of millions of dollars in searching for a clean source in low weight and high efficiency for the Apollo and Gemini space programme. Fuel cell electric vehicles (FCEVs) developed with the Apollo program. In 1966, General Motors (GM) developed the first hydrogen fuel cell road vehicle [12]. Around the same period, Shell started to develop direct methanol fuel cells (DMFCs) [13].

In the1970s, the phosphoric acid fuel cells (PAFCs) were significantly developed due to the oil crisis. Besides, several German, Japanese and US vehicle manufacturers and their partners began to experiment with FCEV to enhance power density of PEMFC stacks. During the 1980s, the government agencies in the USA, Canada and Japan invested heavily for fuel cell research, development and demonstration (RD&D). Fuel cells were employed in the US Navy submarine. In the 1990s, the government of Germany, Japan and the UK started to develop PEMFC and SOFC technologies for residential micro-CHP applications. In 1993, the Canadian company Ballard, the leader of PEMFC, developed the world's first zero emission hydrogen fuel cell powered transit bus with a top speed of 72 km h^{-1}. In 2003, Iceland became the very first country in the world to open a public hydrogen filling station-Shell Hydrogen Station at Grjótháls. Meanwhile, important advances have been achieved by the direct methanol fuel cells (DMFCs) technology for portable devices in 1993 [14]. Companies such as Siemens, SMART, Samsung, and Toshiba, DuPont, Casio, MTI were actively engaged in the research of DMFCs-based cellular phone, portable laptop computers and digital equipment battery chargers [15].

In 2007, fuel cells began to become commercialized in a variety of applications, especially plenty of PEMFC and DMFC auxiliary power units (APU) were commercialized in recreational application, such as on-board transit and aviation [16]. Micro fuel cell units being used in the portable devices, such as laptop, mobile phones, video camera etc. [17]. Though direct ethanol fuel cell (DEFC) is still new in market, it starts to make its mark. On May 13, 2007, Offenburg students demonstrate the world's first DEFC powered vehicle in France [18]. The unique configuration combines the advantage of biofuel ethanol, sidestepping the disadvantage of hydrogen. At Shell Eco-marathon Asia 2018, the Indian team BITS Pilani drive the student-built the 100% ethanol fuelled vehicles, and this ethanol fuel engine gives a very tight competition to the hydrogen fuel cell [19]. The Japanese company Nissan plans to commercialise ethanol fuel-based fuel cell vehicles (FCVs) by 2020 [20]. The historical development of fuel cells and an outlook on the future can be briefly summarized in Figure 1.4.

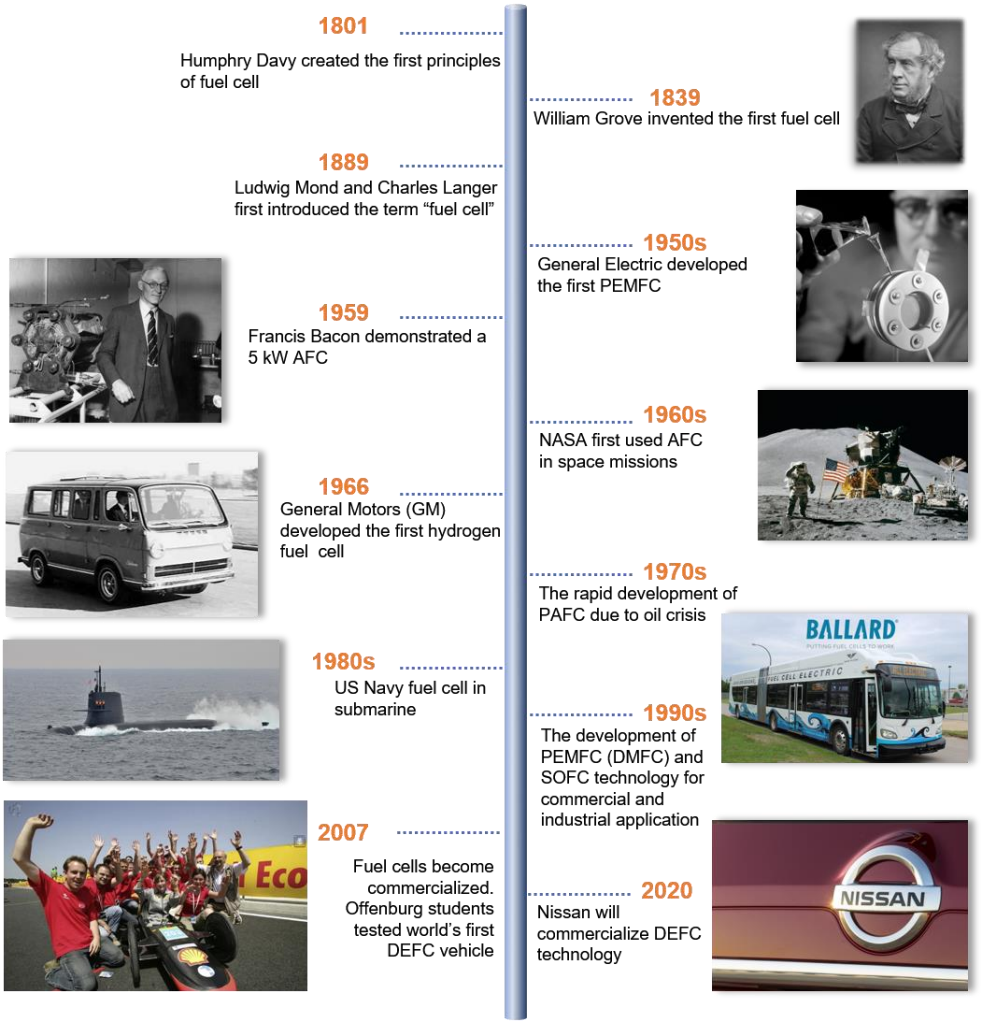

Figure 1.4 The historical development of fuel cells and an outlook on future.

1.2.4 Types of fuel cell and its application

Hitherto, various types of fuel cells have been developed. Fuel cells are sorted by the nature of the electrolyte, which also determines the operation temperature, the type of fuel and range of applications. The electrolyte can be acid, base, salt or a solid ceramic or polymeric membrane, which conducts ions. Accordingly, the fuel cells can be classified into five categories: proton-exchange membrane fuel cells (PEMFCs), alkaline fuel cells (AFCs), phosphoric acid fuel cells (PAFCs) molten-carbonate fuel cells (MCFCs) and solid-oxide fuel cells (SOFCs). Figure 1.5 summarizes the characteristics of the five fuel cells.

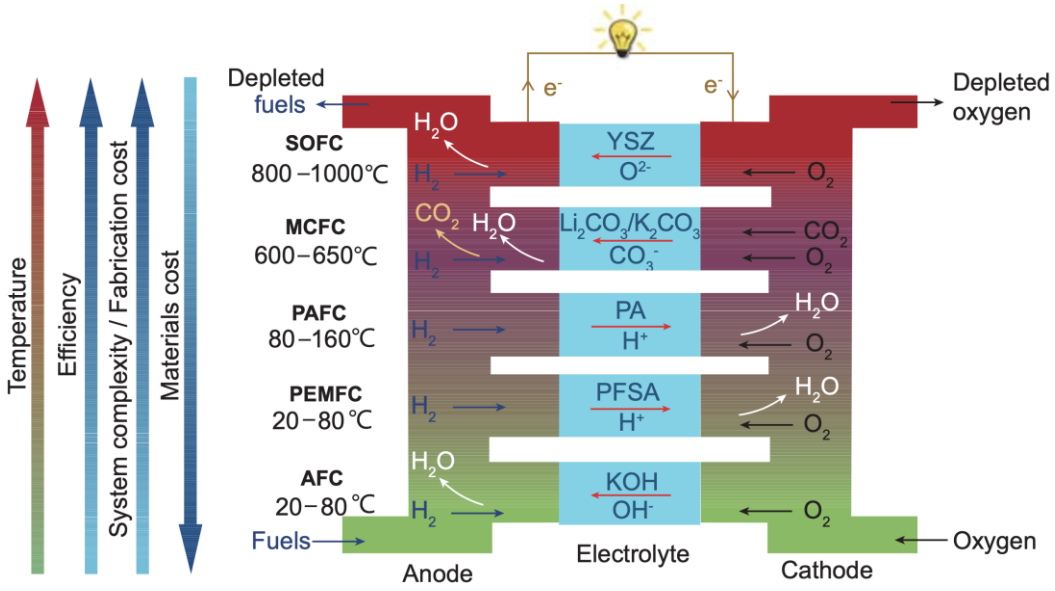

Figure 1.5 **Fuel cell types, illustrating the general trend in the relationship between the operation temperature, efficiency, system complexity, fabrication cost and materials cost of the FC technologies [21].**

High-temperature solid fuel cells (SOFCs) and molten carbonate fuel cells (MCFCs), ranging from kW to MW, are suitable for stationary and distributed power-supply applications. Due to the extremely high operating temperatures (> 600 °C), they can reform fossil fuel (*e.g.,* gasoline, nature gas), resulting in a high efficiency (60%). Besides, no precious platinum catalyst material is needed. On the other hand, high temperature leads to a longer start-up time, short lifetime and mechanical and chemical compatibility issues, such as corrosion and breakdown of cell components, lower electrolyte retention capacity.

Low-temperature proton exchange membrane fuel cells (PEMFCs) and alkaline fuel cells (AFCs) provide an order of magnitude higher power density and have a short start-up time. These features make PEMFCs competitive in mass-market and small-scale CHP application [2]. AFCs are typically applied in the military and aerospace. The major drawbacks of PEMFCs and

AFCs are the low operating efficiency (40-45%), high-cost platinum and sensitive to hydrogen impurity [2, 13]. AFCs is extremely sensitive to CO_2 in fuel and air.

Direct alcohol fuel cells (DAFCs) are a subcategory of proton-exchange fuel cells (PEMFCs), in which the alcohol reacts directly at the fuel cell anode without any reforming process. In DAFCs, liquid fuels can be methanol, ethanol, propanol, and so on.

Moderate-temperature phosphoric acid fuel cells (PAFCs) are typically used for large-scale stationery power generation, heat application and large vehicles with output in the 100 kW to 400 kW range. Unlike PEMFCs and AFCs, PAFCs are tolerant to impurities in the reformed hydrocarbon. Also, PAFCs can tolerate CO_2, even CO with the concentration of *ca.* 1.5 %. The major disadvantage of PAFCs is same as PEMFCs and AFCs, the cost is relatively high, which restricts the market share. Besides, there are other disadvantages of PAFCs, such as low energy density, less fast start-up and aggressive electrolyte.

Figure 1.6 shows the scheme of application types and power range as a function of operation temperatures.

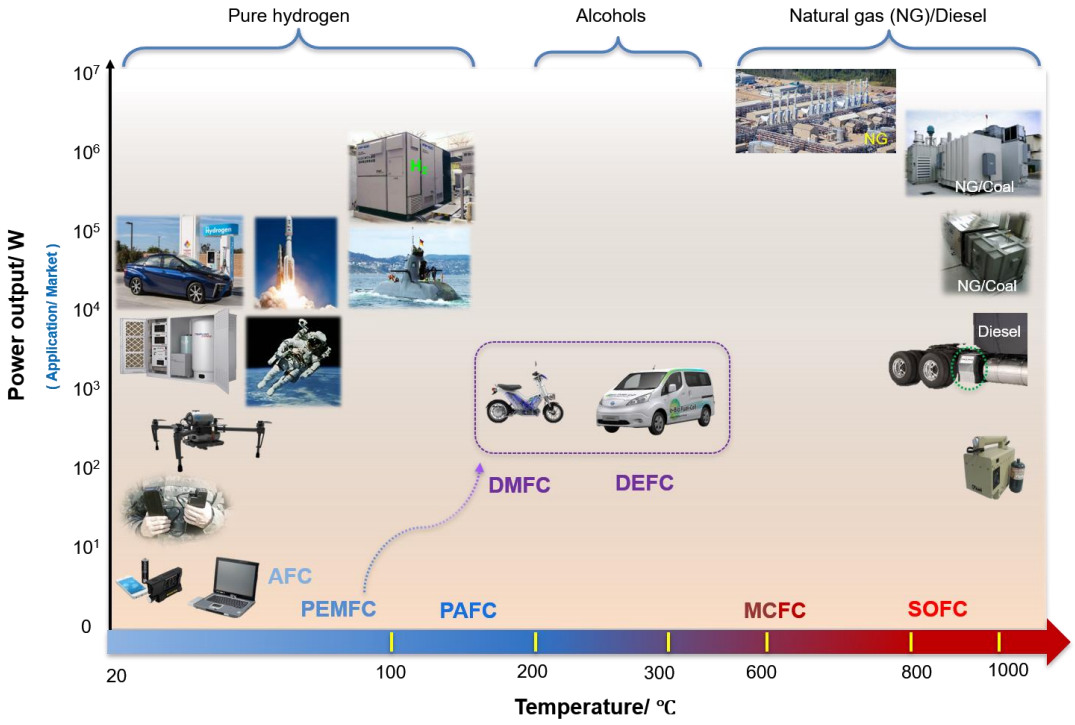

Figure 1.6 **Scheme of the application types and power ranges of main FC types as a function of operation temperatures.**

1.3 Introduction of DEFCs

It is generally acknowledged that PEMFC is one of the most promising technologies due to the outstanding characters of rapid start-up, low noise, zero-pollution emission, high efficiency and high system reliability [22]. Hydrogen is the most favorable fuel by virtue of its high activity in the anode reaction and its environmental benignity, but it is not a primary fuel. First of all, H_2 is not a natural gaseous fuel. Currently, hydrogen is produced by steam reforming of non-renewable natural gas (50%) or oil/naphtha refinery/chemical industrial off-gas (30%), coal gasification (18%), electrolysis of water (3.9%), and other sources (0.1%) [23]. Secondly, the production of pure hydrogen is cost inefficient. Also, hydrogen is extremely flammable, high pressure and special infrastructures are required for its storage, transportation and distribution logistics. The complicated production process raises the cost further. Additionally, the demanding requirement for the hydrogen purity is remarkably high. Once the CO in the hydrogen-rich gas is more than 10 parts per million (ppm), an obvious decay in the cell performance will be observed [24]. In consideration of the cost, storage complication and vigorous quality requirement of hydrogen, operation on liquid fuels like alcohols without the external bulky fuel-reforming progress could significantly simplify the fuel cell system and consequently increase its practical application. Methanol [25], formic acid [26], formaldehyde [27] and ethanol, etc. liquid fuels appear particularly convenient. Among these fuels, methanol has been considered as the first substitute of H_2. Extensive investigation has been working on direct methanol fuel cells (DMFCs) [25, 28-30], and some progress has been achieved in this field by Siemens, Toshiba, Samsung, NEC, MTI [31]. Yet, methanol is non-renewable [32] and methanol is highly toxic, which can damage the central nervous system, possibly leading to blindness. Also, methanol is inflammable with a low boiling point (65 ℃), and it is volatile, which is not quite fit for large-scale consume use [33]. Besides, it might contaminate the environment due to its large miscibility to water [34]. Moreover, methanol permeates through the membrane and reacts with oxygen at cathode, this crossover effect results in a mixed potential and a low power output. The sluggish anode kinetics and serious membrane crossover problem are the two technical challenges encountered by DMFCs. In contrast, ethanol is alternative fuel with attractive features from the following aspects:

(i) **Less toxic**.

(ii) **Easy to transport** due to relatively higher boiling point [35].

(iii) **Lower permeability** than methanol [36] (due to its longer carbon chain [37]).

(iv) **High power density** due to the total electro-oxidation with 12 e^- charge transfer [38]. (8.01 kWh kg^{-1}, 6.1 kWh kg^{-1} methanol [39], 12.89 kWh kg^{-1} gasoline [40]).

(v) **Renewable.** Ethanol can be easily obtained in large quantities from biomass by fermentation of cellulose-containing feedstock from agriculture (*e.g.*, wheat, corn or straw, sugar cane, etc.), agricultural wastes containing lignocellulosic residues) [41], low-grade biomass (*e.g.,* woodchips, bagasse), organic fractions from municipal waste or forestry residue [42]. The global biofuel ethanol production has increased sharply from 13.2 billion gallons in 2013 to 28.6 billion gallons in 2019 [43]. Figure 1.7 depicts the worldwide annual production of ethanol by country.

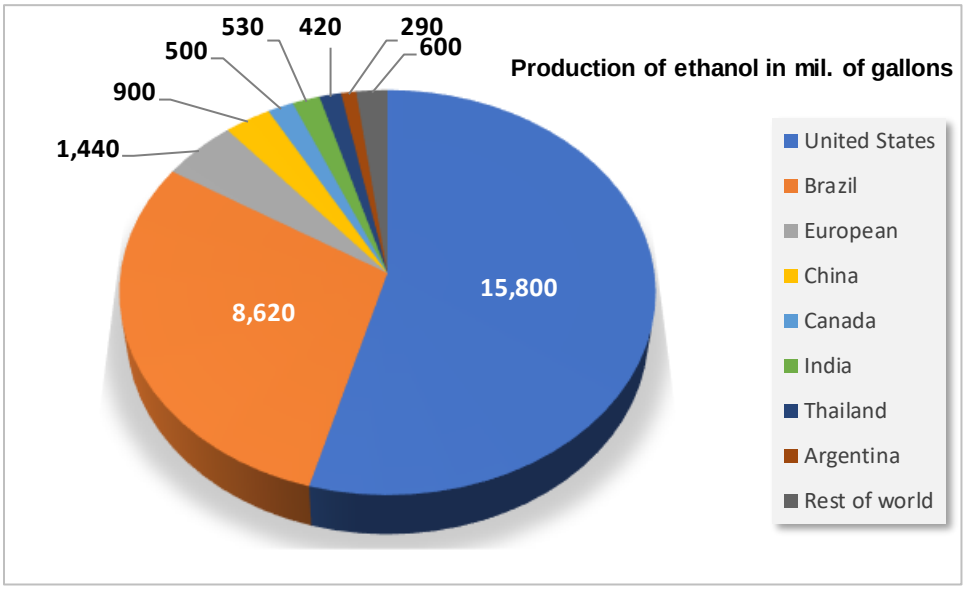

Figure 1.7 Production of ethanol in millions of gallons by worldwide countries in 2019 [43].

(i) **Compatible with the existing storage & delivery infrastructure.** In the USA, Brazil, Australia and France (with the E85 fuel containing 85% of ethanol and 15% gasoline), ethanol is already distributed through the well-established fuel station network for use in conventional automobiles with internal combustion engines (flex-fuel vehicles FFVs. More than 98% of the US gasoline contains E10 (10% ethanol and 90% gasoline) [44]. In Brazil, 88% of automobiles are FFVs. Approximately 70% of automobiles in Brazil can run on ethanol, and the demand of ethanol in Brazil is estimated to increase to ca. 80% by the year 2030 [45]. So, the introduction of direct ethanol fuel cells DEFCs for electricity generation purposes may be possible without requiring any modification of the infrastructure [36].

Theoretically, ethanol is produced from the biomass formation of plants. While plants absorb CO_2 through photosynthesis. This is called carbon neutral. Therefore, the CO_2 emission from the DEFC vehicle literally cannot cause greenhouse effect. Figure 1.8 illustrates the biomass

carbon cycle. In the future, ethanol fuel will be as an essential component for the realization of sustainable low-carbon society.

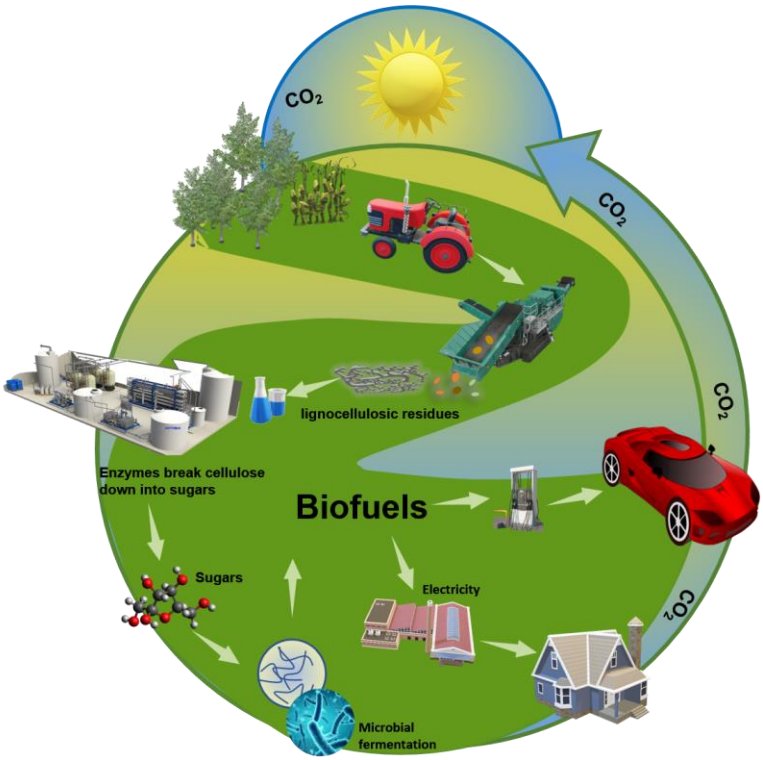

Figure 1.8 The biomass carbon cycle.

1.4 Overview of DEFCs

Generally, DEFCs can be divided into two categories in terms of the employed electrolyte, i.e. acid DEFC (PEM-based) and alkaline DEFC (anion exchange membrane AEM-based). In this project, we work on the acid DEFC.

1.4.1 The working principle of an acid DEFC

The parts of which a DEFC constitutes and its working principle are clearly illustrated in the Figure 1.9. In theory, ethanol is supplied through the anode flow field and transfer from the anode diffusion layer (ADL) to the anode catalyst layer (ACL), where ethanol is completely oxidized into carbon dioxide, protons and electrons. The produced electrons flow through the electrical circuit (load), and the protons migrate through the proton conductive membrane to the cathode. O_2 is fed through the cathode flow field and transfers from the cathode diffusion layer (CDL) to the cathode catalyst layer (CCL). Ultimately, the electrons and protons react with O_2 at

the cathode, where the oxygen reduction reaction (ORR) takes place. Water is the end-product at cathode.

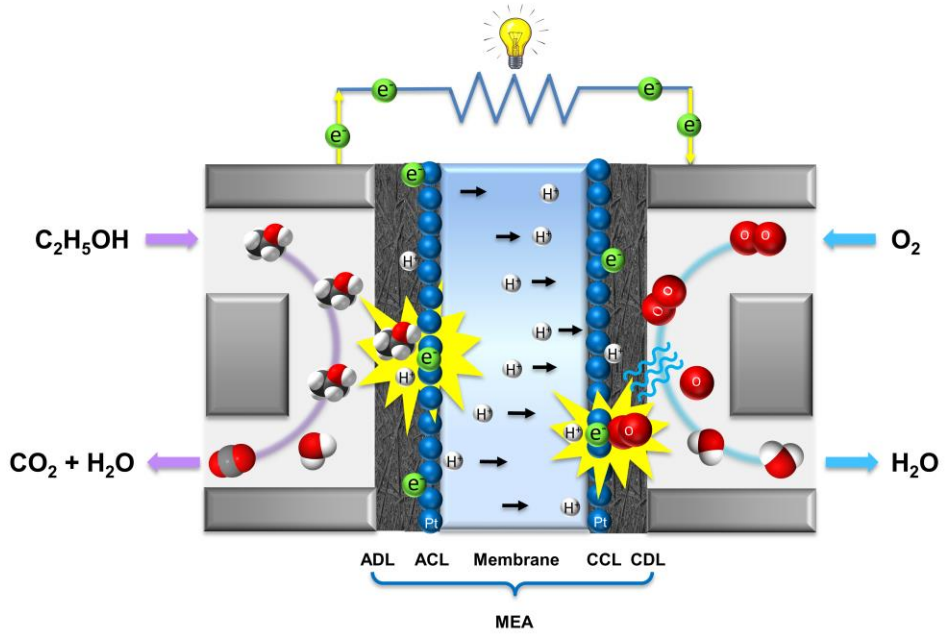

Figure 1.9 The working principle of an acid DEFC.

1.4.2 The fuel cell components

A single fuel cell is generally composed of a pair of (anodic and cathodic) end plates, current collectors, bipolar plates, diffusion layers, catalyst layers and a proton-exchange membrane, as illustrated in Figure 1.10.

(a) The bipolar plates (BPs): serve the purpose of feeding the fuel to the anode and oxidant to the cathode and provide the electrical and thermal conductivity. The BPs connect the membrane electrode assembly (MEAs) physically, thermally and electrically. Generally, bipolar plates are graphite or metallic materials.

(b) The gas diffusion layers (GDLs): GDLs serve important functions in DEFCs (i) allow the reactant and product to pass through evenly to the catalyst layer. (ii) provide an electrically conductive pathway for current collection. (iii) help to remove by-produced water outside of the catalyst layer. (iv) help in effective water removal to prevent flooding. (iv) removal of heat generated by the EOR. The component of the GDLs is a porous material composed of a dense array of carbon fibers. In general, carbon paper and carbon cloth are used as GDL.

(c) The catalyst layers (CLs): the active region of the electrochemical reactions.

(d) The membrane electrode assembly (MEA): one of the most important components in fuel cell that helps produce the electrochemical reaction needed to separate electrons. In general, a proton exchange membrane (PEM) (typically Nafion®, 25-50 μm) as the hardcore component to functionally conducts protons from the anode to the cathode. Membrane electrode assembly (MEA) is composed of the polymer electrolyte membrane sandwiched between ADL, ACL and CDL, CCL. The membrane is an electronic insulator.

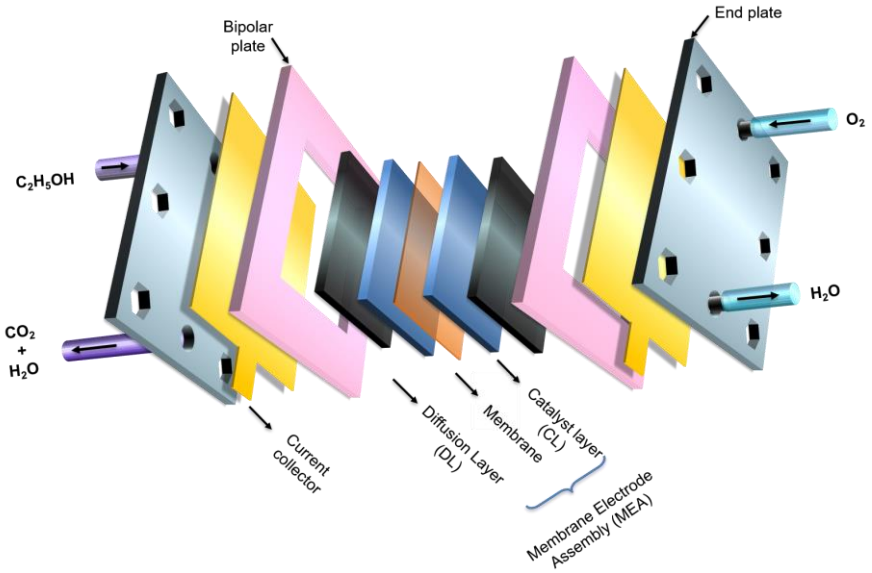

Figure 1.10 Schematic of an acid DEFC components.

1.4.3 Electrochemical reaction and basic thermodynamics of acid DEFC

1.4.3.1 Anode: Electrooxidation of ethanol

In theory, ethanol is completely oxidized into CO_2, protons with 12 e^- transfer in the anodic reaction.

$$\boldsymbol{C_2H_5OH + 3\,H_2O \rightarrow 2\,CO_2 + 12\,H^+ + +12\,e^-\ (E_a^o = 0.084\,V\ vs.SHE)} \qquad \text{Eq. (1.1)}$$

E_a^o is the standard potential of ethanol oxidation at the anode, which is calculated from standard energy of formation of the species involved in Eq. (1.1).

$$\boldsymbol{E_a^o = \frac{-\Delta G_{r,\ a}^o}{n\,F}} \qquad \text{Eq. (1.2)}$$

With:

$$\boldsymbol{-\Delta G_{r,\ a}^o = 2\,\Delta G_{f,CO_2,\ g}^o - G_{f,C_2H_5O,\ l}^o - 3\,\Delta G_{f,H_2O,\ l}^o} \qquad \text{Eq. (1.3)}$$

And:

$\Delta G^{o}_{f,\,CO_2,\ g}$ = - 394.4 *kJ mol*$^{-1}$; $\Delta G^{o}_{f,\,C_2H_5O,\ l}$ = -174.8 *kJ mol*$^{-1}$; $\Delta G^{o}_{f,\,H_2O,\ l}$ = -237.1 *kJ mol*$^{-1}$ [42]; *n* = *12*, the number of electrons involved in the oxidation of ethanol and *F* the Faraday constant (96,485 C mol^{-1}).

$-\Delta G^{o}_{r,\ a}$ = 2 × (-394.4) – (-174.8) – 3 × (-237.1) = 97.3 *kJ mol*$^{-1}$

Thus: $E^{o}_{a} = \frac{-\Delta G^{o}_{r,\ a}}{n\,F} = \frac{97.3\ kJ\ mol^{-1}}{12 \times 96485\ C\ mol^{-1}}$ = 0.084 V *vs.* SHE

1.4.3.2 Cathode: Electroreduction of oxygen

$$\mathbf{3\,O_2 + 12\,H^+ + 12\,e^- \rightarrow 6\,H_2O\ (E^{o}_{c} = 1.229\ V\ vs.\ SHE)} \qquad \text{Eq. (1.4)}$$

$$\boldsymbol{E^{o}_{c} = \frac{-\Delta G^{o}_{r,\ c}}{n\,F}} \qquad \text{Eq. (1.5)}$$

E^{o}_{c} was obtained similarly to E^{o}_{a}, $\Delta G^{o}_{f,\,H_2O,\ l}$ = -237.1 *kJ mol*$^{-1}$; $\Delta G^{o}_{f,\,O_2,\ g}$ = 0 *kJ mol*$^{-1}$, *n = 12.*

$-\Delta G^{o}_{r,\ c}$ = -6 × $\Delta G^{o}_{f,\,H_2O,\ l}$ + 3 $\Delta G^{o}_{f,\,O_2,\ g}$ = 1422.6 *kJ mol*$^{-1}$

1.4.3.3 Overall reaction

Hence, the overall electrochemical ethanol fuel cell reaction can be expressed as below:

$$\mathbf{C_2H_5OH + 3O_2 \rightarrow 2\,CO_2 + 3\,H_2O\ (\Delta\,E^{o}_{eq} = 1.145\ V\ vs.\ SHE)} \qquad \text{Eq (1.6)}$$

E^{o}_{eq} is the electromotive force (emf) of the system at the thermodynamic equilibrium and can be calculated as given below.

$$\boldsymbol{\Delta G^{o}_{r} = \Delta G^{o}_{r,\ c} - \Delta G^{o}_{r,\ a}} \qquad \text{Eq. (1.7)}$$

= -1422.6 + 97.3 = -1325.7 *kJ mol*$^{-1}$

$$\boldsymbol{E^{o}_{eq} = \frac{-\Delta G^{o}_{r}}{n\,F}} \qquad \text{Eq. (1.8)}$$

$= \frac{1325.7\ kJ\ mol^{-1}}{12 \times 96485\ C\ mol^{-1}}$

$= E^{o}_{c} - E^{o}_{a}$ = 1.229 - 0.084

= 1.145 V *vs.* SHE

Hence the energy density based on the low heat value (LHV) can be evaluated as follow [39]:

Gravimetric energy density (kWh kg^{-1}) = $\frac{-\Delta G_r^o}{3600\ M_m} = \frac{1325.7\ kJ\ mol^{-1}}{3600 \times 0.046\ Kg\ mol^{-1}}$ = 8.01 kWh Kg^{-1} Eq. (1.9)

Volumetric energy density (kWh L^{-1}) = $\frac{-\Delta G_r^o\ \rho}{3600\ M_m} = \frac{1325.7\ kJ\ mol^{-1}}{3600 \times 0.046\ Kg\ mol^{-1}}$ = 6.32 kWh L^{-1} Eq. (1.10)

where M_m is the molar mass of ethanol (0.046 kg mol^{-1}) and ρ is the density of ethanol (0.789 kg L^{-1}).

Table 1.1 lists the theoretical energy density of several fuels. As can be seen, ethanol is comparable to gasoline, which indicates ethanol is a promising and alternate fuel for the low temperature direct fuel cells.

Table 1.1 Energy densities of different fuels.

Fuel	kWh L^{-1}	kWh kg^{-1}
Gasoline [40]	9.50	12.89
Diesel [46]	9.17	11.86
Butanol	8.11	10.17
Ethanol	6.32	8.01
Glucose	6.64	4.32
Glycerol [46]	6.26	4.94
Ethylene glycol	5.87	5.30
Hydrazine	5.36	5.42
Methanol [39]	4.82	6.09
Formic acid	1.75	1.74
Hydrogen [42]	2.96×10^{-3}	32.90

1.4.4 Energy efficiency

i) **Reversible cell efficiency** (thermodynamic efficiency) of a fuel cell (under reversible conditions at equilibrium potential with zero current) is defined as the ratio of Gibbs free

energy change ΔG_r^o to the enthalpy change ΔH_r^o of the overall reaction (-1367 kJ mol^{-1}) [47] is shown as below equation [42].

$$\boldsymbol{\varepsilon_{rev}} = \frac{\boldsymbol{\Delta G_r^o}}{\boldsymbol{\Delta H_r^o}} = \frac{\mathbf{1325.7}}{\mathbf{1367.9}} = 0.969 \qquad \text{Eq. (1.11)}$$

In theory, the reversible cell efficiency of the DEFC is similar to the DMFC (ε_{rev}^{DMFC} = 0.967) but greater than PEMFC ($\varepsilon_{rev}^{PEMFC}$ = 0.83). The efficiency of ethanol is much higher than that of the best thermal engines (*e.g.,* diesel engines 0.40) [41].

ii) **Voltage efficiency $\boldsymbol{\varepsilon_E}$** is the ratio of the actual cell voltage E(*j*) under the current density *j* and ideal potential E_{eq}^o.

$$\boldsymbol{\varepsilon_E} = \frac{\boldsymbol{E(j)}}{\boldsymbol{E_{eq}^o}} \qquad \text{Eq. (1.12)}$$

$\boldsymbol{E(j) = E_c - E_a = E_{eq}^o - (|\eta_a| + |\eta_c| + |\eta_{Xover}| + R_i j)}$ [48] Eq (1.13)Where, E(*j*) is the actual cell voltage under internal resistance of the cell, R_i *j* is the ohmic drop in the electrolyte and interface resistance. E(*j*) is typically with 0.5 V at the current density of 100 mA cm^{-2} with complete oxidation (considering η_a = 0.4 V and η_c = 0.2 V), E_{eq}^o *is the reversible cell voltage of 1.145 V.* Thereby, $\varepsilon_E = \frac{E(j)}{E_{eq}^o} = \frac{0.5}{1.145} = 0.437$.

Besides, ethanol crossover will result in a mixed potential at the cathode, since ethanol will react with the adsorbed oxygen there. Moreover, ethanol and its by-products can be adsorbed on the cathode, reducing the ORR rate. Hence, the cathode potential becomes lower, which leads to a reduction of the cell voltage ε_{cell} and a further reduction in the voltage efficiency ε_E.

Figure 1.11 shows a typical polarization curve of a DEFC, illustrating the loss of a cell performance (E*(j)*, the actual cell potential), which due to the factors giving rise to the increase of overpotentials, particularly the kinetic polarization (usually described by the Butler-Volmer model), ohmic resistance polarization (obeying Ohm's Law) and concentration polarization (described by local concentration limitation effect on reaction).

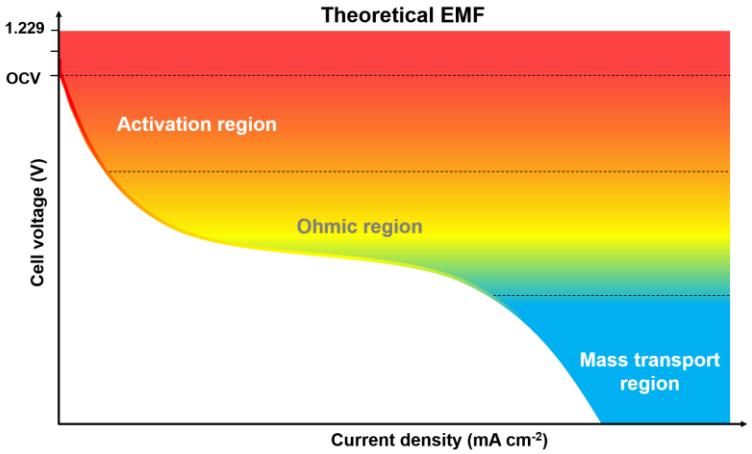

Figure 1.11 Typical polarization curve of a DEFC.

iii) **Faradaic efficiency** ε_F is associate with incomplete oxidation of ethanol and defined as

$\varepsilon_F = \frac{n_{exp}}{n_o}$

where n_{exp} and n_o are the number of electron transfer in a real and ideal reaction, respectively. For complete oxidation of ethanol into CO_2, it involves 12 electrons transfer, $\varepsilon_F = \frac{n_{exp}}{n_o} = \frac{12}{12} = 1$. If the reaction process stops at the acetic acid stage, there are only 4 e^- transfer involved. Then, $\varepsilon_F = \frac{n_{exp}}{n_o} = \frac{4}{12} = 0.3$.

Therefore, the actual efficiency of the cell is defined as [48]:

$$\boldsymbol{\varepsilon_{cell}} = -\frac{\boldsymbol{n_{exp}\, FE(j)}}{\boldsymbol{\Delta H^o}} = \frac{\boldsymbol{n_{exp}}}{\boldsymbol{n_o}} \frac{\boldsymbol{E(j)}}{\boldsymbol{E^o_{eq}}} \frac{\boldsymbol{n_o\, F\, E^o_{eq}}}{\boldsymbol{\Delta H^o}} = \frac{\boldsymbol{n_{exp}}}{\boldsymbol{n_o}} \frac{\boldsymbol{E(j)}}{\boldsymbol{E^o_{eq}}} \frac{\boldsymbol{-\Delta G^o_r}}{\boldsymbol{\Delta H^o}} = \boldsymbol{\varepsilon_F\, \varepsilon_E\, \varepsilon_{rev}} \quad \text{Eq. (1.14)}$$

1) complete oxidation of ethanol ($n_{exp} = n_o = 12$)

$$\varepsilon_{cell}^{complete} = \varepsilon_F\, \varepsilon_E\, \varepsilon_{rev} = \frac{12}{12} \times \frac{0.5}{1.145} \times \frac{1325.7}{1367.9} = 0.423$$

2) partially oxidation of ethanol ($n_{exp} = 4$)

$$\varepsilon_{cell}^{incomplete} = \varepsilon_F\, \varepsilon_E\, \varepsilon_{rev} = \frac{4}{12} \times \frac{0.5}{1.145} \times \frac{1325.7}{1367.9} = 0.141$$

It unambiguously shows that the low efficiency of DEFC is mainly ascribed to the incomplete electro-oxidation of ethanol (sluggish kinetics on EOR). As seen from Eq. (1.14), the improvement of ε_{cell} can be achieved by increasing ε_F and ε_E, in other words, to boost the number of electron transfer or lower the overpotential of the reaction and ohmic drop $R_i\, j$, respectively.

Therefore, developing highly selective catalysts towards EOR is the key to enhance the overall efficiency.

Table 1.2 shows the comparison of the energy density and conversion efficiency of ethanol with hydrogen and other alcohols being considered as fuels for fuel cells. It can be seen that in the case of complete oxidation of ethanol, the overall cell efficiency of DEFC is marginally higher compared with other fuels listed in the table.

Table 1.2 Properties and conversion efficiencies of different alcohols being considered as fuels for fuel cells, and their comparison with hydrogen [42].

Property	Hydrogen	Methanol	Ethanol	Ethylene glycol
Formula	H_2	CH_3OH	C_2H_5OH	$(CH_2OH)_2$
$-\Delta G_r^o$ (kJ /mol)	237	702	1325	1180
$-\Delta H_r^o$ (kJ /mol)	286	726	1367	1192
Energy density, LHV (kW h kg^{-1})	32.9	6.09	8.01	5.29
Energy density, LHV (kW h L^{-1})	2.96×10^{-3}	4.82	6.32	5.80
Energy stored (Ah kg^{-1}/	26,802/	3350/	3350/	3458/
Ah L^{-1})	2.40	2653	2653	3855
E_{eq}^o (V)	1.23	1.21	1.14	1.22
n_{exp}	2	4	4	8
n_o	2	6	12	10
ε_{rev} (%)	83	97	97	99
ε_F (%)	100	67	33	88
[a] ε_E (%)	57	41	44	41
$\varepsilon_{cell}^{incomplete}$ (%)	47	27	14	36
$\varepsilon_{cell}^{complete}$ (%)	57	40 [b]	43 [b]	41 [b]

[a] Assuming cell operating voltage of 0.7 V for hydrogen and 0.5 V for alcohols [42].

[b] In case complete electrochemical reaction occurs with the involvement of all electrons.

1.4.5 The possible reaction mechanism of EOR on Pt in acidic medium

The mechanism of electrooxidation of ethanol is complicated, and not fully understood. Although it involves only four typical chemical bonds (C-C, C-O, O-H and *α*-, *β*-C-H bonds), more than 40 possible highly oxidative and adsorbed intermediates can be generated [49]. The electrochemical oxidation of ethanol has been extensively studied at platinum electrodes. The pioneering work on the mechanism of EOR can be traced back to the 1950s [50], and now it has been evolved into a generally accepted dual-pathway mechanism on Pt based catalysts in acidic as shown in Figure 1.12. Various techniques have been employed for quantitative and qualitative detection of the reaction products and intermediates, such as differential electrochemical mass spectrometry (DEMS) [51-53], in situ Infrared spectroscopy IR [54], *in situ* Fourier transform infrared (FTIR) spectroscopy [51, 55-62], broadband-sum frequency generation (BB-SFG) spectroscopy [63], surface enhanced Raman spectroscopy (SERS) [64], electrochemical mass spectrometry (EC-MS) [65], high-performance liquid chromatography HPLC [66] and Density functional theory (DFT) calculation [49]. Furthermore, DFT calculations have been extensively applied for theoretical analysis and predictions concerning EOR at atomic level [49, 61, 67, 68].

It is well known that saturated ethanol molecules have two reactive sites, the OH group or *α*-C atom [69, 70], where ethanol can interact with Pt sites $*$.

$$* + \boldsymbol{CH_2OHCH_3} \rightleftharpoons * (\boldsymbol{CH_2OHCH_3}) \qquad \text{Eq. (1.15)}$$

$$* \boldsymbol{CH_2OHCH_3} \rightarrow * \boldsymbol{OCH_2CH_3} \qquad \text{Eq. (1.16)}$$

$$* \boldsymbol{CH_2OHCH_3} \rightarrow * \boldsymbol{CHOHCH_3} \qquad \text{Eq. (1.17)}$$

These are the initial steps of ethanol dehydrogenation; they take place during the forward scan when Pt sites are free, and hydrogen begins to be desorbed. The ethoxi species $*OCH_2CH_3$ is relatively stable, while the ethanol derivative $*CHOHCH_3$ can easily dehydrogenate and become acetaldehyde (AAL) [51]. Lamy [56] detected the AAL via FTIR at potential $E < 0.6$ V vs RHE.

$$* \boldsymbol{CHOHCH_3} \rightarrow \boldsymbol{CHOCH_3} \qquad \text{Eq. (1.18)}$$

$$* \boldsymbol{CHOCH_3} \rightleftharpoons \boldsymbol{CHOCH_3} + * \qquad \text{Eq. (1.19)}$$

When the potentials are in the range of $0.8\ \text{V} > E > 0.6$ V (V vs RHE), water molecules start to dissociate at Pt sites, offering OH_{ads} species for further oxidation of the ethanol residuals.

$$\boldsymbol{H_2O} \rightarrow * \boldsymbol{OH_{ads}} \qquad \text{Eq. (1.20)}$$

During this period, $*COCH_3$ and AAL can be oxidized either into acetic acid (AA).

$$* CHOCH_3 + * OH_{ads} \rightarrow CH_3COOH \quad \text{Eq. (1.21)}$$

If free Pt sites are available, further deprotonation of ethanol derivative $*CHOHCH_3$ is possible according to the following reactions.

$$* CHOHCH_3 \rightarrow * COHCH_3 \quad \text{Eq. (1.22)}$$

$$* COHCH_3 \rightarrow * COCH_3 \quad \text{Eq. (1.23)}$$

FTIR [71] explicitly demonstrated that Pt had the capability to split the C-C bond when CO_{ads} species were found at $E < 0.35$ V vs RHE, where CH_4 and CH_3CH_3 were also found. Pastor and Iwasita [69] detected some traces of methane CH_4 at 0.12 V vs RHE during the negative going potential sweep. CH_4 was produced in the hydrogen potential region during the reverse scan, due to the interaction between methyl $*CH_3$ and $*H$. As for the generation of CH_3CH_3, Chong proposed [72] that the adsorbed AAL was responsible for ethane formation during the excursion to negative potentials when AAL was adsorbed on Pt when $E > 0.3$ V. However, Pastor and Iwasita [51, 65] observed that CH_3CH_3 during the negative-going potential scan and attaining a maximum at 0.07 V vs RHE during the positive going sweep.

$$* COCH_3 \rightarrow * CO + * CH_3 \quad \text{Eq. (1.24)}$$

$$* CH_3 + * H \rightarrow CH_4 \quad \text{Eq. (1.25)}$$

$$* COHCH_3 + * H \rightarrow CH_3CH_3 + H_2O \quad \text{Eq. (1.26)}$$

When $E > 0.6$ V vs RHE, the water dissociation takes place on Pt, which can supply adsorbed oxygenated species ($-OH_{ad}$) for further oxidation of the adsorption residues of ethanol. Meanwhile, the oxidation of CO_{ads} intermediates appeared as shown by FTIR and CO stripping experiments [73].

$$* CO + * OH \rightarrow CO_2 \quad \text{Eq. (1.27)}$$

The principal reaction pathway of EOR on Pt in acidic media can be summarized in Figure 1.12. The main products of EOR on Pt are AAL, AA and minute amount of CO_2. The majority of CO_2 come from the dehydrogenation of ethanol, only a handful of CO_2 is generated direct oxidation of AAL.

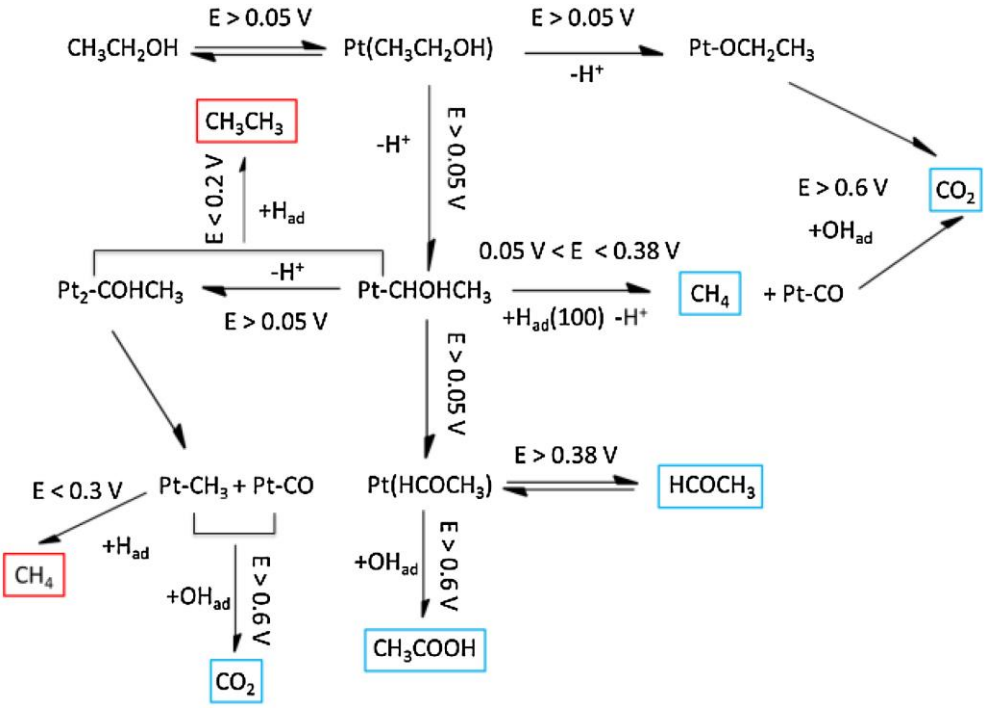

Figure 1.12 **The principal reaction pathway of EOR on Pt in acidic media [65]. The product in red and blue boxes are formed during the backward and forward scans, respectively.**

Many EOR mechanisms have been given to interpret the formation of different reaction products on Pt electrodes in acidic media [47, 56, 74, 75]. The mechanism proposed by Lamy [76] is the most commonly accepted one, as shown in Figure 1.13.

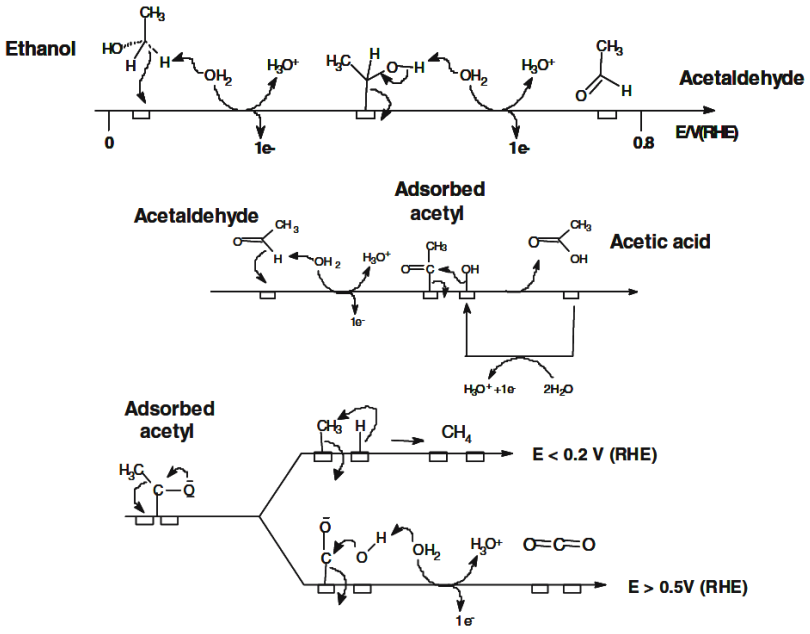

Figure 1.13 **The mechanism of EOR on Pt surface in acidic medium [76].**

The EOR on Pt/C yields AA and AAL as the major products, with CO_2 in the range of 0.7–7.5% depending on the initial concentration of ethanol [77]. Iwasita *et al*. [78] applied FTIR to methodically study the effects of ethanol concentration on the product distribution on polycrystalline Pt. They discovered some patterns: when the ethanol concentration was lower (0.05-0.1 M), AA was in high yield, CO_2 was in much lower yield and AAL was not detected. However, when the concentration was above 0.1 M, the formation of CO_2 and AA undergo a significant inhibition, AAL became favored. When the concentration increased to 0.2 M or more, AAL turned into the dominant product. Iwasita [78] deemed that the high ethanol concentration limited the availability of free Pt sites to dissociate water, thus there was no O-donor can be produced. As a result, CO_{ad} and AAL cannot be oxidized into CO_2 and AA, respectively. Iwasita [78] proposed an EOR parallel pathways (Figure 1.14) based on the effect of ethanol concentration.

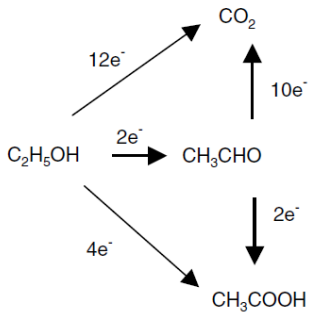

Figure 1.14 **Schematic representation of the parallel pathways for ethanol oxidation on polycrystalline Pt [78].**

The product distribution of EOR also depends on the nature of the electrolyte, such as the surface structure, pH or anion, *etc.* [60, 62, 78, 79]. Colmati *et al.* [80] applied FTIR to study ethanol oxidation on Pt (111), Pt (100) and Pt (110) electrodes in acidic medium. The FTIR spectra (Figure 1.15a [80]) showed that there was no scission of the C-C bond on Pt (111). AA was the major product, and AAL was formed as the secondary product. While on the Pt (100) electrode, CO was readily formed at low potentials and oxidized to AAL and AA at the potential range between 0.65 and 0.8 V. On the contrary, the Pt (110) electrode exhibited the highest reactivity to break the C-C bond, leading to the formation of CO_{ads}, coming from ethanol and AAL at high rate at any potentials [80]. While in alkaline solution (Figure 1.15b [81]), the selectivity of CO_2 was much lower, but surfaces deactivated fast because of the fast reduction of AAL, which readily polymerizes and strongly adsorbed on the Pt surface [81].

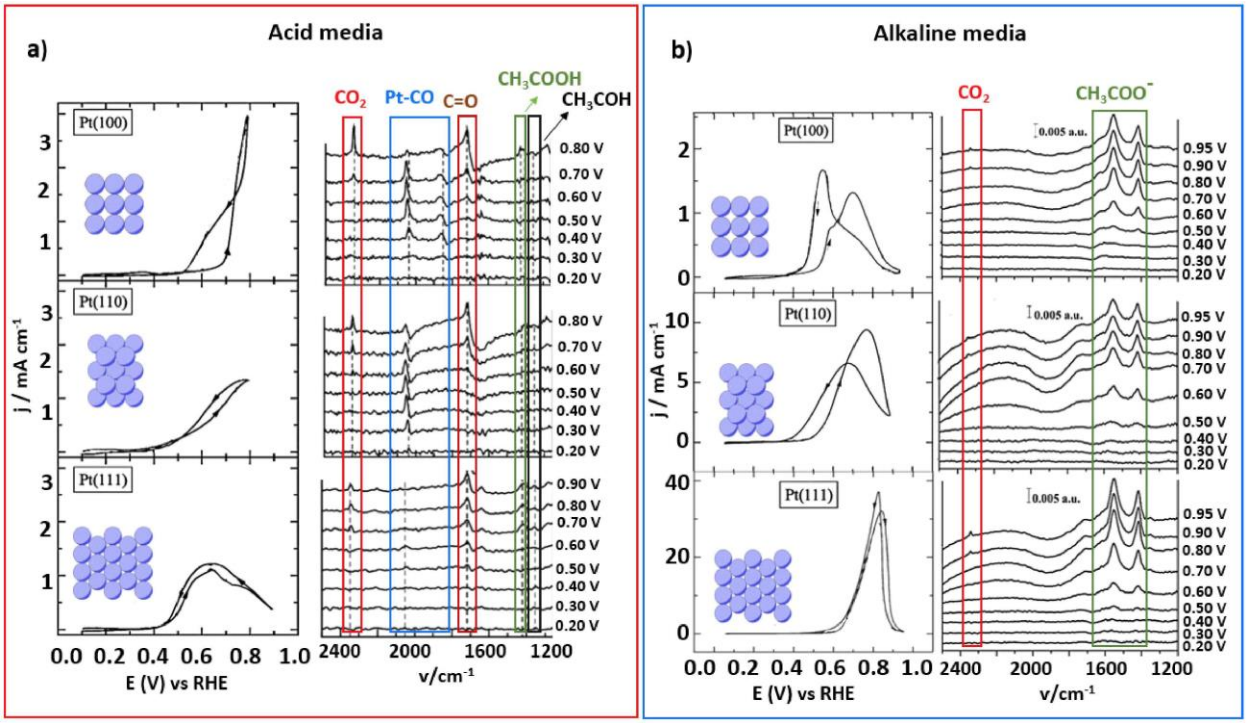

Figure 1.15 **Cyclic voltammograms at 50 mV s^{-1} (left) and FTIR spectra at different potentials (right) for Pt (111), Pt (110) and Pt (100) electrodes in a) 0.1 M $HClO_4$ + 0.2 M EtOH and b) 0.2M EtOH+0.1M NaOH. a) from [80], b) from [81].**

1.5 Literature review of the anode catalysts in DEFCs

In DEFC system, the crucial part in determining the catalytic activity is the membrane electrode assembly (MEA) [82]. As one of the key components of MEA, the catalyst is the site where the core reaction takes place - EOR. Normally, the major problems of DEFCs, such as the overhigh anodic polarization potential or low output voltage, are caused by the anode catalyst. The anode catalyst significantly affects the EOR rate.

The research on the anode catalysts for EOR can go back to last century. At that time, the anode catalyst was pure platinum wire, foil or platinized metal. After one hundred years' development, the catalysts have been expanded from bulk material to nanosized particles, from single Pt to multi-component. Here, the different anode catalysts will be reviewed briefly.

1.5.1 Unitary Pt catalysts

Up till now, platinum is demonstrated as the most active and stable monometallic noble metal with relatively high electrocatalytic performances towards the ethanol oxidation [25, 34], especially in acidic media. Nevertheless, the catalytic activity of Pt drops rapidly because it is poisoned by the intermediate product CO_{ads}. Besides, other products resulting from the partial

ethanol oxidation such as AAL and AA were also detected by electro-modulated infrared reflectance spectroscopy [56]. The research direction of unitary Pt catalyst is focused on the mechanism of different Pt lattice faces on EOR and synthesis of size adjustable and shape controllable Pt nanoparticles.

It is well known that EOR is a structure sensitive reaction [62, 80, 83]. The surface structure and material of the catalyst greatly affect the EOR in acidic media. Different platinum single crystals Pt (*hkl*) with low indices play different roles on the C-C cleavage. The FTIR results from Buso-Rogero *et al.* [62] have confirmed that: the dominating product of ethanol oxidation on (111) preferentially oriented Pt nanoparticles was AA, the amount of CO_2 can be considerably ignored, which was in agreement with Lai *et al.* [60] While nanoparticles with a fraction of Pt (100) terrace had the best capability of cleavage of the C-C bond by generating the CO_{ads} species, which ultimately oxidize to CO_2. Besides, Pt (100) electrode had the highest electrocatalytic reactivity at high potentials; nevertheless, Pt (111) electrode was more productive at low potentials. Buso-Rogero *et al.* [62] also pointed out the polyoriented Pt nanoparticles, which had an intermediate behavior between the (100) Pt and the (111) Pt nanoparticles, demonstrated the highest selectivity towards CO_2. Regarding the effect of stepped surface, Colmati *et al*. [83] used FTIR technique to study on stepped Pt single crystal electrodes in acid media. They discovered the presence of (100) steps on the (111) terraces did not afford considerable improvement of the activity of the surfaces, while (110) steps had a double effect on EOR (Figure 1.16). When the potentials $E<0.7$ V *vs* RHE, the C-C bond was split and the CO_{ads} species oxidized as well. Whereas when $E>0.7$ V *vs* RHE, the (110) step was not only can cut the C-C bond, but also can oxidize ethanol into AAL and AA. They also found Pt (554) electrode had the highest electrocatalytic activity for EOR.

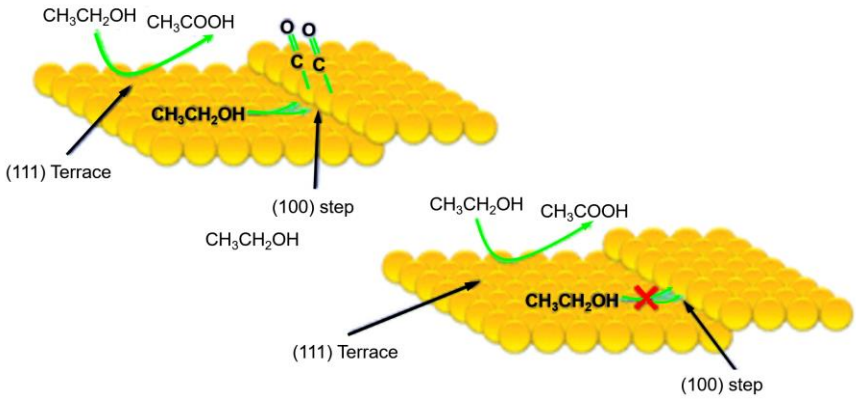

Figure 1.16 **The role of the steps in the cleavage of the C-C bond during ethanol oxidation on platinum electrodes [83].**

Generally, the particle size effect on the specific activity of Pt catalysts for various electrocatalytic reactions is not negligible when the particle sizes are smaller than 5 nm. Antolini *et al*. [84] investigated the particle size effect for EOR on carbon supported catalysts with Pt particle size varying from the range of 2.2 nm to 3.6 nm via linear sweep voltammetry (LSV) and chronoamperometry (CA) in half-cell DEFC. They observed that the mass activity (MA) and specific activity (SA) for ethanol oxidation displayed a maximum at a Pt particle size of 2.6 nm (Figure 1.17). Zhu group [85] synthesized three Pt/MWCNTs catalysts with average particle size of 1.7, 2.4 and 4.0 nm and they studied the size effect on the catalytic activity towards CO as well as ethanol oxidation by cyclic voltammetry (CV). The results showed that (1) in CO stripping experiments, the peak potentials of CO oxidation shifted significantly to the higher positions (0.516, 0.541 and 0.562 V) along with the size decreased. The apparent activation energy increased with the decreasing size. (2) An increase of the MA, but a decrease of SA was observed with the decrease of Pt particle size. Lu *et al.* [86] prepared four Pt/C different Pt particle size (2.10, 3.18, 3.73, 4.17 and 4.80 nm) to study the effect of particle size on EOR. The result manifested that the size of Pt greatly affected the EOR performance. The catalyst with a particle size of 3.2 nm demonstrated the best electrocatalytic activity for the ethanol oxidation. Yahikozawa [87] revealed that the essential reason for the particle size effect was the electronic state of the platinum particles.

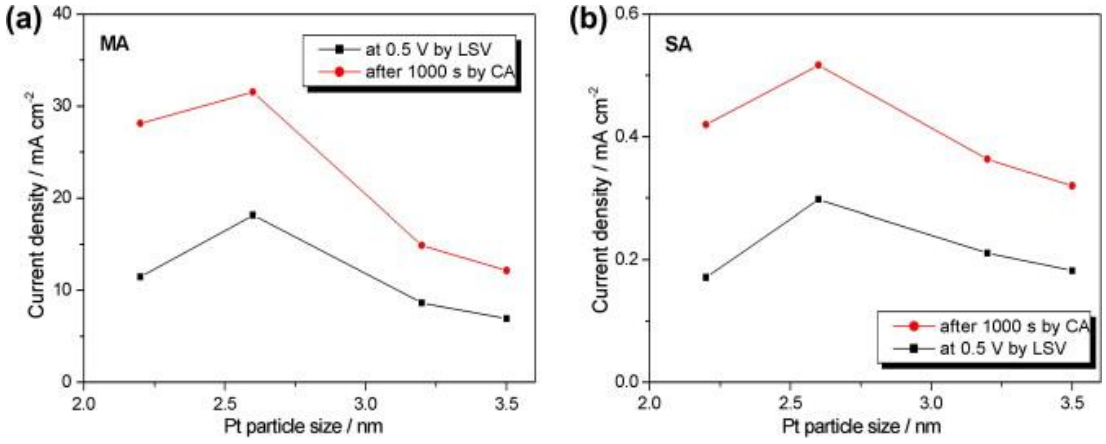

Figure 1.17 **Dependence of the current density in the solution of 1 mol L^{-1} ethanol + 0.1 mol L^{-1} $HClO_4$ at 0.5 V (LSV) and the steady state current density after 1000 s (CA) [84].**

1.5.2 Binary Pt-based catalysts

Regarding the performance of the single unit Pt, monometallic Pt is no longer state-of-the-art material. In order to improve the kinetics of ethanol oxidation on Pt, incorporation of another

metal with Pt is found to be an effective way to reduce the overall usage of expensive Pt and to address the problem of CO poisoning.

1.5.2.1 Bimetallic Pt-M catalysts

Much effort has been devoted to developing the bimetallic alloys Pt-M such as PtSn [25, 48, 54, 73, 76, 88-95], PtRu [25, 55, 89, 96], PtRh [97], PtCo [98], PtNi [99]. Amongst these bimetallic alloys, tin and ruthenium appear to be very promising in enhancing the activity and lowering the onset potential of EOR, especially tin. Zhou *et al.* [90] conducted the CV measurements and single DEFC test to study a series of Pt-M alloys on the EOR. The result showed the electrooxidation activity of ethanol over Pt decreased in the following order: Pt_1Sn_1/C>Pt_1Ru_1/C>Pt_1W_1/C>Pt_1Pd_1/C> Pt/C. From Zhou's comprehensive research [25, 90, 93, 94] (Figure 1.18), it indicated that at a current density of 50 mA/cm^2, the PtSn cell voltage and the power density were increased by about three and five times respectively, compared with PtRu/C and Pt/C, which again confirmed that PtSn had a better performance towards EOR than that of PtRu. Song *et al.* [92] also obtained similar result: PtSn/C had a higher fuel utilization coefficient and higher fuel cell efficiency than PtRu/C. As for the onset potential, Zhu *et al.* [94] reported the onset potential for PtSn/C, PtRu/C and Pt/C were 380 mV, 200 mV and 85 mV vs DHE (Dynamic hydrogen reference electrode), respectively. Although Wang [89] found that PtRu/Vulcan and Pt_3Sn/Vulcan demonstrated a similar highly active for ethanol oxidation by the CV experiment combined with DEMS, the production yields of CO_2 on PtRu/Vulcan (1%), Pt_3Sn/Vulcan (1.2%) decreased in comparison with Pt/ Vulcan (1.3%). According to Motoo [100], PtRu was more efficient for methanol oxidation.

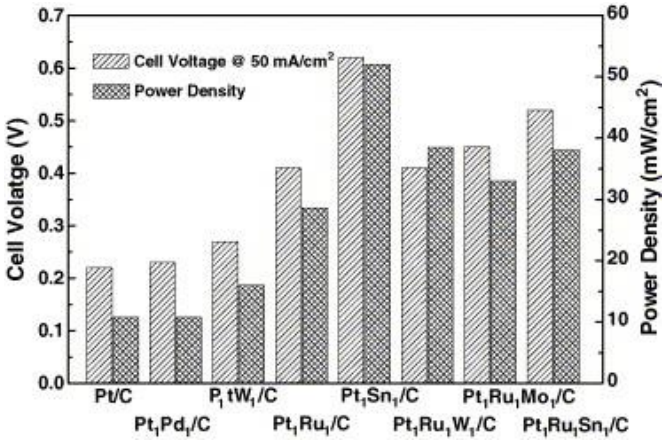

Figure 1.18 The performance of Pt-based catalysts towards ethanol oxidation in single DEFC (Electrolyte: 0.5 M H_2SO_4 solution containing 1.0 M ethanol, T_{cell} = 90 °C) [92].

Song *et al.* [91] compared the product distributions on Pt_2Sn_1/C and the commercial Pt_1Ru_1/C, and they observed the former had a better catalytic activity than the latter. The authors ascribed the higher performance of PtSn catalyst to the capability of Sn to oxidize ethanol to a larger extent than Ru, and they presented a mechanism (Figure 1.19) for the role of Sn in Pt catalysts for the EOR.

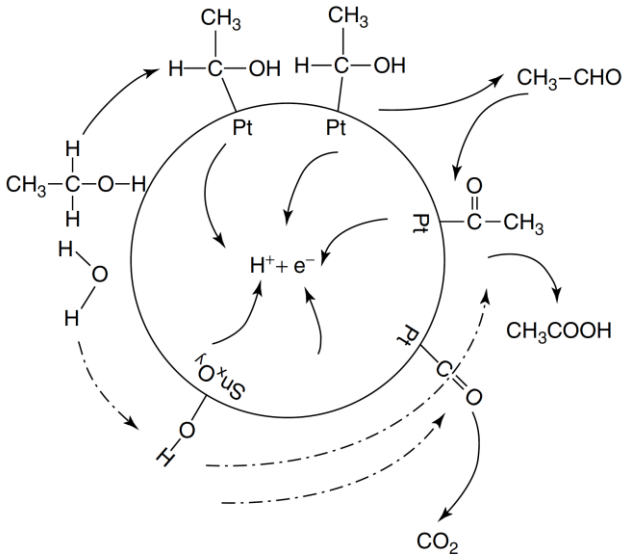

Figure 1.19 Proposed mechanism for ethanol electrooxidation on Pt–Sn/C catalyst [91].

The enhancement of bimetallic PtM catalysts can be ascribed to two main effects:

(1) *bi*-functional mechanism (Figure 1.19) which was originally proposed by Watanabe and Motoo [101]. The added metal in the vicinity of Pt nanoparticles can dissociate water at lower potentials (0.4-0.6 V vs. RHE, lower than Pt 0.8 V vs. RHE), and provide oxygen-containing species (OH_{ad}) to mitigate the poisonous intermediates (CH_x and CO_{ad}), liberating Pt active sites consequently. This CO oxidation goes through a Langmuir-Hinshelwood mechanism as the equations below:

$$\boldsymbol{M + H_2O \rightarrow M - OH_{ads} + H^+ + e^-} \qquad \text{Eq. (1.28)}$$

$$\boldsymbol{M - OH_{ads} + Pt - CO_{ads} \rightarrow Pt + M + CO_2 + H^+ + e^-} \qquad \text{Eq. (1.29)}$$

And/or **(2) The electronic interaction** between two different metals-shift of *d*-band center [102-104], which is induced by the lattice dilation or compression (strain effect) [105] and by orbital interaction between the two different metal (electronic or ligand effect) [99, 106-108]. According to the *d*-band model proposed by Nørskov *et al*. [106, 109], the reactivity of metals on the adsorption strength of adsorbates can be rationalized in terms of d-band center (ε_d) respect to the Fermi level (E_F). When the ε_d of metal far away from the E_F (*e.g.,* larger ΔE (E_F - ε_d), as

shown in Figure 1.20, the *d*-states of metal become occupied and the anti-bonding states decrease. As a result, the bandwidth *W* decreases. The binding strength between the metal and the adsorbates become weaker. In this case of the EOR, this downshift of *d*-band center can decrease the energy of the CO binding on Pt, resulting in the decrease of CO poisoning.

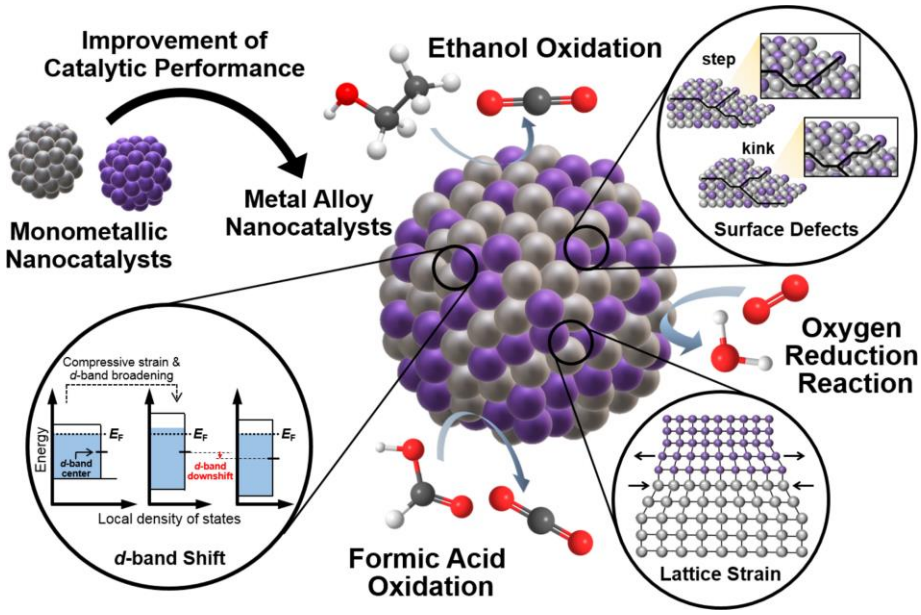

Figure 1.20 **Illustration of the d-band shift and surface defects of metal alloy for enhancement of the electrochemical activity [110].**

It is well known that temperature has an influence the performance of PtM on the EOR. According to R. Gonzalez [111], when *T*=70 °C, the DEFC cells with PtRu and Pt_3Sn demonstrated the same activity for ethanol oxidation. Whereas when *T*>70 °C, the cells with Pt_3Sn had better performance than that of PtRu. Gonzalez explained that at low temperatures and/or low current densities, the bifunctional mechanism prevailed. While at high temperatures, electronic effect between Sn and Pt preponderated over the *bi*-functional mechanism, which benefited the CH_3CH_2OH adsorption and the C-C breakage. Zhu [112] evaluated the performance of five catalysts Pt_5Sn_1/C, Pt_4Sn_1/C, Pt_2Sn_1/C, Pt_3Sn_2/C and Pt_1Sn_1/C towards EOR activity and DEFC single cell. It showed that Pt_3Sn_2/C was more suitable in DEFC at 60 °C and Pt_2Sn_1/C at 90 °C. At 75 °C, Pt_2Sn_1/C and Pt_3Sn_2/C demonstrated the best performance, since they had the similar performance.

Besides, the composition of the electrode material also plays a key role in the catalytic performance of ethanol electro-oxidation. Gonzala group [113] found that the catalytic activity towards the EOR increased in the following order: Pt/C<Pt_3Sn/C<Pt_1Sn_1/C. While the onset potential showed the opposite trend. The FTIR and DEMS analysis revealed that the C-C

cleavage took place at the same potential whatever Sn loading was. But the amount of the C-C bond scission decreased with the increasing of Sn loading. It is agreed with Tsiakaras's [114] result: five Pt-Sn catalysts (Pt_1Sn_1, Pt_2Sn_1, Pt_3Sn_1, Pt_3Sn_2, Pt_4Sn_1) were tested in single DEFC and it was observed that the performance of power density displayed a "volcano-type" behavior along with the increasing Sn content at different operation temperatures. Tsiakaras [114] pointed out the catalysts with Sn content ranging between 33 at% and 45 at% had the highest values of maximum power density. Nevertheless, Lamy *et al*. [73] reported the optimum composition of Sn in PtSn alloy was in the range of 10-20 at. %, which was lower than Gonzala and Tsiakaras' data [113-114].

Furthermore, the carbon support has a distinctive effect on the activity towards CO stripping and the EOR. J. Asgardi *et al*. [115] found that the PtSn supported catalysts (Pt_1Sn_1/C and Pt_3Sn_1/C) on carbon black showed higher catalytic activity than those supported on carbon nanofibers (Pt_1Sn_1/CNF and Pt_3Sn_1/CNF). Specifically, Pt_1Sn_1/C exhibited the best capability for ethanol electrooxidation in a DEFC, in terms of power density. Whereas the onset potential for CO electrooxidation decreased in the order: Pt_3Sn_1/C> Pt_3Sn_1/CNF>Pt_1Sn_1/C>Pt_1Sn_1/CNF.

Based upon the combined results of Lamy [54], Zhou [25, 90, 93, 94, 112] and Song [91], Tsiakaras [92] proposes a possible mechanism of EOR on PtSn catalysts as shown schematically in Figure 1.21. The *bi*-functional role of Pt and Sn is demonstrated in the steps tagged with stars.

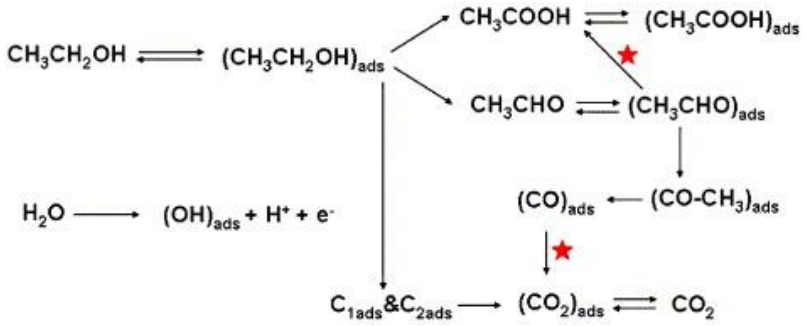

Figure 1.21 The schematic diagram of mechanism of EOR on PtSn catalysts [92].

Until now, bimetallic catalysts PtSn and PtRu have been regarded as the most efficient catalysts for EOR [25, 34, 116, 117], which give a higher Faradaic current of ethanol oxidation than pure Pt. Regrettably, the high current is predominantly contributed to high yield of incomplete oxidation product AA. Or rather, it was found that PtSn [48, 73, 89] and PtRu [55, 89, 96] catalysts interrupt the splitting of C-C bond, and the selectivity towards CO_2 is still low.

Recently, rhodium has drawn intensive attention due to its great potential of C-C bond scission during EOR [97, 121-122]. As illustrated in the diagram below (Figure 1.22a), a five-member ring oxametallacyclic configuration was formed on Rh surface during ethanol dissociation, which can split the C-C bond efficiently. While η^2–CH_3CHO (Figure 1.22b) is preferred on Pt or Pd surface [118-120], which the C-C bond can barely be cut. Lamy *et al*. [121] studied the electrocatalytic oxidation of ethanol at Ir and Rh electrodes in $HClO_4$ solutions by means of in-situ FTIR. The analysis showed that major product at Ir electrode was AA, while CO_2 was the primary product at Rh electrodes. However, Rh is inactive for ethanol oxidation [122].

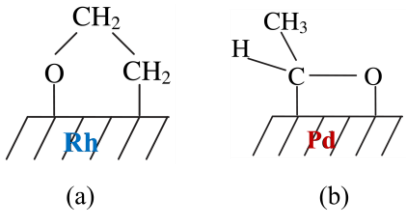

Figure 1.22 **Schematic diagram of an oxametallacyclic structure formed on Rh (111) surface during ethanol dissociation (a) and η^2–CH_3CHO formed on Pd (111) surface (b) [118].**

PtRh/C-based catalysts show promising results in increasing current density for ethanol oxidation and enhancing CO_2 yield under mild operating conditions (T≤ 90 °C) [97, 123-127]. After alloying Rh with Pt, there is a down-shift of the Pt 5 *d*-band center, which is mainly caused by the lattice mismatch, and this strong electronic interaction between Pt and Rh atoms leads to a reduced adsorption strength of reaction absorbates on the Pt surface [128]. F.C. Nart *et al*. [123] detected CO_2 on all PtRh catalysts by DEMS and FTIR and the activities for CO_2 production was in decreasing order: $Pt_{73}Rh_{27}$>$Pt_{55}Rh_{45}$>Pt>$Pt_{90}Rh_{10}$≅Rh. But the normalized electric currents of EOR decreased along with increasing Rh content, and the electrocatalytic activity of EOR on $Pt_{90}Rh_{10}$ was a little bit higher than that of pure Pt. The authors also elaborated the reason why $Pt_{73}Rh_{27}$ electrode had a high CO_2 production was because it had the right balance between the number of Rh sites for the C-C bond cleavage and the number of Pt sites for ethanol dissociative adsorption. When Rh content was high, there were not enough Pt active sites and therefore the adsorption of ethanol was restrained. On the other hand, with low Rh content, there might be no adequate Rh sites to effectually break the C-C bond. Delpeuch *et al.* [129] and Cantane *et al*. [128] also found the Faradaic current on PtRh/C or Pt_2Rh_1/C were lower than that of on Pt/C, although the CO_2 selectivity improved. While some others have just the opposite opinions-the overall performances improve with the addition of Rh to Pt. Lima *et al*. [124] observed the currents of ethanol oxidation were just a little bit higher on PtRh catalysts with respect to pure Pt, but with much higher CO_2 production ratio and faster CO

electrooxidation. The CO oxidation was more obvious on catalysts Pt-Rh/C (40 wt.%) with larger crystallite sizes. The authors attributed the beneficial effect to a lower Pt-CO adsorption strength and/or higher water activation, which facilitates the CO-O coupling. Conversely, the higher CO_2/AAL production ratios were more pronounced on in catalysts with a smaller crystallite size. Bergamaski *et al*. [125] synthesized $Pt_{83}Rh_{17}$, $Pt_{70}Rh_{30}$, $Pt_{47}Rh_{53}$ catalysts by the formic acid method and they recorded that the faradaic current efficiency for the oxidation of ethanol to CO_2 on $Pt_{47}Rh_{53}$/C was 6.25-fold higher than that of Pt/C at 0.7 V vs. RHE. Sun *et al*. [97] got a much better result than that of Bergamaski *et al*. [125]. Sun group prepared four Pt_xRh_y catalysts with different Pt/Rh atomic ratio of 3:1, 1:1, 1:2 and 1:3 on the reduced graphene oxide (RGO). Their *in-situ* FTIR results manifested that Pt_1Rh_1/RGO had the highest activity towards EOR as well as the C-C bond breakage. The CO_2 selectivity of EOR on Pt_1Rh_1/RGO was 16.2 times greater than that of commercial Pt/C at 0.4 V (SCE). Sun proposed an EOR mechanism on Pt_1Rh_1/RGO *vs* Pt/C, as depicted in Figure 1.23. Zhu *et al*. [130] also recorded the optimal Pt/Rh molar ratio was 1:1. The catalyst PtRh/nanowires/C exhibited 3-fold improvement in catalytic activity and excellent durability by comparison with commercial Pt/C and Pt nanowires/C. In XPS of PtRh alloy, they observed the Pt 4*f* shifted to higher position and Rh negatively shifted synchronously. Meanwhile, they also noticed the *d*-band center moved downward. The authors ascribed this electronic effect as one of the reasons for the enhancement of EOR. The other reason they considered is the oxophilicity of Rh (*bi*-functional mechanism). While Gupta *et al.* [131] illustrated the optimal catalyst composition for EOR was the $Pt_{76}Rh_{24}$ electrode. Almeida [132] reported a similar result that Pt_3Rh_1 had the best catalytic activate based on polarization current density, while Tabet-Aoul *et al.* [133] synthesized catalysts by pulsed laser deposition method and they found that PLD-synthesized $Pt_{90}Rh_{10}$/CNT was superior to $Pt_{75}Rh_{25}$/CNT, $Pt_{45}Rh_{55}$/CNT and $Pt_{25}Rh_{75}$/CNT. Tabet-Aoul *et al.* [133] also pointed out that when Rh content was higher than 55 at%, EOR was impeded due to the insufficient Pt active sites. Alcaide *et al*. [134] used electrodeposition method to fabricate catalysts $Pt_{60}Rh_{40}$ and $Pt_{80}Rh_{20}$. They noticed that $Pt_{60}Rh_{40}$ had the highest activities for the CO and the ethanol electrooxidation, compared with $Pt_{80}Rh_{20}$, Rh and Pt. Besides the apparent activation energy for ethanol oxidation were established: $Rh>Pt>Pt_{80}Rh_{20}>Pt_{60}Rh_{40}$, which demonstrated that $Pt_{60}Rh_{40}$ was the most active.

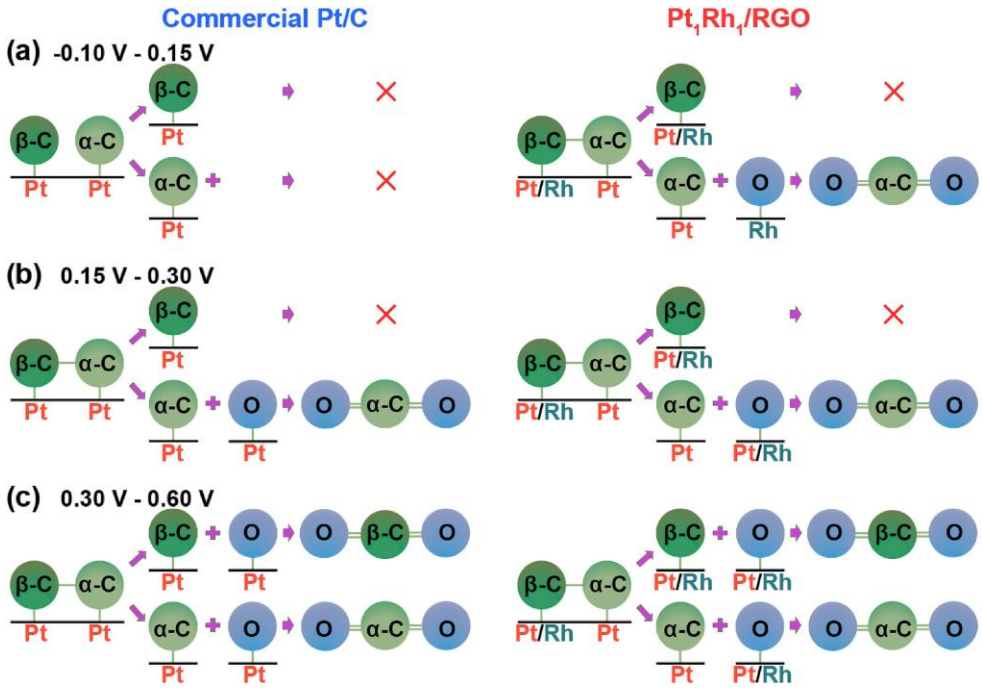

Figure 1.23 **Diagram of EOR mechanism on commercial Pt/C and Pt_1Rh_1/RGO catalysts at the potential ranges of (a) -0.10-0.15 V, (b) -0.15-0.30 V, (c) 0.30-0.60 V [97].**

1.5.2.2 Pt-MO_x catalysts

After years of striving on anode catalysts, substantial progress has been achieved on improving the electrocatalytic activity of EOR. However, a further increase in electrochemical activity and CO_2 selectivity is needed for DEFCs to become commercially [135]. Durability, on the other hand, is still a big challenge. The usual approach to enhance the performance of Pt towards EOR is to incorporate Pt with oxophilic metal oxides (MO_x), which can facilitate the formation of OH_{ad} species, for promoting the oxidation of poisoning CO_{ad} and CH_x intermediates (*bi*-functional mechanism). Among the numerous metal oxides, only those who meet the following requirements can be considered for fuel cells applications [136].

- *High stability in acidic media*. This is the precondition for the acid DEFCs that the MO_x cannot dissolve in acidic solutions.
- *High resistance against electrochemical corrosion and oxidation*. If the MO_x are not electrochemically stable enough under operating conditions of fuel cell, the materials will peel off from the support and MO_x will agglomerate, thus resulting in the degradation of catalytic performance.

- *Compatibility with the catalyst layer*. MO_x should bond well with noble metal nanoparticles so as to maintain adhesion and a conductive link to noble metal nanoparticles to form a good three-phase boundary.
- *Oxophilicity*. MO_x should demonstrate a good tolerance to CO poisoning [137], by providing enough OH species at lower potentials for removal of adsorbed CO.

In consideration of the above-mentioned selection criteria, metal oxides, such as SnO_2, CeO_2 and MnO_2 were employed for Pt based DEFCs.

(1) Pt-SnO_2 catalysts

Tin oxide (SnO_2), an *n*-type oxide and wide-band gap semiconductor (3.6 eV) with its transparency and relatively high electronic mobility and conductivity [138-141], has been widely applied for optical, electrochemical and catalytic applications, such as solar cells [142], lithium-ion batteries [143], transparent conductors and gas sensors [144]. SnO_2 is the most stable compound in Sn-H_2O system in polymer electrolyte fuel cells [145]. Recent studies have shown that SnO_2 is the promising catalyst support for Pt based acid-DEFCs applications [46, 135, 137, 146-159], due to its superior performance of providing hydroxyl groups to migrate CO-like intermediates on Pt active sites (*bi*-functional mechanism).

Teng *et al*. [146] synthesized alloy $Pt_{70}Sn_{30}$/C, $Pt_{46}Sn_{54}$/C catalysts and non-alloyed Pt_{70}-$(SnO_2)_{30}$/C and Pt_{46}-$(SnO_2)_{54}$/C core-shell catalysts by via a “surfactant-free” polyol process. They found that composition and crystalline structure of the Sn element had a great influence on the product distribution of EOR: non-alloyed Pt_{46}-$(SnO_2)_{54}$/C core-shell electrode established a stronger ability of the C-C bond scission of ethanol than the rest catalysts. The CO_2 formation found on Pt_{46}-$(SnO_2)_{54}$/C electrode was 2.0- and 4.1-fold higher than those of the intermetallic counterpart and commercial Pt/C (ETEK). Hu *et al*. [149] synthesized a series of Pt-*n*SnO_x/N-doped carbon nanocage (NCNC) (*n*=0, 0.3, 0.5, 0.8, 1.0 and 1.7). The catalyst with Sn/Pt ratio of 0.5 exhibited superior EOR performance and CO resistibility in 0.5 mol L^{-1} H_2SO_4 solution with remarkable mass activity of 1187 mA mg_{Pt}^{-1} and high durability. Zhu *et al*. [147] prepared SnO_x/Pt (111) catalysts with different SnO_x coverage (37, 40 and 48 at%) for EOR. The results demonstrated that the activity of SnO_x/Pt catalysts strongly depended on the surface SnO_x coverage. When SnO_x coverage was 40%, SnO_x/Pt(111) catalyst displayed a considerably higher activity as well as a lower onset potential at *ca*. 0.25 V. Spinacé group [158] used an alcohol-reduction approach to fabricate $PtSnO_2$/C with Pt:SnO_2 molar ratios of 9:1, 3:1 and 1:1. The result showed that the $Pt_3(SnO_2)$/C established the best DEFC performance in comparison with Pt_3Sn/C and other $PtSnO_2$ catalysts. Okazaki *et al*. [150] synthesized Pt-SnO_2/C catalysts

with various Sn/Pt molar ratios (from 0 to 1.4) by an electron beam irradiation method. The catalyst with Sn/Pt molar ratio of 0.13 exhibited the promoted electrocatalytic activity for EOR in acid medium. Wang *et al*. [154] applied cross-beam pulsed laser deposition (CBPLD) technique to prepare $PtSnO_2$/CNT under different Helium background pressures (vacuum, 0.5 and 2 Torr). The catalyst Pt $(SnO_2)_{0.5T}$/CNT exhibited the highest specific mass activity and durability, 1.6 and 2.2 times greater than those on CNT/Pt electrodes, respectively. Zhang *et al*. [160] synthesized core-shell (CNT@SnO_2)/Pt catalyst via a simple chemical-solution route. The CV and durability test showed that (CNT@SnO_2)/Pt represented higher catalytic activity for ethanol electro-oxidation than that of Pt/CNT. Zhang attributed the excellent performance to two reasons: (i) the high conduction of CNT made SnO_2 more easily to transform CO_{ads} into CO_2 (Figure 1.24). (ii) the strong chemical interaction between Pt and SnO_2.

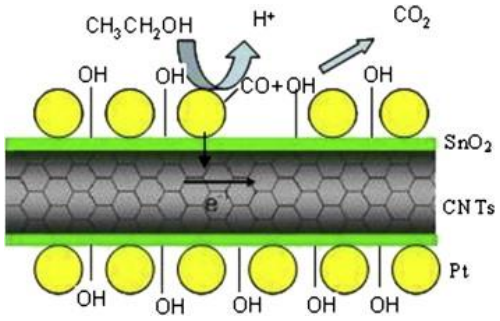

Figure 1.24 Schematic diagram of EOR on Pt/SnO_2/CNT [160].

The substrate also plays an indispensable role in EOR. Pang *et al.* [137] used sol-gel and simple chemical method to construct four Pt/SnO_2/CNT/graphite with different mass ratio of CNT to SnO_2 (R_{CNTs/SnO_2} =1:12.6, 1:6.3, 1:4.3 and 1:3.2). The results of CV, durability test, electrochemical impedance spectroscopy (EIS) and the long-term cycle stability indicated that the catalysts Pt/SnO_2/CNT/graphite with R_{CNTs/SnO_2} of 1:6.3 exhibited the best performance. Qu *et al*. [148] used multi-step microwave polyol process to prepare a layer-by-layer SnO_2/Pt/ graphene catalyst. The result revealed that SnO_2 indeed improved the durability and stability of Pt catalyst, all the SnO_2/Pt/G catalysts had higher durability than that of Pt/G. The authors attributed the good performance to the metal-support interaction within the $PtSnO_2$/G ternary hybrids. Besides, it indicated that the content of graphene has a significant influence on the EOR activity. The catalyst SnO_2/Pt/G_{30} had best the EOR activity, followed by SnO_2/Pt/G_{40}, then SnO_2/Pt/G_{20}. Ryan *et al*. [153] used an ethylene glycol reduction method for synthesis of $PtSnO_2$- single-walled carbon nanotube (SWNT) with different mass ratio of SWNT to $SnCl_2 \cdot 2H_2O$ (1:10, 1:50 and 1:250). The $PtSnO_2$-SWNT (1:50) demonstrated the highest current density for EOR. The authors believed this ratio allowed for optimization of the bifunctional

mechanism to increase surface specific activity without oversaturation of SnO_2 to cause a decline in electron conductivity of the material [153].

(2) Pt-CeO_2 catalysts

Cerium oxide (or Ceria), with a wide bandgap (E_g = 3.15 eV for coarse-grained material) [161], is one of the most reactive rare earth oxides. CeO_2 crystallized in fluorite structure, whose cations can reversibly transform between +3 and +4 ($Ce^{3+} \leftrightarrow Ce^{4+}$) by releasing lattice oxygen at the catalyst surface in oxygen-lean conditions. CeO_2 is well known for its high oxygen storage capacity [162, 163]. The reaction can be expressed, following the Kröger-Vink notation [162, 163].

$$\mathbf{2}\,\boldsymbol{Ce}_{\boldsymbol{Ce}}^{\times} + \boldsymbol{O}_{\boldsymbol{O}}^{\times} \longrightarrow \boldsymbol{V}_{\boldsymbol{O}}^{\bullet\bullet} + \mathbf{2}\,\boldsymbol{Ce}_{\boldsymbol{Ce}}^{\prime} + \frac{\mathbf{1}}{\mathbf{2}}\boldsymbol{O}_{\mathbf{2}} \qquad \text{Eq. (1.30)}$$

Due to the oxygen vacancies and the lattice oxygen on CeO_2 surface, it strengthens CeO_2's ability for CO removal [164] and adsorption of oxygenated species, *e.g.,* -OH [165]. In addition, the oxygen vacancies also can boost the interaction between CeO_2 and Pt to form a strong metal oxide interaction that can modify the electronic structure of Pt, improving the catalytic activity [166]. $PtCeO_2$ based catalysts have been used as catalytic converters in the automotive exhaust emission, like NO reduction, stem reforming of ethanol and water-gas-shift (WGS) [167].

Nowadays, CeO_2 has been investigated extensively in ethanol oxidation in acidic media [161, 168-175]. Cordeiro *et al*. [161] synthesized four $PtCeO_2$/C/Glassy carbon discs (23.5 wt.% Pt and 76.5 wt.% Ce) electrocatalysts under different temperatures (60 ℃, 400 ℃, 600 ℃ and 800 ℃) with different bandgaps. They discovered that the promotional effect of the CeO_2 nanocrystals was affected by calcination temperatures. The $PtCeO_2$/C/GCE catalysts calcined at 600 ℃ demonstrated a much higher mass activity (1.13 mA mg_{Pt}^{-1}) and better durability than that of Pt/C (0.46 mA mg_{Pt}^{-1}) and other $PtCeO_2$ catalysts. The authors suggested that calcination strengthened the metal-support interaction between CeO_2 and Pt, meanwhile it also boosted the electron transportation to catalyst due to the shrinkage of CeO_2 bandgap, consequently increasing the oxidation of the vigorous adsorbates. Wang *et al*. [169] applied CBPLD technique to prepare three $PtCeO_2$ catalysts under different Helium background gas pressures (vacuum, 0.5T and 2T). The results indicated that $(PtCeO_2)_{0.5T}$ displayed highest peak current density and durability. De Souza *et al*. [170] utilized polymeric precursor method to prepare Pt-CeO_2 catalysts with different mass ratios of Pt/CeO_2 (3:1, 2:1, 1:1, 1:2, 1:3). They observed that all the Pt-CeO_2/C catalysts, except Pt-CeO_2/C (1:1), exhibited enhanced performance in comparison with Pt/C. The catalyst Pt-CeO_2/C (1:3) demonstrated a higher ethanol oxidation activity and

stability, which was superior to the other three catalysts, even better than Pt-Ru/C (ETEK). The authors attributed its higher catalytic activity to the strongly bounded intermediates, and high utilization of Pt. From the results of Kakaei *et al*. [175], it showed that $PtCeO_2$/sulfonated reduced graphene oxide (SRGO) revealed a good performance for EOR, in terms of high current density, lower activation energy and lower ionic resistance with respect to Pt/ SRGO and Pt/RGO. Zhang and Shen [173] used one-pot method to synthesis of $PtCeO_2$/graphene nanosheet (GNS) hybrids. The result indicated that Pt-CeO_{2-x}/GNS hybrids presented a better catalytic activity and durability for methanol, ethanol, ethylene glycol, and glycerol electrooxidation compared with the Pt/GNS catalyst. The author attributed the excellent performance of the Pt-CeO_{2-x}/GNS catalyst to the synergistic effects of the catalyst constituents: the GNSs facilitated the electron transport and offered a large surface area. CeO_2 promoted the EOR by strong metal support interaction SMSI associated with the charge transfer from ceria to Pt (downshift of Pt 5*d*-band center), the existence of Ce^{4+}/Ce^{3+} redox couple (Eq. (1.31) and Eq. (1.32)).

$$\boldsymbol{Ce_2O_3 + 2\,H_2O \rightleftharpoons 2CeO_2 + 2H^+ + 2\,e^-} \quad \text{Eq. (1.31)}$$

$$\boldsymbol{Pt - CO_{ads} + 2CeO_2 + 2H^+ + 2\,e^- \rightarrow Ce_2O_3 + Pt + CO_2 + H_2O} \quad \text{Eq. (1.32)}$$

and *bi*-functional effect (Eq. (1.33) and Eq. (1.34)):

$$\boldsymbol{CeO_{2-x} + H_2O \rightarrow CeO_{2-x} - OH_{ads} + H^+ + e^-} \quad \text{Eq. (1.33)}$$

$$\boldsymbol{Pt - CO_{ads} + CeO_{2-x} - OH_{ads} \rightarrow Pt + CeO_{2-x} + CO_2 + H^+ + e^-} \quad \text{Eq. (1.34)}$$

(3) Pt-MnO_2 catalysts

Manganese oxide is cheap, environmentally friendly and in abundant reserves. MnO_2 is widely used to oxide small organic molecules, due to its excellent proton conductivity, various structures and oxidation states in electrolyte [176]. In particular, MnO_2 possesses good proton-electron intercalation properties and exhibits good electrochemical activity under different working conditions [177], because of the presence of the Mn^{4+}/Mn^{3+} redox couple and the extent of participation of oxygen, MnO_2 reveals high activity and poisoning-resistant ability for ethanol oxidation in acid medium [176-178]. Cai *et al*. [176] used microwave-assisted polyol method to synthesize a series of Pt/MnO_x-CNT catalysts with different MnO_{2-x}/CNT mass ratios (1:5, 1:2, 1:1, 2:1 and 3:1). The voltammetry results manifested that the optimal mass ratio of MnO_x to CNT was 1:1. The catalyst Pt/MnO_x-CNT (1:1) exhibited higher ethanol oxidation peak current (1141.4 mA mg_{Pt}^{-1}) than Pt/CNT (626.4 mA mg_{Pt}^{-1}) and PtRu/C (888.6 mA mg_{Pt}^{-1}). Also, the catalyst Pt/MnO_x-CNT (1:1) displayed excellent stability and durability for EOR. The authors

ascribed the superb performance to the synergistic effect between Pt and MnO_x and the good proton conductivity of MnO_x ("hydrogen spillover effect"), as shown in the following equations [176]

$$Pt - MnO_2 + CH_3CH_2OH_{ads} \rightarrow \cdots \rightarrow Pt - CO_{ads} + MnOOH \quad \text{Eq. (1.35)}$$

$$MnOOH \rightarrow MnO_2 + H^+ + e^- \quad \text{Eq. (1.36)}$$

$$Pt - MnO_2 + H_2O \rightarrow Pt - OH_{ads} + MnOOH \quad \text{Eq. (1.37)}$$

$$Pt - OH_{ads} + Pt - CO_{ads} \rightarrow 2Pt + CO_2 + H^+ + e^- \quad \text{Eq. (1.38)}$$

where "…" denotes the C–C bond break.

Meher *et al.* [177] prepared Pt/MnO_2-nanorods (NR)/C and Pt/MnO_2-microcubes(B)/C catalysts for methanol and ethanol oxidation in sulfuric acid solution. They found that Pt/MnO_2-NR/C and Pt/MnO_2-B/C showed higher catalytic activity and duration stability towards methanol and ethanol than that of Pt/C. The authors believed the promotional performance was caused by the synergic effect between MnO_2 and Pt (*bi*-functional mechanism), as proposed in Eq. (1.39)-Eq. (1.41).

$$MnO_2 + H_2O \rightarrow MnO_2 - OH_{ads} + H^+ + e^- \quad \text{Eq. (1.39)}$$

$$Pt - CO_{ads} + Mn - OH_{ads} \rightarrow Pt + MnO_2 + CO_2 + H^+ + e^- \quad \text{Eq. (1.40)}$$

$$Pt - MnO_2 + xCO \rightarrow Pt - MnO_{2-x} + x\,CO_2 \quad \text{Eq. (1.41)}$$

Besides, they noticed the performance of Pt/MnO_2-NR/C was superior to that of Pt/MnO_2-B/C. The authors suggested MnO_2-nanorods offered more oxygenate species than MnO_2-microcubes (Figure 1.25).

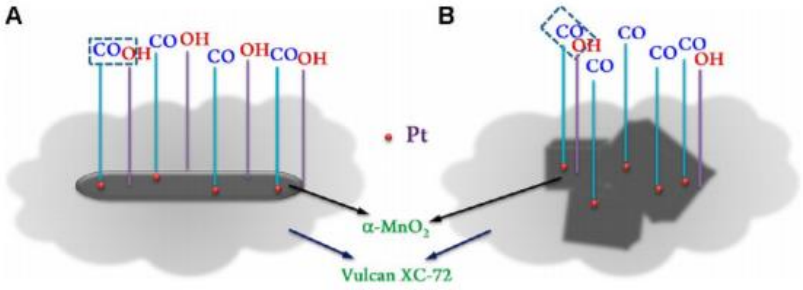

Figure 1.25 The schematic diagram of CO oxidation on (A) Pt/MnO_2-NR/C (B)Pt/MnO_2-B/C [177].

1.5.3 Ternary Pt-based catalysts

To further enhance the activity of the binary catalysts towards EOR and the ability of cleavage of the C-C bond, a third ingredient is added PtRhFe [179], PtSnAg [180], PtAuIr [181] and PtRuSn [93], etc. Among the ternary catalysts, $PtRhSnO_2$ catalysts make a breakthrough to achieve the unprecedented catalytic activity towards EOR and high efficiently of the C-C bond cleavage [67, 182-185].

Li *et al.* [182] used a modified polyol method to synthesize a series of ternary PtRh-SnO_2/C catalysts with the atomic ratio Pt:Rh:Sn = 3:1:x (x=2, 3, 4, 5, 6) for investigation their catalytic activity towards EOR. The results showed $Pt_3Rh_1Sn_4$ had the highest current density, the most negative onset potential and the capability to break the C-C bond. Li and co-worker [183] observed that the catalytic activity of the catalysts towards EOR decreased in the order of $PtRhSnO_2$>$PtSnO_2$>Pt>PtRh>Rh>$RhSnO_2$. In situ infrared reflection-absorption spectroscopy (IRRAS) results demonstrated Rh can split the C-C bond, the selectivity of the catalysts to CO_2 decreased in the order of: $PtRhSnO_2$>$RhSnO_2$>PtRh>Pt>$PtSnO_2$>Rh. Elena Baranova *et al.* [184] had novel insights in the synthesis−structure−catalytic activity relationships of nanostructured trimetallic Pt−Rh−Sn for EOR. They synthesized five catalysts with different structures and atomic ratios: PtRhSn/C (41:9:50), PtRh/C (74:26), Sn+Rh+Pt/C (46:7:47), Sn+RhPt/C (45:8:47) and Sn+Pt/C (56:44). They found that the single-phase Niggliite PtRhSn/C (PtRh alloy are atomically mixed with a SnO_2 phase) outperformed other catalysts in an electrolyte of 0.5M C_2H_5OH + 0.5M H_2SO_4. Meanwhile, they also confirmed the C-C bond cleavage in ethanol by in situ FTIR. They provided one of the earliest onsets of $12e^-$ pathway, since CO_2 evolution started at 0.45 V. Adzic group [185] synthesized multimetallic nanoislands MM′/SnO_2 (MM′ = PtIr, PtRh, IrRh, PtIrRh) and they found that PtRh/SnO_2/C catalysts ($PtRh_{1/3}$/SnO_2/C and $PtRh_{1/2}$/SnO_2/C) can break the C-C bond of ethanol in $HClO_4$ solution at room temperature and the catalyst PtRh/SnO_2/C had the highest ethanol conversion efficiency. They also pointed out that the catalysts' selectivity was highly dependent on their composition (Pt/Rh ratio), PtRh/SnO_2 catalyst with a moderate Rh content showed the best selectivity for the C-C bond splitting. They ascribed this phenomenon to the synergistic effect of the geometric "ensemble effect" and the electronic "ligand effect": the scission of the C-C bond was due to the formation of M-CH_2CH_2O, which generated by the back donation from π orbitals of *CH_2CH_2O to the d-orbital of the metal atoms; and the strong interaction between Pt and Rh lead to the electron of Rh transfer to Pt, as a result of which, the *d*-states of Rh became available above the Fermi level, whereas d-states of Pt shifted away from the Fermi level. Rh became more active

and Pt became less active, which facilitated the splitting of the C-C bond and impeded ethanol partial oxidation on Pt. Adzic *et al*. [67] used DFT to calculate the possible pathway for the C-C scission of ethanol on RhPt/SnO_2 (110) surface in Figure 1.26 and present an optimum pathway (the blue line) for the C-C bond cleavage at the Rh, Pt/SnO_2 interface:

$*CH_3CH_2OH \rightarrow *CH_3CHO + H*$

$\rightarrow *CH_2CH_2O + 2H*$

$\rightarrow *CH_2 + *CH_2O + 2H*$

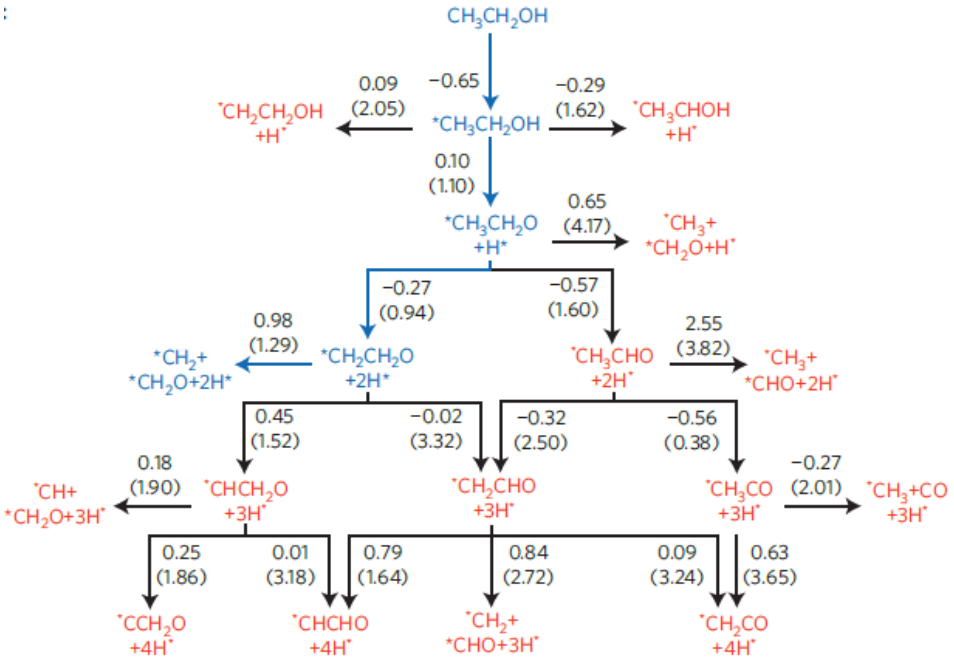

Figure 1.26 **DFT calculation of the possible pathway for the C-C scission of ethanol on RhPt/SnO_2 (110) surface. The reaction energies and parenthesized barriers in this figure are presented in eV [67].**

1.5.4 Supporting materials

It is well known that a good supporting material can enhance the stability and activity of the catalysts [186]. Hence, the supporting material plays a pivotal role in the DEFCs. Based on the selection criteria from Pollet *et al*. [187], an ideal support should have the following characteristics:

- Higher specific surface area to enhance the dispersion of metal nanoparticles.
- Good catalyst-support interaction to accelerate charge transfer.
- High electrical conductivity to assure the electrical contact.

- Mesoporous structure to promote alcohol diffusion.
- Good water handling/capability to avoid flooding.
- Good corrosion resistance.

There are two categories of catalyst supports: (1) carbonaceous supports (Figure 1.27), such as the carbon nanotubes (CNT), carbon nanofibers (CNFs), mesoporous carbons (MCs), nanodiamonds, and doped diamonds and graphene. Among the carbon based on carbon nanomaterials, carbon nanotubes (CNTs) and carbon nanofibers (CNFs) are more stable [186]. (2) Non-carbonaceous supports, *e.g.,* TiO_2, SnO_2, In_2O_5Sn, SiO_2, W, and $Zr(SO_4)_2$.

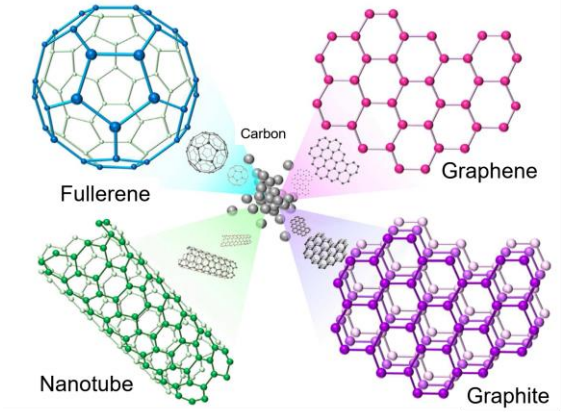

Figure 1.27 Different forms of carbon-based materials [188].

1.5.5 Problematic

As a renewable resource, ethanol is playing an increasingly important role in improving the global climate and energy supply. Direct fuel cells using ethanol as liquid fuels without reforming steps providing a promising concept for a clean and efficient way for energy conversion. DEFCs have great potential to be used in vehicle applications and portable devices (laptop, cellphone and batteries). Nevertheless, Pt has difficulty in cleavage of the C-C bond of ethanol. As a result, the EOR goes through parallel C2 pathway (Figure 1.28) by yielding the unwanted products acetaldehyde (AAL, $2e^-$), which can desorb from the electrocatalyst surface and diffuse to the electrolyte. Ultimately, AAL further oxidize to acetic acid (AA, $4e^-$). While AAL can also reabsorb on the catalyst surface and dissociate to the poisonous carbon monoxide CO_{ad} and hydrocarbons species $CH_{x,\,ad}$. Only very few ethanol molecules are dissociated to carbon CO_{ad} or $CH_{x,\,ad}$ [77, 193], and eventually oxidized to CO_2 ($12e^-$ per ethanol molecule) in C1 pathway. The incomplete EOR not only lowers the Faradaic efficiency ($2e^-$ transfer *vs* $12e^-$ transfer in the

complete oxidation reaction), but also gives rise to acetate or (*bi*) sulfate that strongly adsorbs on the surface of catalysts and considerably affects the reactivity of the catalysts [80].

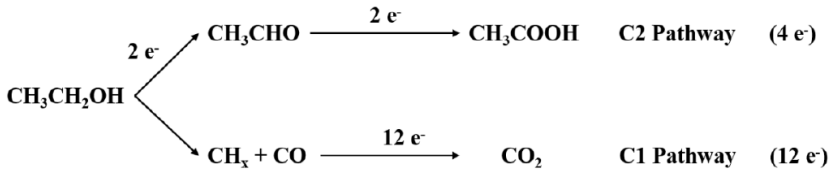

Figure 1.28 Schematic diagram of the parallel pathway for ethanol oxidation on Pt surface in acidic media [116].

Besides, Pt is highly susceptible to be poisoned by the strongly adsorbed intermediates such as CO_{ad} and $CH_{x,ad}$, which come from the dissociative adsorption of ethanol [73]. This poisoning leads to the sluggish EOR kinetics and low efficiency (even with the electrodes highly loaded with Pt electrocatalysts). In addition, the unbearable cost of platinum is another factor to hinder the large-scale production of DEFCs, because Pt accounts for approximately 54% of the total FC stack cost [194]. Furthermore, the durability of the electrode materials is critical. Pt is easily dissolved and aggregated under poor operation conditions, leading to poor durability [195, 196].

The sluggish kinetics of ethanol oxidation reaction (EOR) [34] and the poor stability of Pt-based electro-catalysts are the major impediments for the commercialization of DEFCs [123, 127, 189-192]. Therefore, selectively enhancing the C1 pathway by rational design of high-performance catalysts is an effective way to increase the DEFC efficiency.

1.6 Thesis objectives

Based on the problematic presented above and the relevant literature review on Pt-based catalysts for PEM-based DEFCs, our main objective focuses on designing and synthesizing by pulsed laser deposition technique binderless nanostructured ternary anode catalysts Rh-Pt-MO_2 (M = Sn, Ce, Mn and Ti) and Pt_xRh_{100-x} alloys supported either on carbon paper or carbon nanotubes substrates towards improved tolerance to CO poisoning, enhanced electrooxidation of ethanol and excellent durability. To achieve the main goal, we commit ourselves in the following sub-objectives:

(1) Discuss the influence of the number of laser pulses (N_{lp}) and by that the effect of the thickness of the Rh layer on the electrochemical oxidation of CO oxidation.

(2) Investigate the role of Pt, SnO_2 and Rh in carbon paper supported catalysts Rh$PtSnO_2$ as well as study of the effect of the thickness of the Rh layer towards CO and ethanol electrooxidation.

(3) Explore the supporting catalytic properties of carbon nanotubes in Pt- and $PtSnO_2$-based catalysts on the electrooxidation of ethanol.
(4) Study the effect of the atomic ratio of PtRh in CBPLD-made catalysts Pt_xRh_{100-x} on EOR.

1.7 Organization of the thesis

This thesis consists of 7 chapters including abstract and the references. The organization of the thesis is listed as below:

Chapter 1 introduces in outline the background and motivation of the research on acid DEFCs. A detailed literature review of the research status of Pt-based DEFCs is reported.

Chapter 2 presents the methodology of this thesis, including the experimental scheme, methods and procedures. A detailed introduction on various physicochemical and electrochemical characterization techniques and the corresponding experimental parameters are also given in this chapter.

Chapters 3-6 report four articles.

Chapter 7 summarizes the results and proposes future research directions for this project.

References

[1] B. Dudley, BP statistical review of world energy, BP Statistical Review, London, UK, accessed Aug, 6 (2018) 2018.

[2] P.P. Edwards, V.L. Kuznetsov, W.I. David, N.P. Brandon, Energy Policy, 36 (2008) 4356-4362.

[3] A.B. Stambouli, E. Traversa, Renew. Sust. Energ. Rev., 6 (2002) 295-304.

[4] Y. Shao, M.F. El-Kady, J. Sun, Y. Li, Q. Zhang, M. Zhu, H. Wang, B. Dunn, R.B. Kaner, Chem. Rev., 118 (2018) 9233-9280.

[5] C.F. Schönbein, The London, Edinburgh, and Dublin Philosophical Magazine and Journal of Science, 14 (1839) 43-45.

[6] W.R. Grove, The London, Edinburgh, and Dublin Philosophical Magazine and Journal of Science, 14 (1839) 127-130.

[7] L. Mond, C. Langer, V. Proceedings of the Royal Society of London, 46 (1890) 296-304.

[8] W. Nernst, Z. Electrochem, 6 (1899) 41-43.

[9] E. Baur, H. Preis, Zeitschrift für Elektrochemie und angewandte physikalische Chemie, 43 (1937) 727-732.

[10] F.T. Bacon, Electrochim. Acta, 14 (1969) 569-585.

[11] W. Grubb, L. Niedrach, J. Electrochem. Soc., 107 (1960) 131-135.

[12] B. Johnston, M.C. Mayo, A. Khare, Technovation, 25 (2005) 569-585.

[13] A. Kirubakaran, S. Jain, R. Nema Renew. Sust. Energ. Rev., 13 (2009) 2430-2440.

[14] S.K. Kamarudin, F. Achmad, W.R.W. Daud, Int. J. Hydrogen Energy, 34 (2009) 6902-6916.

[15] R.J. Farrauto, L. Dorazio, C.H. Bartholomew, John Wiley & Sons, 2016.

[16] P. Agnolucci, Int. J. Hydrogen Energy, 32 (2007) 4306-4318.

[17] X. Chen, T. Li, J. Shen, Z. Hu, Renew. Sust. Energ. Rev., 80 (2017) 669-678.

[18] M. Kamarudin, S.K. Kamarudin, M. Masdar, W.R.W. Daud, Int. J. Hydrogen Energy, 38 (2013) 9438-9453.

[19] R. Chauhan, V. Srivastava, Nanomaterials for Alcohol Fuel Cells, 49 (2019) 293-320.

[20] N. Tajitsu, Reuters, June, (2016).

[21] S. Wang, S.P. Jiang, Natl. Sci. Rev., 4 (2017) 163-166.

[22] D. Hart, G. Hörmandinger, J. Power Sources, 71 (1998) 348-353.

[23] C.M. Kalamaras, A.M. Efstathiou, in: Conference papers in science, Hindawi, 2013.

[24] C.-Y. Chen, C.-C. Chen, S.-W. Hsu, M.-P. Lai, W.-H. Lai, W.-M. Yang, Energy Procedia, 29 (2012) 64-71.

[25] W. Zhou, B. Zhou, W. Li, Z. Zhou, S. Song, G. Sun, Q. Xin, S. Douvartzides, M. Goula, P. Tsiakaras, J. Power Sources, 126 (2004) 16-22.

[26] X. Yu, P.G. Pickup, J. Power Sources, 182 (2008) 124-132.

[27] V. Selvaraj, M. Alagar, K.S. Kumar, Appl. Catal., 75 (2007) 129-138.

[28] H. Dohle, H. Schmitz, T. Bewer, J. Mergel, D. Stolten J. Power Sources, 106 (2002) 313-322.

[29] X. Li, A. Faghri, J. Power Sources, 226 (2013) 223-240.

[30] A.A. Khuhro, Y. Ali, M. Najam-Uddin, S. Khan, IEEE, 2018, pp. 1-4.

[31] G. Apanel, E. Johnson, Fuel Cells Bulletin, 2004 (2004) 12-17.

[32] J. Pereira, D. Falcão, V. Oliveira, A. Pinto, J. Power Sources, 256 (2014) 14-19.

[33] L. An, T. Zhao, Y. Li, Renew. Sust. Energ. Rev., 50 (2015) 1462-1468.

[34] E. Antolini, J. Power Sources, 170 (2007) 1-12.

[35] W. Du, Q. Wang, D. Saxner, N.A. Deskins, D. Su, J.E. Krzanowski, A.I. Frenkel, X. Teng, J. Am. Chem. Soc., 133 (2011) 15172-15183.

[36] J. Wang, S. Wasmus, R. Savinell, J. Electrochem, 142 (1995) 4218-4224.

[37] S. Song, W. Zhou, Z. liang, R. Cai, G. Sun, Q. Xin, V. Stergiopoulos，P. Tsiakaras, Appl. Catal. B: Environ, 55 (2005) 65.

[38] L.B. Lave, W.M. Griffin, H. MacLean, Issues Sci. Technol., 18 (2001) 73-78.

[39] C. Lamy, A. Lima, V. LeRhun, F. Delime, C. Coutanceau, J.-M. Léger, J. Power Sources, 105 (2002) 283-296.

[40] R. Schulz, J. Huot, G. Liang, S. Boily, G. Lalande, M. Denis, J. Dodelet, Mater. Sci. Eng. A, 267 (1999) 240-245.

[41] C. Lamy, C. Coutanceau, J.M. Leger, Catalysis for sustainable energy production, (2009) 1.

[42] S. Badwal, S. Giddey, A. Kulkarni, J. Goel, S. Basu, Appl. Energy, 145 (2015) 80-103.

[43] G. Sorda, M. Banse, C. Kemfert, Energy Policy, 38 (2010) 6977-6988.

[44] J. Rimatzki, From Farm to Table to Board Room: The Impact of Industrial Agriculture on US Corn Production, in, 2020.

[45] J. Belincanta, J. Alchorne, M. Teixeira da Silva, Braz. J. Chem. Eng., 33 (2016) 1091-1102.

[46] K. Sundmacher, Ind. Eng. Chem. Res., 49 (2010) 10159-10182.

[47] C. Lamy, E. Belgsir, J. Leger, J. Appl. Electrochem., 31 (2001) 799-809.

[48] F. Vigier, C. Coutanceau, A. Perrard, E. Belgsir, C. Lamy, J Appl Electrochem, 34 (2004) 439-446.

[49] H.-F. Wang, Z.-P. Liu, J. Am. Chem. Soc., 130 (2008) 10996-11004.

[50] S. Srinivasan, B. Dave, K. Murugesamoorthi, A. Parthasarathy, A. Appleby, in: Fuel cell systems, Springer, 1993, pp. 37-72.

[51] T. Iwasita, E. Pastor, Electrochim. Acta, 39 (1994) 531-537.

[52] H. Wang, Z. Jusys, R. Behm, Fuel Cells, 4 (2004) 113-125.

[53] S. Sun, M.C. Halseid, M. Heinen, Z. Jusys, R. Behm, J. Power Sources, 190 (2009) 2-13.

[54] F. Vigier, C. Coutanceau, F. Hahn, E. Belgsir, C. Lamy, J. Electroanal. Chem., 563 (2004) 81-89.

[55] Q. Wang, G. Sun, L. Jiang, Q. Xin, S. Sun, Y. Jiang, S. Chen, Z. Jusys, R. Behm, Phys. Chem. Chem. Phys., 9 (2007) 2686-2696.

[56] H. Hitmi, E. Belgsir, J.-M. Léger, C. Lamy, R. Lezna, Electrochim. Acta, 39 (1994) 407-415.

[57] V. Del Colle, J. Souza-Garcia, G. Tremiliosi-Filho, E. Herrero, J.M. Feliu, Phys. Chem. Chem. Phys., 13 (2011) 12163-12172.

[58] V. Del Colle, A. Berna, G. Tremiliosi-Filho, E. Herrero, J. Feliu, Phys. Chem. Chem. Phys., 10 (2008) 3766-3773.

[59] J. Souza-Garcia, E. Herrero, J.M. Feliu, ChemPhysChem, 11 (2010) 1391-1394.

[60] S.C. Lai, S.E. Kleijn, F.T. Öztürk, V.C. van Rees Vellinga, J. Koning, P. Rodriguez, M.T. Koper, Catal. Today, 154 (2010) 92-104.

[61] A. Ferre-Vilaplana, C. Buso-Rogero, J.M. Feliu, E. Herrero, J. Phys. Chem. C, 120 (2016) 11590-11597.

[62] C. Busó-Rogero, V. Grozovski, F.J. Vidal-Iglesias, J. Solla-Gullón, E. Herrero, J.M. Feliu, J. Mater. Chem. A, 1 (2013) 7068-7076.

[63] R.B. Kutz, B. Braunschweig, P. Mukherjee, R.L. Behrens, D.D. Dlott, A. Wieckowski, J. Catal., 278 (2011) 181-188.

[64] S.C. Lai, S.E. Kleyn, V. Rosca, M.T. Koper, J. Phys. Chem. C, 112 (2008) 19080-19087.

[65] J. Flórez-Montaño, G. García, O. Guillén-Villafuerte, J.L. Rodríguez, G.A. Planes, E. Pastor, Electrochim. Acta, 209 (2016) 121-131.

[66] S. Rousseau, C. Coutanceau, C. Lamy, J.-M. Léger, J. Power Sources, 158 (2006) 18-24.

[67] A. Kowal, M. Li, M. Shao, K. Sasaki, M. Vukmirovic, J. Zhang, N. Marinkovic, P. Liu, A. Frenkel, R. Adzic, Nat. Mater., 8 (2009) 325-330.

[68] H.A. Asiri, A.B. Anderson, J. Electrochem. Soc., 162 (2015) F115-F122.

[69] E. Pastor, T. Iwasita, Electrochim. Acta, 39 (1994) 547-551.

[70] R. Rightmire, R. Rowland, D. Boos, D. Beals, J. Electrochem. Soc., 111 (1964) 242.

[71] J. Perez, B. Beden, F. Hahn, A. Aldaz, C. Lamy, Chem. Interf. Electrochem., 262 (1989) 251-261.

[72] J. Silva-Chong, E. Méndez, J. Rodrıguez, M. Arévalo, E. Pastor, Electrochim. Acta, 47 (2002) 1441-1449.

[73] C. Lamy, S. Rousseau, E. Belgsir, C. Coutanceau, J.-M. Léger, Electrochim. Acta, 49 (2004) 3901-3908.

[74] Q. He, B. Shyam, K.i. Macounová, P. Krtil, D. Ramaker, S. Mukerjee, J. Am. Chem. Soc., 134 (2012) 8655-8661.

[75] S.C. Lai, M.T. Koper, Faraday Discuss., 140 (2009) 399-416.

[76] F. Vigier, S. Rousseau, C. Coutanceau, J.-M. Leger, C. Lamy, Top. Catal., 40 (2006) 111-121.

[77] H. Wang, Z. Jusys, R. Behm, J. Phys. Chem. B, 108 (2004) 19413-19424.

[78] G.A. Camara, T. Iwasita, J. Electroanal. Chem., 578 (2005) 315-321.

[79] M.E. Paulino, L.M. Nunes, E.R. Gonzalez, G. Tremiliosi-Filho, Electrochem. Commun., 52 (2015) 85-88.

[80] F. Colmati, G. Tremiliosi-Filho, E.R. Gonzalez, A. Berná, E. Herrero, J.M. Feliu, Faraday Discuss., 140 (2009) 379-397.

[81] C. Busó-Rogero, E. Herrero, J.M. Feliu, Chemphyschem, 15 (2014) 2019-2028.

[82] M. Akhairi, S.K. Kamarudin, Int. J. Hydrogen Energy, 41 (2016) 4214-4228.

[83] F. Colmati, G. Tremiliosi-Filho, E.R. Gonzalez, A. Berná, E. Herrero, J.M. Feliu, Phys. Chem. Chem. Phys., 11 (2009) 9114-9123.

[84] J. Perez, V.A. Paganin, E. Antolini, J. Electroanal. Chem., 654 (2011) 108-115.

[85] X. Li, X. Qiu, H. Yuan, L. Chen, W. Zhu, J. Power Sources, 184 (2008) 353-360.

[86] Y.-W. Tang, G.-X. Ma, Y.-M. Zhou, J.-C. Bao, L.-D. Lu, T.-H. Lu, Acta Physico-Chimica Sinica, 24 (2008) 1615-1619.

[87] Y. Takasu, N. Ohashi, X.-G. Zhang, Y. Murakami, H. Minagawa, S. Sato, K. Yahikozawa, Electrochim. Acta, 41 (1996) 2595-2600.

[88] L. Jiang, G. Sun, S. Sun, J. Liu, S. Tang, H. Li, B. Zhou, Q. Xin, Electrochim. Acta, 50 (2005) 5384-5389.

[89] H. Wang, Z. Jusys, R. Behm, J. Power Sources, 154 (2006) 351-359.

[90] W. Zhou, W.Z. Li, S.Q. Song, Z.H. Zhou, L. Jiang, G. Sun, Q. Xin, K. Poulianitis, S. Kontou, P. Tsiakaras, J. Power Sources, 131 (2004) 217-223.

[91] S. Song, W. Zhou, Z. Zhou, L. Jiang, G. Sun, Q. Xin, V. Leontidis, S. Kontou, P. Tsiakaras, Int. J. Hydrogen Energy, 30 (2005) 995-1001.

[92] S. Song, P. Tsiakaras, Appl. Catal. B, 63 (2006) 187-193.

[93] W. Zhou, Z. Zhou, S. Song, W. Li, G. Sun, P. Tsiakaras, Appl. Catal. B, 46 (2003) 273-285.

[94] W. Zhou, S. Song, W. Li, G. Sun, Q. Xin, S. Kontou, Solid State Ion., 175 (2004) 797-803.

[95] J.-M. Jin, T. Sheng, X. Lin, R. Kavanagh, P. Hamer, P. Hu, C. Hardacre, A. Martinez-Bonastre, J. Sharman, D. Thompsett, Phys. Chem. Chem. Phys., 16 (2014) 9432-9440.

[96] L. Colmenares, H. Wang, Z. Jusys, L. Jiang, S. Yan, G. Sun, R. Behm, Electrochim. Acta, 52 (2006) 221-233.

[97] F. Zhu, K. Tu, L. Huang, X. Qu, J. Zhang, H. Liao, Z. Zhou, Y. Jiang, S. Sun, Electrochim. Acta, 292 (2018) 208-216.

[98] P. Bai, F. Tian, H. Wang, T. Yang, X. Bi, Z. Chai, X. Wang, Adv. Mater. Interfaces, 6 (2019) 1900946.

[99] E. Antolini, Energies, 10 (2017) 42.

[100] M. Watanabe, Y. Furuuchi, S. Motoo, J. Electroanal. Chem. Interf. Electrochem., 191 (1985) 367-375.

[101] M. Watanabe, S. Motoo, J. Electroanal. Chem. Interf. Electrochem., 60 (1975) 275-283.

[102] B. Hammer, J.K. Norskov, Nature, 376 (1995) 238-240.

[103] B. Hammer, J.K. Nørskov, Surf. Sci., 343 (1995) 211-220.

[104] A. Nilsson, L. Pettersson, B. Hammer, T. Bligaard, C.H. Christensen, J.K. Nørskov, Catal Letters, 100 (2005) 111-114.

[105] P. Strasser, S. Koh, T. Anniyev, J. Greeley, K. More, C. Yu, Z. Liu, S. Kaya, D. Nordlund, H. Ogasawara, Nat. Chem., 2 (2010) 454.

[106] E. Christoffersen, P. Liu, A. Ruban, H.L. Skriver, J.K. Nørskov, J. Catal., 199 (2001) 123-131.

[107] M. Pedersen, S. Helveg, a. Ruban, I. Stensgaard, E. Lægsgaard, JK Nøskov, F. Besenbacher, Surf. Sci, 426 (1999) 395.

[108] P. Waszczuk, A. Wieckowski, P. Zelenay, S. Gottesfeld, C. Coutanceau, J.-M. Léger, C. Lamy, J. Electroanal. Chem., 511 (2001) 55-64.

[109] J.K. Nørskov, T. Bligaard, J. Rossmeisl, C.H. Christensen, Nat. Chem., 1 (2009) 37.

[110] M. Kim, C. Lee, S.M. Ko, J.-M. Nam, J. Solid State Chem., 270 (2019) 295-303.

[111] F. Colmati, E. Antolini, E.R. Gonzalez, J. Power Sources, 157 (2006) 98-103.

[112] W. Zhou, S.Q. Song, W.Z. Li, Z.H. Zhou, G. Sun, Q. Xin, S. Douvartzides, P. Tsiakaras, J. Power Sources, 140 (2005) 50-58.

[113] R. Rizo, M.J. Lázaro, E. Pastor, G. García, Molecules, 21 (2016) 1225.

[114] P. Tsiakaras, J. Power Sources, 171 (2007) 107-112.

[115] J. Asgardi, J.C. Calderón, F. Alcaide, A. Querejeta, L. Calvillo, M.J. Lázaro, G. García, E. Pastor, Appl. Catal., 168 (2015) 33-41.

[116] Y. Wang, S. Zou, W.-B. Cai, Catalysts, 5 (2015) 1507-1534.

[117] Z.W. Chia, J.Y. Lee, Encyclopedia of Inorganic Chemistry, (2006).

[118] M. Mavrikakis, D. Doren, M. Barteau, . Phys. Chem. B, 102 (1998) 394-399.

[119] E. Vesselli, A. Baraldi, G. Comelli, S. Lizzit, R. Rosei, Chemphyschem, 5 (2004) 1133-1140.

[120] P.-Y. Sheng, A. Yee, G. Bowmaker, H. Idriss, J. Catal., 208 (2002) 393-403.

[121] N. De Tacconi, R. Lezna, B. Beden, F. Hahn, C. Lamy, J. Electroanal. Chem., 379 (1994) 329-337.

[122] Z.-X. Liang, T.S. Zhao, R. Soc. Chem., 2012.

[123] J. De Souza, S. Queiroz, K. Bergamaski, E.R. Gonzalez, F.C. Nart, J. Phys. Chem. B, 106 (2002) 9825-9830.

[124] F. Lima, D. Profeti, W. Lizcano-Valbuena, E. Ticianelli, E. Gonzalez, J. Electroanal. Chem., 617 (2008) 121-129.

[125] K. Bergamaski, E.R. Gonzalez, F.C. Nart, Electrochim. Acta, 53 (2008) 4396-4406.

[126] L. Rao, Y.-X. Jiang, B.-W. Zhang, Y.-R. Cai, S.-G. Sun, Phys. Chem. Chem. Phys., 16 (2014) 13662-13671.

[127] A.B. Delpeuch, M. Chatenet, M.S. Rau, C. Cremers, Phys. Chem. Chem. Phys., 17 (2015) 10881-10893.

[128] D. Cantane, W. Ambrosio, M. Chatenet, F. Lima, J. Electroanal. Chem., 681 (2012) 56-65.

[129] A.B. Delpeuch, T. Asset, M. Chatenet, C. Cremers, J. Electrochem. Soc., 161 (2014) F918.

[130] Y. Zhu, L. Bu, Q. Shao, X. Huang, ACS Catal., 9 (2019) 6607-6612.

[131] S.S. Gupta, J. Datta, J. Electroanal. Chem., 594 (2006) 65-72.

[132] C.V. Almeida, D.S. Ferreira, H. Huang, A.C. Gaiotti, G.A. Camara, A.E. Russell, K.I. Eguiluz, G.R. Salazar-Banda, Appl. Catal. B, 254 (2019) 113-127.

[133] A. Tabet-Aoul, H. Wang, Y. Wang, M. Mohamedi, J. Electrochem. Soc., 164 (2017) F685.

[134] F. Alcaide, G. Álvarez, P.L. Cabot, R.V. Genova-Koleva, H.-J. Grande, M.V. Martínez-Huerta, O. Miguel, J. Electroanal. Chem., 861 (2020) 113960.

[135] P. Jovanovič, F. Ruiz-Zepeda, M. Šala, N. Hodnik, J. Phys. Chem. C, 122 (2018) 10050-10058.

[136] Z. Zhang, J. Liu, J. Gu, L. Su, L. ChengEnergy Environ. Sci., 7 (2014) 2535-2558.

[137] H. Pang, J. Lu, J. Chen, C. Huang, B. Liu, X. Zhang, Electrochim. Acta, 54 (2009) 2610-2615.

[138] J. Maier, John Wiley & Sons, 2004.

[139] L. Levinson, H. Philipp, R. Buchanan, by Buchanan, RC, Marcel Dekker, New York, (1991) 349-377.

[140] C. Fonstad, R. Rediker, J. Appl. Phys., 42 (1971) 2911-2918.

[141] S. Das, V. Jayaraman, Prog. Mater Sci., 66 (2014) 112-255.

[142] J. Morgado, N. Barbagallo, A. Charas, M. Matos, L. Alcácer, F. Cacialli, J. Phys. D: Appl. Phys., 36 (2003) 434.

[143] C. Wang, Y. Zhou, M. Ge, X. Xu, Z. Zhang, J. Jiang, J. Am. Chem. Soc., 132 (2010) 46-47.

[144] L. Sun, B. Wang, Y. WangACS Appl. Mater. Interfaces, 12 (2020) 21808-21817.

[145] A. Masao, S. Noda, F. Takasaki, K. Ito, K. Sasaki, Electrochem. Solid-State Lett., 12 (2009) B119.

[146] W. Du, G. Yang, E. Wong, N.A. Deskins, A.I. Frenkel, D. Su, X. TengJ. Am. Chem. Soc., 136 (2014) 10862-10865.

[147] W.-P. Zhou, S. Axnanda, M.G. White, R.R. Adzic, J. Hrbek, Phys. Chem. C, 115 (2011) 16467-16473.

[148] Y. Qu, C. Li, L. Wang, Y. Gao, J. Rao, G. Yin, Int. J. Hydrogen Energy, 41 (2016) 14036-14046.

[149] Z. Zhang, Q. Wu, K. Mao, Y. Chen, L. Du, Y. Bu, O. Zhuo, L. Yang, X. Wang, Z. Hu, ACS Catal., 8 (2018) 8477-8483.

[150] T. Okazaki, S. Seino, T. Nakagawa, J. Kugai, Y. Ohkubo, T. Akita, H. Nitani, T.A. Yamamoto, Radiat. Phys. Chem., 108 (2015) 1-6.

[151] L. Jiang, G. Sun, Z. Zhou, S. Sun, Q. Wang, S. Yan, H. Li, J. Tian, J. Guo, B. Zhou, J. Phys. Chem. B, 109 (2005) 8774-8778.

[152] N. Hongjun, L. Cancan, W. Xuhong, J. Xuefan, T. Dong, Journal of Jiangsu University: Natural Science Edition, 33 (2012) 379-384.

[153] R.S. Hsu, D. Higgins, Z. Chen, Nanotechnology, 21 (2010) 165705.

[154] Y. Wang, A. Tabet-Aoul, M. Mohamedi, J. Electrochem. Soc., 163 (2016) F1272.

[155] H. Gharibi, S. Sadeghi, F. Golmohammadi, Electrochim. Acta, 190 (2016) 1100-1112.

[156] D.F. Silva, A.N. Geraldes, A.O. Neto, E.S. Pino, M. Linardi, E.V. Spinacé, W.A. Macedo, J.D. Ardisson, Mater. Sci. Eng. B, 175 (2010) 261-265.

[157] R. Antoniassi, J. Silva, A.O. Neto, E. Appl. Catal. B, 218 (2017) 91-100.

[158] R. Antoniassi, A.O. Neto, M. Linardi, E. Spinacé, Int. J. Hydrogen Energy, 38 (2013) 12069-12077.

[159] J. Silva, R. De Souza, L. Parreira, E.T. Neto, M. Calegaro, M. Santos, Appl. Catal. B, 99 (2010) 265-271.

[160] X. Zhang, H. Zhu, Z. Guo, Y. Wei, F. Wang, Int. J. Hydrogen Energy, 35 (2010) 8841-8847.

[161] G.L. Cordeiro, E.F.d. CAMARGO, M.C. Santos, C.V. Pereira, V. Ussui, A.O. NETO, D.R. LAZAR, Int. J. Electrochem. Sci., (2018).

[162] M.A. Scibioh, S.-K. Kim, E.A. Cho, T.-H. Lim, S.-A. Hong, H.Y. Ha, Appl. Catal. B, 84 (2008) 773-782.

[163] H. Yao, Y.Y. Yao, J. Catal., 86 (1984) 254-265.

[164] Y. Gao, W. Wang, S. Chang, W. Huang, ChemCatChem, 5 (2013) 3610-3620.

[165] S.K. Meher, G.R. Rao, ACS Catal., 2 (2012) 2795-2809.

[166] G.N. Vayssilov, Y. Lykhach, A. Migani, T. Staudt, G.P. Petrova, N. Tsud, T. Skála, A. Bruix, F. Illas, K.C. Prince, Nat. Mater., 10 (2011) 310-315.

[167] J. Thormann, L. Maier, P. Pfeifer, U. Kunz, O. Deutschmann, K. Schubert, Int. J. Hydrogen Energy, 34 (2009) 5108-5120.

[168] A. Tabet-Aoul, M. Mohamedi, Phys. Chem. Chem. Phys., 14 (2012) 4463-4474.

[169] Y. Wang, A. Tabet-Aoul, M. Gougis, M. Mohamedi, J. Power Sources, 273 (2015) 904-913.

[170] R. De Souza, A. Flausino, D. Rascio, R. Oliveira, E.T. Neto, M. Calegaro, M. Santos, Appl. Catal. B, 91 (2009) 516-523.

[171] Y. Bai, J. Wu, X. Qiu, J. Xi, J. Wang, J. Li, W. Zhu, L. Chen, Appl. Catal. B, 73 (2007) 144-149.

[172] C. Xu, R. Zeng, P.K. Shen, Z. Wei, Electrochim. Acta, 51 (2005) 1031-1035.

[173] L. Zhang, Y. Shen, ChemElectroChem, 2 (2015) 887-895.

[174] P.S. Murphin Kumar, S. Thiripuranthagan, T. Imai, G. Kumar, A. Pugazhendhi, S.R. Vijayan, R. Esparza, H. Abe, S.K. Krishnan ACS Sustain. Chem. Eng., 5 (2017) 11290-11299.

[175] K. Kakaei, A. Rahimi, S. Husseindoost, M. Hamidi, H. Javan, A. Balavandi, Int. J. Hydrogen Energy, 41 (2016) 3861-3869.

[176] J. Cai, Y. Huang, B. Huang, S. Zheng, Y. Guo, Int. J. Hydrogen Energy, 39 (2014) 798-807.

[177] S.K. Meher, G.R. Rao, J. Phys. Chem. C, 117 (2013) 4888-4900.

[178] Y. Wang, M. Mohamedi, ChemElectroChem, 3 (2016) 1787-1793.

[179] P. Wang, S. Yin, Y. Wen, Z. Tian, N. Wang, J. Key, S. Wang, P.K. Shen, ACS Appl. Mater. Interfaces, 9 (2017) 9584-9591.

[180] S. Dai, T.-H. Huang, X. Yan, C.-Y. Yang, T.-Y. Chen, J.-H. Wang, X. Pan, K.-W. Wang, ACS Energy Lett., 3 (2018) 2550-2557.

[181] Z. Liang, L. Song, S. Deng, Y. Zhu, E. Stavitski, R.R. Adzic, J. Chen, J.X. Wang, J. Am. Chem. Soc., 141 (2019) 9629-9636.

[182] M. Li, A. Kowal, K. Sasaki, N. Marinkovic, D. Su, E. Korach, P. Liu, R. Adzic, Electrochim. Acta, 55 (2010) 4331-4338.

[183] M. Li, W.-P. Zhou, N. Marinkovic, K. Sasaki, R. Adzic, Electrochim. Acta, 104 (2013) 454-461.

[184] N. Erini, R. Loukrakpam, V. Petkov, E.A. Baranova, R. Yang, D. Teschner, Y. Huang, S.R. Brankovic, P. Strasser, ACS Catalysis, 4 (2014) 1859-1867.

[185] M. Li, D.A. Cullen, K. Sasaki, N.S. Marinkovic, K. More, R.R. Adzic, J. Am. Chem. Soc., 135 (2013) 132-141.

[186] A.M. Pinto, V.S. Oliveira, D.S.C. Falcão, Academic Press, 2018.

[187] S. Sharma, B.G. Pollet, J. Power Sources, 208 (2012) 96-119.

[188] J. Sengupta, in: Handbook of Nanomaterials for Industrial Applications, Elsevier, 2018, pp. 172-194.

[189] F. Delime, J. Leger, C. Lamy, J. Appl. Electrochem., 29 (1999) 1249-1254.

[190] V. Rao, C. Cremers, U. Stimming, L. Cao, S. Sun, S. Yan, G. Sun, Q. Xin, J. Electrochem. Soc., 154 (2007) B1138-B1147.

[191] A.B. Delpeuch, F. Maillard, M. Chatenet, P. Soudant, C. Cremers, Appl. Catal. B, 181 (2016) 672-680.

[192] S. Shen, T. Zhao, J. Xu, Int. J. Hydrogen Energy, 35 (2010) 12911-12917.

[193] D.A. Cantane, F.H.B.d. LimaElectrocatalysis, 3 (2012) 324-333.

[194] X. Teng, Mater. Sci, (2013) 473-484.

[195] V. Mazumder, Y. Lee, S. SunAdv. Funct. Mater., 20 (2010) 1224-1231.

[196] X. Ren, Q. Lv, L. Liu, B. Liu, Y. Wang, A. Liu, G. Wu, Sustain. Energy Fuels, 4 (2020) 15-30.

2 EXPERIMENTAL METHODS

This chapter introduces the synthetic process of the electrocatalysts used in this thesis. Detailed information is provided on the experimental techniques, which were applied for the physicochemical and electrochemical characterization of the electrocatalysts.

2.1 Material synthesis

We use single-beam pulsed laser deposition (PLD) to synthesize a series of unitary, bi- and tri-catalysts (Pt, Rh, Pt/Rh, Pt/MO_2 and Rh/Pt/MO_2, where M =Sn, Ce, Mn and Ti) with carbon paper (CP) and carbon nanotubes (CNTs) as substrate, respectively. CNTs are fabricated by chemical vapor deposition (CVD). Then we use cross-beam pulsed laser deposition (CBPLD), a variant of PLD, to obtain four Pt_xRh_{100-x} alloys with different atomic ratios of Pt and Rh by adjusting the laser fluence.

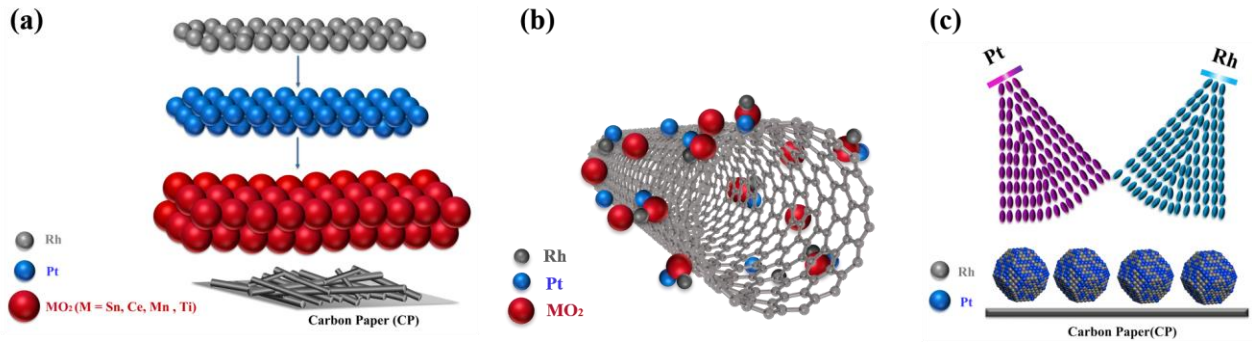

Figure 2.1 **The layer-by-layer deposited catalysts were made by PLD (a and b) and the co-deposited catalysts were synthesized by CBPLD (c).**

There are two types of deposition in the as-prepared catalysts:

(1) layer-by-layer deposited catalysts (Figure 2.1a and b). These catalysts are fabricated by the method of PLD, *e.g.,* the carbon paper CP (Figure 2.1a) and CNTs supported (Figure 2.1b) Pt-, Rh-, and MO_2- based electrocatalysts (Pt, Rh, Pt/Rh, Pt/MO_2 and Rh/Pt/MO_2). Here is the synthetic process: the metal oxide MO_2 target firstly is ablated by the pulsed laser under the optimized pressure of helium, and the MO_2 nanoparticles are deposited onto the substrate as the first layer. Then the target is switched to Pt and the scaled nanostructured Pt is deposited on the MO_2 layer. In the same way, Rh film is lastly deposited on Pt as the top layer.

With CP as substrate (Figure 2.1a), we synthesize unitary catalysts Pt_{50}/CP, Rh_n/CP (Rh_5/CP, Rh_{10}/CP, Rh_{20}/CP, Rh_{50}/CP), MO_2 (M = Sn, Ce, Mn and Ti)/CP; binary catalysts Pt/MO_2/CP,

Rh_5/Pt/CP, and Rh_{10}/Pt/CP; ternary catalysts Rh_5/Pt/MO_2/CP, Rh_{10}/Pt/MO_2/CP, Rh_{20}/Pt/SnO_2/CP, Rh_{20}/Pt/CeO_2/CP, Rh_{50}/Pt/SnO_2/CP and Rh_{50}/Pt/CeO_2/CP.

With CNTs as substrate (Figure 2.1b), we synthesize CNTs supported unitary catalysts by Pt_{50}/CNT, Rh_n/CNT (Rh_5/CNT, Rh_{10}/CNT), MO_2 (M = Sn, Ce, Mn and Ti)/CNT; binary catalysts Pt/MO_2/CNT, Rh_5/Pt/CNT, and Rh_{10}/Pt/CNT; ternary catalysts Rh_5/Pt/SnO_2/CNT, Rh_{10}/Pt/CeO_2/CNT, Rh_5/Pt/MnO_2/CNT and Rh_5/Pt/TiO_2/CNT.

(2) Co-deposited catalysts (Figure 2.1c), which is achieved by means of CBPLD. During the deposition, two laser beams with different laser fluences strike the Pt and Rh targets synchronously, ablating Pt and Rh nanoparticles out of the targets. Meanwhile, the two targets are moved reversely and continuously across the laser beam (via a dual rotation and translation motion) to obtain a uniform ablation over the entire surface of the target. The ejected Pt and Rh nanoparticles are simultaneously deposited on the substrate and form a film. We synthesize four co-deposited Pt_xRh_{100-x}/CP catalysts with different atomic composition of Pt to Rh: $Pt_{90}Rh_{10}$/CP, $Pt_{75}Rh_{25}$/CP, $Pt_{50}Rh_{50}$/CP and $Pt_{25}Rh_{75}$/CP.

2.1.1 Synthesis of primary support CNTs

There are two steps for fabricating the CNTs.

(a) *Synthesis of Ni-coated substrate by PLD*

At room temperature, Nickel nanoparticles were grown) in a high-vacuum deposition chamber (residual pressure 10^{-6} Torr) by PLD with a pulsed KrF excimer laser (wavelength λ=248 nm, pulse width τ≈17 ns, repetition rate υ=30 Hz). The laser beam (laser fluence F=4 J cm^{-2}) was focused by a UV grade fused silica lens at 45 ° angle of incidence, and ablated the polycrystalline Ni target (99.95%, Kurt J. Lesker Co.). The target-to-substrate distance is fixed at 5 cm. During the deposition, the substrate and target rotate at 10° s^{-1} in the opposite direction thereby obtaining a uniform thin film with a thickness of ca. 5 nm.

(b) *Synthesis of CNTs* via CVD at atmospheric pressure

The schematic diagram of chemical vapor deposition (CVD) set-up is illustrated in Figure 2.2. Here are the detailed procedures on growing CNT by CVD. Firstly, the Ni-covered substrate was put in a quartz board, which was placed in the center of a horizontal quartz tubular reactor with a diameter Φ of 40 mm and a length L of 800 mm. Argon (Ar), as the carrier, was initially delivered for 5 min to purge all gaseous species from the reaction chamber. Next, a mixed flow of Ar (30 cm^3 min^{-1}, standard cubic centimeters per minute, sccm) and H_2 (70 sccm) were

introduced for 10 min to deoxidize the Ni coated CP film. H_2 and Ar play a role in enhancing surface reaction and improving reaction rate. Afterwards, the furnace was programmed heated to 700 ℃ with H_2 gas at a flow rate of 70 sccm for 30 min. In this period, the nickel film will be broken into spherical Ni nanoparticles, dispersed homogeneously on the carbon fibers. Subsequently, Ar and the precursor gases acetylene C_2H_2 and H_2 were added with flow rates of 100, 20 and140 sccm, respectively. The growth time was 35 min. After the CVD process, the furnace was cooled down to room temperature under the H_2 ambient (60 sccm) to prevent oxidation of the CNTs. Lastly, the volatile by-product hydrogen (H) was expelled from the reaction chamber by an anti-backflow bubbler.

2.1.2 Synthesis of layer-by-layer structure catalysts by PLD

In this project, PLD and CBPLD are both conducted at room temperature in a stainless-steel ultra-high vacuum chamber where the base pressure is 4×10^{-5} Torr evacuated by a turbo pump. A pulsed KrF excimer laser (λ=248 nm, τ=17 ns and υ=50 Hz) is used for all the ablation experiments with different pressure values of Helium (He, N5.0, Praxair) as background gas. In all cases, the distance of the substrate-to-target is fixed at 5 cm. Targets Pt (99.8%), Rh (99.99%), SnO_2 (99.99%), CeO_2 (99.99%), MnO_2 (99.99%) and TiO_2 (99.99%) are purchased from Kurt J. Lesker Co.

The deposition parameters for the synthesis of layer-by-layer catalysts are listed in Table 2.1.

Table 2.1 The parameters of PLD deposition for the synthesis of layer-by-layer catalysts.

Target	Background Pressure (Torr)	F (J cm^{-2})	Number of laser pulses (N_{lp}, 10^3)
MO_2	0.5	4	20
Pt	2	4	50
Rh	2	7	5, 10, 20 and 50

2.1.3 Synthesis of co-deposited structure catalysts by CBPLD

The CBPLD deposition parameters for Pt_xRh_{100-x} are listed in Table 2.2.

Table 2.2 The parameters of CBPLD deposition for the synthesis of co-deposited catalysts

Target	Background Pressure (Torr)	F (J cm^{-2})	Number of laser pulses (N_{lp}, 10^3)
Pt	2	From 1 to 7	50
Rh	2	From 1 to 7	50

2.2 Synthesis methods

2.2.1 Chemical vapor deposition (CVD)

CVD is a classical deposition method, which is widely used to grow carbon nanotubes (CNTs) in large-scale and high quality, due to its simple equipment, low operation cost and high energy efficiency. A simple presentation of the thermal CVD process is illustrated in Figure 2.2. CVD is a chemical reaction/deposition of volatile hydrocarbon gaseous precursor on the surface of heated substrate coated with catalytic materials. The particles of these supported materials act as a seed of nanotubes, so that they strongly influence the structure and quality of the nanotubes. Generally, the supported materials are the transition metal in Group VIII of the periodic table such as Nickel, iron, or Cobalt. The main reason for using transition metals is that they have unfilled “d” shells [1]. As a result, they have a relatively high carbon solubility and carbon diffusion coefficient, transition metal carbides can be formed, nucleation and growth of carbon atoms can be carried out [2]. Besides, Ni, Fe and Co have stronger adhesion with CNTs than other transitions metals. Hence, they are more efficient in producing high-curvature or low diameter CNTs [3].

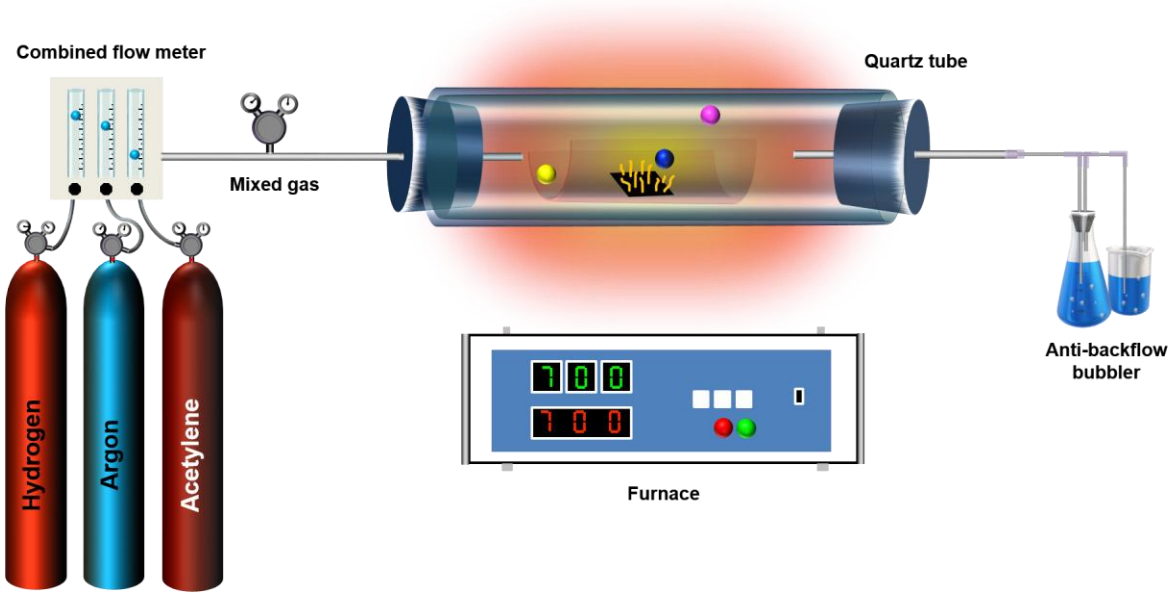

Figure 2.2 The schematic diagram of a thermal CVD apparatus for synthesis of CNTs.

In addition, due to the high melting point of these metals and the low equilibrium vapor pressure, this provides a wide range of CVD temperatures for various carbon sources and can be used to grow carbon nanotubes at different temperatures. Typical CVD temperatures vary between 600 °C and 1000 °C.

2.2.1.1 The categories of CVD

CVD technique can be classified based on the parameters of chamber pressure, reactor type, carbon source and heating ways. Table 2.3 shows the categories of CVD [4].

Table 2.3 Type of CVD techniques used for CNTs synthesis.

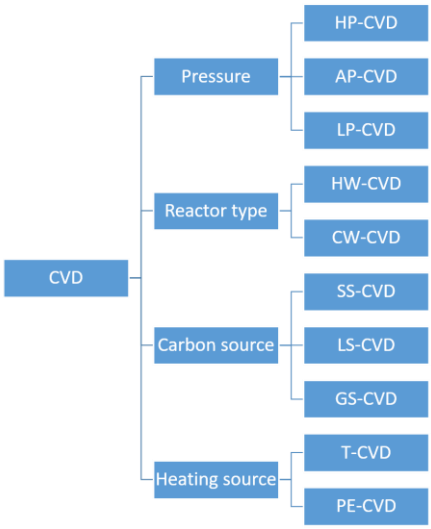

i) **Pressure**. High-pressure CVD (HP-CVD), atmospheric pressure CVD (AP-CVD), and low-pressure CVD (LP-CVD).

ii) **Reactor type**. Hot wall (HW-CVD) and cold wall (CW-CVD).

iii) **Carbon source**. Catalyst can be introduced into the reactor in various forms, *e.g.,* solid, liquid, and gas. Based on the physical form of the catalyst used the CVD process can be categorized as solid source CVD (SS-CVD), liquid source CVD (LS-CVD), and gas source CVD (GS-CVD).

iv) **Heating source**. When a traditional heat source such as resistive or inductive or infrared heater is used for the deposition process, then the method is called thermal CVD (T-CVD). If a plasma source is used to create a glow discharge, then it is called plasma-enhanced CVD (PE-CVD).

2.2.1.2 The mechanism of CNTs growth by CVD

There has been controversy towards the mechanism of CNTs growth since its discovery. Based on the reaction conditions (temperature, vapor pressure, type of catalyst and support) and analysis of product CNTs, many possibilities are proposed while they are invariably contradictory. Hitherto, it has not reached a uniform conclusion. Nonetheless, two mechanisms are widely accepted (Figure 2.3) [4]: (a) tip growth mode and (b) base growth mode.

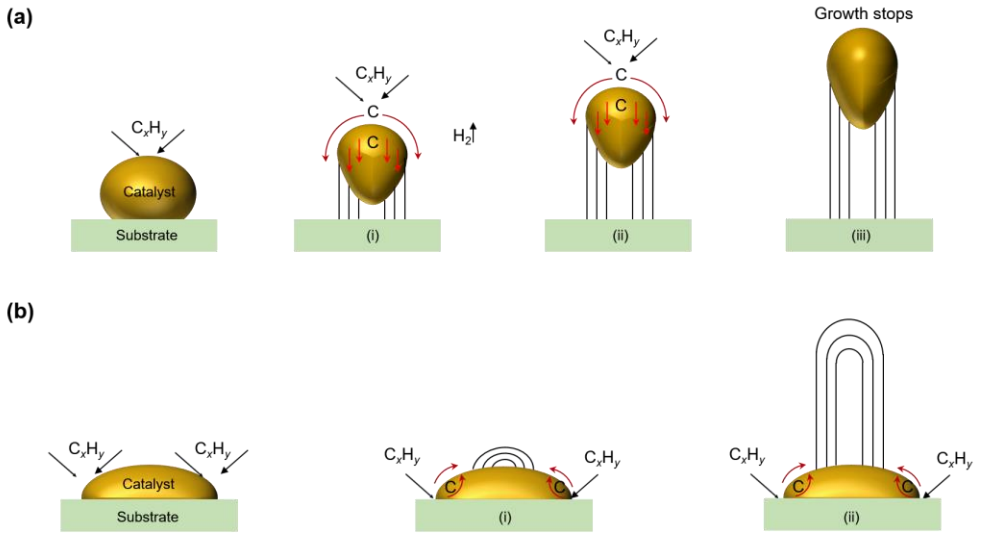

Figure 2.3 Two typical CNTs growth modes: (1) tip-growth mode and (2) base-growth mode.

For tip growth model (Figure 2.3a), the catalyst-substrate interaction is weak, namely, the contact angle θ between catalyst and substrate is less than 90°. When the hydrocarbon precursors C_xH_y is brought into contact with heated nanostructured catalyst, C_xH_y decomposes into C and H_2; C diffuses down through the catalyst, H_2 goes away with flow, and the CNT precipitates out across the metal bottom, lifting the whole nanoparticle off the substrate (Figure 2.3a-i). The CNT continues to grow as long as the top catalyst is open for incoming C_xH_y decomposition and the concentration gradient still exists in the catalyst enabling carbon diffusion (Figure 2.3a-ii). Once reaching the carbon-solubility limit in the catalyst, the CNT stops growing (Figure 2.3a-iii).

For the base growth mode (Figure 2.3b), the catalyst-substrate interaction is strong ($\theta > 90°$). The initial C_xH_y decomposition and carbon diffusion are similar to that of the tip-growth mode. However, the CNT precipitation does not lift the nanoparticle. On the contrary, the precipitation is forced to get out from metal vertex. In the first place, carbon crystallizes out as a hemispherical dome (Figure 2.3b-i). Then, it extends up in the form of seamless graphitic cylinder. Successive C_xH_y decomposition takes place on the lower peripheral surface of the metal, and as-dissolved C diffuses upward. Therefore, CNT grows up with the catalyst particle rooted in its base (Figure 2.3b-i). Like tip-growth mode, the CNT stops to grow when the catalyst is fully covered with C (Figure 2.3b-ii).

The base growth model is due to the strong metal-support interaction of catalyst and CNTs, whereas tip-growth model is applied to CNTs grown by catalyst with weak metal-support interaction.

2.2.2 Pulsed laser deposition (PLD)

PLD, also called Laser Ablation Deposition (LAD), is a physical vapor deposition technique for producing thin films. This technique was first used by Smith and Turner in 1965 [5].

2.2.2.1 Single-beam PLD

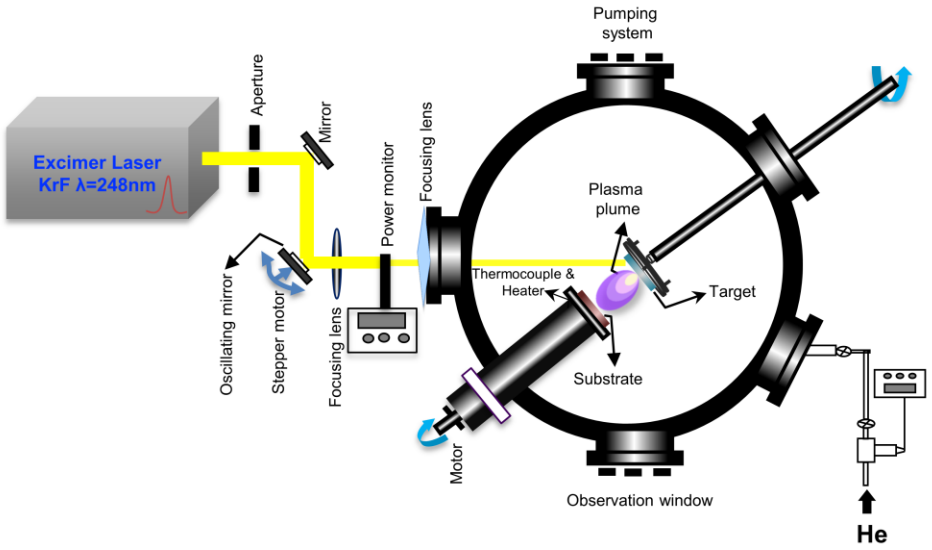

Figure 2.4 Schematic diagram of single beam PLD set-up.

Figure 2.4, the high-power ultraviolet (UV) pulsed laser is irradiated through a quartz window and focused by a quartz lens onto a solid or liquid surface (or so-called the “target”). At a certain power density and laser pulse duration, the material will be heated locally to the melting point, then rapidly melt, vaporize and leave the target in the form an ejected luminous plasma plume. Subsequently, the plume is collected on the substrate, where film starts to grow. The chamber can be vacuumed or with nonactive/reactive gas. In general, the target is continually rotating to avoid repeatedly ablating at the same spot.

PLD is one of the flexible and powerful tools for producing high-quality thin films. There are many advantages for using PLD to grow thin film.

- Simple set-up and growth process.
- Almost any type of materials, such as complex oxides, nitrides, carbides and borides as well as polymer-metal composites, can be ablated due to the flexibility in wavelength and power density.
- The congruent transfer of the target composition (stoichiometry) can be achieved for most ablated materials [6].

- The thickness of the film can be controlled precisely by the number of laser pulses [7].
- Different composition/multi-layer films can be obtained.
- Versatility. Film with different morphologies, structure and functionality can be synthesized by control of deposition conditions (chamber pressure, reactive or passive gases, target-substrate separation distance, number of pulses), laser beam parameters (wavelength λ, pulse duration fluence and laser density) [8].

Currently, excimer lasers like KrF (248 nm), ArF (193 nm), and F_2 (157 nm), emitting in the UV range, are wildly used in PLD. UV light is preferred due to its short penetration depth in materials, only removal of atoms near to the surface. The longer wavelengths can lead to a deeper penetration, which would cause subsurface evaporation and eruptions that can lead to larger clusters being ejected [9].

3.2.2.1.1 Mechanism of PLD

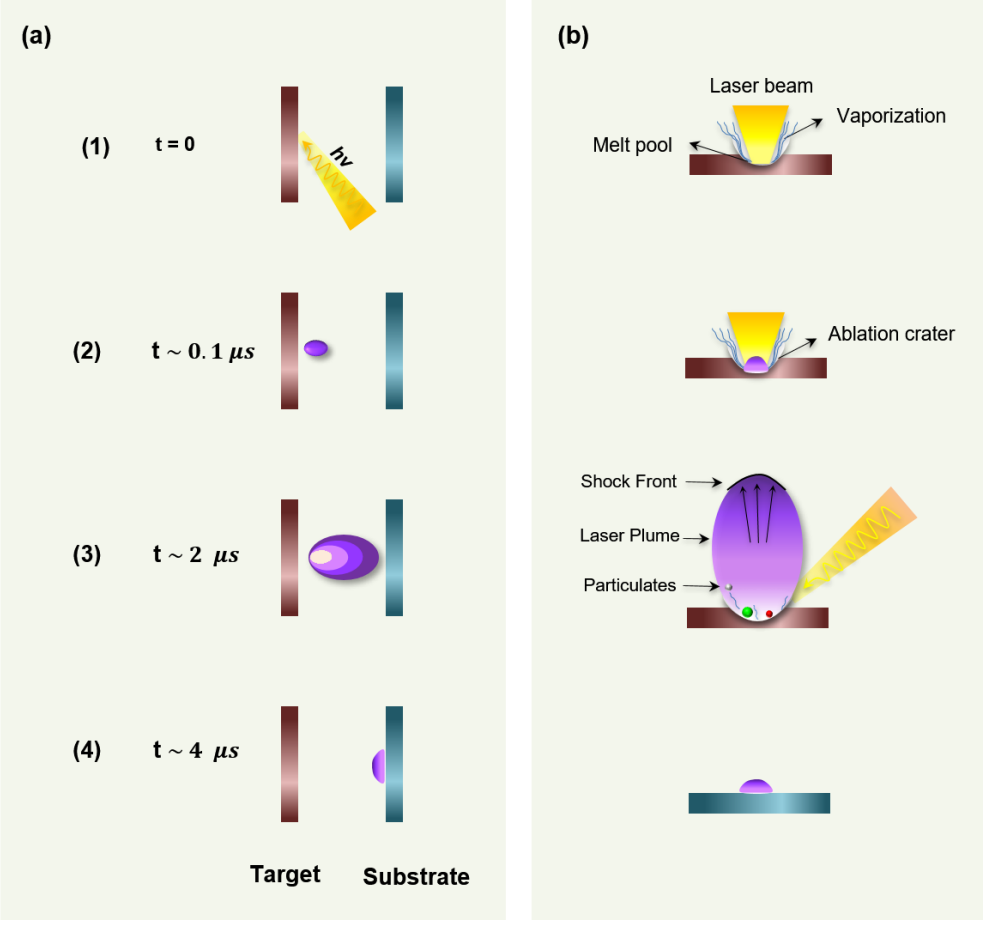

Figure 2.5 **The four stages of PLD (a) Time evaluation of deposition processes in PLD and (b) Corresponding physical phenomena of material removal and deposition.**

The principle of PLD, in contrast to the simplicity of the system set-up, is a very complex physical phenomenon. It involves all the physical processes of laser-material interaction during the impact of the high-power pulsed radiation on a solid target. It also includes the formation of the plasma plume with highly energetic species, the subsequent transfer of the ablated material through the plasma plume onto the heated substrate surface and the final film growth process. The PLD process can be generally divided into four stages (Figure 2.5) [10].

(1) Laser radiation interaction with the target material (Figure 2.5-1).

Intrinsically, laser beam is electromagnetic (EM) radiation, which can be represented as an electric vector field and magnetic field (Figure 2.6).

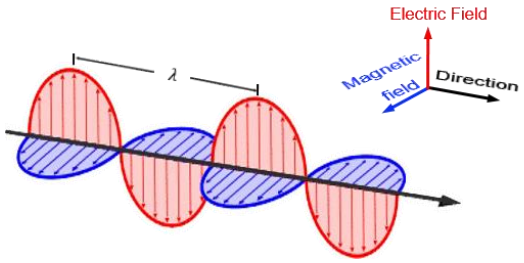

Figure 2.6 The electric and magnetic field vectors of EM radiation.

The electronic field amplitude *E* of an electromagnetic wave is given by:

$$\boldsymbol{E} = \left(\frac{\boldsymbol{2\Phi}}{\boldsymbol{cn\varepsilon_0}}\right)^{\boldsymbol{1/2}} \qquad \text{Eq. (2.1)}$$

Where, Φ is the power density; ε_0, the permittivity of free space, c, the velocity of light; n, the refractive index. Normally, when power density of laser is greater than $2 \times 10^8\ W\ cm^{-2}$, atomic excitation and ionization take place.

When the laser beam strikes the target, the incident laser makes the nuclei lattice and electrons vibrating. During the irritation, some laser can be reflected, some refracted, scattered or transmitted, some absorbed. The absorbed laser leads to the excess energy of the electrons, such as kinetic energy of the free electrons, excitation energy of the bound electrons [11]. Oscillating within the electromagnetic field of the laser beam, the free electrons with excess energy collide with the excited and ground stated neutrals, part of their energy is transferred to the lattice resulting in the generation of heat [12]. The target surface is heated up. When the temperature reaches the melting threshold, a solid-liquid interface is created at the surface, material starts melting, boiling, vaporizing and ionizing (Figure 2.5-1b) [13]. Materials are dissociated from the target and ablated out with stoichiometry as in the target. The intensity of absorbed laser in the target can be expressed through Beer Lambert law [14].

$$\boldsymbol{I(z) = I_0 e^{-\alpha z}}$$ Eq. (2.2)

Where, I_0 is the incident intensity; $I(z)$, the intensity at depth z; α, the optical absorption coefficient for the respective laser wavelength. $I(z)$ decays with the depth z inside the material. The reciprocal of the absorption coefficient α is the optical penetration depth l_o [15].

$$\boldsymbol{l_o = \frac{1}{\alpha}}$$ Eq. (2.3)

Typically, the optical penetration depth l_0 is on the order of 10 nm. The thermal diffusion depth l_τ, controlling the heating diffusion of target, is expressed as [16]:

$$\boldsymbol{l_\tau = 2\sqrt{D\tau}}$$ Eq. (2.4)

Where, τ is the laser pulse duration and D is the thermal diffusion constant. The l_0 and l_τ can illustrate the mode of the heating as follows:

i) $l_o \gg l_\tau$, weakly absorbing. Thermal contributions will dominate when using longer (nanosecond duration) pulsed laser, there is a sufficient duration allowing photo coupling with both electronic and vibrational modes of the target material. For ns laser, the effective l_τ is reduced to $l_\tau^{\text{eff}} = 2\sqrt{D\tau_{\text{eff}}}$, where τ_{eff} is the time needed to produce an erosion plasma when starts the laser pulse.

ii) $l_o \ll l_\tau$, strongly absorbing. All the photonic energy is absorbed when using ultra-short (femtosecond or picosecond duration) pulsed laser. The strong photonic absorption can generate high temperature at the surface and fasten vaporization. Target material: metal target and narrow band gap semiconductor.

The ejection species from the target do not only depend on the adsorption of the substrate, but also depend on its reflection and cohesive energy. For example, the cohesive energy has an impact on the quantity of ejected species. It is reported that the W, Mo and Ta have the lowest ablation yields with the order of 1×10^{16} atoms/pulse, while Sn and In have the most ablation yields (1×10^{16} atoms/pulse) [17].

(2) Plasma generation (Figure 2.5-2)

The vaporized materials, containing large numbers of energetic species like charged electrons, ions, neutral atoms or occasionally entire molecules, cluster, etc., continue to interact with the laser beam, which further increases the temperature. A nascent erosion cloud is formed with local high temperature ($\sim 10^5\ K$) and high concentration. The intense 'white' continuum emission observed very close to the target is Bremsstrahlung, associated with free-free

transitions within the hot plasma [18].

When using ns laser pulses, material ejection is likely to be dominated by thermal processes. The degree of ionization in a gas at local thermodynamic equilibrium can be estimated using the Saha equation:

$$\boldsymbol{n_i = (2.4 \times 10^{15}\, T^{3/2} n_n e^{-U_i/kT})^{1/2}} \quad \text{Eq. (2.5)}$$

where n_i and n_n are the respective number of single and neutrals in cm^{-3}; T is the gas temperature in K; U_i, the first ionization potential of the gas atoms in question in electron volts.

The nascent plasma cloud continues to absorb laser energy through the inverse-bremsstrahlung mechanism, it is consequently heated up to 10^4 K and becomes a dense-core luminous plasma [16].

The absorptivity by inverse-bremsstrahlung of this cloud to radiation of frequency υ (in Hz) is given by [19]:

$$\boldsymbol{\alpha_{IB} = 3.7 \times 10^{8} \frac{Z^3 n_i^2}{T^{1/2} \nu^3} (1 - e^{-h\nu/kT})} \quad \text{Eq. (2.6)}$$

where Z=1 is the elementary charge of the ion, n_i is in cm^{-3}, and α_{IB} is given in cm^{-1}. It will become hotter, more ionized and in turn absorb more efficiently.

The initial plasma pressure will be the highest for materials with high bulk optical absorption. In turn, the particle density in plasma depends on the degree of ionization, evaporation rate, and the plasma expansion velocities.

(3) Plasma expansion and condensation (Figure 2.5-3)

The ejected plasma plume expands in the direction perpendicular to the substrate into a vacuum or an ambient gas according to the laws of gas-dynamic and shows the forward peaking phenomenon [20-21]. The particles cannot escape without collision, since the ablation yield is more than 0.1 monolayers per nanosecond in most cases of PLD [16]. Therefore, there is a layer in contact with the target in which reflections and collisions occur which will tend to thermally equilibrate the plasma and lower its degree of ionization. This so-called Knudsen layer modifies the distribution to a drifted Maxwellian with the center-of mass velocity $\bar{v}$ normal to the surface given by $P(v) \sim v^3 \exp m_p\,(v - v)^2/2\,kT$ [16]. In a vacuum, the plasma expands freely the collision rates are low, the matter is ejected in all directions with high kinetic energies in a large range of 1-500 eV. There are two phases during this spatial expansion [22-23]. In the first phase, the plasma goes through isothermal expansion during laser irradiation. During this

process, the temperature of the plasma increases when absorbing laser energy and decreases when outward inflation. The energy is offset, leading to a constant temperature in plasma. In the second phase, the plasma undergoes adiabatic expansion. Instead of absorbing laser energy, the plasma continues to expand, resulting in a sharp drop of the temperature. Assuming that in vacuum, the plasma is an ideal gas, and it expands with at an extremely high velocity and acts as a continuous fluid [24-26]. The spatial distribution of the plum is in the form of $f(\theta) = cos^n \theta$ [27], where *n* varies from 7 to more than 20 and θ is measured from the target normal.

Background gas is applied either for reduction of the kinetic energy of the plasma species through multiple collisions, or for increase of the number of the chemical reactions between the plume and gas molecules thereby forming atomic (O, N) and diatomic species. The plume dynamics is affected by the ambient gas type and gas pressure.

- At low background pressure ($< 1\ Pa$), the plume expansion is similar to the ablation in a vacuum. Few scatterings take place especially affecting the fastest ions, and the background gas atoms are scattered out of the deposition path as well [28].
- At medium background pressures (10-100 Pa), the influence of the background gas over the plume becomes progressive. The fluorescence of all the species is enhanced due to enhanced collisions on the expansion front and subsequent inter-plume collisions [29]. The plume pushes the gas away thereby introducing a compression of the gas/plasma plume, leading to the reduction of the mean free path of plume species, the formation of shock wave and finally plume pressure equilibrates the background pressure [30]. The plume mass m_p can be estimated based on the mode of Zeldovich and Raizer [31]:

  $$m_p \approx \frac{2}{3} \pi R_{SKW}^3 \rho_g \qquad \text{Eq. (2.7)}$$

  Where, ρ_g is the gas density and R_{SKW} is the distance at which the hemispherical shock wave starts.

  The spherical expansion can be determined by using the blast wave model:

  $$R_{b.w.}(t) = \varepsilon_0 \left(\frac{2E_0}{\rho_g}\right)^{1/5} t^{2/5} \qquad \text{Eq. (2.8)}$$

  Where, ε and ρ_g are constant determined by the specific heat ratio and the mass density of the layer.

- At higher pressure ($> 100\ Pa$), a short stopping distance occurs due to the strong spatial confinement of the plasma.

Besides, the laser spot size also affects the plume dynamics. When the spot size is small, plume expands spherically. While with larger spot sizes, the plume propagation is more cylindrical [31].

(4) Nucleation and growth of a thin film on the substrate surface (Figure 2.5-4)

When the plume species impinge on the substrate, the first arriving pulse causes the nucleation of high numbers of smaller clusters. These subcritical clusters are inclined to dissociate into mobile species that will nucleate new clusters of different sizes during the time of no vapor arrival. The next pulse will initiate the same process again, with the difference that some of the mobile atoms will reach previously formed clusters [17]. The deposition rate per laser pulse can range from 1×10^{-3} to 1 Å. When the condensation rate is higher than the rate of particles reaching the substrate, nucleation and film growth processes occur on the substrate [33]. In general, the energy of arriving species and energy of the atom/aggregates on the substrate surface have big influence on the film growth way. While these energies depend on several predominant parameters, such as the substrate, background gas pressure, target-to-substrate distance D_{ts} [34].

- **Substrate**. *e.g.*, its material, temperature and translation/rotation.
- **Background gas pressure**. In a vacuum, the ejected matter with high energies and speeds are bombarding the substrate surface caused damage (by sputtering of atoms from the previously deposited layers) or defect formation (dislocations, cracks, holes) [35]. Under low pressure, the deposited layers are with compact thin film. When increasing gas pressure, the deposition rate first increases, shows a maximum and then decreases again, due to the resputtering from the substrate.
- **Target-to-substrate distance D_{ts}**. In order to have a uniform, homogeneous film with stoichiometric structure, the optical position is achieved when the plasma length is identical with target-to-substrate separation distance.

PLD yields thin films of significantly lower thickness uniformity than an equivalently small sized area thermal evaporation source, characterized by $\cos\theta$ and $\cos^4\theta$ polar atomic flux and thickness distributions, respectively [27]. The deposition area is usually of a few square centimetres only. The addition of an inert background gas (Ar) was found to dramatically lower the flux of ions, thus lowering the internal stress of the films and limiting blistering. Finally, the synthesis of high-quality, uniform, blister-free thin films

2.2.3 Cross-Beam Pulsed laser deposition (CBPLD)

CBPLD is considered as a particular variant of the PLD with two colliding ablation plumes from simultaneously laser-irradiated targets [36]. In CBPLD (Figure 2.7), the droplets are effectively filtered in the intersection region of two synchronized plasma beams. It was also reported that the maximal plasma particle energy could be reduced by macroparticle separation [37]. These characteristics enable CBPLD to produce high-quality multi-layer nanostructured materials with minimal intermixing of the successive layers, such as binary (ternary) alloys, metal oxides, etc.

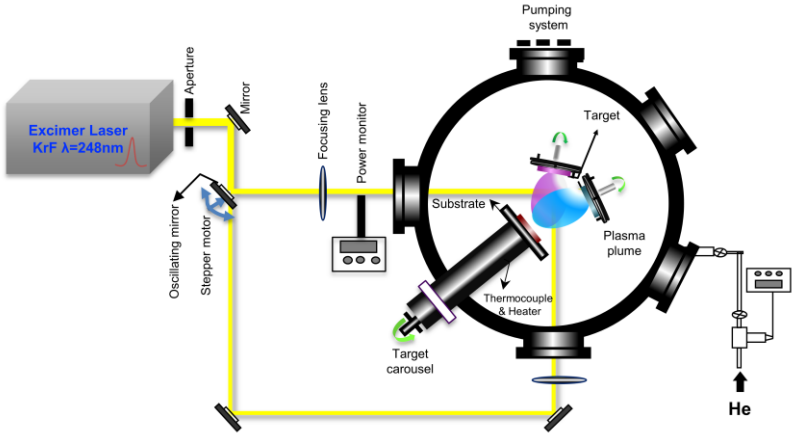

Figure 2.7 Schematic diagram of CBPLD set-up.

Figure 2.8 demonstrates the principle of thin-film deposition by CBPLD: (a) symmetric CBPLD with two same targets. (b) asymmetric CBPLD with two different targets. In order to obtain the correct direction and composition of the resulting plasma plume, an adjustment of the respective laser fluence on each target is needed. Consequently, the plasma fluxes will be “balanced” [38].

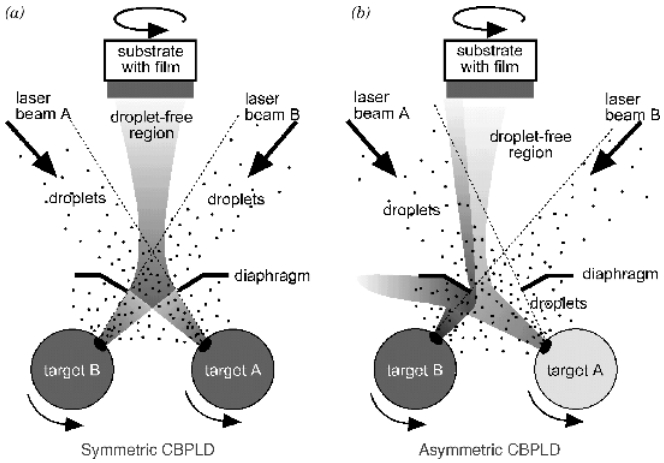

Figure 2.8 Principle of operation of (a) symmetric and (b) asymmetric CBPLD [37].

2.3 Structural characterizations of electrode materials

This part deals with various physical techniques employed for morphological and microstructural characterization of the electrode materials prepared in this project. The principal methods of characterization include scanning electron microscopy (SEM), Transmission Electron Microscopy (TEM), Energy Dispersive X-ray Spectroscopy (EDX), X-Ray Diffraction (XRD) and X-Ray Photoelectron Spectroscopy (XPS). Additionally, Neutron Activation Analysis (NAA) was employed for determining the mass loading (μg cm^{-2}) of Pt.

2.3.1 Scanning electron microscopy (SEM)

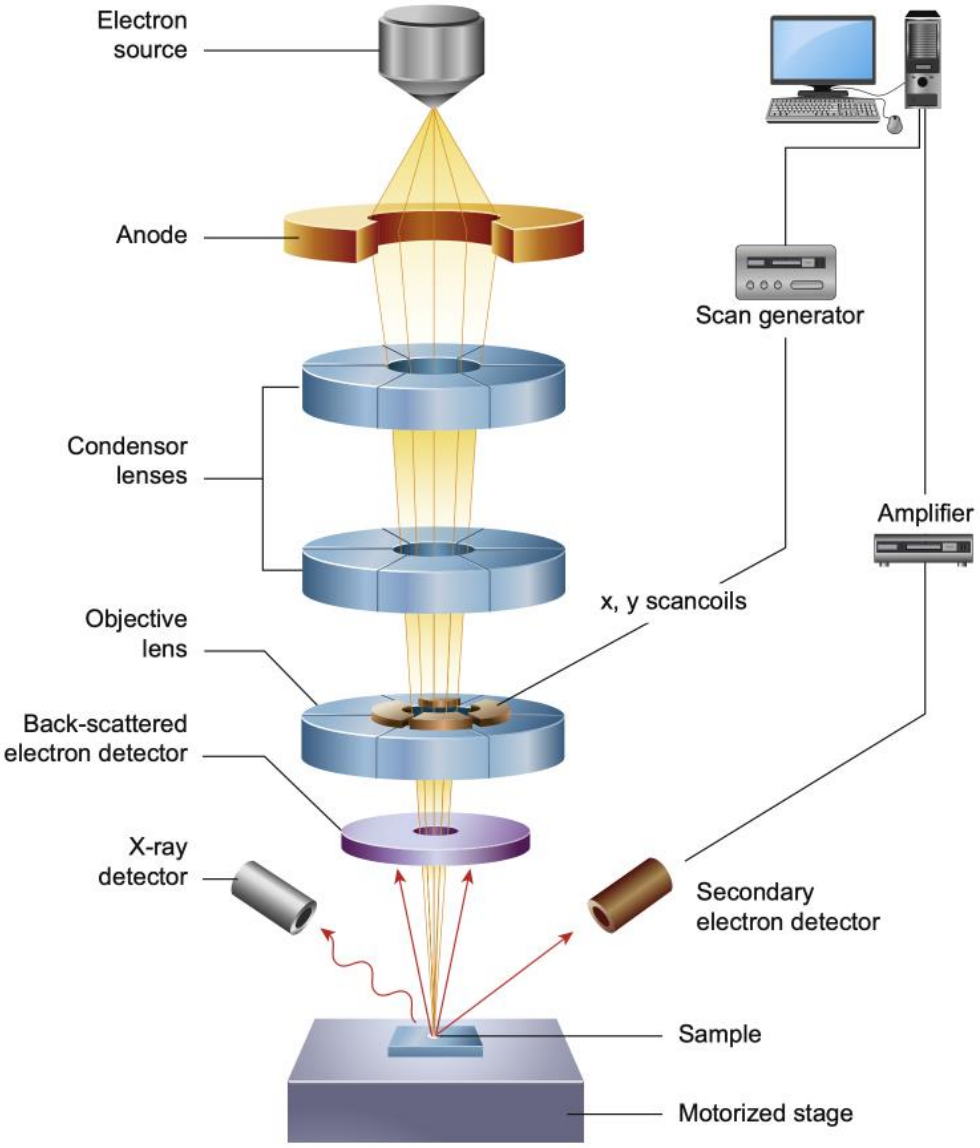

Figure 2.9 **Schematic diagram of the core components of an SEM microscope [39].**

Scanning electron microscopy (SEM) has been a standard technique for analysis of the specimen surface. SEM images of surfaces have high resolution and depth of field, with a 3D quality that offers a visual perspective of topography, morphology of the bulk specimen garnered from different detectors.

As presented in Figure 2.9, the key components of an SEM encompass the electron gun (electron source and accelerating anode), electromagnetic lenses to focus the electrons, a vacuum chamber housing the specimen stage, and a selection of detectors to collect the signals emitted from the specimen.

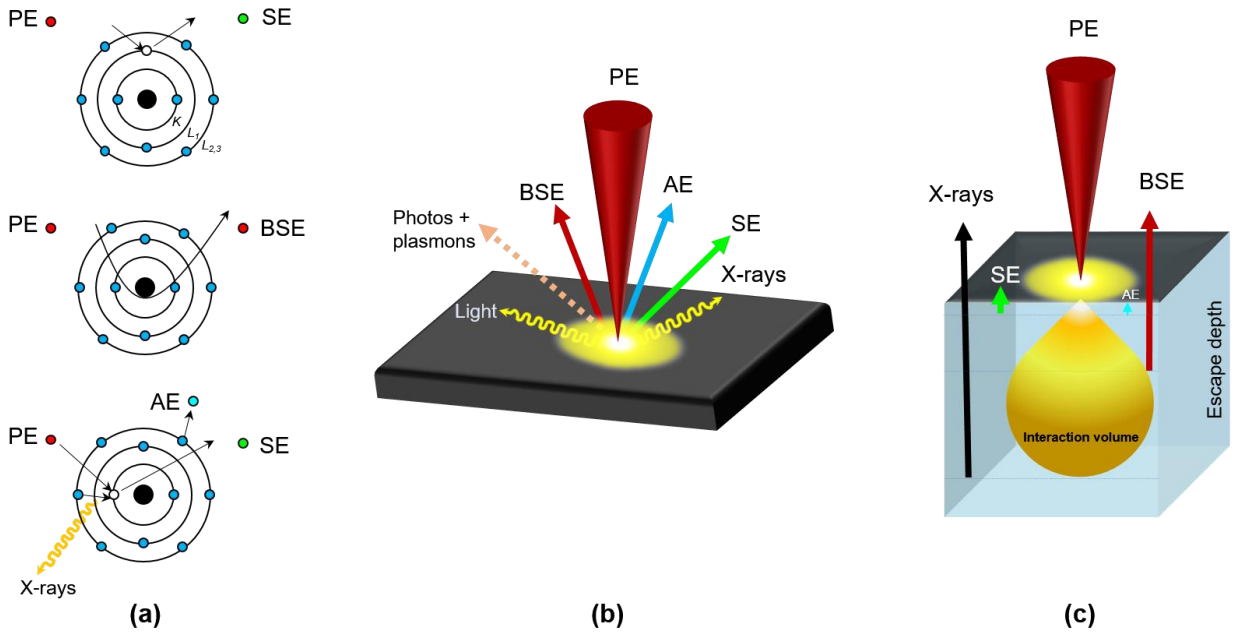

Figure 2.10 **(a) Mechanism of the emission of SE, BSE, AE and X-rays from atom of specimen. (b) Different signals generated by electron matter interactions with bulk specimen. (c) Absorption of SE, BSE, and X-rays in samples, by inelastic scattering within the interaction volume, limits the thick specimen depth from which they can escape.**

Electron beam, emitted from an electron gun atop by heating thermionic or field emission of tungsten filament at the cathode, is accelerated downwards where it travels through a combination of condenser lenses, apertures and electromagnetic field (1-30kV), which focus the beam down towards the sample. When the primary electron (PE) beam (2-10 KeV) interacts with the sample (3-20 cm in diameter), the electrons lose energy by repeated random scattering and absorption within a teardrop-shaped volume of the specimen known as the interaction volume (Figure 2.10c). Most SEM produce images using two types of electrons. Secondary electrons (SE) are generated by the inelastic interaction between the electron beam and sample, in which the electrons escaped from the orbiting atoms of the surface sample in unique patterns

with low energy electrons. When an outer shell (L_1) electron jumps into the core shell (K) vacancy left by the secondary electron and releases energy in the form of characteristic X-rays, which can be used in energy dispersive spectrometry (EDS). Sometime, the surplus energy can make a second outer shell ($L_{2,3}$) in excited state, Augur electrons (AE) will be emitted. While backscattered electrons (BSEs) are extremely high energy electrons, they pass close to an atomic nucleus and are reflected back after elastic interactions between the beam and the deeper region part of sample. Figure 2.10a summarizes the mechanism of the emission of SE, BSE, AE and X-rays from the atom of the specimen. Figure 2.10b depicts different signals generated by electron matter interactions with the bulk specimen (Figure 2.10c).

A secondary electron detector attracts AE, additional sensors detect BSE and X-rays. Dot by dot, row by row, an image of the original object is scanned onto a monitor for viewing. Different types of signals give different information, secondary electrons are mainly used for imaging the surface topography; backscattered electrons for surface structure and average elemental information, because BSEs are sensitive to atomic number Z; X-rays and Auger electrons for qualitative elemental composition with different thicknesses and sensitivity. The form of image processing is only in gray scale. That is the reason why SEM images are always in black and white.

In this thesis, two SEM facilities, JEOL-JSM-6300F (INRS) and JEOL-JSM-7401F (located in the cleanroom of INRS-EMT), have been used to examine the surface morphology of the prepared samples.

2.3.2 Transmission electron microscopy (TEM)

TEM is similar to SEM with the exception that the beam passes through the sample, but with different working principle. In terms of the design principles, SEM is designed to primarily to examine material surfaces. TEM is a powerful and unique technique to characterize the internal microstructure of particles, membranes, even imaging of atoms. In SEM (**Figure 2.11**a), the e-beam is focused to a spot, and is scanned sequentially across the sample [39]. At each place, signals are emitted from the sample and received by detectors. The continuously signals are become an image. In TEM (**Figure 2.11**b), e-beam is incident onto a defined area of the sample, and the electrons transmitted through the specimen are focused by lenses and collected by a parallel detector to form an image [39].

In TEM, electrons, emitted from the electron gun are attracted to the anode and accelerated by the high voltage (80~300 kV) in a vacuum. After focused by electrostatic and electromagnetic condenser lenses, primary electrons directly transmit through a thin specimen up to 200 nm in thickness. The incident high energy electrons interact with thin sample as shown in **Figure 2.11**c. Transmitted electrons, undergoing coherent scattering or diffraction from lattice planes in the crystalline phase of materials, are magnified by projector lenses and impinged on viewing screen. We can obtain inner structure information of the sample (crystal structure, morphology and stress state).

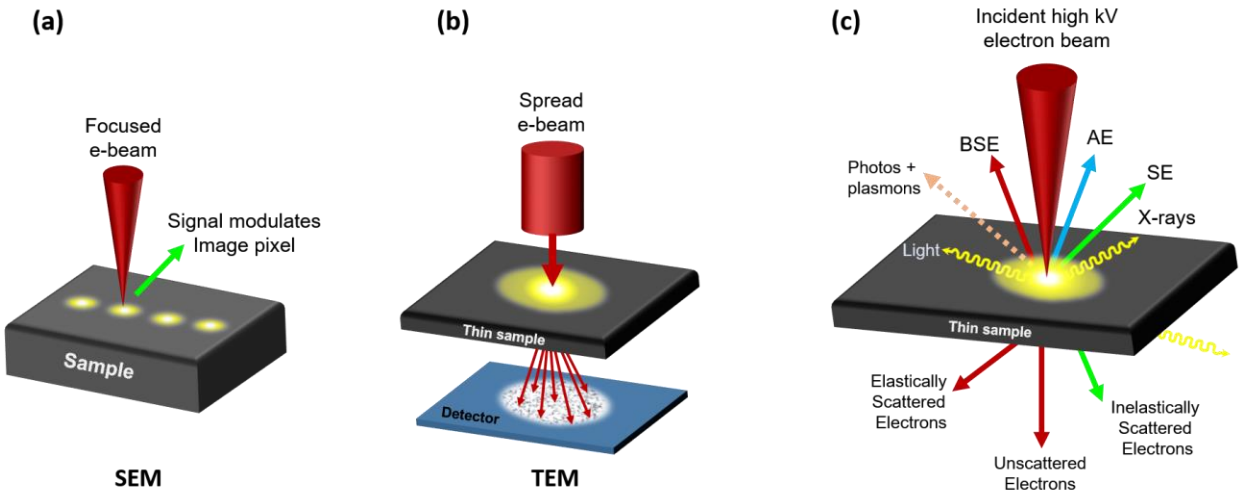

Figure 2.11 Schematic of SEM (a) and TEM (b) imaging methodology. (c) Diagram illustration of the interaction of electrons and thin specimen.

Figure 2.12 shows the essential components of a TEM microscope, which includes the electron gun, electrostatic lenses to focus the electrons before and after the specimen, and a transmitted electron detection system.

In the thesis, TEM is used to observe the morphology and size of as-prepared catalysts on the substrate. TEM images were obtained with JEOL-JEM-2100F (École Polytechnique de Montréal, Montréal, Canada) operating at 200 kV. Particle size distributions were determined by measuring more than 100 individual particles in TEM images.

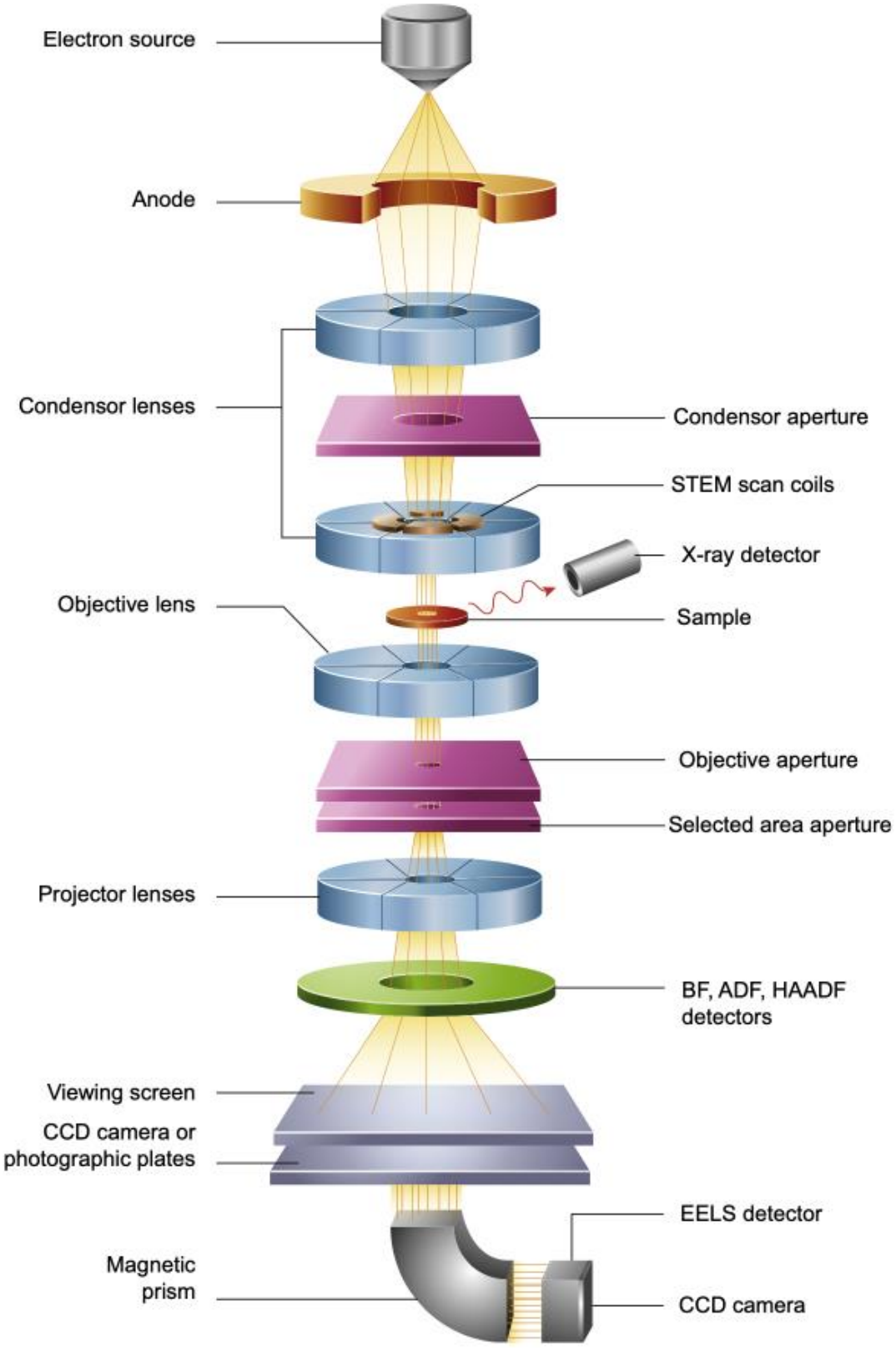

Figure 2.12 Schematic of core components of a TEM microscope [39].

2.3.3 Energy Dispersive X-ray Spectroscopy (EDS)

Normally, energy dispersive X-ray spectroscopy (EDS) is combined with SEM, and it is applied for determining the elemental composition of a sample. SEM is used for imaging, and the SEM image is obtained from the interaction between the sample and secondary electron. As for EDS, the elemental analysis is achieved by X-rays (Figure 2.10a-3). When the sample is struck by SEM electron beam, the electrons are ejected from an inner shell, the electron vacancies are filled by electrons from a higher state, accompanied by the emitting of X-ray. The X-ray energy is characteristic of the atomic structure of the element in the sample. In the end, a spectrum is formed, which reveals the elements in the sample. The quantitative analysis can be done by the peak area ratios.

2.3.4 X-Ray Diffraction (XRD)

X-ray diffraction (XRD) is a powerful non-destructive technique for characterization of crystalline materials (fingerprint). It provides information on average crystallite size and lattice parameters.

X-ray diffraction is based on constructive interference of monochromatic X-rays and a crystalline sample. These X-rays are generated in a cathode ray tube by heating a tungsten filament in a vacuum to produce electrons, accelerating electrons toward a target (at the anode) through a high potential field, and bombarding the target material with electrons. When electrons have sufficient energy to dislodge inner shell electrons of the target material, the electrons from the out shells jump into these gaps, characteristic spectra $K_{\alpha1}$, $K_{\alpha2}$, $K_{\beta1}$,$K_{\beta2}$, $L_{\alpha1}$, $L_{\alpha2}$, $L_{\beta1}$ and $L_{\beta2}$ are produced, as illustrated in Figure 2.13a and b. In general, the highest intensity K_{α} radiation is the only characteristic radiation used in XRD, the rest of the radiation is screened by filters or monochromators.

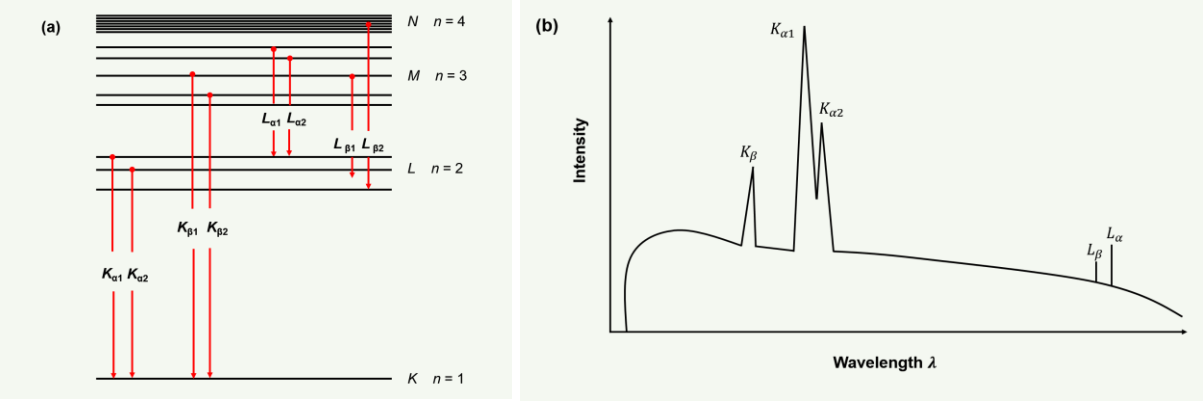

Figure 2.13 **(a) Atomic Energy level transition for Copper atom (b) Scheme of a typical spectrum of emitted X-rays from X-ray tube.**

Then the K_α radiation is collimated to concentrate and directed toward the sample. When the geometry of the incident X-rays impinging the sample satisfies the Bragg's law (Eq. (2.9)), constructive interference occurs. Figure 2.14 provides the geometrical condition for diffraction in detail.

$$n\lambda = 2d_{hkl}\, sin\theta \qquad \text{Eq. (2.9)}$$

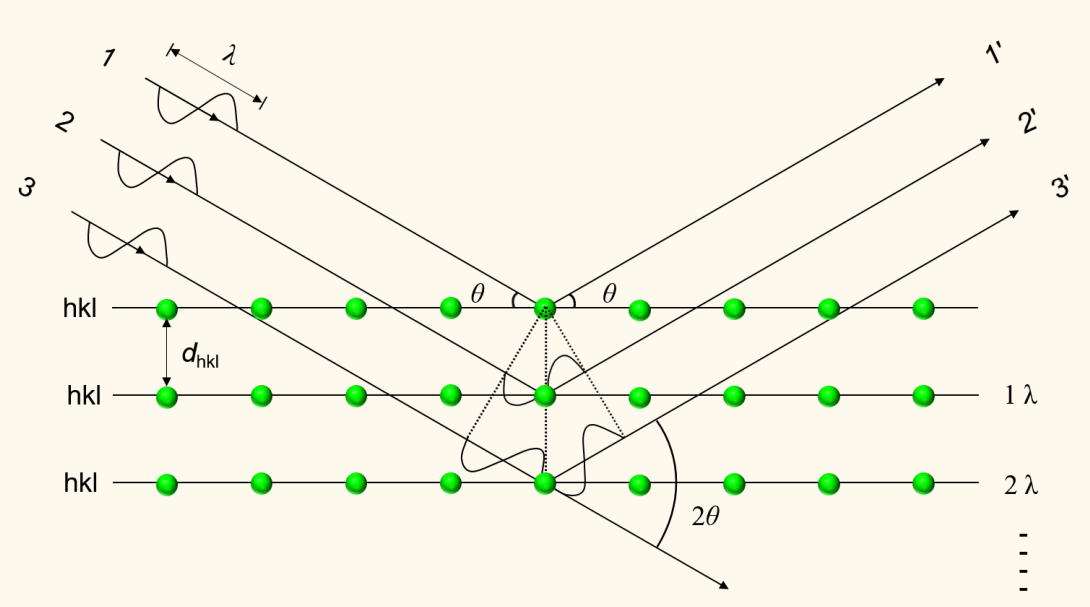

Figure 2.14 Geometrical condition for diffraction from lattice planes.

Where, *n* is an integer called the order of reflection, *λ* the wavelength of the incident X-ray beam, d_{hkl} the distance between the crystallographic planes with (*hkl*) orientation (*h*, *k* and *l* are also known as the Miller indices) of the crystalline lattice, *θ,* the angle of incident (scattering) ray to the crystal planes.

During the acquisition, the sample is scanned through a range of 2θ, all possible diffraction directions of the lattice can be attained.

The average crystallite size *L* was estimated by Scherrer's equation:

$$L = \frac{K\lambda_{K_\alpha}}{\beta\ cos\ \theta_{max}} \qquad \text{Eq. (2.10)}$$

K is the shape factor, a constant which is often taken as unity (typical value 0.89), *λ* the wavelength of the incident K_α X-ray radiation. *β* the line broadening at half the maximum intensity (FWHM) of the selected peak (in radians). *θ* the Bragg angel.

In this thesis, XRD analysis was performed by means of a Bruker D8 Advance diffractometer equipped with a Cu K_α source (λ= .15406 nm) operating at 40 kV and 40 mA. All diffractograms were acquired in the symmetric $\theta-2\theta$ scan mode from 2θ=20°-90° with a low incident angle of 2° and a 2θ angular step size of 0.04° with an acquisition time of 4 s per step. The diffraction peaks position (2θ) and the corresponding FWHM values were evaluated by the software DIFFRAC.EVA V14.

2.3.5 X-ray photoelectron spectroscopy (XPS)

X-ray photoelectron spectroscopy (XPS), also known as electron spectroscopy for chemical analysis (ESCA), is a quantitative technique for defining the surface elemental composition, empirical formula, chemical state and electronic state of the elements within a material. XPS analysis is ultimate surface-sensitive, normally it can probe to a depth of approximately 10 nm of any solid substrate. XPS is a very powerful tool to effectively analyze all the elements except for hydrogen and helium. It is because the photoelectron cross sections of H and He are extremely low and the fact that XPS is not highly sensitive to valence electrons, whereas H and He only have valence electrons. The XPS is performed under high vacuum ($P<10^{-7}$ mbar) or ultra-high vacuum (UHV, $P<10^{-9}$ Pa) with the photon source of Mg $K\alpha$ ($h\nu$=1253.6 eV) or Al $K\alpha$ ($h\nu$=1486.6 eV). A typical XPS set-up is shown in Figure 2.15.

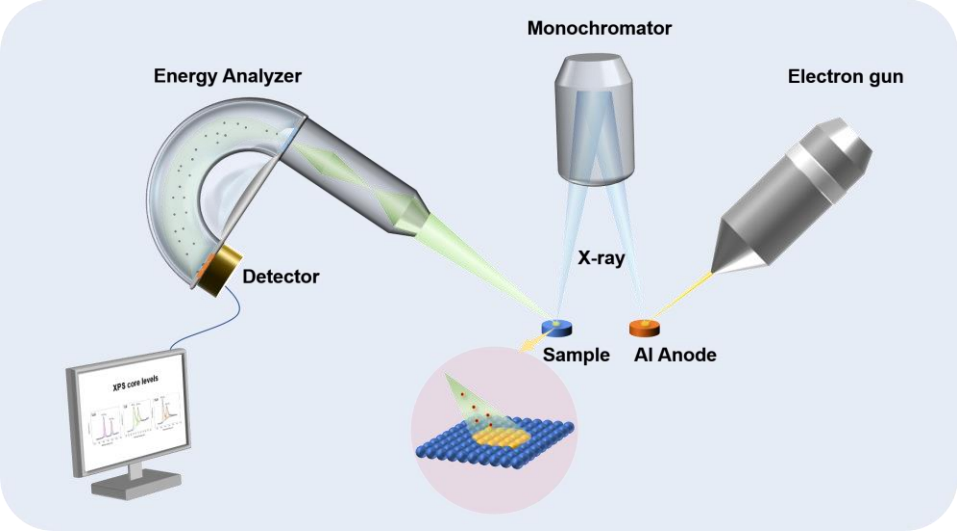

Figure 2.15 Schematic illustration of a typical XPS set-up with photo source.

In XPS, a sample is bombarded with the X-ray in a vacuum, the electrons are ejected from the core shell of the atom and escape from the surface to vacuum, then collected and dispersed to an energy analyzer, where their kinetic energies are measured, and then to a detector, which

counts the number of photoelectrons at various kinetic energies. A simplified diagram of this process is illustrated in Figure 2.16. The emitted electron with a certain kinetic energy E_K is referred to as the photoelectron.

The balance between $h\nu$ and E_K, is expressed as:

$$\boldsymbol{E_B = h\nu - E_K - \Phi} \qquad \text{Eq. (2.11)}$$

where E_B is a binding energy of the electron to nucleus relative to the Fermi level. $h\nu$, the energy of the X-ray photons being used. Φ, the work function, the minimum energy required to eject a photoelectron into the vacuum from the highest occupied energy level. It depends on the spectrometer and the material. E_K, the kinetic energy of emitted photoelectron. The value of E_B and chemical shift (difference from elemental state) are utilized for identification of an element and estimation of its chemical bonding state in the specimen.

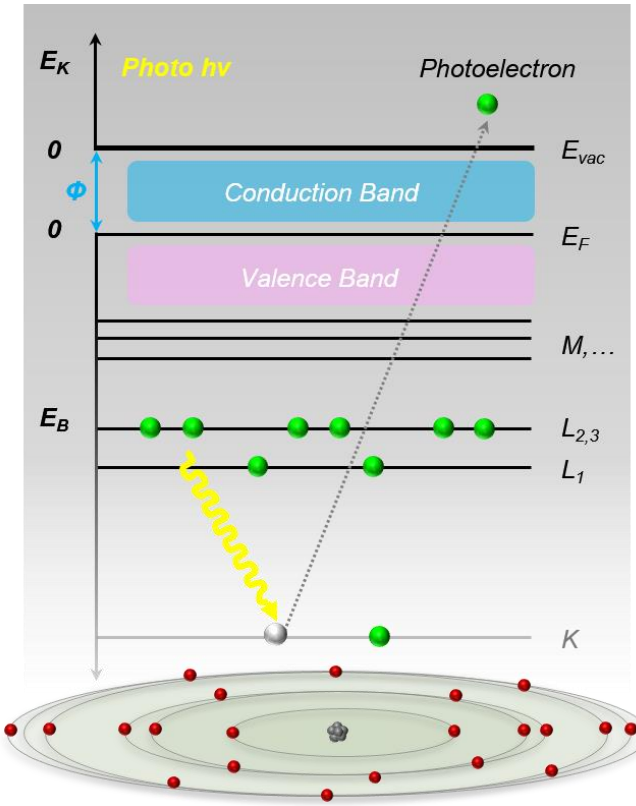

Figure 2.16 Scheme of the principle of XPS.

XPS measurements were carried out via a VG Escalab 220i-XL set with Al *Kα* source (1486.6 eV). The anode was operated at 10 kV and 20 mA. The pass energy of the analyzer was fixed at 20 eV. The base pressure of the system was 10^{-9} mbar. All samples were analyzed with a spot size of 250×1000 μm located approximately in the center of the sample. A survey spectrum

ranging from 0 to 1300 eV was first acquired, and then higher resolution multiplex scan spectra (Pt 4*f*, Rh 3*d*, Sn 3*d*, Ce 3*d*, Mn 2*p*, Ti 2*p*, O 1*s* and C 1*s* core levels) were obtained. Quantification of the elements was performed with Casa XPS software version 2.3.12 (Casa Software Ltd.) by fitting the core level spectra after a Shirley background removal. The metallic components were fitted using a Gaussian/Lorentzian asymmetrically modified line shape, also symmetrical Gaussian/Lorentzian were used to fit other components. The C 1*s* core level peak at 284.6 eV, resulting from hydrocarbon contaminants at the surface, was taken as an internal reference binding energy for charge correction.

2.3.6 Neutron activation analysis (NAA)

Neutron activation analysis (NAA) is a non-destructive, sensitive analytical technique useful for determining both qualitative and quantitative multi-element analysis of major, minor and trace elements in samples from almost every possible field of scientific or technical interest [40]. Unlike many other analytical techniques, NAA is based on neutron activation rather than electronic transitions. In principle, the sample is bombarded with electrons, which causes elements to form radioactive isotopes. The excited isotope undergoes nuclear decay and loses energy by emitting β particles and γ ray photons (as shown in Figure 2.17). The radioactive emission and radioactive decay path are unique for each element on the periodic table, which allows to identity and concentration of the element to be determined by studying its special spectra.

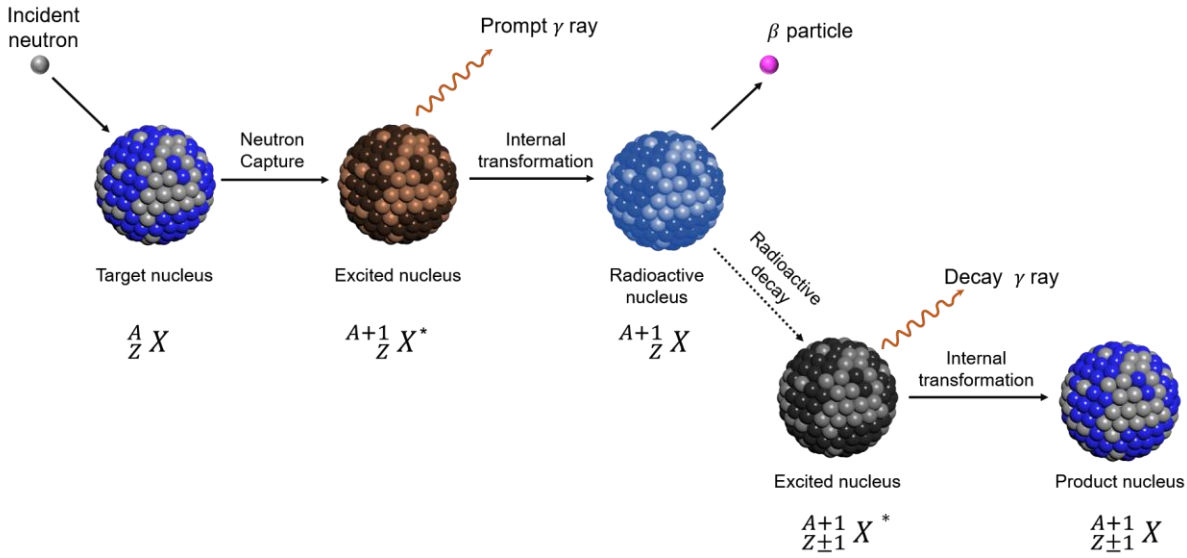

Figure 2.17 **Schematic diagram of neutron activation analysis steps and illustration of the neutron capture process.**

In our work, the Pt loading is determined by NAA technique on all our samples using a nuclear reactor (École Polytechnique de Montréal, Montréal, Canada). The mass loading of Pt in Pt-based catalysts was 120 μg cm^{-2}.

2.4 Electrochemical characterizations

2.4.1 Three electrode assembly

The system consists of a working electrode (WE), a counter electrode (CE) and a reference electrode (RE). Generally, WE is often used in conjunction with a CE and a RE in a three electrode system. The reaction of interest takes place at WE. The RE is separated from the analyte solution by a Luggin capillary, which is close to WE at a distance of 1 mm so as to minimize the ohmic drop (engendered by the electrolyte resistance). The measured cell voltage *E* is the potential difference between WE and RE. The RE should not be polarized in order to provide a reliable potential over time or with changing temperature. Its position should, however, not interfere with the ions/molecules mass transport. The CE, also known as auxiliary electrode, is made of an inert material (*e.g.,* Pt, Au, graphite, glassy carbon). Normally, it does not participate in the electrochemical reaction but conducts electricity from the signal source into the solution, maintaining the correct current. Because the current is flowing between the WE and the CE, the total surface area of the CE must be higher than the area of the WE so that it will not be a limiting factor in the kinetics of the electrochemical process under investigation. Figure 2.18 shows the experiment set-up in this project.

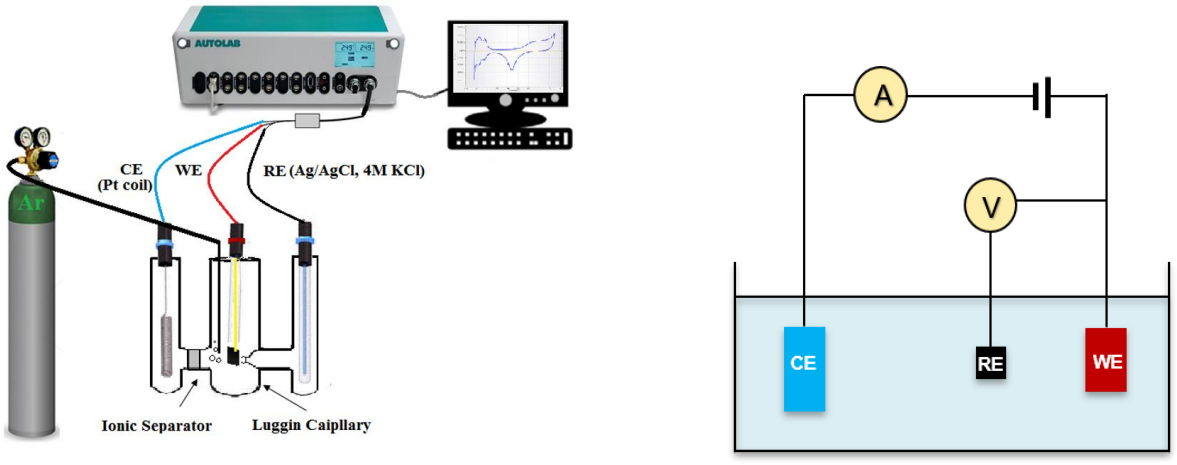

Figure 2.18 Schematic diagram of experimental set-up.

2.4.2 Cyclic Voltammetry and linear sweep voltammetry

Cyclic voltammetry (CV) is potentiodynamic electrochemical measurement in which the working electrode potential is scanned linearly as a function of time, between two selected potentials (initial potential E_i to the switching potential E_λ), as shown in Figure 2.19a. Normally, the potential range is set at a range that all expected reactions can occur. Whereas in aqueous electrolytes, the potential range should be in the water window of the electrode, as potentials of the onset of hydrogen and oxygen evolution should not be exceeded [41]. The scan rate $v = \frac{dE}{dT}$ is the speed of the potential variation, and it is the most important parameter in CV. Faster scan rate will lead to a diminish in the size of the diffusion layer; as a result, higher current is obtained. Besides, the kinetics of electrochemical redox reaction can be obtained by changing the scan rate. Typical values of v vary from 1 mV s^{-1} to 1000 mV s^{-1}.

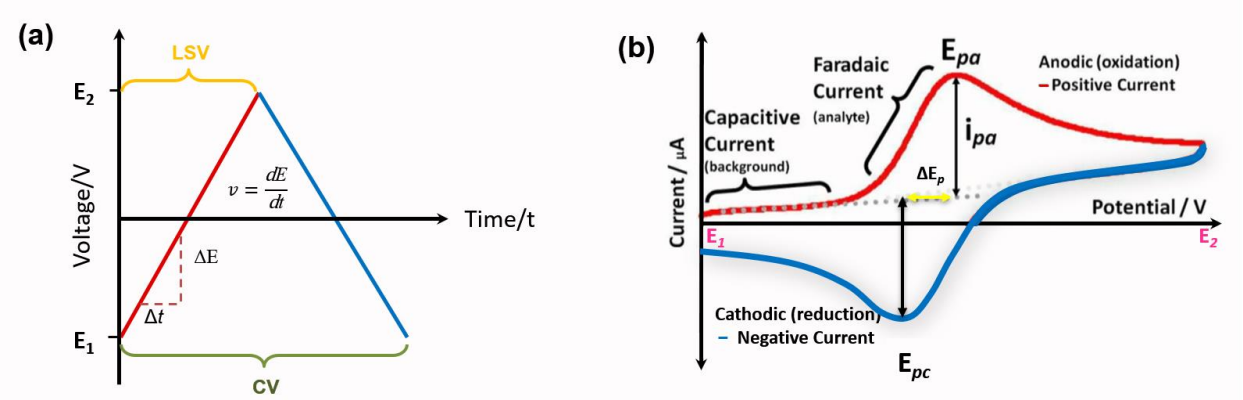

Figure 2.19 (a) Voltage-time profile that is used for LSV and CV (b) Typical CV trace.

In forward scan as shown in Figure 2.19b (red line, from E_1 to E_2), the current keeps constant primitively as the potential is applied. This initial current is due to electro-double layer capacitance generated at the surface of the electrode. This is a non-faradaic process, which means there is no electro transfer. This capacitive current i_c (also called non-faradaic or double layer) can be written as follows [41]:

$$|\boldsymbol{i_c}| = \boldsymbol{A C_d v} \qquad \text{Eq. (2.12)}$$

where A (cm^2) is the electrode area, C_d (F cm^{-2}) the double-layer capacitance and v (mV s^{-1}) the scan rate.

When reaching to the oxidation potential of analyte, electroactive species begin to oxidize, and the anodic current starts to rise up. The current arising from the electron transfer between species and the electrode is called faradaic current, which obeys the power law:

$$\boldsymbol{i = av^b}$$ Eq. (2.13)

Where a and b are adjustable values. The b value can be regarded as the sum of the Faradaic (diffusion-controlled) and non-Faradaic (capacitive) currents. For the electrochemical reversible electron transfer process at 298 K, it involves freely diffusing redox species, the corresponding current i is proportional to $v^{\frac{1}{2}}$, according to Randles-Sevcik equation. The peak current i_p^{rev} will be [42]:

$$\boldsymbol{i_p^{rev} = \pm \left(2.69 \times 10^5\right) n^{\frac{3}{2}} ACD\, v^{\frac{1}{2}}}$$ Eq. (2.14)

Where i_p^{rev} (A) is the peak current, n the total number of electrons transfer, A (cm^2) the electrode area, D ($cm^2\ s^{-1}$) the diffusion coefficient of the oxidized analyte, C ($mol\ cm^{-3}$) the bulk concentration of the analyte, and ν ($mV\ s^{-1}$) the scan rate.

The electrochemical reaction causes a decline of analyte concentration at the electrode surface and mass transport of fresh analyte to the electrode from the bulk solution. With the increasing of potential, the reduced product of the analyte is entirely consumed from the electrode surface, resulting in the mass transport of fresh analyte to the electrode and achieve its peak. When the analyte and its reduced product reach equilibrium (this equilibrium can be described by the Nernst equation), the peak occurs. The peak current i_{pa} and peak potential E_{pa} are shown in Figure 2.19b. Continue raising potential, the analyte depletion zone becomes wide, resulting in a broadening of the diffusion layer. The mass transport to the electrode slows down, and the current decreases accordingly. When reaching to the switching potential E_2, the scan direction is reversed, and the backward scan begins (Figure 2.19b, blue line, from E_2 to E_1). The oxidized species are reduced during the backward scan. In consideration of the reversibility of the electrochemical reaction, a cathodic peak with similar shape is observed. This complete cycle is one cycle of the cyclic voltammogram.

In addition to providing information about kinetics, CV can also yield information on the reversibility of an electrochemical system via the peak current ratio i_{pa}/i_{pc} and peak potential separation ΔE_p. For a chemically and electrochemically reversible reaction, its peak current ratio i_{pa}/i_{pc} is 1, and the ΔE_p is 59/n mV (2.3 RT/nF) at 298 K, where n denotes the number of electrons transferred in the reaction.

CV is based on the principle of linear sweep voltammetry (LSV). Different from CV, LSV finishes with a single sweep within a fixed voltage range.

2.4.3 Chronoamperometry

Chronoamperometry (CA) is an electrochemical technique where a square-wave potential of the working electrode is stepped, the resulting current from faradaic processes occurring at the electrode (caused by the potential step) and the resulting current is recorded as a function of time.

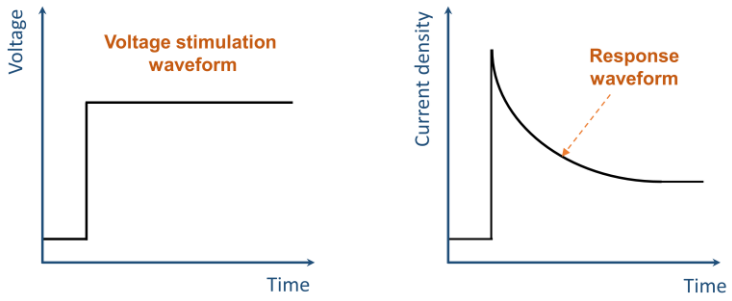

Figure 2.20 Waveform and response for CA.

Figure 2.20 illustrates a typical potential excitation waveform and the corresponding current response for CA. Like CV, in CA the current response to the step potential attribute to the contribution of a capacitive i_c and Faradaic i_F current. The capacitive current, only occurring primevally in a short time, corresponds to the double layer charging. The Faradaic current, caused by the electron transfer, is the current of interest. This current decline followed by the Cottrell equation [41].

$$\boldsymbol{i} = \frac{\boldsymbol{nFAD^{0.5}C_b}}{\boldsymbol{\pi^{0.5}t^{0.5}}} \qquad \text{Eq. (2.15)}$$

where n (mol^{-1}) is the number of the electron transferred in half cell, F is the Faraday's Constant (96,485 C mol^{-1}), D (cm^2 s^{-1}) is the diffusion coefficient of the oxidized analyte, A (cm^2) is the electrode area, C_b (mol cm^{-3}) is the bulk concentration, and t (s) is the time.

As can be seen from the equation, the Faradaic current is proportional to $1/t^{0.5}$. The response is suitable for semi-infinite linear diffusion, which means the solution is unstirred; there is a linear diffusion to the flat electrode (with a supporting electrolyte to ensure the absence of ion migration) and no other reactions [43]. Generally, the response current decays exponentially with time more or less rapidly subjected to the double layer capacity C_d and the ohmic resistance R_Ω of the electrolyte.

Chronoamperometry is applied to evaluate the durability of electrocatalysts for ethanol oxidation. The criterion of a good electrocatalyst is that it should maintain a high steady state current density.

2.4.4 CO stripping voltammetry

CO stripping voltammetry is a powerful technique for the surface morphology and structure study [44]. It is commonly accepted that the oxidation of absorbed CO_{ads} on Pt or Rh surface follows the Langmuir-Hinshelwood mechanism in which CO_{ads} reacts with oxygenous species on its surface [45]. Reaction (2.17) is the rate determining step (RDS).

$$Pt + H_2O \rightarrow OH_{ads,\ Pt} + H^+ + e^- \quad \text{Eq. (2.16)}$$

$$C \equiv O_{ads,\ Pt} + OH_{ads,\ Pt} \rightarrow COOH_{ads} \ (RDS) \quad \text{Eq. (2.17)}$$

$$COOH_{ads,\ Pt} \rightarrow CO_2 + H^+ + e^- + 2Pt \quad \text{Eq. (2.18)}$$

Figure 2.21 shows the CO stripping on Pt surface in acid solution, and the shadow area is the CO oxidation area in insert. It is obtained from the CV (the 1st potential cycle) and corrected with respect to double layer charge by subtracting of the 2nd potential cycle. In this project, CO stripping experiments were conducted according to the following steps: Firstly, 0.5 M H_2SO_4 solution was bubbling with high-purity N_2 for 30 min. Then continuously flowing N_2 in the solution, the electrode surface was cleaned and completely activated by potential cycling to steady state for 30 cycles at a sweep rate of 50 mV s^{-1} within the potential range from −0.197 to 1.03 V *vs* Ag/AgCl. Subsequently, the pure CO (99.5%) was purged into the above-mentioned solution at a polarized potential of -0.003 V vs Ag/AgCl for 30 min. Potential being remained constant, the pure N_2 was purged for 30 min to remove redundant CO dissolved in the solution and the CO physically adsorbed on the surface of the electrode. Finally, the CO stripping voltammetry started at the open-circuit voltage.

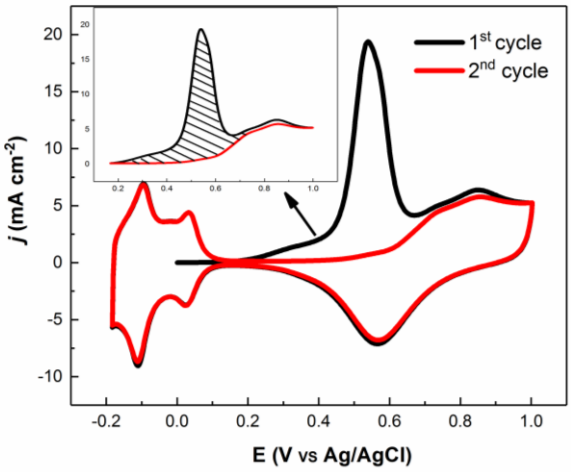

Figure 2.21 **The 1st and 2nd cycle of a CO stripping CV in 0.5 M H_2SO_4 solution. Insert: subtraction of the 1st cycle by the 2nd cycle.**

2.4.5 Experimental Procedures

In this project, all the experiments are recorded in a three-electrode cell with a potentiostat/galvanostat (PGSTAT) Autolab from EcoChemie at room temperature. The PLD and CBPLD-made catalysts were worked as WE, a Pt coil as CE and an Ag/AgCl (4 M KCl) as RE. The electrocatalytic activities towards EOR are investigated in the deaerated solutions of 1 M C_2H_5OH + 0.5 M H_2SO_4.

2.4.5.1 Cyclic Voltammetry on polycrystalline Pt

Figure 2.22 illustrates a typical CV profile of polycrystalline Pt electrode in sulfuric acid electrolyte at a particular scanning rate $\nu = dE/dt$. There are three characteristic potential regions: hydrogen region (*H*-region), double layer (*DL*) region and oxide region (*O*-region).

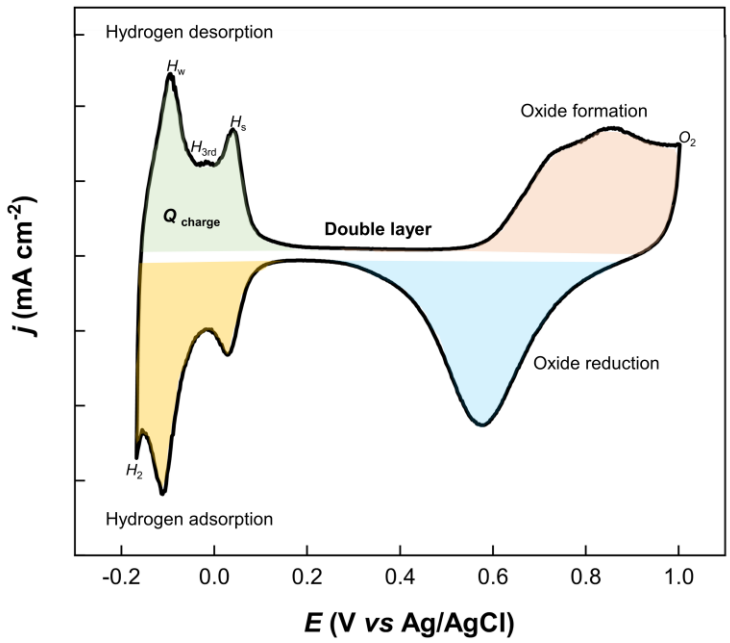

Figure 2.22 CV of polycrystalline Pt electrode in 0.5 M H_2SO_4 solution at scan rate of 50 mVs^{-1}.

1) *H*-region

In the positive-going sweep, the potential region from -0.17 to 0.2 V (vs Ag/AgCl) is the hydrogen underpotential deposition reaction (H_{upd}).

$$\boldsymbol{Pt + H^+ + e^- \leftrightarrow Pt - H_{ads}} \qquad \text{Eq. (2.19)}$$

As can be seen from Figure 2.22, it obviously presents three well-defined peaks (H_w, H_s *and* H_{3rd}) in H_{upd}. Peak H_w is attributed to the weakly bonded hydrogen on Pt (110) and (111) plane [46-47], while peak H_s is assigned to Pt (100) plane for the strongly bonded hydrogen

[46], and UPD H_2 [48] is responsible for the peak H_{3rd}, which is between the H_w and H_s. In reverse, in the negative-going sweep, there are the well-defined peaks in underpotential hydrogen adsorption region.

$$\boldsymbol{Pt - H_{ads} \leftrightarrow Pt + H^+ + e^-} \quad \text{Eq. (2.20)}$$

When the negative-going sweep goes lower than 0.17 V, the hydrogen evolution reaction (HER) occurs:

$$\boldsymbol{2H + 2e^- \rightleftharpoons H_{2\,(g)}} \quad \text{Eq. (2.21)}$$

Hydrogen desorption H_{des} and adsorption H_{ads} peaks have similar peak potentials and peak shape, which is the characteristic of reversible reaction.

2) *DL region*

Double layer (DL) undergoes charging and discharging processes without Faradaic reaction. In *DL* region, it can reflect the characters of the solution: solution impurities, surface contamination, trace amount of O_2, and heavy metal desorption may appear in this region [49].

3) *O*-region

The peaks occur at 0.5-1.0 V is the region where OH_{ads}, chemisorbed oxygen, subsurface oxygen, initial Pt oxide structures and surface-oxide phases coexist. Their existence strongly depends on the electrode potential and total surface coverage [50].

$$\boldsymbol{Pt + H_2O \leftrightarrow Pt^{\delta+}\, O^{\delta-}_{chem} + 2\, H^+_{aq} + 2\, e^-} \quad \text{Eq. (2.22)}$$

$$\boldsymbol{Pt^{\delta+} - O^{\delta-}_{chem} \longrightarrow Pt^{2+} - O^{2-}} \quad \text{Eq. (2.23)}$$

When the positive-going potential is greater than 1 V, the oxygen evolution reaction (OER) occurs:

$$\boldsymbol{2H_2O \leftrightarrow O_{2\,(g)} + 4e^- + 4H^+} \quad \text{Eq. (2.24)}$$

In reverse, a big shark peak, positioned between 1 V and 0.5V in the negative-going sweep, is the peak of reduction of Pt oxides.

$$\boldsymbol{PtO_{ads} + 2H^+ + 2e^- \rightarrow Pt + H_2O} \quad \text{Eq. (2.25)}$$

As can be seen from Figure 2.22, the peaks of Pt oxide formation (O_{form}) and oxidation reduction (O_{red}) are asymmetric, which indicates this reaction is irreversible.

2.4.5.2 Cyclic Voltammetry on polycrystalline Rh

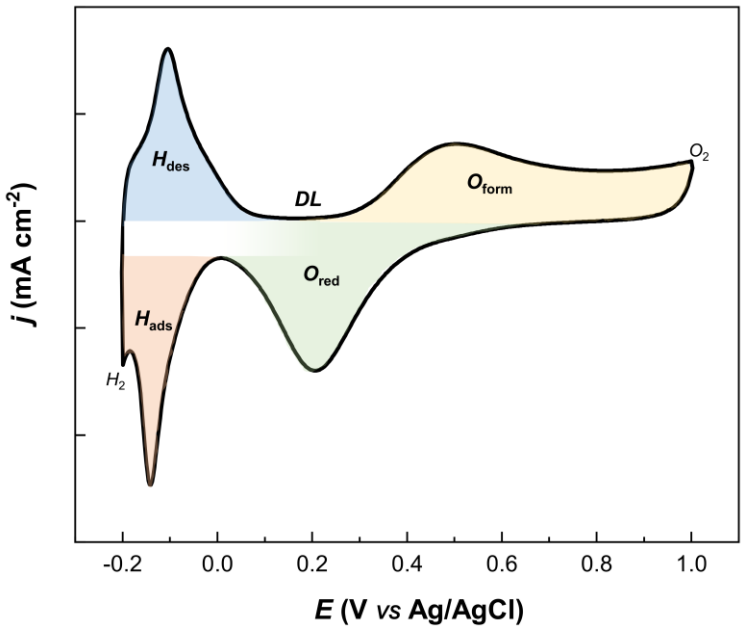

Figure 2.23 CV of polycrystalline Rh electrode in 0.5 M H_2SO_4 solution at scan rate of 5 mVs^{-1}.

Figure 2.23 presents the typical CV curve of Rh electrode. At low potentials on the anodic part, there is a single peak in the hydrogen desorption region, while at high potentials, the surface oxidation forms (O_{form}). Peuckert *et al*. [51] proposed that rhodium was oxidized to tetravalent as the following reactions.

$$\boldsymbol{Rh + H_2O \rightarrow Rh(OH) + H^+ + e^-} \quad \text{Eq. (2.26)}$$

$$\boldsymbol{Rh(OH) + 2H_2O \rightarrow Rh(OH)_3 + 2H^+ + 2e^-} \quad \text{Eq. (2.27)}$$

$$\boldsymbol{2Rh(OH)_3 + Rh \rightarrow 3RhO(OH) + 3H^+ + 3e^-} \quad \text{Eq. (2.28)}$$

Double layer (DL), between hydrogen and oxygen regions, is in a narrow range. Normally there is no faradaic current. Nevertheless, Wasberg and Horányi [52] pointed out that in DL region, both OH and H species were appeared simultaneously on the surface of Rh electrode with low coverage. In the cathodic part, the surface oxidation reduction (O_{red}) occurs at higher potentials. It can be presented as the following equations:

$$\boldsymbol{3RhO(OH) + 3H^+ + 3e^- \rightarrow 2Rh(OH)_3 + Rh} \quad \text{Eq. (2.29)}$$

$$\boldsymbol{Rh(OH)_3 + 3H^+ + 3e^- \rightarrow Rh + 3H_2O} \quad \text{Eq. (2.30)}$$

The potential of surface oxidation reduction (O_{red}) peak on Rh is at 0.2 V, which is much lower than that of on Pt (0.6 V).

2.4.5.3 Electrochemical active surface area (ESA) measurement

The characteristic value of charge density (Q_H) associated with a monolayer hydrogen adsorbed on polycrystalline platinum (assuming an adsorption charge of 210 μC cm^2 for a full H_{upd} monolayer) is widely used to determine the true electrochemically active surface area (*ESA*) of Pt electrodes. The *ESA* value is calculated by the following equations [53]:

(i) For Pt- based catalyst:

$$\boldsymbol{ESA}\ (\boldsymbol{cm^2}) = \boldsymbol{Q^H_{des}/\theta_{H,Pt}\, Q^H_{ox,ML,Pt}} \quad \text{Eq. (2.31)}$$

(ii) For Rh-based catalyst:

$$\boldsymbol{ESA}\ (\boldsymbol{cm^2}) = \boldsymbol{Q^H_{des}/\theta_{H,Rh}\, Q^H_{ox,ML,Rh}} \quad \text{Eq. (2.32)}$$

(iii) For PtRh alloyed catalyst:

$$\boldsymbol{ESA}\ (\boldsymbol{cm^2}) = \boldsymbol{Q^H_{des}/\left(x_{Pt}\cdot Q^H_{ox,ML,Pt} + x_{Rh}\cdot Q^H_{ox,ML,Rh}\right)(x_{Pt}\cdot\theta_{H,Pt} + x_{Rh}\cdot\theta_{H,Rh})} \quad \text{Eq. (2.33)}$$

Where, Q^H_{des} is the measured coulombic charge due to the oxidation of the hydrogen for a given cathodic vertex potential, θ_H is the surface coverage with adsorbed hydrogen at the potential ($\theta_{H,Pt}$ = 0.79, $\theta_{H,Rh}$ = 0.59). x_{Pt} and x_{Rh} are atomic fractions of the metals on the alloy surface, and assuming that the H_{ads} properties are intermediate with respect to those of pure metal, being a linear function of the alloy surface composition. $Q^H_{ox,ML,S}$ is the charge due to oxidation of the monolayer hydrogen adsorbed on the metal surface. And the accepted values of $Q^H_{ox,ML,S}$ for the polycrystalline Pt and Rh are 210 μC cm^{-2} and 221 μC cm^{-2}, respectively.

The ratio of the ESA to the geometric area (A_g) gives the roughness factor (R*F)*.

$$\boldsymbol{RF = ESA/A_g} \quad \text{Eq. (2.34)}$$

2.4.5.4 Ethanol oxidation reaction (EOR)

There are two important parameters to evaluate the catalytic activity of a catalyst: (1) the onset potential of ethanol oxidation E_{onset}. It is the potential where the anodic current starts to flow. E_{onset} is controlled by CO_{ad} + OH_{ad} interactions and it is related to the thermodynamics reactions [54]. (2) the forward anodic peak current density (j_{pa}). The value of j_{pa} is in connection with the kinetic factors of the electrocatalytic reactions and electronic transfer rate, where a higher j_{pa} suggests a higher ethanol oxidation rate [55]. In general, the forward oxidation peak corresponds to the oxidation of freshly chemisorbed species from ethanol adsorption, resulting

in acetaldehyde, acetic acid and CO_2, whereas the backward oxidation peak is related to the removal of residual carbonaceous species, which are not completely oxidized in the positive scan, rather than caused by freshly chemisorbed species [56]. The catalyst exhibits a better performance in terms of a lower onset potential and a higher peak current at a relatively low potential.

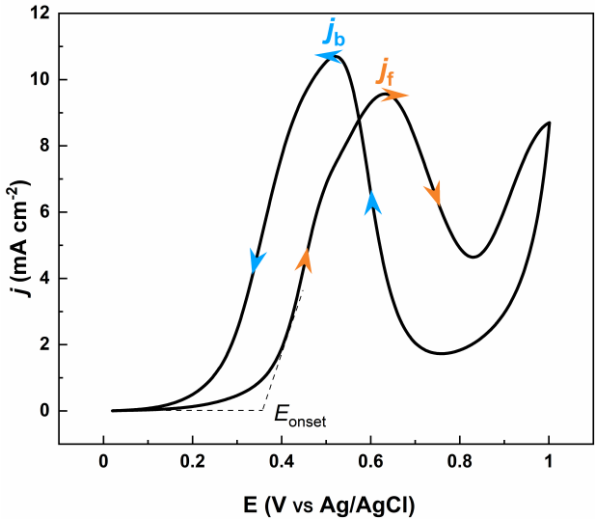

Figure 2.24 CV of Pt/CP electrode in 0.5 M H_2SO_4 + 1 M C_2H_5OH solution at scan rate of 5 mVs^{-1}.

Figure 2.24 represents a typical CV profile of ethanol oxidation on Pt electrode in H_2SO_4 solution. As illustrated, the current density values in the $H_{des/ads}$ region (E<0.2 V) are very small, probably caused by the absorbed CO poisoning intermediates or ethanol adsorption on the catalyst surface, which hinder hydrogen adsorption and other surface reactions [57]. When E>0.2 V, the EOR current density j_f starts to grow, and it reaches the maximum value at 0.63 V due to the formation of Pt-OH which facilitates the migration of CO poisoning species. Subsequently, the current density drops. It can be ascribed to the competition between the adsorption of ethanol and the activation of water molecules forming Pt-O species. In the backward scan, the reaction is still inhibited until the Pt-O electro-reduction at 0.53 V, and then j_b increases suddenly due to the liberation of active metallic Pt sites for ethanol adsorption [56].

2.4.5.5 Durability and stability of the electrocatalyst

The durability and stability of a catalyst is of vital importance for the fuel cell, especially in the practical application. In theory, the kinetic data for the ethanol oxidation can be deduced from chronoamperometric measurements. The chronoamperometry was carried out at room temperature by stepping the potential from open circuit potential (OCP) to 0.6 V for 1hour in the

mixed solution of 0.5 M H_2SO_4 + 1 M C_2H_5OH. The polarization potential of 0.6 V was selected because it was near to the ethanol oxidation peak potential of the electrocatalysts.

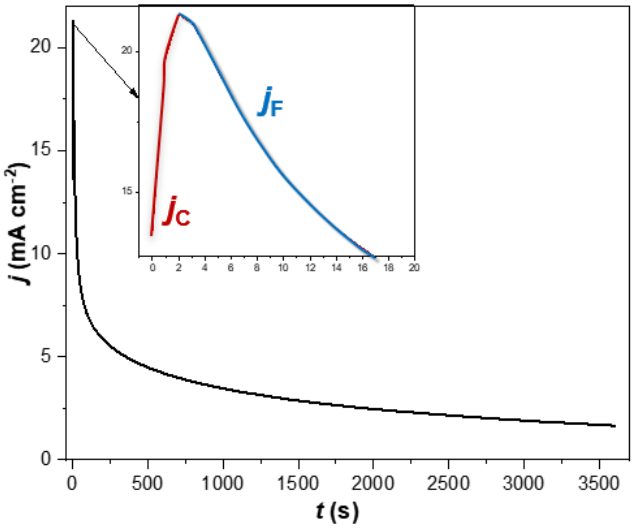

Figure 2.25 CA profile of Pt/CP electrode in 0.5 M H_2SO_4 + 1 M C_2H_5OH solution at 0.6 V for 1 h.

As shown in Figure 2.25, the transient current density (j_c) soared up rapidly in the first 10 s, due to the double layer charging effect. Subsequently, the current density (j_F) dropped down sharply and decayed with time, which was caused by the poison from the accumulation of intermediate species, such as CO_{ads}, CHO_{ads} species during the EOR. Later, the current density arrived at a quasi-stable state within 3600 s.

References

[1] A.R. Mohamed, A.Z. Abdullah, S.-P. Chai, J. Nanomater, 2010 (2010).

[2] G. Zhong, S. Hofmann, F. Yan, H. Telg, J. Warner, D. Eder, C. Thomsen, W. Milne, J. Robertson, J. Phys. Chem., 113 (2009) 17321-17325.

[3] R.B. Mathur, B.P. Singh, S. Pande, CRC Press, 2016.

[4] J. Sengupta, Elsevier, 2018, pp. 172-194.

[5] H.M. Smith, A. Turner, Appl. Opt., 4 (1965) 147-148.

[6] C.W. Schneider, T. Lippert, Springer, 2010, pp. 89-112.

[7] C. Popescu, G. Dorcioman, A.C. Popescu, Laser ablation applied for synthesis of thin films: insights into laser deposition methods, Applications of Laser Ablation: Thin Film Deposition, Nanomaterial Synthesis and Surface Modification, (2016) 1.

[8] E. Papadopoulou, V. Zorba, A. Pagkozidis, M. Barberoglou, E. Stratakis, C. Fotakis, Thin Solid Films, 518 (2009) 1267-1270.

[9] A.A. Tseng, World Scientific, 2008.

[10] R. Eason, John Wiley & Sons, 2007.

[11] M. Datta, L. Romankiw, D. Vigliotti, R. Von Gutfeld, Appl. Phys. Lett., 51 (1987) 2040-2042.

[12] M. von AUmen, in, Springer-Verlag, Berlin, 1987.

[13] N. Roy, A. Kuar, S. Mitra, in: Microfabrication and Precision Engineering, Elsevier, 2017, pp. 189-212.

[14] W.M. Steen, in: Laser Material Processing, Springer, 1991, pp. 69-107.

[15] A. Welch, C. Gardner, in: Lasers in medicine, CRC Press, 2001, pp. 39-58.

[16] P. Willmott, J. Huber, Pulsed laser vaporization and deposition, RMP, 72 (2000) 315.

[17] V. Nazabal, P. Němec, in: Springer Handbook of Glass, Springer, 2019, pp. 1293-1332.

[18] M.N. Ashfold, F. Claeyssens, G.M. Fuge, S.J. Henley, Chem. Soc. Rev., 33 (2004) 23-31.

[19] T.P. Hughes, Plasmas and laser light, nyhp, (1975).

[20] A. Namiki, T. Kawai, K. Ichige, Surf. Sci., 166 (1986) 129-140.

[21] R. Kelly, A. Miotello, Appl. Phys. B, 57 (1993) 145-158.

[22] A. Saeed, A. Khan, F. Jan, M. Abrar, M. Khalid, M. Zakaullah, Appl. Surf. Sci., 273 (2013) 173-178.

[23] S.P. Koenig, L. Wang, J. Pellegrino, J.S. Bunch, Nat. Nanotechnol., 7 (2012) 728-732.

[24] W.J. Fader, Phys. Fluids, 11 (1968) 2200-2208.

[25] A. Guha, S. Samanta, J. Aerosol Sci, 77 (2014) 85-101.

[26] X. Tan, D. Zhang, X.A. Li, Z. Li, R. Fang, J. Phys. D: Appl. Phys., 41 (2008) 035210.

[27] I. Weaver, C. Lewis, J. Appl. Phys., 79 (1996) 7216-7222.

[28] K. Sturm, S. Fähler, H.-U. Krebs, Appl. Surf. Sci., 154 (2000) 462-466.

[29] D. Bäuerle, Springer Science & Business Media, 2013.

[30] S. Amoruso, R. Bruzzese, N. Spinelli, R. Velotta, J. Phys. B, 32 (1999) R131.

[31] A. Zawadzka, P. Płóciennik, Z. Łukasiak, K. Bartkiewicz, A. Korcala, H. El Ouazzani, B. Sahraoui, in: 2011 13th International Conference on Transparent Optical Networks, IEEE, 2011, pp. 1-4.

[32] S. Harilal, J. Appl. Phys., 102 (2007) 123306.

[33] D. Marla, U.V. Bhandarkar, S.S. Joshi, J. Appl. Phys., 109 (2011) 2.

[34] E. Morintale, C. Constantinescu, M. Dinescu, Physics AUC, 20 (2010) 43-56.

[35] J. Yang, Z. Zhang, X. Men, X. Xu, X. Zhu, Langmuir, 26 (2010) 10198-10202.

[36] A. Gorbunoff, in: Photon Processing in Microelectronics and Photonics V, International Society for Optics and Photonics, 2006, pp. 61060U.

[37] A. Gorbunov, W. Pompe, A. Sewing, S. Gaponov, Appl. Surf. Sci., 96 (1996) 649-655.

[38] A. Gorbunoff, John Wiley & Sons, Inc. (2007) 131-160.

[39] B. Inkson, Elsevier, 2016, pp. 17-43.

[40] M.D. Glascock, Columbia, MO: University of Missouri Research Reactor (MURR), (2006).

[41] A.J. Bard, L.R. Faulkner, Fundamentals and applications, Electrochemical Methods, 2 (2001) 580-632.

[42] K. Ngamchuea, S. Eloul, K. Tschulik, R.G. Compton, J. Solid State Electrochem., 18 (2014) 3251-3257.

[43] K. Scott Elsevier, 2016, pp. 29-66.

[44] J. Flórez-Montaño, G. García, O. Guillén-Villafuerte, J.L. Rodríguez, G.A. Planes, E. Pastor, Electrochim. Acta, 209 (2016) 121-131.

[45] T. Housmans, J. Feliu, M. Koper, J. Electroanal. Chem., 572 (2004) 79-91.

[46] B. Loo, T. Furtak Electrochim. Acta, 25 (1980) 505-508.

[47] K. Kinoshita, P. Stonehart, Electrochim. Acta, 20 (1975) 101-107.

[48] T. Frelink, W. Visscher, J. Van Veen, Electrochim. Acta, 40 (1995) 545-549.

[49] V. Climent, J.M. Feliu, J. Solid State Electrochem., 15 (2011) 1297.

[50] M. Alsabet, M. Grden, G. Jerkiewicz, J. Electroanal. Chem., 589 (2006) 120-127.

[51] M. Peuckert, F. Coenen, H. Bonzel, Surf. Sci., 141 (1984) 515-532.

[52] M. Wasberg, G. Horányi, J. Electroanal. Chem., 386 (1995) 213-219.

[53] M. Łukaszewski, M. Soszko, A. Czerwiński, Int. J. Electrochem. Sci, 11 (2016) 4442-4469.

[54] M. De Souza, R. Gomes, A. De Bortoli, Int. J. Hydrogen Energy, 43 (2018) 13475-13488.

[55] M.A.R. Queiroz, J. Ribeiro, Catalysts, 9 (2019) 277.

[56] Z. Liu, L. Hong, J. Appl. Electrochem., 37 (2007) 505-510.

[57] J. Asgardi, J.C. Calderón, F. Alcaide, A. Querejeta, L. Calvillo, M.J. Lázaro, G. García, E. Pastor, Appl. Catal. B, 168 (2015) 33-41.

3 THE 1ST ARTICLE

Study on the influence of the thickness of nanostructured rhodium films towards electrooxidation of adsorbed carbon monoxide

Étude de l'influence de l'épaisseur des films nanostructurés de rhodium sur l'électrooxydation du monoxyde de carbone adsorbé

Authors:

Haixia Wang, Shuhui Sun and Mohamed Mohamedi

Énergie, Matériaux et Télécommunications (EMT), Institut National de la Recherche Scientifique (INRS), 1650 Boulevard Lionel Boulet, Varennes, Quebec, J3X 1S2, Canada

Title of the journal or book:

SN Applied Sciences

SN Applied Sciences (2020) 2:1462.

DOI: 10.1007/s42452-020-03254-4

Contribution:

I synthesized all the samples and I conducted all the physicochemical characterizations and electrochemical measurements. I analyzed the data and interpreted the results. I participated in the writing with the help of the other authors.

Abstract

Carbon supported rhodium thin films with various thicknesses are grown by varying the number of laser pulses, N_{lp} (from 5000 to 50000) under 2 Torr of He background atmosphere using the pulsed laser deposition method. The thin films are characterized for their morphological features and structural properties. It is observed that smooth dense 2D nanosheets of Rh are obtained with 5000 $N_{lp,}$ whereas higher N_{lp} yields to highly porous Rh films. X-ray photoelectron spectroscopy reveals that both metallic Rh and Rh^{3+} are present at the surface of the Rh films. Nevertheless, the amount of metallic Rh increased as the N_{lp} increased. The influence of the

thickness of the Rh films on the tolerance to CO , a poison that strongly adsorbs on the surface of catalysts in fuel cells reactions, was investigated through anodic stripping voltammetry. It is found that Rh film deposited with 50000 N_{lp} exhibits the highest electroactive surface area (27.90 cm^2 *vs* 1.20 cm^2 of Pt), the lowest onset potential of CO electrooxidation (0.47 V *vs* 0.60 V Pt), and a net charge corresponding to electrooxidation of the CO adlayer of 424 µC cm^{-2} (*vs* 358 µC cm^{-2} of Pt). Such high tolerance to CO poisoning is explained on the basis of the elevated porosity and roughness of the Rh surface. Indeed, a roughness factor of 90.5 for Rh against about 3.8 for Pt grown under analogous deposition conditions of pressure and number of laser pulses.

Key words:

Rhodium; Thin films; Pulsed laser deposition; Carbon monoxide; Electrooxidation

Résumé :

Des films minces de rhodium supportés par du papier carbone avec différentes épaisseurs sont développés en faisant varier le nombre d'impulsions laser, N_{lp} (de 5000 à 50000) sous une atmosphère de fond de 2 Torrs de He en utilisant la méthode de dépôt par laser pulsé. Les films minces se caractérisent par leurs caractéristiques morphologiques et leurs propriétés structurelles. On observe que des nanofeuilles 2D lisses et denses de Rh sont obtenues avec N_{lp} de 5000, alors que des N_{lp} plus élevés donnent des films Rh hautement poreux. La spectroscopie photoélectronique par rayons X révèle que les Rh métallique et Rh^{3+} sont présents à la surface des films Rh. Néanmoins, la quantité de Rh métallique a augmenté avec le N_{lp}. L'influence de l'épaisseur des films Rh sur la tolérance au CO, un poison qui s'adsorbe fortement à la surface des catalyseurs dans les réactions des piles à combustible, a été étudiée par voltampérométrie inverse anodique. On constate que le film Rh déposé avec N_{lp} de 50000 présente la plus grande surface électroactive (27.90 cm^2 *vs* 1.20 cm^2 Pt), le potentiel d'apparition le plus bas de l'électrooxydation du CO (0,47 V vs 0,60 V Pt), et une charge nette correspondante à l'électrooxydation de la couche de CO de 424 µC cm^{-2} (*vs* 358 µC cm^{-2} Pt). Une telle tolérance élevée à l'empoisonnement au CO est expliquée par la porosité et la rugosité élevées de la surface Rh. En effet, un facteur de rugosité de 90,5 pour Rh contre environ 3,8 pour Pt synthétisé dans des conditions de dépôt analogues de pression et de nombre d'impulsions laser.

Mots clés :

Rhodium; Films minces; Dépôt laser pulsé; Monoxyde de carbone; Électrooxydation

3.1 Introduction

Noble metal nanoparticles (NPs) are of scientific interest and technological significance and have a wide range of potential applications in optoelectronics, sensors, catalysis, energy conversion/storage and biotechnology to medicine [1-5]. This is essentially attributed to their remarkable catalytic properties, which are radically different from that of their bulk form [6]. Rhodium is widely acknowledged as one of the most essential component in heterogeneous catalysis and often used in the fields of carbon monoxide (CO) oxidation [7], hydrocarbonylation [8], hydroformylation [9], hydrogenation [10], electroreduction of nitrates [11], and CO elimination from exhaust stream [12]. Rh is also becoming cumulatively important in energy conversion systems such as direct ethanol fuel cells (DEFCs) [13-16], a promising green technology for transportation and portable electronic devices. However, CO poisoning is a critical problem in direct alcohol fuel cells, where CO is a reaction intermediate generated throughout the decomposition of ethanol [2-5]. To sustain their activity, catalysts must achieve the electrooxidation of CO alongside the fuel. Towards a rational design of new CO-tolerant catalysts, it is thus becoming important to understand how and where CO oxidation takes place on the highly inhomogeneous surface of a typical Rh catalyst.

Miscellaneous methods have been employed for the synthesis of Rh NPs. In 1978, Hirai and co-workers [17] first reported the synthesis of colloidal dispersion Rh NPs by refluxing a mixed solvent of poly (vinyl alcohol) (PVA) and $RhCl_3$ at 79 ºC under argon or air on a boiling water bath for 0.2-16 h. Nishida et al. [18] synthesized various sizes of RhNPs via microwave-assisted alcohol reduction in a closed vessel under 165 °C for 17 min. Grass et al. [19] used poly (vinylpyrrolidone) (PVP) as capping agent to stabilize monodisperse Rh through one-step polyol method at 140 ºC under vacuum. Zettsu et al. [20] prepared branched Rh multipods in large quantities, and the reaction was continued up to 120 h. Ramírez-Meneses et al. [21] reported the synthesis of Rh nanoparticles through an organometallic approach starting from the tris(allyl) rhodium complex, $Rh(\eta^3\text{-}C_3H_5)_3$, as precursor and using an alcohol as both a solvent and a stabilizer, under mild reaction conditions (room temperature; 3 bar H_2). Park and co-workers [22] mentioned another approach by decomposing organometallic precursor to prepare spherical nanoparticles at 170 ºC. However, the aforementioned wet-chemistry approaches are conducted under rigourous conditions by refluxing admixture of precursor (Rh salts), reductor polyol and stablizer PVP or PVA at high temperature (60-190 ºC) for 0.4-120 h, which is labor-intensive and time-consuming. Kundu et al. [23] reported a photochemical approach to obtain shape-selective RhNPs, where the reaction was performed under 6 h of UV-photoirradiation

with alkaline 2,7-dihydroxynapthalene (2,7-DHN) as reducing agent. Yet 2,7-DHN needs cautious treatment due to its acute toxicity and instability.

In the present work, we endeavour to take protocols for synthesizing Rh catalysts by the pulsed laser deposition (PLD) method and explore the effect of number of laser pulses (N_{lp}) on thickness, the structure, properties of Rh films and electrochemical performance towards the CO tolerance. The electrochemical experiments were conducted through a combination of cyclic voltammetry (CV) in CO-free electrolyte and anodic stripping voltammetry (ASV) of CO adsorbed on Rh thin films surface.

3.2 Experimental

3.2.1 Materials and methods

The Current collector is an untreated carbon paper (CP, Toray from Electrochem) made of a 3D network of carbon fibers with a diameter between 7 and 10 μm. Targets Rh (99.8%) and Pt (99.99%) were purchased from Kurt J. Lesker Co. Sulfuric acid (96% purity) and ethanol (100% purity) were purchased from Agros Organics and Commercial Alcohols Inc., respectively. The reactants were used as received without further purification.

3.2.2 Rhodium synthesis

Rh was deposited onto CP by PLD at room temperature by means of a pulsed KrF excimer laser (λ=248 nm, τ=17 ns, ν=50 Hz). The specific experimental parameters are listed in Table 3.1. Rh samples were synthesized under 2 Torr He background with various N_{lp} of 5000, 10000, 20000 and 50000, and they were denoted to Rh_5, Rh_{10}, Rh_{20} and Rh_{50}, respectively. During the deposition, the target was moved continuously across the laser beam to obtain a uniform ablation over the entire surface of the target. Further information about PLD set up and its working principle are given elsewhere [24].

Table 3.1 Experimental parameters used during PLD-synthesis of Rh thin films

	Experimental Parameters
Background gas Helium	2 Torr
Working vacuum	4×10^{-5} Torr
Target	Rh
Substrate	CP
Laser fluence	7 J cm^{-2}
Distance between the target and the substrate	5 cm

3.2.3 Materials characterization

The surface morphology of the as-prepared samples was examined by means of a scanning electron microscope (SEM, JEOL, JSM 6300 F apparatus) operated at an accelerating voltage of 10 kV in the secondary electron mode and a working distance of 10 mm. The measurements were performed in a working pressure of 8×10^{-6} mbar.

The crystalline structure of all samples was determined by X-ray diffraction (XRD) using Bruker D8 Advance diffractometer equipped with a Cu Kα source (λ=1.5406 Å). The tube current was 40 mA with a tube voltage of 40 kV. All diffractograms were acquired in the Grazing Incidence Diffraction (GID) scan mode with a low incident angle of 2° and a 2θ angular step size of 0.04° with an acquisition time of 4 s per step in the range of 20-90º.

The surface compositions of the samples were determined by X-ray photoelectron spectroscopy (XPS). The XPS was carried out via a VG Escalab 220i-XL set with an Al Kα source (1486.6 eV). The anode was operated at 10 kV and 20 mA. The pass energy of the analyzer was fixed at 20 eV. The base pressure of the system was 10^{-9} mbar. All samples were analyzed with a spot size of 250×1000 μm located approximately in the center of the sample. A survey spectrum ranging from 0 to 1000 eV was first acquired, and then higher resolution multiplex scan spectra (Rh 3d, O 1s, and C 1s core levels) were obtained. Quantification of the elements was performed with Casa XPS software version 2.3.12 (Casa Software Ltd.) by fitting the core level spectra after a Shirley background removal. The metallic components of the Rh 3d region were fitted using a Gaussian/Lorentzian asymmetrically modified line shape, also symmetrical Gaussian/Lorentzian were used to fit other components. The C 1s core level peak at 284.6 eV, resulting from hydrocarbon contaminants at the surface, was taken as an internal reference binding energy for charge correction.

3.2.4 Electrochemical measurements

The electrocatalytic characterization were evaluated by CV in Ar-saturated 0.5 M H_2SO_4 solutions in a three-compartment electrochemical cell containing an Ag/AgCl, 4 M NaCl reference electrode, a platinum coil as a counter electrode and the PLD-deposited Rh/CP samples as working electrodes. A Luggin capillary close to the working electrode served to minimize the ohmic drop. Before each test, dissolved oxygen was removed from the solution by bubbling argon for 30 min. Then the surfaces of the working electrodes were cleaned and completely activated by potential cycling to steady-state in 0.5 M H_2SO_4 for 30 cycles at a sweep rate of 50 mV s^{-1} between the range from -0.2 to 1.0 V. The electrochemical data

acquisition was conducted at room temperature (22 ± 0.5 ^{o}C) by a computer-controlled potentiostat-galvanostat (Autolab, PGSTAT 20, GPES). In this work, all the currents are normalized by the geometric area of the working electrode (0.308 cm^2).

Carbon monoxide anodic stripping experiments were conducted as follows: first, the 0.5 M H_2SO_4 solution was bubbled for 30 min with pure N_2. While keeping N_2 flowing, the electrode surface was electrochemically cleaned and completely activated by potential cycling to steady-state in the above-mentioned solution for 30 cycles at a sweep rate of 50 mV s^{-1} within the range from -0.20 to 1.03 V. Then pure CO (99.5%) was purged into the solution at a polarized potential of 0 V *vs* Ag/AgCl for another 30 min, in order to get the complete adsorption of CO onto the Rh/CP. While keeping the electrode potential at the same value, the gas was switched to pure N_2 for another 30 min, so as to remove redundant CO dissolved in the solution. Finally, the CO anodic stripping voltammetry to electrooxidize the adsorbed CO was started at open-circuit potential with v=50 mV s^{-1}.

3.3 Results and discussion

3.3.1 Structure characterization

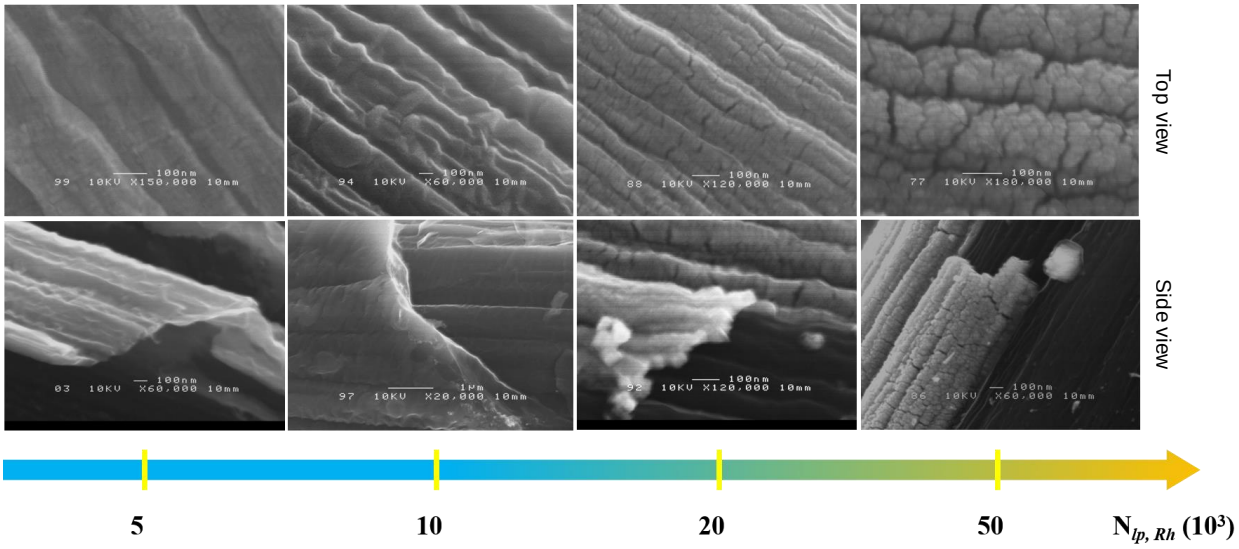

Figure 3.1 **SEM images of Rh thin films grown by PLD with increasing number of laser pulses. Upper are top view and lower are cross-section images.**

Figure 3.1 shows SEM images of PLD-synthesized Rh films with increasing N_{lp}. When N_{lp} was 5000, a smooth dense 2D nanosheets (8 ± 1.6 nm thickness) was obtained. Increasing N_{lp} to 10000, the surface morphology became less flat but hilly, and the thickness augmented to 20 ± 2.4 nm. Doubling the N_{lp} to 20000 led to a rougher layer with a thickness estimated to be 40

±1.9 nm. A dramatic change occured when N_{lp} turned to 50000, which yielded to a highly porous nanostructured layer (~200 ±1.3 nm) of Rh deposit appearing as an ensemble of agglomerated particles.

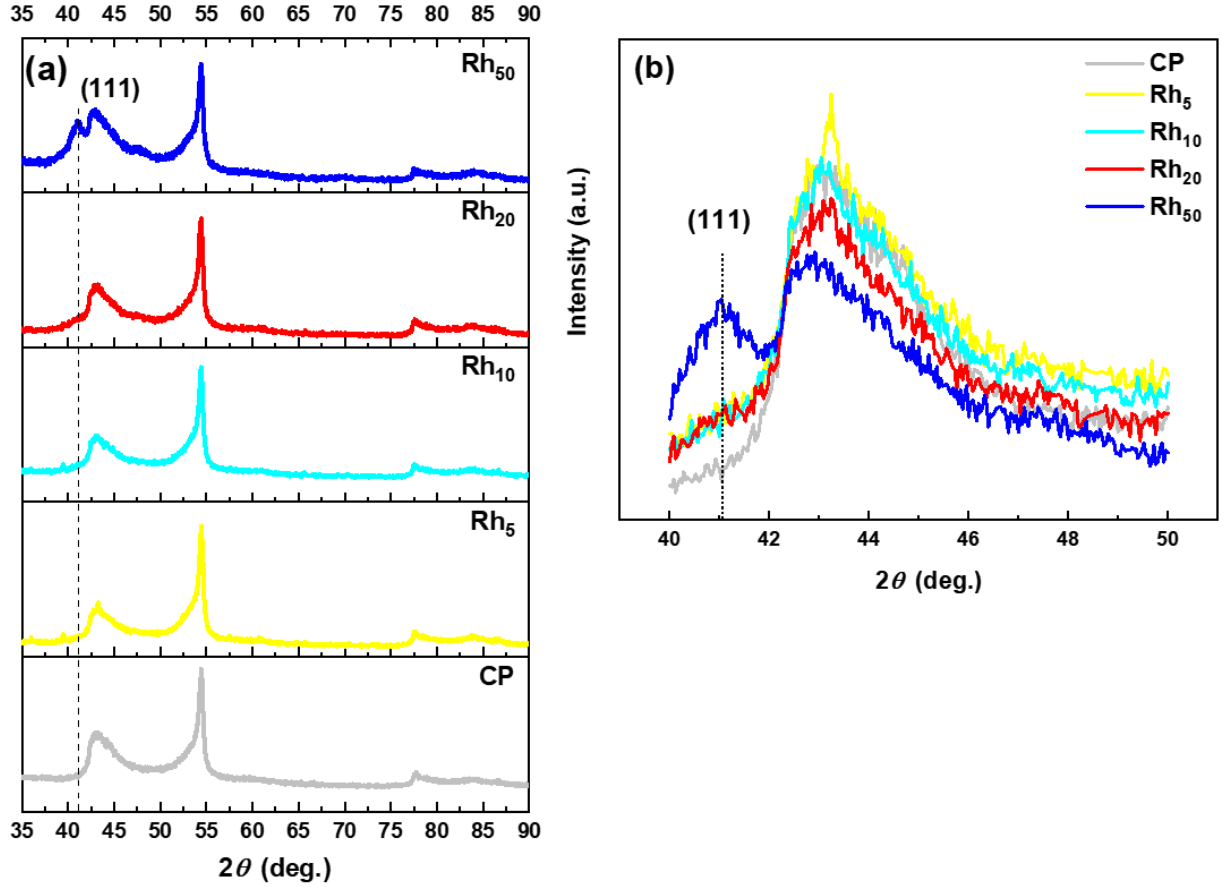

Figure 3.2 **(a) XRD patterns of PLD-grown Rh thin films on to carbon paper substrate. (b) Zoom in of the (111) diffraction peak.**

Figure 3.2 reports the XRD diffraction patterns of Rh_5, Rh_{10}, Rh_{20} and Rh_{50}, and the pattern of CP substrate was given as reference. In the pattern of Rh_{50}, it exhibited diffraction peaks at ca. 40.8°, which can be indexed to (111) plane, characteristic of a face-centered cubic *fcc* structure (JCPDS PDF No.05-0685). Nevertheless, the distinct diffraction peaks in the vicinity of 2θ = 40.8° can barely be seen in the electrocatalysts of Rh_5, Rh_{10} and Rh_{20} (Fig. 2b), implying bulk crystalline Rh was not generated during the deposition process. Delpeuch et al explained that Rh nanoparticles had been highly dispersed or in amorphous nanoparticles [25]. The most intensive diffraction peak Rh (111) was chosen to evaluate the lattice parameters of Rh_{50} electrode. The average crystallite size *D* was calculated by the Scherrer formula, whereas the lattice constant *a* and the interplanar space d_{hkl} were estimated by Bragg law, and the chemical surface area (*CSA*) of the catalyst calculated using Eq. 1 [26].

$$CSA\ (m^2 g^{-1} Rh) = \frac{6000}{\rho D} \qquad (1)$$

Where ρ is the density of Rh (12.41 g cm^{-3}). The values of *D* and *CSA* for the Rh_{50} electrode were 7.7 ± 0.2 nm and 62.6 ± 1.4 m^2 g^{-1}, respectively. A lattice constant *a* of 3.821Å was obtained, which was in good agreement with previous calculations [27].

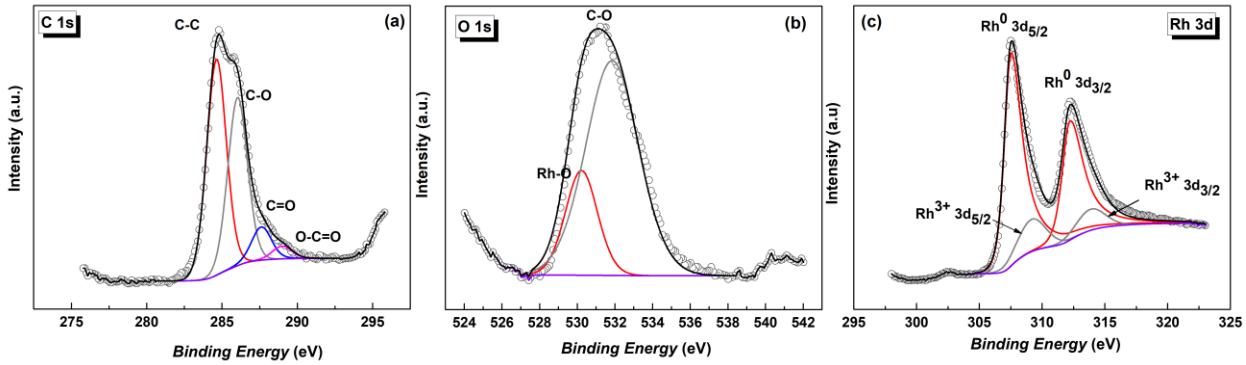

Figure 3.3 **Typical high-resolution XPS peaks of (a) C 1s (b) O 1s and (c) Rh 3d in PLD-grown Rh_{20} thin films.**

XPS was carried out to investigate the chemical state and electronic structure of the four Rh catalysts (Figure S1). Figure 3.3 shows typical high-resolution XPS spectra of (a) C 1s, (b) O 1s and (c) Rh 3d core level peaks. As shown in Figure 3.3a, the C 1s spectra were deconvoluted into four components and ascribed to: (1) the non-oxygenated the C-C (284.60 eV), (2) the hydroxyl carbon in C-OH (285.40 eV), (3) the O-C-O of epoxy groups (286.5 eV), and (4) the carbonyl C (C=O/C-OOH) (288.0 eV) [28]. The O 1s core level peaks (Figure 3.3b) were resolved into two contributions located at 530.5 eV and 532.2 eV, which were attributed to lattice oxide Rh-O and C-O, respectively. The two pairs of overlapping doublets peaks (Figure 3.3c) revealed that rhodium was in two different states. The relatively intensive doublet from the spin-orbital splitting (ca. 4.7 eV) of the $3d_{5/2}$ and $3d_{3/2}$ states, which presented at 307.4-307.5 eV and 312.1-312.2 eV, respectively, correspond to metallic Rh (Rh^0), and the other less intensive doublet at 308.6-308.7 eV and 313.3-313.4 eV, was due to rhodium oxide Rh_2O_3 species [29]. The partial oxidation of Rh occurred as a result of post-exposure in air. There is no clear trend for the oxygenated species at the carbon surface (C-O and C=O) groups (the at% sum of C-O, C=O and O-C=O in Rh_5, Rh_{10} and Rh_{20} and Rh_{50} are 9.46, 9.18, 30.09, 24.69, respectively). The surface atomic concentrations of Rh^0 and Rh^{3+} are displayed in Table 3.2. The estimation revealed that metallic Rh was the predominant species in all the Rh samples. One can further see that as the number of laser pulses increased, the amount of Rh^0 at the surface increased, while that of Rh^{3+} species decreased, implying smaller particles were easily oxidized [30]. In

addition to that, Rh $3d_{5/2}$ peak slightly shifted towards negative values of the binding energies *(BE)* as the number of laser pulses increased. Grass et al. [30] and Suarez-Martinez et al. [31] considered the increasing of the Rh particle size caused the blue shift.

Table 3.2 The surface concentration of Rh^0 and Rh^{3+} species and the *BE* of Rh^0 in Rh catalysts

Sample	Rh^0 (at %)	Rh^{3+} (at %)	BE of Rh^0 $3d_{5/2}$ (eV)
Rh_5	61.16	38.84	307.43
Rh_{10}	64.62	35.38	307.35
Rh_{20}	77.74	22.26	307.30
Rh_{50}	83.65	16.35	307.26

3.4 Electrochemical studies

3.4.1 CO-free electrolyte

Figure 3.4a shows CVs at the Rh_5, Rh_{10}, Rh_{20} and Rh_{50} electrocatalysts in the Ar-deaerated 0.5 M H_2SO_4 solution at the scanning rate of 50 mV s^{-1} within the potential range of $-0.2 \leq E \leq 1$ V. As can be seen, the four electrodes presented the typical CV profile of Rh with its characteristic potential regions: (i) H-region (-0.2 - 0.15 V), corresponding to the underpotential deposition of hydrogen H_{UPD} and (ii) double layer (DL)-region (0 - 0.3 V). Wasberg and Horányi [32] pointed out that in DL range, both OH and H species are present simultaneously at low coverage on the surface of Rh electrode. (iii) O-region (0.3 - 1.0 V), related to the formation of Rh surface oxides. Peuckert et al. [29] proposed that rhodium is oxidized to tetravalence according to the following reactions.

Oxidation

$Rh + H_2O \rightarrow Rh(OH) + H^+ + e^-$

$Rh(OH) + 2H_2O \rightarrow Rh(OH)_3 + 2H^+ + 2e^-$

$2Rh(OH)_3 + Rh \rightarrow 3RhO(OH) + 3H^+ + 3e^-$

Reduction

$3RhO(OH) + 3H^+ + 3e^- \rightarrow 2Rh(OH)_3 + Rh$

$Rh(OH)_3 + 2H^+ + 2e^- \rightarrow Rh + H_2O$

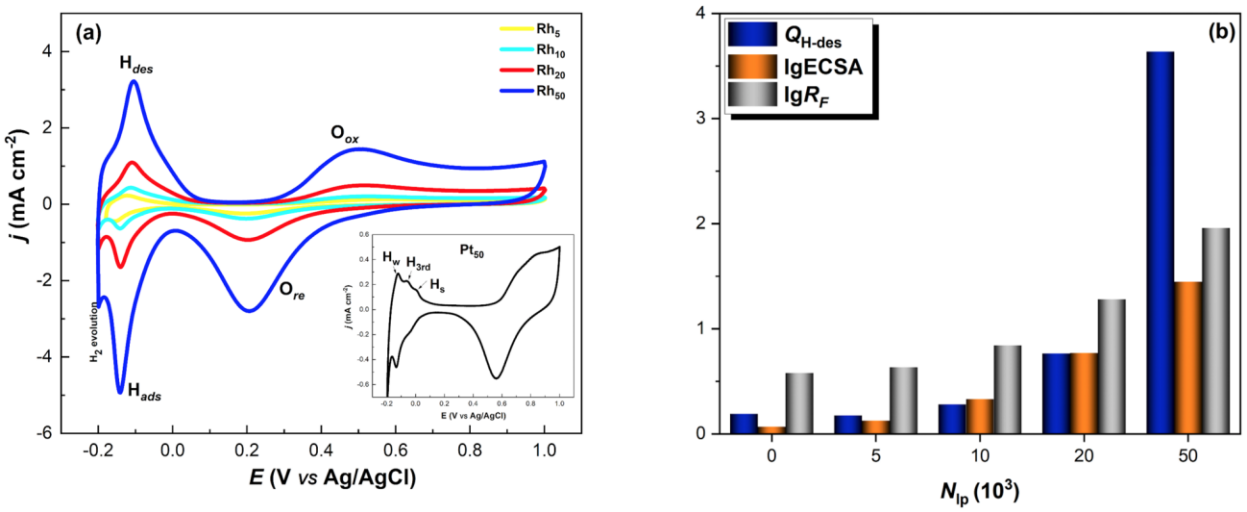

Figure 3.4 **(a)Cyclic voltammograms at Rh/CP electrocatalysts in 0.5 M H_2SO_4 solution recorded with 50 mV s^{-1} scan rate. Insert is the CV related to Pt/CP electrocatalyst. (b) logarithmic representation of $Q_{H\text{-}des}$, *ECSA* and R_F as function of N_{lp}.**

Figure 3.4a further demonstrates that the hydrogen adsorption/desorption area increased remarkably when increasing N_{lp} of Rh from 5000 to 50000. In addition, the oxophilicity character of the catalyst appeared to increase as well. Since the onset potential (defined here as the potential at which the current starts flowing) of formation of surface oxides $E_{onset\text{-}ox}$ shifted negatively, whereas the onset potential of formation of surface oxides reduction $E_{onset\text{-}re}$ shifted positively. It has to be clarified that the onset potential is not to be confused with the potential required obtaining a determined current density as frequently done when comparing the current activity among catalysts. In that case, the onset potential is determined by choosing an arbitrary criterion such as at a fixed current density or standardizing the CVs at the current density peak or by *ECSA* and then takes a normalized current density value that would be equivalent to the reach of a certain percentage of the peak current density. In our analysis here, the onset potential is for the sake of discussing only the oxophilicity properties of the catalysts. Pt, serving as a benchmark, was deposited with 50000 laser pulses and its structural characterization is reported in Figure S3.2-Figure S3.4. The inset of Figure 3.4a displays the CV profile of Pt_{50} benchmark electrode ($N_{lp,\,Pt}$ = 50000), it exhibits three well-defined peaks: the weakly bonded hydrogen H_w, the strongly bonded hydrogen H_s and a third anodic peak H_{3rd}, which were due to hydrogen adsorption on the plane of (111) and (110) facets [33], (100) facets [34] and UPD H_2 [35], respectively. Meanwhile, it is noteworthy that H desorption on Rh starts earlier than that of Pt. It may be because of the low H chemisorption energy on Rh compared with Pt [36]. Furthermore, Pt_{50} electrode had a wide and thin DL region. Whereas, in the case of Rh_{50} electrode, the DL region, superimposed with surface oxide reduction peak, became narrow but

bulky, consequently. This can be attributed to the presence of Rh $(OH)_x$ at the particle surface, increasing the electrode capacitance. The reduction peak of Rh surface oxides appeared at lower potentials than that of Pt, implying Rh oxides were more stable [37].

The true electrochemically active surface area (*ECSA*) and the roughness factor (R_F) of the electrocatalysts were estimated using the following equations [38]:

$$ECSA = \frac{Q^H{}_{ox}}{\theta_{H,M} \cdot Q^H{}_{ox,ML,S}} \quad (2)$$

$$R_F = ECSA/A_g \quad (3)$$

Where, $Q^H{}_{ox}$ (mC) is the integrated charge of voltammetric areas corresponding to H_{des} on Rh sites for a given cathodic vertex potential after correcting for the charge of the double layer. θ_H is the surface coverage with adsorbed hydrogen at that potential. $Q^H{}_{ox,ML,S}$ stands for charge of oxidizing a monolayer of hydrogen on Rh per unit area. A_g represents the geometric area of the electrode. $\theta_{H,Rh}$=0.59, $Q^H{}_{ox,Rh}$ =221 μC cm^{-2}, $\theta_{H,Pt}$=0.77, $Q^H{}_{ox,Pt}$ =210 μC cm^{-2}, A_g=0.308 cm^2.

The $Q^H{}_{ox}$, *ECSA* and R_F plotted in a logarithmic scale as function of N_{lp} of Rh are depicted in Figure 3.4b. ($N_{lp,Rh}$ = 0 corresponds to Pt_{50}). It is observed that the $Q^H{}_{ox}$, *ECSA* and R_F increase with the increasing of $N_{lp,Rh}$. Rh_{50} had the highest values of $Q^H{}_{ox}$(3.6 mC), *ECSA* (27.9 cm^2) and R_F (90.5). Two factors might account for the high performance of Rh_{50} with regards to Pt: *(1)* the number of nanoparticles (high porous surface). Since the density of Rh (12.4 g cm^{-3}) is almost half of Pt (21.4 g cm^{-3}), at equivalent particles size and metal loading, the number of Rh particles will be nearly two times higher than that of Pt. *(2)* Capability of hydrogen chemisorption. As mentioned before, Rh needs lower energy than Pt for hydrogen chemisorption, which is confirmed by the fact that the Rh_{50} catalyst exhibited a $Q^H{}_{ox}$ almost 30 times higher than that of Pt_{50}.

3.4.2 CO-containing electrolyte

It is generally accepted that on pure Rh surface, the electrooxidation of the adsorbed CO follows the Langmuir-Hinshelwood (LH) mechanism [39]:

H_2O +*Rh ⇔$OH_{ads,Rh}$ + H^++ e^-

C≡$O_{ads,Rh}$ + $OH_{ads,Rh}$ →COOH (rate determine step)

C≡$O_{ads,Rh}$ + $OH_{ads,Rh}$ → CO_2 + H^++ e^- +2 *Rh

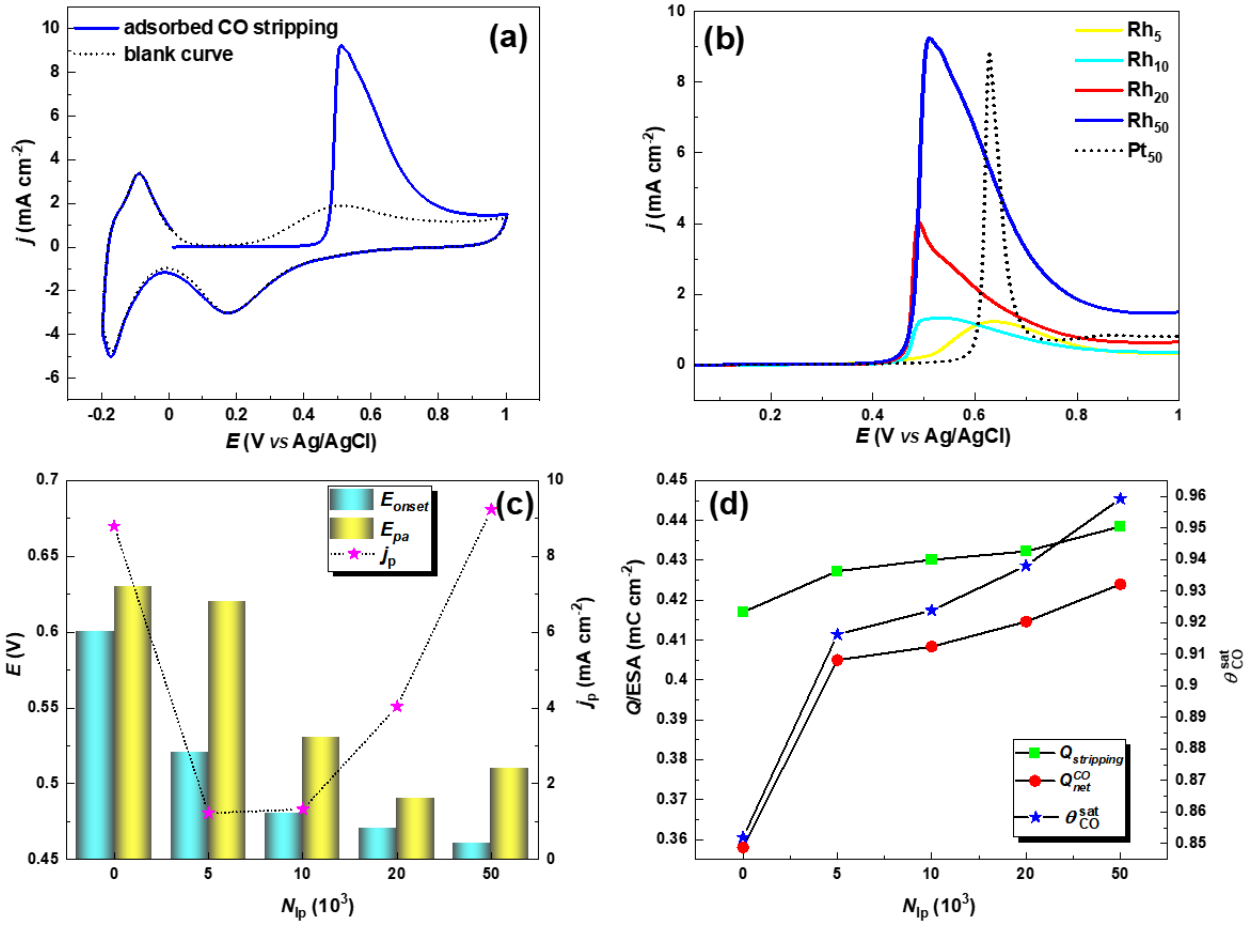

Figure 3.5 **(a) typical CVs CO-stripping in 0.5 M H_2SO_4 recorded at 50 mV s^{-1}. (b) ASVs of CO at Rh/CP and Pt/CP electrocatalysts. As function of N_{lp}: (c) E_{onset}, E_{pa} and j_{pa} extracted from Fig. 5b, and (d) Q_{CO}^{net}, $Q_{stripping}$ and θ_{CO}^{sat}.**

As illustrated in Figure 3.5a, the CO_{ox} peak was only observed during the first anodic cycle suggesting that all adsorbed CO was completely removed from the surface under such conditions (2nd cycle). The characteristics of the CO_{ox} peaks on the electrodes are summarized in Figure 3.5b. As can be seen, the CO_{ox} peak on Rh electrodes are broad, which is mostly likely due to low CO mobility on Rh resulting in overlap of CO and Rh surface oxidation processes [40]. Conversely, in the case of Pt_{50}, its CO_{ox} peak was sharp and symmetrical, which was attributed to the fast CO mobility on Pt. Besides, it was observed that the CO_{ox} peak potential E_{pa} shifted to lower values as the N_{lp} of Rh increased (Figure 3.5c). Besides, E_{pa} of Rh was lower than that of Pt, which indicates that CO_{ads} was easily removed from the surface of Rh than Pt [41]. $E_{onset\text{-}CO}$ is one of the main design parameters of electrocatalysts highly tolerant to CO poisoning or removal for liquid fuel cells. A similar trend was observed in the onset potential E_{onset} (measured at the potential at which the anodic current starts flowing) of CO electrooxidation when Rh N_{lp} increased. It declined in sequence from Pt_{50} (0.6 V), Rh_5 (0.52 V),

Rh_{10} (0.48 V), Rh_{20} (0.47 V) to Rh_{50} (0.46 V). Rhodium is an oxophilic metal and has the lower *d*-band center (-1.73 eV) than that of Pt (-2.25 eV) [42], indicating that Rh can provide oxygenic or OH species at potentials lower than that of Pt, which also concurs the observation in CO-free electrolyte (Figure 3.4a). As a result, Rh electrodes have a lower onset potential E_{onset} of CO electrooxidation than that of Pt. Finally, the order of CO oxidation peak current density j_{pa} increased with the increasing of N_{lp}, with Rh_{50} displaying the highest peak current density (9.23 mA cm^{-2}), which was 8-fold greater than that of Rh_5 (1.22 mA cm^{-2}). In addition, the E_{onset} of Rh_{50} was 130 mV negatively than that of Pt. Such significant shift in the E_{onset} demonstrates that Rh_{50} greatly facilitates the electrooxidation of CO at potentials lower than that of Pt.

In order to correct the contribution of anion adsorption during CO oxidation, the net charge of oxidation and desorption of the CO adlayer was estimated based on a strategy proposed by Gómez et al. [43, 44]:

$$Q_{net}^{CO} = Q_{stripping} - |Q_T| - \int_{E_T}^{E_+} \frac{j}{v} dE \quad (4)$$

Where, E_T is the potential that displacement has been performed, and E_+ is Q_{net}^{CO} is the sought-after net charge density corresponding exclusively to the faradaic oxidation of the CO adlayer. $Q_{stripping}$ is the experimentally determined charge density obtained by integration of the CO-stripping voltammogram between E_T and E_+. Q_T is the reduction charge density displaced by CO adsorption at a certain potential E_T in the double layer region. This charge is attributed to the adsorption of bisulfate at the adlayer. The last term equals the total charge density between the potential at which the displacement is performed and E_+. This contribution corresponds to the double layer charging and Rh oxide formation.

The saturated coverage θ_{CO}^{sat} are obtained from the Q_{net}^{CO} values from the following equation [44]:

$$\theta_{CO}^{sat} = Q_{net}^{CO} / n\ 221 \quad (5)$$

Where, *n* is the number of electrons exchanged per CO molecule during its oxidation (*n*=2) and 221 μC cm^{-2} is the charge density for a process involving one electron per Rh surface site. The $Q_{stripping}$, the calculated Q_{net}^{CO} (normalized to *ESA*) and the corresponding CO coverage θ_{CO}^{sat} are depicted in Figure 3.5d. It showed that Rh_{50} electrode had the highest value of 424 μC cm^{-2} with a CO coverage θ_{CO}^{sat} of 0.95 (*vs* Pt_{50} 358 μC cm^{-2}, 0.85).

3.5 Conclusions

The pulsed laser deposition PLD technique was employed for the first time to grow Rh films with different thicknesses by varying the number of laser pulses N_{lp}. SEM analysis revealed that Rh films deposited with low N_{lp} had a smooth surface topography. On the other hand, Rh films with higher N_{lp} were rougher. XPS showed all Rh films contained both metallic Rh and Rh^{3+} at their surfaces. Yet, the concentration of metallic Rh augmented as the N_{lp} increased. As for the CO tolerance, it is found that Rh film deposited with 50000 N_{lp} demonstrated the utmost electroactive surface area of 27.90 cm^2, which was almost 23 times higher than that displayed by the benchmark Pt catalyst, and the onset potential of CO electrooxidation was 130 mV negative than that of Pt, suggesting a faster kinetics at the former catalyst. In addition, Rh_{50} electrode delivered a net charge density as high as 424 µC cm^{-2} with a surface saturated CO coverage of 0.95, demonstrating more active sites to CO coverage.

These insights provide important information on designing of highly tolerant electrocatalysts towards CO poisoning and emphasize the importance of considering the influence of the film thickness on the electrochemical performance of Rh, no matter used as single catalyst or combined with other elements in fuel cells reactions, including H_2/O_2 or direct alcohol energy conversion systems.

References

[1] D. Wang, H.L. Xin, R. Hovden, H. Wang, Y. Yu, D.A. Muller, F.J. DiSalvo, H.D. Abruña, Nat Mater., 12 (2013) 81.

[2] D. Zhai, B. Liu, Y. Shi, L. Pan, Y. Wang, W. Li, R. Zhang, G. Yu, ACS nano, 7 (2013) 3540-3546.

[3] J. Suntivich, Z. Xu, C.E. Carlton, J. Kim, B. Han, S.W. Lee, N.p. Bonnet, N. Marzari, L.F. Allard, H.A. Gasteiger, J. Am. Chem. Soc., 135 (2013) 7985-7991.

[4] J. Wu, H. Yang, Acc. Chem. Res., 46 (2013) 1848-1857.

[5] I. Willner, R. Baron, B. Willner, Biosens Bioelectron, 22 (2007) 1841-1852.

[6] G.S. Fonseca, J.B. Domingos, F. Nome, J. Dupont, J. Mol. Catal. A: Chem., 248 (2006) 10-16.

[7] W. Song, C. Popa, A.P. Jansen, E.J. HensenJ Phys Chem C., 116 (2012) 22904-22915.

[8] W.-H. Chiou, Y.-W. Wang, C.-L. Kao, P.-C. Chen, C.-C. Wu, Organometallics, 33 (2014) 4240-4244.

[9] Q. Sun, Z. Dai, X. Liu, N. Sheng, F. Deng, X. Meng, F.-S. Xiao, J. Am. Chem. Soc., 137 (2015) 5204-5209.

[10] Q. Yan, D. Kong, M. Li, G. Hou, G. Zi, J. Am. Chem. Soc., 137 (2015) 10177-10181.

[11] P.N. Bartlett, J. Marwan, Microporous Mesoporous Mater., 62 (2003) 73-79.

[12] M. Shelef, R.W. McCabe, Catal Today, 62 (2000) 35-50.

[13] N. Nakagawa, Y. Kaneda, M. Wagatsuma, T. Tsujiguchi, J. Power Sources, 199 (2012) 103-109.

[14] F. Zhang, D. Zhou, Z. Zhang, M. Zhou, Q. Wang, Rsc Adv, 5 (2015) 91829-91835.

[15] T. Sheng, W.-F. Lin, C. Hardacre, P. Hu, Phys Chem Chem Phys, 16 (2014) 13248-13254.

[16] Y. Suo, I.-M. Hsing, J. Power Sources, 196 (2011) 7945-7950.

[17] H. Hirai, Y. Nakao, N. Toshima, J MACROMOL SCI A., 12 (1978) 1117-1141.

[18] Y. Nishida, K. Sato, T. Yamamoto, D. Wu, K. Kusada, H. Kobayashi, S. Matsumura, H. Kitagawa, K. Nagaoka, Chem. Lett., 46 (2017) 1254-1257.

[19] M.E. Grass, S.H. Joo, Y. Zhang, G.A. Somorjai, J Phys Chem C., 113 (2009) 8616-8623.

[20] N. Zettsu, J.M. McLellan, B. Wiley, Y. Yin, Z.Y. Li, Y. Xia, Angew. Chem. Int. Ed., 45 (2006) 1288-1292.

[21] E. Ramírez-Meneses, K. Philippot, M. Domínguez-Crespo, M. Ibrahim, I. Betancourt, A. Torres-Huerta, A. Ezeta-Mejia, J Mater Sci, 53 (2018) 8933-8950.

[22] K.H. Park, K. Jang, H.J. Kim, S.U. Son, Angew. Chem. Int. Ed., 46 (2007) 1152-1155.

[23] S. Kundu, K. Wang, H. Liang, J Phys Chem C, 113 (2009) 18570-18577.

[24] D. Riabinina, E. Irissou, B. Le Drogoff, M. Chaker, D. Guay, J. Appl. Phys., 108 (2010) 034322.

[25] A.B. Delpeuch, T. Asset, M. Chatenet, C. Cremers, J. Electrochem. Soc., 161 (2014) F918-F924.

[26] E.A. de Souza, M.J. Giz, G.A. Camara, E. Antolini, R.R. Passos, Electrochim. Acta, 147 (2014) 483-489.

[27] J.-H. Cho, M. Scheffler, Phys. Rev. Lett., 78 (1997) 1299.

[28] L. Tang, Y. Wang, Y. Li, H. Feng, J. Lu, J. Li, Adv. Funct. Mater., 19 (2009) 2782-2789.

[29] M. Peuckert, F. Coenen, H. Bonzel, Surf. Sci., 141 (1984) 515-532.

[30] M.E. Grass, Y. Zhang, D.R. Butcher, J.Y. Park, Y. Li, H. Bluhm, K.M. Bratlie, T. Zhang, G.A. Somorjai, Angew. Chem. Int. Ed., 47 (2008) 8893-8896.

[31] I. Suarez-Martinez, C.P. Ewels, X. Ke, G. Van Tendeloo, S. Thiess, W. Drube, A. Felten, J.-J. Pireaux, J. Ghijsen, C. Bittencourt, ACS nano, 4 (2010) 1680-1686.

[32] M. Wasberg, G. Horányi, J. Electroanal. Chem., 386 (1995) 213-219.

[33] B. Loo, T. Furtak Electrochim. Acta, 25 (1980) 505-508.

[34] K. Kinoshita, P. Stonehart, Electrochim. Acta, 20 (1975) 101-107.

[35] T. Frelink, W. Visscher, J. Van Veen, Electrochim. Acta, 40 (1995) 545-549.

[36] E. Christoffersen, P. Liu, A. Ruban, H.L. Skriver, J.K. Nørskov, J. Catal., 199 (2001) 123-131.

[37] K. Bergamaski, E.R. Gonzalez, F.C. Nart, Electrochim. Acta, 53 (2008) 4396-4406.

[38] M. Łukaszewski, M. Soszko, A. Czerwiński, Int. J. Electrochem. Sci, 11 (2016) 4442-4469.

[39] C.T. Campbell, S.-K. Shi, J. White, Appl Surf Sci., 2 (1979) 382-396.

[40] Y. Sung, S. Thomas, A. Wieckowski, J. Phys. Chem., 99 (1995) 13513-13521.

[41] A. Kowal, M. Li, M. Shao, K. Sasaki, M. Vukmirovic, J. Zhang, N. Marinkovic, P. Liu, A. Frenkel, R. Adzic, Nat. Mater., 8 (2009) 325.

[42] I. Takigawa, K.-i. Shimizu, K. Tsuda, S. Takakusagi, Rsc Adv, 6 (2016) 52587-52595.

[43] R. Gomez, J. Feliu, A. Aldaz, M. Weaver, Surf. Sci., 410 (1998) 48-61.

[44] R. Gómez, A. Rodes, J. Perez, J. Feliu, A. Aldaz, Surf. Sci., 344 (1995) 85-97.

Supporting Information

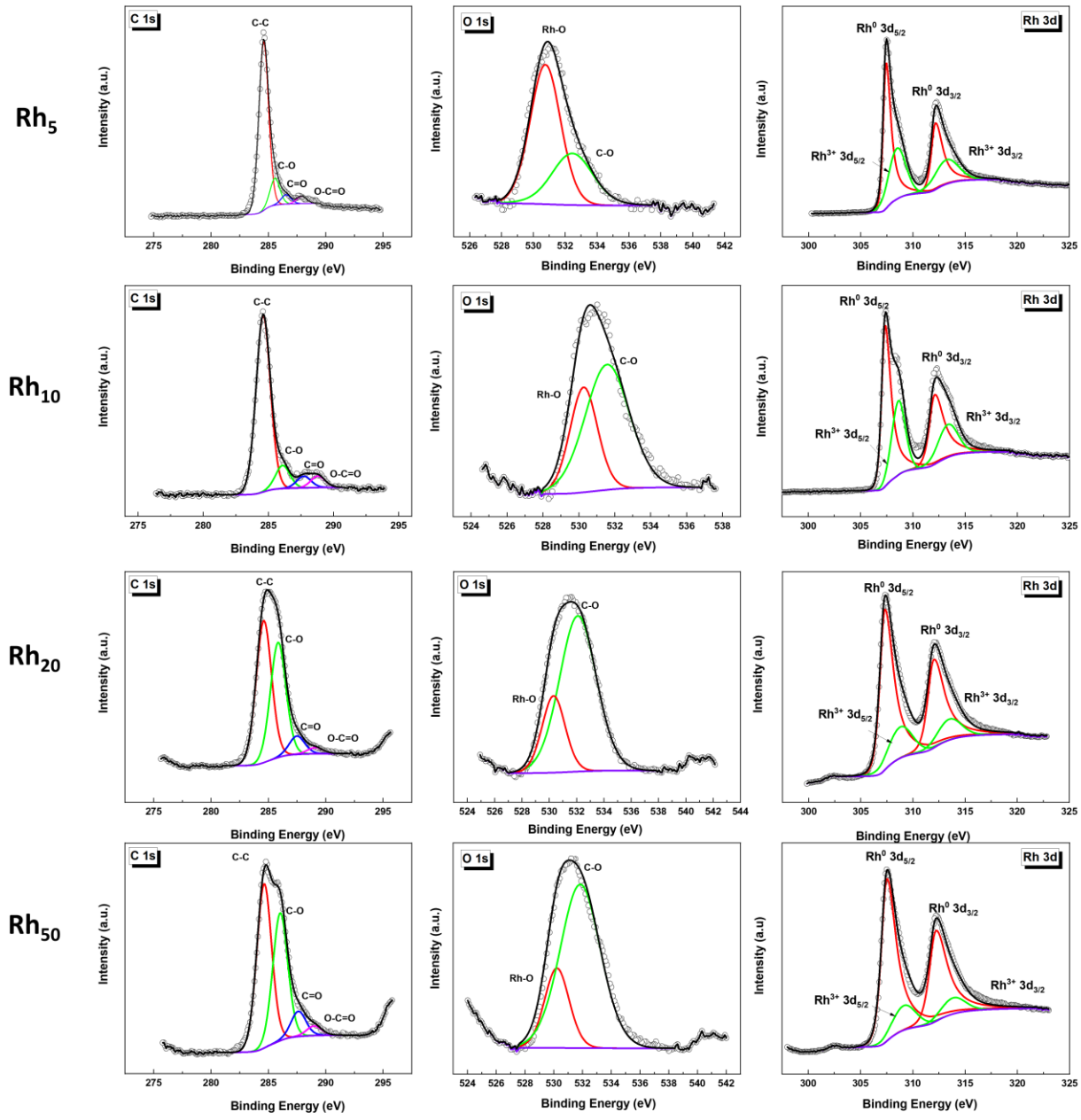

Figure S3.1 High-resolution XPS peaks of (a) C 1s (b) O 1s and (c) Rh 3d in PLD-grown thin films onto carbon paper substrate.

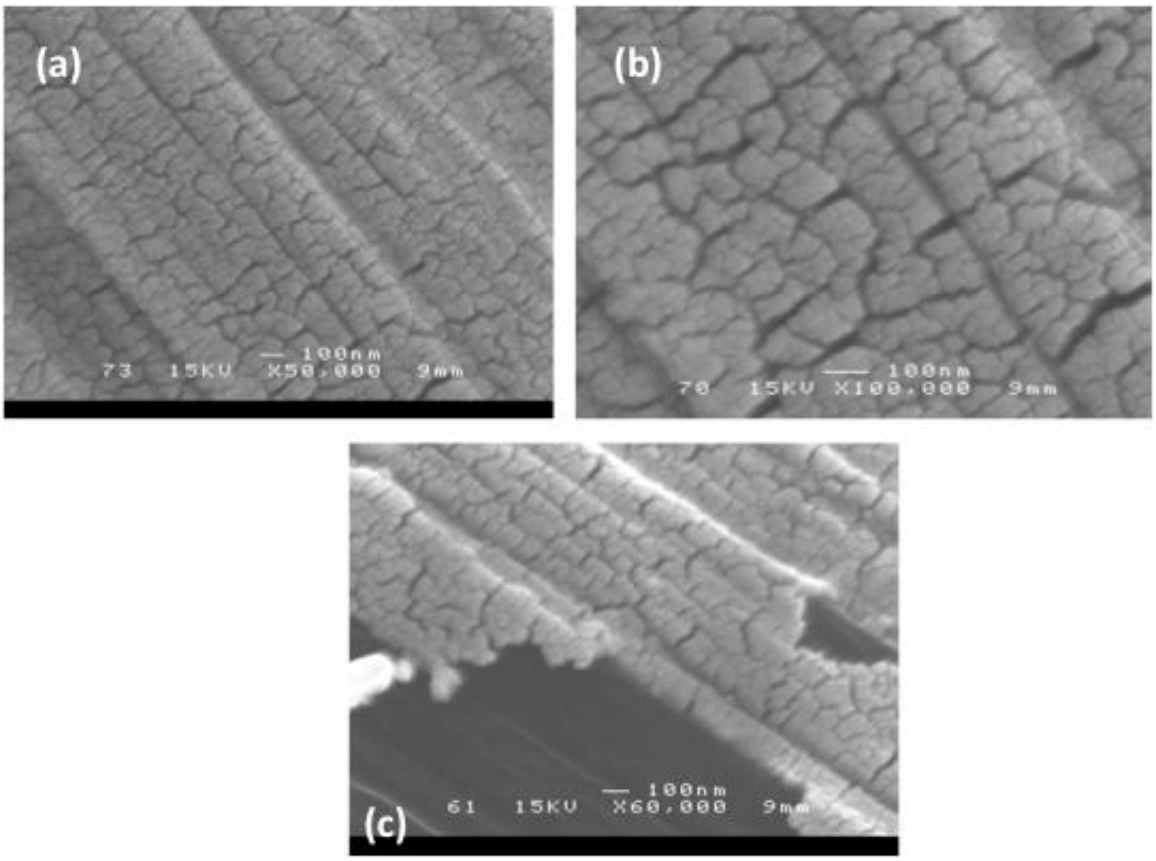

Figure S3.2 SEM images of Pt_{50} thin film grown by PLD onto carbon paper substrate. Upper (a-b) are top view and lower (c) are cross-section images.

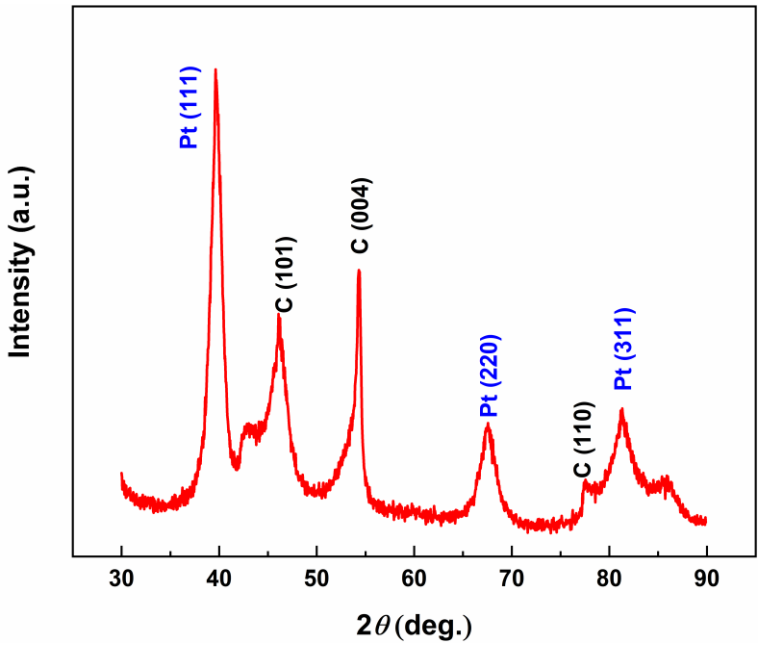

Figure S3.3 XRD patterns of PLD-grown Pt_{50} thin film onto carbon paper substrate.

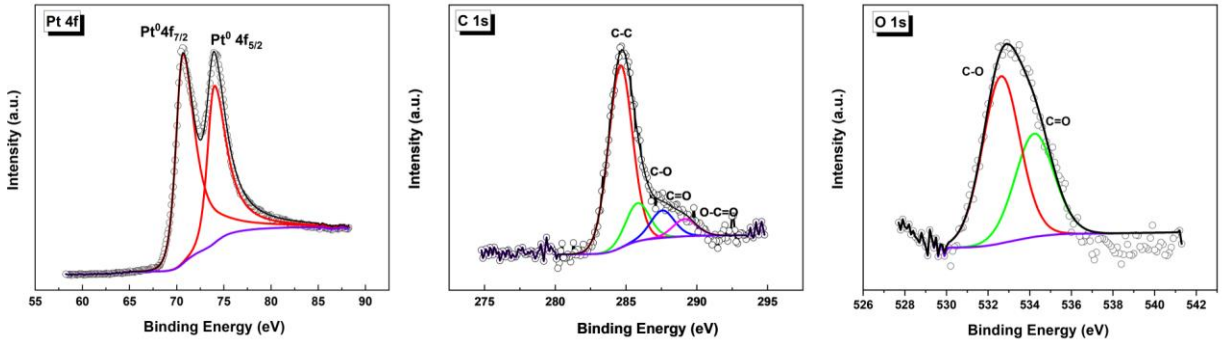

Figure S3.4 High-resolution XPS peaks of Pt 4f, C 1s and O 1s core-levels in PLD-grown Pt_{50} thin film onto carbon paper substrate.

4 THE 2ND ARTICLE

Plasma Synthesized Tri-Layered Rhodium−Platinum−Tin Oxide Nanostructures with Enhanced Tolerance to CO-Poisoning and High Electroactivity for Ethanol Oxidation

Catalyseur Rhodium−Platinum−Tin Oxide tricouche synthétisé au plasma avec une tolérance accrue à l'empoisonnement au CO et une électroactivité élevée pour l'oxydation de l'éthanol

Authors:

Haixia Wang, Shuhui Sun and Mohamed Mohamedi

Énergie, Matériaux et Télécommunications (EMT), Institut National de la Recherche Scientifique (INRS), 1650 Boulevard Lionel Boulet, Varennes, Quebec, J3X 1S2, Canada

Title of the journal or book:

Energy Technology

(2020), in Press

Contribution:

I synthesized all the samples and I conducted all the physicochemical characterizations and electrochemical measurements. I analyzed the data and interpreted the results. I participated in the writing with the help of the other authors.

Link between the previous and the next article:

After studying the CO stripping in Rh catalysts with various numbers of laser pulses of Rh ($N_{lp,Rh}$), we start to investigate the effect of the $N_{lp,Rh}$ on EOR and CO stripping in carbon paper supported $RhPtSnO_2$ catalysts. Meanwhile, we also try to study the role of SnO_2 and Rh in enhancing the ethanol electrooxidation.

The Graphic Summary:

DOI : 10.1002/ente.202000949

5 THE 3RD ARTICLE

Synthesis of free-standing ternary Rh-Pt-SnO_2-carbon nanotubes nanostructures as highly active and robust catalyst towards ethanol oxidation

Synthèse de nanostructures ternaires autoportantes de nanotubes de carbone-Rh-Pt-SnO_2 comme électrocatalyseur hautement actif et robuste vers l'oxydation de l'éthanol

Authors:

Haixia Wang, Shuhui Sun and Mohamed Mohamedi

Énergie, Matériaux et Télécommunications (EMT), Institut National de la Recherche Scientifique (INRS), 1650 Boulevard Lionel Boulet, Varennes, Quebec, J3X 1S2, Canada

Title of the journal or book:

RSC Advances

RSC Advances, 10 (2020), 45149

DOI: 10.1039/D0RA10030G

Contribution:

I synthesized all the samples and I conducted all the physicochemical characterizations and electrochemical measurements. I analyzed the data and interpreted the results. I participated in the writing with the help of the other authors.

Link between the previous and the next article:

After exploring the series of $RhPtSnO_2$ with carbon paper with substrate, we begin to investigate the effect of carbon nanotubes as substrate in Rh_5PtSnO_2 towards EOR and CO stripping.

The Graphic Summary:

6 THE 4TH ARTICLE

Nanostructured shrub-like bimetallic Pt_xRh_{100-x} alloys grown on carbon paper for the oxidative removal of adsorbed carbon monoxide for ethanol fuel cells reaction

Alliages Pt_xRh_{100-x} bimétalliques nanostructurés en forme d'arbuste déposés sur du papier carbone pour l'élimination par oxydation du monoxyde de carbone adsorbé pour la réaction des piles à combustible à l'éthanol

Authors:

Haixia Wang, Xin Tong, Shuhui Sun and Mohamed Mohamedi

Énergie, Matériaux et Télécommunications (EMT), Institut National de la Recherche Scientifique (INRS), 1650 Boulevard Lionel Boulet, Varennes, Quebec, J3X 1S2, Canada

Title of the journal or book:

Electrochimica Acta

Electrochimica Acta 355 (2020) 136823

DOI: 10.1016/j.electacta.2020.136823

Contribution:

I synthesized all the samples and I conducted all the electrochemical measurements and various physicochemical characterizations (XRD, SEM, EDS and XPS) except TEM and NAA measurements, which had been done by technicians. I analyzed the data and interpreted the results. I participated in the writing with the help of other authors.

Link between the previous and the next article:

After systemically studying the EOR and CO stripping in a series of PLD-made layer-by-layered structure catalysts $PtRhSnO_2$ with CP as substrate, we, in this paper, try to explore the effect of the arrangement of Pt and Rh, as well as the effect of atomic ratios of PtRh towards EOR and CO stripping. Therefore, we conducted this experiment on CBPLD-synthesized catalysts Pt_xRh_{100-x}/CP.

The Graphic Summary:

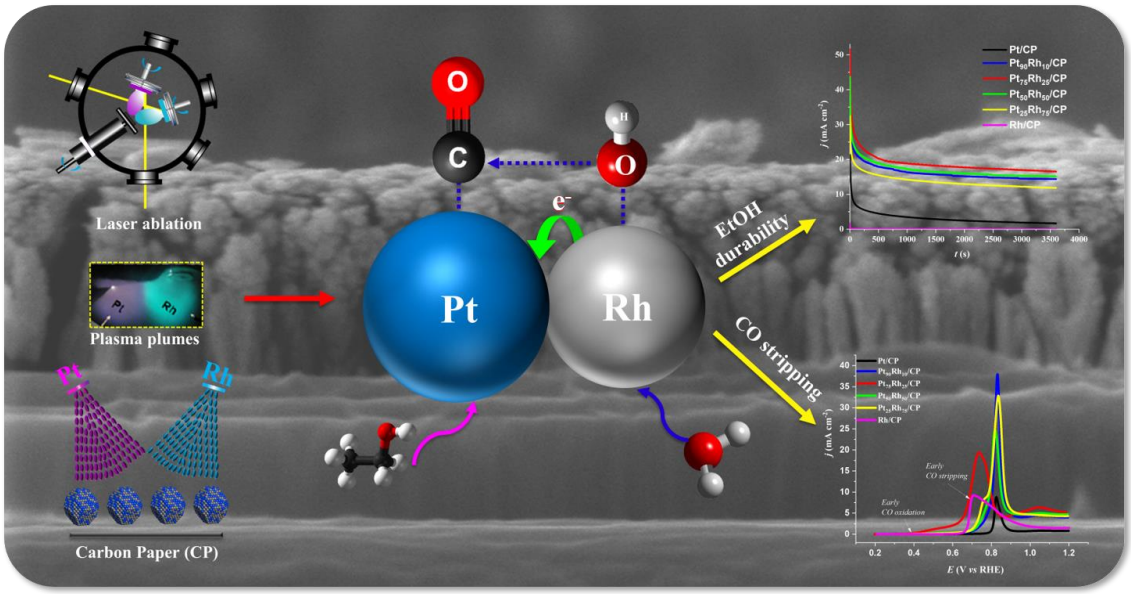

Abstract:

Plasmas techniques are novel routes to prepare complex nanostructured materials for catalysis and clean hydrogen energy such as fuel cells. Cross-beam pulsed laser deposition (CBPLD) technique allows enhanced interaction between the catalyst and the support and improved catalytic properties. Herein, a highly active and durable vertically aligned nanostructured shrub-like bimetallic Pt_xRh_{100-x} alloys with atomic ratios close to nominal values are grown on carbon paper substrate. The tolerance to CO poisoning and ethanol electrooxidation reactions are studied over these new types of shrub-like bimetallic Pt_xRh_{100-x}/CP catalysts, demonstrating that such structures effectively facilitate both processes and very low long-term poisoning rates. Such high catalytic activity accounts for two mechanisms: Rh a highly oxophilic transition metal activates water dissociation at lower potentials than Pt (bifunctional mechanism), and the ligand effect where Rh alters the electronic structure of the neighboring Pt suggesting a faster supply in adsorbed hydroxide species OH_{ads}.

Key words:

Carbon monoxide electrooxidation; Ethanol electrooxidation; Pulsed laser deposition; Nanostructured PtRh electrocatalysts; Fuel cells.

Lien entre l'article ou les articles précédents et le suivant :

Après avoir étudié systématiquement la tolérance à la réaction d'empoisonnement au CO et l'ROE dans une série de catalyseurs $PtRhSnO_2$ couche par couche fabriquée par PLD avec CP comme substrat, nous essayons, dans cet article, d'explorer l'effet de l'arrangement de Pt et Rh, ainsi que l'effet des rapports atomiques de PtRh sur la tolérance à la réaction d'empoisonnement au CO et d'électrooxydation à l'éthanol. Ensuite, nous avons mené cette expérience sur les catalyseurs Pt_xRh_{100-x}/CP synthétisés par CBPLD.

Résumé

Les techniques des plasmas sont de nouvelles voies pour préparer des matériaux nanostructurés complexes pour la catalyse et l'énergie hydrogène propre comme les piles à combustible. La technique d'ablation laser à flux croisés (CBPLD) permet d'améliorer l'interaction entre le catalyseur et le support et d'améliorer les propriétés catalytiques. Ici, un alliage Pt_xRh_{100-x} bimétallique nanostructuré en forme d'arbuste hautement actif et durable aligné verticalement avec des rapports atomiques proches des valeurs nominales est déposé sur un substrat en papier carbone. La tolérance aux réactions d'empoisonnement au CO et d'électrooxydation à l'éthanol sont étudiés sur ces nouveaux types de catalyseurs Pt_xRh_{100-x}/CP, démontrant que de telles structures facilitent efficacement à la fois les processus et les taux d'empoisonnement à long terme très faibles. Une telle activité catalytique élevée est due à deux mécanismes: Rh un métal de transition hautement oxophile active la dissociation de l'eau à des potentiels inférieurs à Pt (mécanisme bifonctionnel), et l'effet ligand que le Rh modifie la structure électronique du Pt adjacent suggérant un apport plus rapide en adsorbé espèces d'hydroxyde OH_{ads}

Mots clés

Électrooxydation au monoxyde de carbone; Électrooxydation à l'éthanol; Le dépôt par laser pulsé; Électrocatalyseurs nanostructurés PtRh; Pile à combustible.

6.1 Introduction

As a common contaminant in H_2 feedstocks, carbon monoxide (CO) poisons catalysts by strongly adsorbing on the surface, blocking actives sites during the operation of H_2/O_2 fuel cells, which leads to a considerable drop in the overall cell performance [1]. The CO poisoning is even more critical in many other candidate fuels (*e.g.,* formic acid, methanol, ethanol, glycerol), wherein CO is generated as a reaction intermediate during the decomposition of these liquid fuels [2-5]. To sustain their activity, catalysts must therefore accomplish the oxidation of CO alongside the fuel.

Ethanol, as the fuel for next generation low temperature fuel cells, is drawing much attention in recent years. This interest comes from the fact that ethanol is non-toxic, can be produced from biomass (agricultural residue, wood waste, cellulose and algae), easy to store and transport. Besides, it has a high energy density (20.9 MJ/L) (vs. hydrogen gas (5.6 MJ/L at 700 bar) [6-7]. This could make low temperature direct ethanol fuel cells (DEFCs) advantageous low greenhouse gas emission power sources for portable electronics and for electric vehicles [8]. Platinum is acknowledged to be the most used electrocatalyst for oxidation of organic molecules [9]. To summarize, under acidic conditions, dissociative adsorption of ethanol onto Pt generates the adsorbed acetaldehyde, which can desorb as a byproduct and further oxidized to acetic acid (byproduct) or be dissociated to become the adsorbed CO (CO_{ads}) and other species that can be oxidized to CO_2 [10-12]. However, the selectivity for complete EOR to CO_2 is low at room temperature [13] due to the C-C bond is still intact [14]. Consequently, it is of importance to circumvent oxide formation on Pt, and add a second component, oxophilic, to offer the oxygen-containing species to remove CO poionsing [15-17]. Subsequently, there have been numerous endeavors to ease the electrooxidation of CO adsorbed on Pt surface by developing bimetallic catalysts, such as PtRu [18-20], PtSn [21-22], PtMo [23], and PtNi [24]. Above all, PtSn and PtRu bimetallic catalysts exhibited higher performance for electrooxidation of CO compared to other Pt alloy catalysts. This was mainly attributed to the electronic tuning of the Pt *d*-band structure (electronic effect) and/or Ru or Sn sites instead adsorbs OH species resulting in the enhancement of the CO oxidation rate at lower potentials than Pt, thus causing a decrease in the onset potential for CO oxidation (bifunctional effect) [25]. Still, the complete oxidation of ethanol to CO_2 is a 12-electrons exchange reaction, which not only requires dehydrogenation of ethanol and oxidation of CO, but the C-C bond dissociation as well [26]. According to *in*

situ Fourier transform infrared (FTIR) spectroscopy and differential electrochemical mass spectroscopy (DEMS) studies [27], PtRu or PtSn catalysts did not favor the selectivity of CO_2 formation; instead, acetaldehyde (AAL) and acetic acid (AA) were the major products during the EOR, which indicates that the breaking of the C-C bond was not achieved at these catalysts.

Research now has turned to discover other elements to combine with Pt. So far, only rhodium (Rh) [28-30] has shown potential capability of splitting the C-C bond and enhancing selectivity of CO_2 as demonstrated by *in situ* FTIR studies [31-32]. Yet, there still unanswered questions regarding not only the role of Rh towards direct electrooxidation of surface adsorbed CO but does it also plays the same role during the EOR, where CO and adsorbed $CH_{x,ads}$ are generated from dissociative adsorption of ethanol in the low potential region. Indeed, mechanistic studies on the role of Rh are still a debate on whether the enhancement of the reaction rate by adding Rh to Pt catalyst is due to the electronic effect, enabling of CO oxidation by supplying oxygen species (bifunctional effect) and/or to the innate capacity of the Pt-Rh catalyst to break the C-C bond. Furthermore, the content of the rhodium in the PtRh alloy for optimum performance whether towards the direct electrooxidation of adsorbed CO or for the EOR has yet to be defined. A systematic study of the effect of the concentration of Rh in the bimetallic alloy for the oxidation of CO would have made it possible to obtain a comprehensive image and would have also allowed to advance our knowledge on the role of Rh towards the electrooxidation of surface adsorbed CO and therefore that of electrooxidation of ethanol.

The advent of emerging technologies such as fuel cells necessitating porous or highly structured layers has fostered the development of thin film deposition procedures aimed at enhancing these morphological characteristics [33]. Recent breakthroughs in nanotechnology have achieved control nanosized and composition of films that are relevant for catalyst design. Pulsed laser deposition (PLD) is one of the best methods to grow high-quality functional thin films whereas cross-beam PLD (CBPLD) a specific modification of the PLD permits growing desired thin film materials with precisely controlled composition by employing pure target materials in controlled inert atmosphere in the growth chamber [34]. Therefore, in the synthesized materials neither impurity can be neither introduced nor other additives that can impact the performances. We undertook in the present work to study the effect of Rh and its content towards the

electrooxidation of CO adsorbed on the surface of the Pt_xRh_{100-x} bimetallic alloys synthesized by the CBPLD method. In order to avoid an eventual interference of the substrate on the electrochemical results, we have chosen the carbon paper (CP) (typically used substrate in fuel cells), which has less electronic conductivity than other nanostructured carbon materials such as carbon nanotubes (CNTs), graphene or other type of activated carbon. Like this, all the structural properties and electrochemical performances will reflect the behavior of Pt_xRh_{100-x} in neat form. The objective is to design an optimized Pt_xRh_{100-x} material with the appropriate composition that provide the highest tolerance to CO and by that the highest catalytic activity towards EOR in particular and for other liquid fuel cells in general for which CO is the main poisoning intermediate formed. However, even if the objective here is to advance our knowledge on the role of Rh (when combined with Pt) towards the electrooxidation CO, in this work the syntheses, characterizations as well as electrochemical characterizations towards EOR are presented first followed by studies of adsorbed CO species and their removal (CO-stripping) from surface of the catalysts.

6.2 Experimental

6.2.1 Catalyst preparation

Thin films of Pt_xRh_{100-x} were deposited onto CP (Toray) by CBPLD ablating pure Pt (99.99%) and Rh (99.8%) targets acquired from Kurt J. Lesker. Briefly, two laser beams KrF (λ = 248 nm, 17 ns pulse width, repetition rate of 50 Hz, fluence changing from 1 to 7 J cm^{-2}) are synchronously concentrated onto the Pt and Rh targets. Before each deposition, the chamber was evacuated with a turbo pump (4 x 10^{-5} Torr). The deposition was performed at a background pressure of 2 Torr of high-purity He (Helium N5.0, Praxair). The number of laser pulses was 50000. further details of our experimental equipment can be found elsewhere [35]. The [Pt]/[Pt]+[Rh] concentration ratio of the catalyst was adjusted by independently varying the laser fluence on the two targets. During this manuscript, the notation Pt_xRh_{100-x} is employed to designate the atomic composition of the electrocatalyst, i.e., $Pt_{90}Rh_{10}$, $Pt_{75}Rh_{25}$, $Pt_{50}Rh_{50}$, and $Pt_{25}Rh_{75}$.

6.2.2 Material characterization

The surface morphology of the samples was observed with scanning electron microscopy (SEM) (JEOL, JSM 6300 F equipment) operated at an accelerating voltage

of 10 kV equipped with energy-dispersive X-ray spectroscopy (EDS) for elemental analysis of the samples. A transmission electron microscope (TEM, JEOL JEM-2100F) functioning at 200 kV was employed to examine the particle size. The crystalline structure of all samples was determined by X-ray diffraction (XRD) using a Bruker D8 Advance diffractometer equipped with a Cu Kα source (λ=1.5406 Å). The tube current was 40 mA with a tube voltage of 40 kV. All diffractograms were acquired in the Grazing Incidence Diffraction (GID) scan mode with a low incident angle of 2° and a 2θ angular step size of 0.04° with an acquisition time of 4 s per step in the range of 20-90°.

6.2.3 Electrochemical characterization

Sulfuric acid (H_2SO_4, 96 %) and ethanol (100% purity) were procured from Agros Organics and Commercial Alcohols inc., respectively. The electrocatalytic activity was assessed by cyclic voltammetry (CV) or linear scan voltammetry (LSV) in 0.5 M H_2SO_4 and in 1 M C_2H_5OH + 0.5M H_2SO_4 solutions by a conventional three compartment electrochemical cell having an Ag/AgCl, 4M NaCl reference electrode, platinum coil as a counter electrode and Pt_xRh_{100-x} films as working electrodes (geometric area 0.308 cm^2). All potentials in this work are quoted versus reversible hydrogen reference (RHE) electrode. Prior to each electrochemical measurement, the electrolyte is deaerated by bubbling argon through the solution for 30 min. Then the surface of the Pt_xRh_{100-x} working electrode is cleaned electrochemically in 0.5 M H_2SO_4 by potential cycling within 0.1 to 1.2 V range with 50 mV s^{-1} until a steady state is reached. EOR measurements were conducted in 1 M C_2H_5OH + 0.5 M H_2SO_4 with potential ranges from 0.2 to 1.2 V at the sweep rate of 5 mV s^{-1} (quasi-steady state). The electrochemical data were acquired at room temperature by a computer-controlled potentiostat-galvanostat (Autolab, PGSTAT 20, GPES). Durability studies were conducted using chronoamperometry technique by pulsing the potential from the open circuit potential to 0.8 V for 3600 s in a deaerated solution of 1 M C_2H_5OH + 0.5 M H_2SO_4.

The electrochemical removal of CO was examined by anodic stripping voltammetry (ASV). For CO stripping experiments, CO adsorption was conducted as follows: following 30 min of N_2 bubbling in the 0.5 M H_2SO_4 solution, the electrode surface is activated by multi-cycling at 50 mV s^{-1} from 0.1 to 1.2 V (RHE) under a continuous flow of N_2. Then pure CO (99.5%) is purged into the aforementioned solution at a polarized potential of 0.2 V for 30 min. Afterwards, while maintaining the potential at 0 V, pure N_2 is purged for

30 min to eliminate the remaining CO from the solution. Subsequently, ASVs were acquired again within 0 to 1.2 V (RHE) at 50 mV s^{-1} for two cycles. The first ASV cycle provided the total charge of CO oxidation, while the second cycle served to check that the adsorbed CO was completely stripped from the electrode surface.

6.3 Results and discussion

6.3.1 Physicochemical characterization

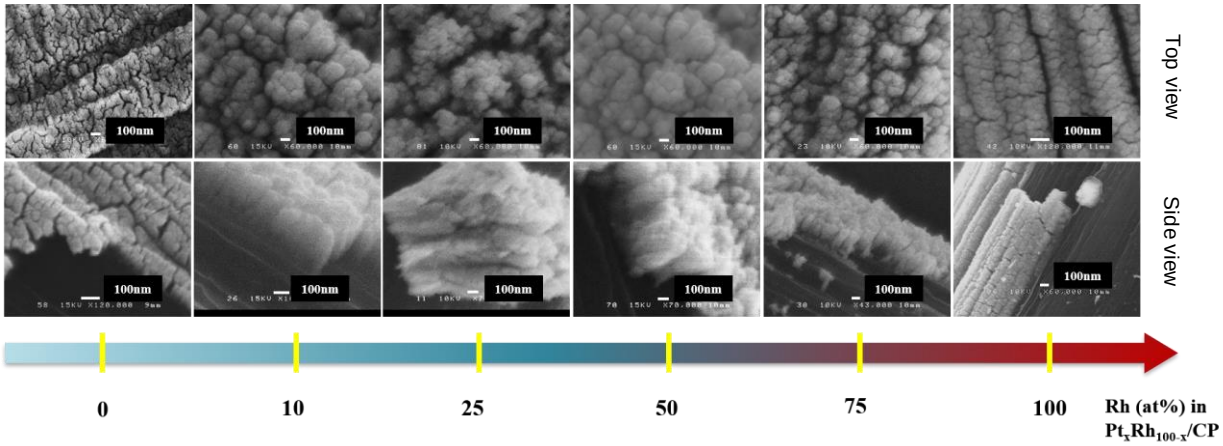

Figure 6.1 **Top and cross-section SEM images of Pt_xRh_{100-x} grown at room temperature by CBPLD on carbon paper substrate.**

EDS analysis (Table 6.1) reveals that the compositions of the as-grown PtRh samples are close to the nominal Pt:Rh ratios, showing a correct preparation route. Figure 6.1 reports top surface and cross-section SEM images of the as grown Pt_xRh_{100-x} films onto CP substrate. As can be seen from the cross-section images, the Pt_xRh_{100-x} films are porous and consisting of vertically aligned shrub-like arranged particles. Conversely, Pt and Rh films are dense and composed of closely packed particles. HR-TEM images of Pt_xRh_{100-x} films are displayed in Figure 6.2. The images distinctly show nanoparticles with apparent lattice fringes, which reveals that they are highly crystallized. A statistical size examination of the particles shows that they have a medium size of 5.2, 2.6, 4.3 and 3 nm (insert histograms) for $Pt_{90}Rh_{10}$, $Pt_{75}Rh_{25}$, $Pt_{50}Rh_{50}$, and $Pt_{25}Rh_{75}$, respectively.

Table 6.1 **Composition of the Pt_xRh_{100-x}/CP samples obtained from EDS and XRD**

	Nominal content	EDS	XRD*
Pt:Rh atomic ratio	90:10	91:9	92:8
	7:25	76:24	78:22
	50:50	52:48	56:44
	25:75	24:76	28:72

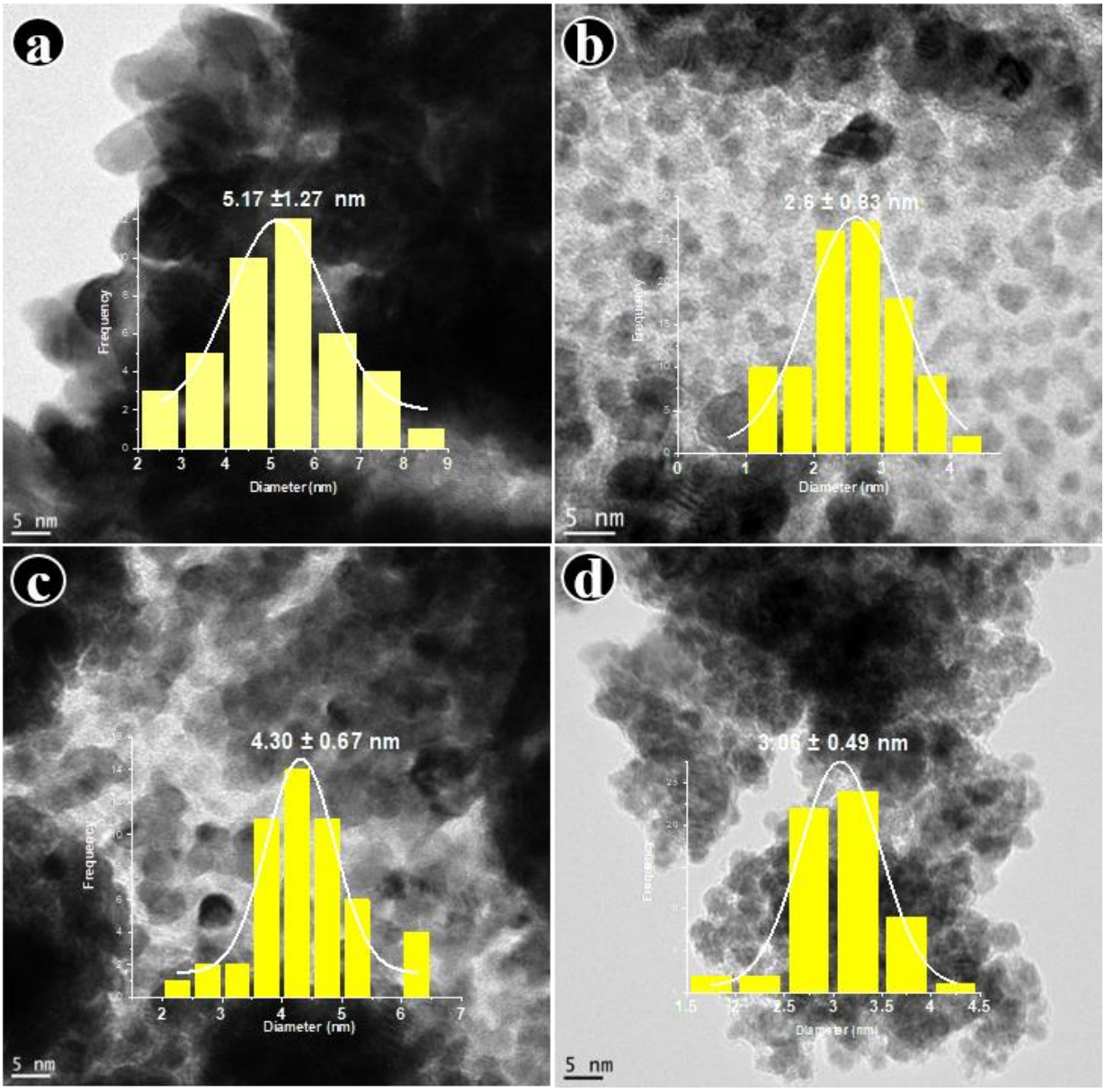

Figure 6.2 **HR-TEM images and corresponding particle size distribution histograms (inset to a–d) for (a) $Pt_{90}Rh_{10}$, (b) $Pt_{75}Rh_{25}$, (c) $Pt_{50}Rh_{50}$ and (d) $Pt_{25}Rh_{75}$.**

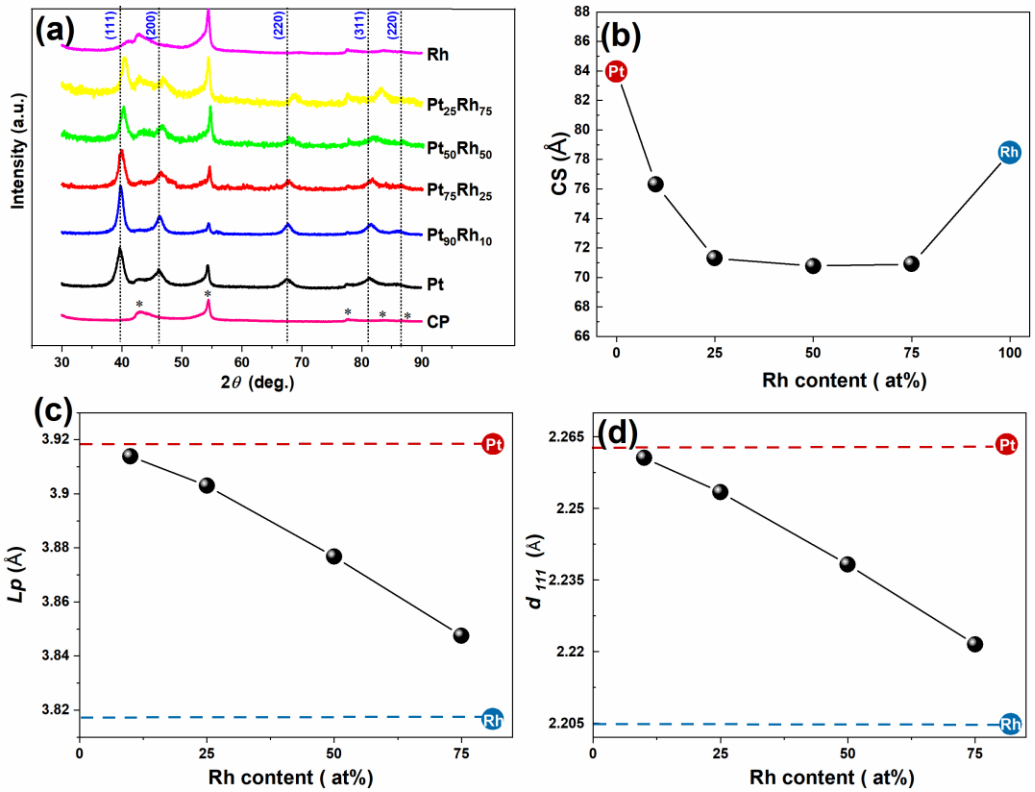

Figure 6.3 **XRD analysis of Pt_xRh_{100-x}/CP samples as function of Rh content. (a) XRD patterns, (b) crystallite size, (c), lattice parameter and (d) d_{111} space.**

Figure 6.3a displays the XRD profiles of the Pt_xRh_{100-x}/CP catalysts, altogether with those of pure Pt/CP, Rh/CP and the CP substrate. The diffraction peaks corresponding to the CP substrate are labeled with (∗) in the XRD patterns. The diffraction peaks located at ca. 39.8°, 46.2°, 67.5°, 81.3° and 85.7°, are respectively assigned to (111), (211), (100), (311) and (222) planes, which are characteristic of a face-centered cubic (fcc) phase of polycrystalline Pt [36]. It can be further noticed that Pt (111) plane shifted toward higher 2θ values with increasing Rh content showing a lattice contraction and alloy formation. The lattice parameters *Lp* and interplanar spacing d_{111} were estimated by Bragg law, and the average crystallites sizes (*CS*) were calculated by Vegard-Debye-Scherrer formula employing full width at half maximum (FWHM) from the most intense diffraction peak Pt (111). Owing to likely microstrains present in Pt–Rh nanocrystals, the average crystallites size (*CS*) of PtRh bimetallic catalysts were smaller than the pure metals (Pt, Rh), but there was no significant difference among Pt_xRh_{100-x} samples (Figure 6.3b). In addition, *Lp*, and d_{111} (Figure 6.3c and Figure 6.3d)) decreased linearly with the increasing Rh content, which is an indication of lattice contraction and alloy formation induced by the inclusion of smaller atomic radius Rh (1.345 Å) in the fcc-like structure of the larger

atomic radius Pt atoms (1.380 Å) [37]. Based on Vegard's law of $x = (\alpha - \alpha_{Rh})/(\alpha_{Pt} - \alpha_{Rh})$, where x is atomic fraction of Pt, α is the lattice parameter of Pt_xRh_{100-x} alloy, and with α_{Pt} (3.923 Å) and α_{Rh} (3.821Å) the calculated composition of Pt and Rh is in accordance with the elemental compositions measured by EDS (Table 6.1). The samples were further characterized by X-Ray photon electron spectroscopy (XPS). The acquisition parameters, the resulting XPS spectra, their brief description and interpretation are reported in the supplementary data (Figure S1-S3).

6.3.2 Electrochemical characterization

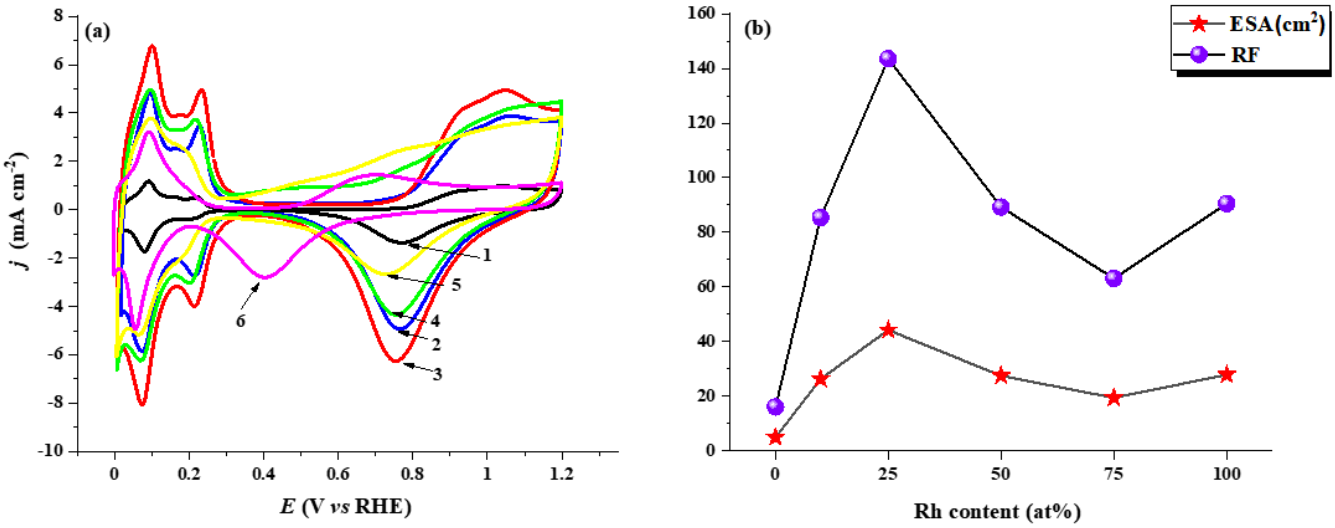

Figure 6.4 **Cyclic voltammograms at Pt/CP, Rh/CP and Pt_xRh_{100-x}/CP electrocatalysts in 0.5 M H_2SO_4 solution recorded with 50 mV s^{-1} scan rate. (b) *ESA* and *RF* as function of Rh content. 1) Pt/CP, 2) $Pt_{90}Rh_{10}$/CP, 3) $Pt_{75}Rh_{25}$/CP, 4) $Pt_{50}Rh_{50}$/CP, 5) $Pt_{25}Rh_{75}$/CP, and 6) Rh/CP.**

The CV curves acquired in 0.5M H_2SO_4 solution with 50 mV s^{-1} corresponding to Pt_xRh_{100-x}/CP, Pt/CP and Rh/CP electrocatalysts are grouped in Figure 6.4. At the Pt/CP catalyst, the characteristics of polycrystalline Pt in H_2SO_4 solution are clearly seen, specifically, the hydrogen adsorption/desorption (H_{ads}/H_{des}) peaks located between 0 and 0.3 V domain, the double layer region, the formation of Pt oxides commencing at 0.73 V and its resultant reduction peak centered at 0.7 V [38-39]. Likewise, the Rh/CP electrode exhibits three potential regions, the first region denotes a limited range of H_{ads}/H_{des} inside 0.02 and 0.27 V, the second region is the double layer charging governed by the specific adsorption of (hydrogen-) sulfate ions, and the third region corresponding to the creation of a Rh surface oxide that begins at 0.4 V and its reduction at 0.27 V. The CV shape of Rh/CP electrode is similar to that of electrodeposited thin polycrystalline Rh layers [40].

The lower onset potential for oxide formation on Rh/CP might be attributed to its oxophilic character. Therefore, electronic interactions between Pt and Rh may likewise alter the electronic structure of Pt and, as a result, promote its affinity for water dissociation. The CVs of Pt_xRh_{100-x}/CP catalysts display in-between profiles among those of pure Pt/CP and Rh/CP materials. In addition, Figure 6.4a reveals an important trend in the features of the bimetallic PtRh, specifically the onset potential of oxide formation and its corresponding onset potential of reduction shift to less positive potentials with increasing of Rh content. The double layer charging current significantly increased for high content of Rh ($Pt_{50}Rh_{50}$/CP and $Pt_{25}Rh_{75}$/CP). This behavior can be ascribed to the existence of Rh-oxides at the particle surface, enhancing by that the electrode capacitance ($Rh+3H_2O \rightarrow Rh(OH)_3+3H^+ +3e^-$, $Rh(OH)_3+H_2O \rightarrow RhO(OH)_3+2H^+ +2e^-$) [41].

The real surface area (*RSA*) or commonly meant by the true electrochemically active surface area (*ESA*) is one of the most significant parameters describing the surface catalytic activity of solid electrodes [42-44]. For the estimation of the *ESA* of the Pt-Rh system, the following equation has been suggested [45-46]:

$$ESA = Q_{des}^{H} / \left[\left(x_{Pt} \cdot Q_{ox,ML,Pt}^{H} + x_{Rh} \cdot \theta_{H,Rh}\right)\left(x_{Pt} \cdot Q_{ox,Pt}^{H} + x_{Rh} \cdot Q_{ox,ML,Rh}^{H}\right)\right] \quad (1)$$

Where Q_{des}^{H} is the coulombic charge induced by the oxidation of the hydrogen for a fixed cathodic vertex potential, θ_H is the surface coverage by adsorbed hydrogen ($\theta_{H,Pt}$=0.79, $\theta_{H,Rh}$=0.59), and x_{Pt} and x_{Rh} are atomic fractions of the Pt and Rh on the Pt-Rh surface. $Q_{ox,ML,S}^{H}$ is the charge corresponding to the oxidation of the monolayer hydrogen adsorbed on metal surface and accepted values of $Q_{ox,ML,S}^{H}$ for polycrystalline Pt and Rh are respectively 210 μC cm^{-2} and 221 μC cm^{-2}. Furthermore, the roughness factor *RF* was calculated by using the *ESA*/geometric area of the electrode (0.308 cm^2) ratio. Figure 6.4b shows that alloying Pt with Rh results in an increased electrocatalytic activity when comparing to pure Pt. Among the Pt_xRh_{100-x} alloys, $Pt_{75}Rh_{25}$/CP exhibited an *ESA* of about 44 cm^2 that is remarkably 8.8 times higher than pure Pt. The same result is observed as to *RF*, where the $Pt_{75}Rh_{25}$/CP stands out with an *RF* of 8.9 times greater than pure Pt.

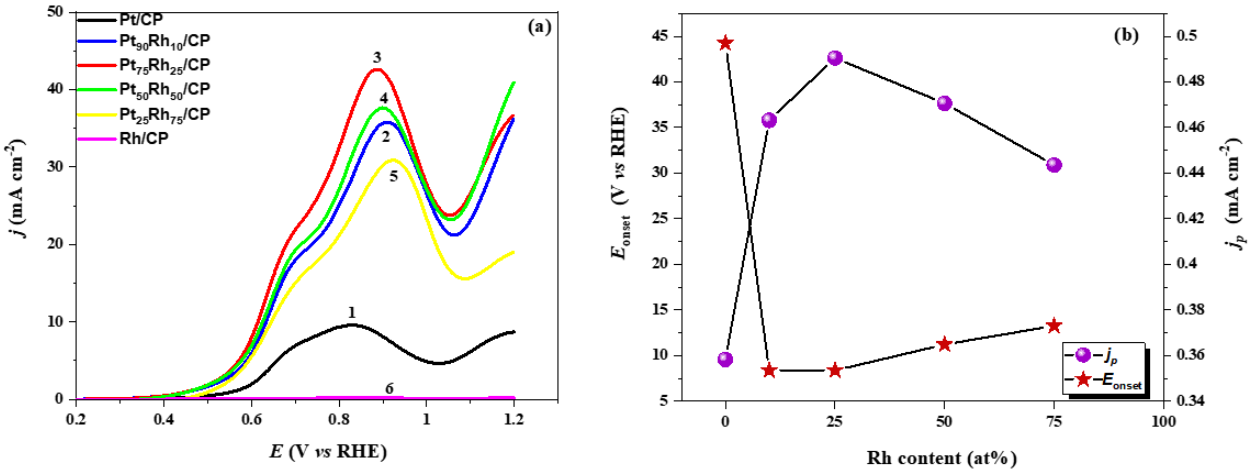

Figure 6.5 **Electroactivity of Pt/CP, Rh/CP and Pt_xRh_{100-x}/CP electrocatalysts toward ethanol oxidation reaction. (a) Cyclic voltammograms taken in 1 M C_2H_5OH + 0.5 M H_2SO_4 solution recorded with 5 mV s^{-1} scan rate. (b) E_{onset} and j_p as function of Rh content. 1) Pt/CP, 2) $Pt_{90}Rh_{10}$/CP, 3) $Pt_{75}Rh_{25}$/CP, 4) $Pt_{50}Rh_{50}$/CP, 5) $Pt_{25}Rh_{75}$/CP, and 6) Rh/CP**

Figure 6.5a reports LSVs of the EOR at the Pt_xRh_{100-x}/CP electrocatalysts in 1 M C_2H_5OH + 0.5 M H_2SO_4 solution with a scan rate of 5 mV s^{-1}. The LSVs shows that bare Rh/CP exhibited insignificant activity towards EOR, since Rh alone is less proficient than Pt for the dehydrogenation of ethanol. To relate the electrocatalytic activity of the different electrodes towards EOR, both the onset potential of ethanol oxidation, E_{onset} at which the anodic current commences to flow, and the peak current density (j_p) were extracted from LSVs of Figure 6.5a are displayed in Figure 5b as function of Rh content. Figure 6.5b, reveals that all the Pt_xRh_{100-x} catalysts exhibited E_{onset} values of about 150 mV significantly negative than the E_{onset} displayed by pure Pt. These observations seem to suggest at first glance that whatever the atomic composition in the CP/Pt_xRh_{100-x} catalyst, Rh greatly facilitates the electrooxidation of CO at potentials lower than that of Pt. On the other hand, the content of Rh in the bimetallic alloy affects the current activity. Indeed, j_p increased at electrocatalysts containing up to 25 at% of Rh and later declined for greater contents of Rh. Depending on the Rh content, j_p values exhibited by the Pt_xRh_{100-x} catalysts are 3 to 4.5 times greater than those delivered by Pt.

Durability of Pt_xRh_{100-x}/CP electrocatalysts investigated by chronoamperometry is shown in Figure 6.6a. Before reaching a stable value after around 500 sec, j decayed with time on all the catalysts owing to the buildup of CO-like byproducts generated throughout EOR [47]. After the 1-hour durability test, the steady-state current densities (j_{ss}) were plotted versus the Rh content and are shown in Figure 6.6b. In agreement with the voltammetric observations, all Pt_xRh_{100-x} demonstrated current density activities and

durability outperforming by far the Pt catalyst. Depending on the Rh content, j_{ss} values exhibited by the Pt_xRh_{100-x} catalysts are about 6 to 8 times higher than those recorded at Pt catalyst.

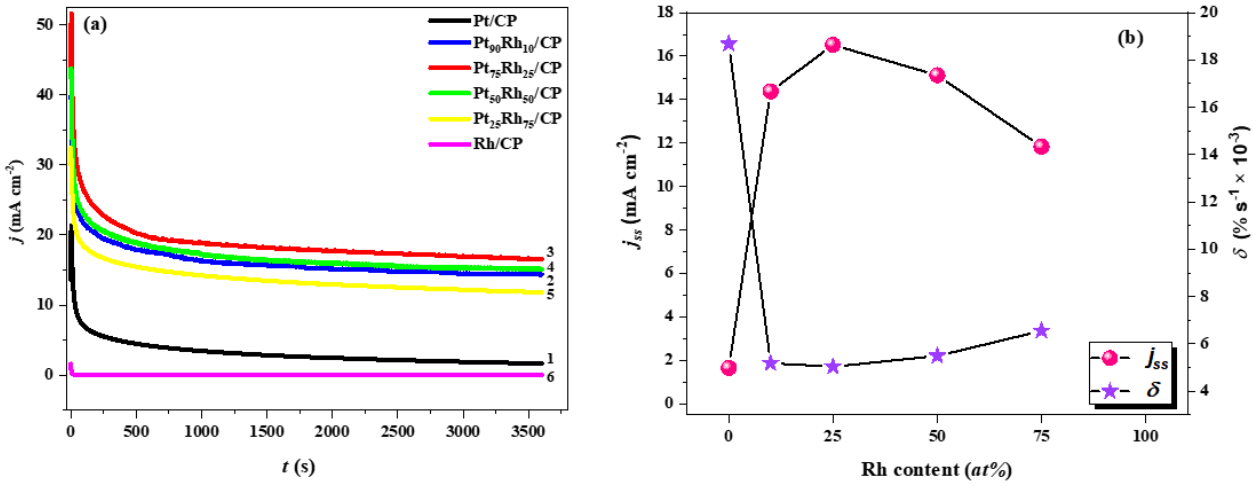

Figure 6.6 **Durability evaluation of of Pt/CP, Rh/CP and Pt_xRh_{100-x}/CP electrocatalysts toward ethanol oxidation reaction. (a) Chronoamperograms taken over 1 hour in 1 M C_2H_5OH + 0.5 M H_2SO_4 solution, and (b) j_{ss} and δ as function of Rh content. 1) Pt/CP, 2) $Pt_{90}Rh_{10}$/CP, 3) $Pt_{75}Rh_{25}$/CP, 4) $Pt_{50}Rh_{50}$/CP, 5) $Pt_{25}Rh_{75}$/CP, and 6) Rh/CP.**

The long-term poisoning rate (δ) can be evaluated by estimating the linear decay of the current at times superior than 500 s from Figure 6a and using the following equation [48]:

$$\delta = \frac{100}{I_0} \times \left(\frac{dI}{dt}\right)_{t>500\ s} (\%\ s^{-1}) \qquad (2)$$

Where $\left(\frac{dI}{dt}\right)_{t>500\ s}$ is the slope of the linear portion of the current decay, and I_0 is the current at the start of polarization back extrapolated from the linear current decay. Accordingly, δ values were calculated and are reported in Figure 6b, where it can be seen that Pt catalyst is prone to a long-term poisoning rate significantly higher compared to Pt_xRh_{100-x} catalysts. For a future application, the durability of the Pt_xRh_{100-x} catalysts will have to be confirmed in real DEFC systems over longer periods of up to thousands of hours.

In resume, the electrochemical performances show that as compared to Pt catalyst, the CBPLD-grown Pt_xRh_{100-x}/CP materials considered in this work displayed significantly higher real surface areas, current activities, outstanding low onset potentials towards the EOR, considerably greater stability and substantially lower long-term poisoning rates. One can presume therefore by analogy to PtSn and PtRu systems that Rh behaves in the same way as Sn or Ru does towards EOR when combined with Pt. The below electrochemical CO oxidation studies at Pt_xRh_{100-x} catalysts might shed light into these hypotheses.

6.3.3 Adsorbed CO electrooxidation (CO stripping)

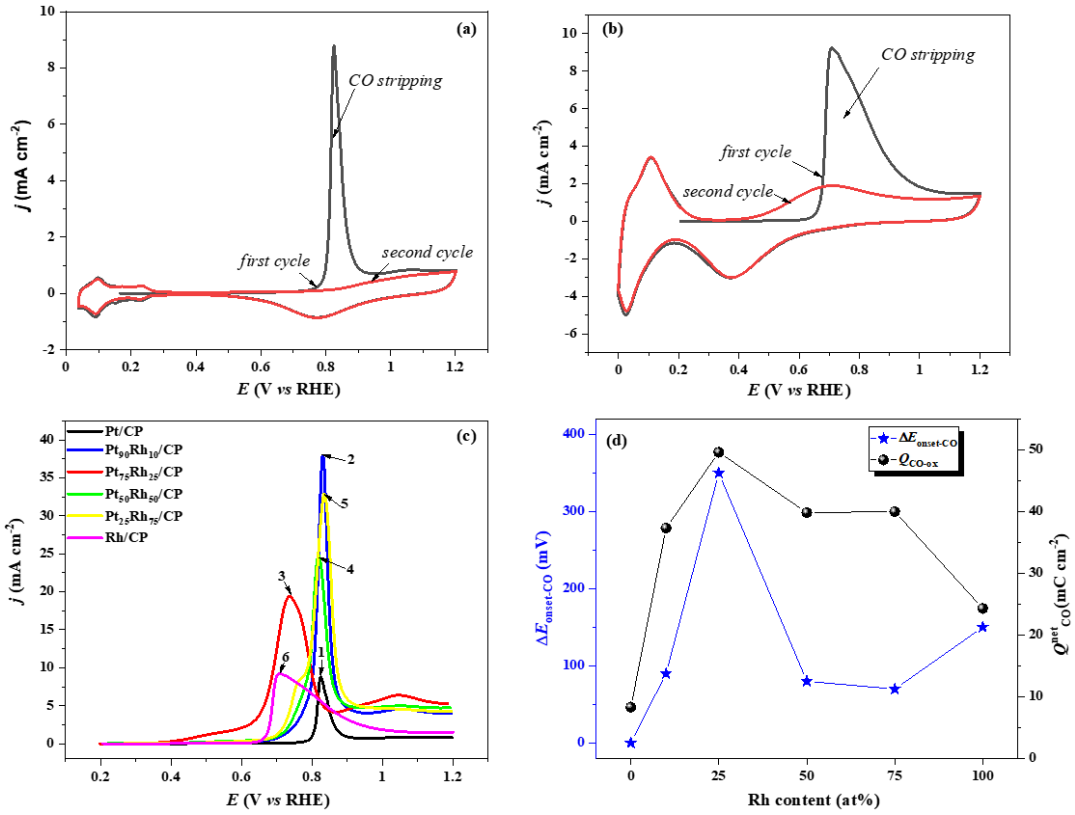

Figure 6.7 **CO-stripping voltammetry and CV in the base electrolyte 0.5 M H_2SO_4 recorded at 50 mV s^{-1}. (a) Pt/CP, (b) Rh/CP and (c) LSVs at Pt/CP, Rh/CP and Pt_xRh_{100-x}/CP electrocatalysts. (d) $\Delta E_{onset\text{-}CO}$ ($E_{onset\text{-}CO}$ @Pt - $E_{onset\text{-}CO}$ @Pt_xRh_{100-x}) and Q_{CO}^{net} as function of Rh content. 1) Pt/CP, 2) $Pt_{90}Rh_{10}$/CP, 3) $Pt_{75}Rh_{25}$/CP, 4) $Pt_{50}Rh_{50}$/CP, 5) $Pt_{25}Rh_{75}$/CP, and 6) Rh/CP.**

Figure 6.7a and b show the comparison of CO_{ads} ASVs at pure Pt/CP and Rh/CP electrodes, respectively. The H_{ads}/H_{des} characteristics are plainly visible throughout the reversal and consecutive scans at both electrodes. Actually, the hydrogen profile region is similar to that measured before CO adsorption, which indicates that the entire adsorbed CO was totally oxidized and stripped from the electrode surface through the first cycle. For the Pt/CP catalyst, the onset potential for CO oxidation begins at around 0.76 V, and the maximum of CO oxidation peak located at 0.85 V (Figure 6.7a). On the other side, at the Rh/CP catalyst the onset potential for CO oxidation commences at about 0.61 V and the maximum peak is situated at 0.7 V (Figure 6.7b). The fact that the onset potential and maximum peak potential of CO oxidation are lower for the Rh/CP catalyst compared to Pt/CP catalyst indicates that the activity of the Rh/CP catalysts for CO oxidation is superior to that of Pt/CP catalyst, demonstrating by that that Rh facilitates the oxidation of adsorbed CO at lower potentials.

Figure 6.7c groups together the CO-stripping peaks recorded at the Pt_xRh_{100-x} electrodes with those of Rh and Pt electrodes. Even though the equal amount of CO was adsorbed at the surfaces of all the electrocatalysts, the electrochemical CO oxidation is intensely affected by the content of Rh in the Pt_xRh_{100-x} catalysts. These differences can be quantified by analyzing the onset potential of the CO electrooxidation reaction ($E_{onset\text{-}CO}$), and the Q_{CO}^{net} that is the net charge due to oxidation and desorption of the CO adlayer. $E_{onset\text{-}CO}$ is the main design parameter of electrocatalysts highly tolerant to CO poisoning or removal for liquid fuel cells. A better method to value the variation of the activity of catalysts towards CO electrooxidation is to observe the difference between $E_{onset\text{-}CO}$ at Pt/CP and $E_{onset\text{-}CO}$ at Pt_xRh_{100-x}/CP: $\Delta E_{onset\text{-}CO}$ ($E_{onset\text{-}CO}$ @Pt - $E_{onset\text{-}CO}$ @Pt_xRh_{100-x}). Like this, any variation of $\Delta E_{onset\text{-}CO}$ is solely linked to the effect of Rh. The variation $\Delta E_{onset\text{-}CO}$ versus the [Rh] content is displayed in Figure 7d, which shows that Rh, whether it is alloyed or not to Pt, oxidizes CO at lower potentials than the latter. The second observation is that $\Delta E_{onset\text{-}CO}$ depended on the Rh content, it augmented as [Rh] increased from 10 to 25 at. %, and then diminished for greater [Rh] contents. Above all, the $Pt_{75}Rh_{25}$/CP catalyst exhibited a remarkably lower $E_{onset\text{-}CO}$ of 350 mV compared to that of Pt/CP.

The net charge corresponding to oxidation and desorption of the CO adlayer was assessed following an approach suggested by Gomez and coworkers [49]:

$$Q_{CO}^{net} = Q_{strip} - |Q_T| - \int_{E_T}^{E_+} \frac{j}{v} dE \qquad (3)$$

where, Q_T is the reduction charge density displaced by CO adsorption at a fixed potential E_T in the double layer region. E_+ is the positive potential limit chosen to conduct the peak integration, j is the voltammetric current density and v is the scan rate in cyclic voltammetry. The integral term on the right-hand side of the equation counterparts the total integrated charge density between the potential at which the displacement was performed and E^+. Thus calculated Q_{CO}^{net} on the alloy surfaces (*i.e.,* the extent of poisoning) were found to change with Rh content (Figure 6.7d). Indeed, Q_{CO}^{net} values exhibited a maximum as high as about 50 mC cm^{-2} at the $Pt_{75}Rh_{25}$/CP electrode compared to 8.3 mC cm^{-2} of that displayed by Pt/CP electrode.

6.4 Discussion

Mechanistic aspects regarding the Rh-promoted electrooxidation of ethanol on Pt are still not well understood. For example, a decade ago Gupta and Datta undertook studies on the catalytic activity for EOR at electrodeposited Pt and PtRh alloys with different atomic compositions [50]. The authors discovered that the best ethanol oxidation performance was obtained with $Pt_{74}Rh_{26}$ electrode. The authors did not however detect any important variation in the onset potential for EOR between Pt and PtRh catalysts and thus attributed the improvement in electrocatalytic activity for this PtRh catalyst relative to Pt itself to an enhancement of C–C bond dissociation instead to a bifunctional mechanism [50]. De Souza and coworkers reported the same conclusions for Pt and PtRh alloys of different atomic compositions synthesized by potentiostatic deposition [51]. Thus, the prevalent understanding reported in the literature suggests that Rh due to its intrinsic ability to break the C-C bond increases the yield of CO_2 rather than to provide supplementary oxygen for the oxidation of CO-related species (bifunctional effect) or to other effects (ligand or electronic) as with PtSn or PtRu catalysts. Nonetheless, there is a reason that this hypothesis does not represent an ample picture of the role of Rh in this class of catalysts. This comes down to the fact that the role of Rh alone and in PtRh has not been much studied particularly towards the electrooxidation of CO. Among the very few works, Lima and coworkers studied CO anodic stripping at Pt/C and Pt-Rh/C electrodes prepared by solution impregnation and did not notice any important change of the onset potential of CO oxidation among the two electrocatalysts [52]. By employing the modified polyol method with Br^- as a shape-directing agent, Rao and coworkers prepared graphene-supported cubic with different atomic ratios of Pt and Rh [53]. The authors observed a positive shift of the onset potential of CO_{ads} oxidation on cubic Rh and on PtRh alloys compared to cubic Pt, indicating that CO adsorption on Rh is stronger than that on Pt. Alfredo Calderón-Cárdenas and coworkers prepared Pt-Rh/C with atomic ratios close to Pt: Rh 3:1, 1:1 and 1:3 electrocatalysts by chemical reduction with formic acid [54]. The authors noticed a displacement towards positive values of the onset potential for the oxidation of adsorbed CO for the three Pt: Rh catalysts compared to Pt/C, revealing that Rh renders more difficult to oxidize adsorbed CO compared with pure Pt. Surprisingly, when they subjected Pt-Rh/C to thermal treatment in H_2 atmosphere, the three Rh containing catalysts exhibited onset potentials lower than that of Pt [54]. More recently, Juan Bai and coworkers prepared bimetallic PtRh alloy nanodendrites via a complex-reduction method [55]. The authors observed that Pt1Rh1

nanodendrites display a negative shift in the onset oxidation potential and the peak potential for the CO_{ad} oxidation reaction as compared to Pt nanocrystals electrocatalyst, implying that Pt1Rh1 nanodendrites have weak affinity to CO. The authors explained that Pt1Rh1 nanodendrites easily produce the OH_{ads}, which speeds the CO_{ads} electrooxidation due to the bifunctional mechanism at potentials lower than that of Pt nanocrystals electrocatalyst.

Returning to our materials CBPLD-synthesized, a first evaluation between Pt/CP and Rh/CP indicates that the stripping of adsorbed CO originates at lower potentials at the Rh/CP catalyst (see Figure 6.7a and Figure 6.7b), which may have facilitated CO_{ads} electrooxidation into CO_2. On pure Pt surfaces, it is now commonly acknowledged that the electrooxidation of adsorbed CO proceeds according to a Langmuir-Hinshelwood mechanism in which CO reacts with an oxygen-containing species available on the surface [56]:

On Pure Pt:

$$H_2O + Pt \rightarrow OH_{ads,\ Pt} + H^+ + e^- \quad (4)$$

$$CO_{ads,\ Pt} + OH_{ads,Pt} \rightarrow CO_2 + H^+ + e^- + 2{*}Pt \quad (5)$$

On Pure Rh:

$$H_2O + Rh \rightarrow OH_{ads,\ Rh} + H^+ + e^- \quad (6)$$

$$CO_{ads,\ Rh} + OH_{ads,\ Rh} \rightarrow CO_2 + H^+ + e^- + 2{*}Rh \quad (7)$$

("*" indicates the edge sites),

As to PtRh, two mechanisms describe the positive effect of Rh: the bifunctional mechanism, where Rh a highly oxophilic transition metal initiates water dissociation at lower potentials than Pt, and the ligand effect where rhodium changes the electronic structure of the adjacent platinum suggesting a faster supply in OH_{ads}. By analogy to the PtRu system [57], one can propose that at PtRh:

$$H_2O + {*}Rh \rightarrow OH_{ads,\ Rh} + H^+ + e^- \quad (8)$$

$$H_2O + {*}Pt \rightarrow OH_{ads,\ Pt} + H^+ + e^- \quad (9)$$

$$CO_{ads,\ Rh} + OH_{ads,\ Rh} \rightarrow CO_2 + H^+ + e^- + {*}Rh + {*}Pt \quad (10)$$

$$CO_{ads,\ Pt} + OH_{ads,Pt} \rightarrow CO_2 + H^+ + e^- + {*}Rh + {*}Pt \quad (11)$$

Indeed, taking the alloying effect on the lattice contraction and electronic structure into consideration, there should exist an optimal composition for CO oxidation reaction. Our results showed that $Pt_{75}Rh_{25}$/CP exhibited the highest catalytic activity toward CO electrooxidation where Rh atoms activate water dissociation at lower potentials than Pt (the difference being as high as 350 mV, Figure 7d). At higher Rh content, the onset potential of CO oxidation shifts back to higher potentials but remain more negative than that of Pt.

Interestingly, the observed trend in the electrocatalytic activity of the Pt_xRh_{100-x}/CP materials towards ethanol is similar to that observed for CO species, *i.e.*, electrooxidation of ethanol commences at potentials significantly lower than Pt (Figure 5b). Based on the CO-studies, it is clear to see that Rh supplies OH species to oxidize the dissociated CO at Rh sites, whereas Pt eases ethanol dehydrogenation. This is in line with quantum mechanics calculation, which showed that the dissociation of water molecules on Rh is superior to Pt [58]. The ligand effect, i.e., Rh alters the electronic properties of Pt in a manner that Pt-adsorbate is weakened, therefore lessening the energy barriers for the oxidation of adsorbates [59-60]. In addition, XRD revealed that compressive strains happened in the Pt alloy crystals (strain effects), engendering downshifts of Pt 5*d*-band center regarding Fermi levels [61]. Conferring to *d*-band theory, diminution in the density of *d* states of the metal nearby the Fermi level could be useful in eliminating intermediates on the alloyed Pt surface [62], which therefore enables the adsorption and/or desorption of ethanol. The Rh-rich catalyst formulation can impede the dissociative adsorption of ethanol that have taken place principally on Pt sites and by that decreases the oxidation current densities of EOR, thus lowering the overall catalytic current density activity.

Our future work will focus on either employing DEMS or PM-IRRAS (Polarization Modulation-InfraRed Reflection-Adsorption Spectroscopy) are planned for CBPLD synthesized Pt_xRh_{100-x}/CP materials to identify and quantify *in situ* intermediates and/or products formed upon electrooxidation of CO and ethanol. Such studies will not only unravel the role of Rh (activity or selectivity) in Pt_xRh_{100-x} materials grown by pulsed laser deposition technique but will also help to review spectroelectrochemical studies of PtRh synthesized by other reported methods and will confirm or infirm if the conflicting observations regarding the role of Rh are due to the synthesis method of PtRh materials.

6.5 Conclusions

Cross-beam pulsed laser deposition allowed the preparation of vertically aligned shrub-like porous Pt_xRh_{100-x} thin films uniformly coating a carbon paper substrate with atomic ratios close to nominal values. Irrespective of the Rh content in the alloys examined in this work, they are all by far much tolerant to CO poisoning than pure Pt. Such superior ability accounts for two mechanisms: Rh a highly oxophilic transition metal activates water dissociation at lower potentials than Pt (bifunctional mechanism), and the ligand effect where Rh modifies the electronic structure of the neighboring Pt suggesting a faster supply in OH_{ads}. These observations contradict for instance the very few works reported in the literature related to electrooxidation of surface adsorbed CO, which claim that Rh in PtRh has no effect or makes it more difficult to oxidize CO_{ads} compared with pure Pt.

Remarkably and qualitatively speaking, the same tendency in the catalytic performance is observed for the EOR, i.e., ethanol oxidation is by far superior both in terms of onset potential of the oxidation reaction (shifted to more negative values) or current density at the Pt_xRh_{100-x}/CP as compared to pure Pt/CP catalyst. It can thus be envisaged that Rh serves to nucleate OH_{ads} species at lower potentials than on a pure Pt electrode, leading to the oxidative removal of CO_{ad} on Pt sites nearby, liberating Pt sites for further ethanol oxidation (bifunctional mechanism). In addition, the variation in the electronic structure of Pt induced by the addition of Rh contributes to the higher catalytic activity of the PtRh catalysts (ligand effect) by facilitating the adsorption of ethanol.

Above all, the composition of PtRh materials applies a strong impact on the catalytic activity of these materials towards CO and ethanol electrooxidation. The $Pt_{75}Rh_{25}$/CP catalyst displayed the highest performance in either reaction. Summarizing, results of this work provide an appropriate route to synthesize nanostructured PtRh bimetallic materials with a high degree of tolerance to carbon monoxide, a principal catalytic poison for H_2/O_2 and several liquid fuel cells.

'Declarations of interest: none.

Acknowledgements

This work was supported by the Natural Sciences Engineering Research Council of Canada (NSERC) and the Centre Québécois sur les Matériaux Fonctionnels (CQMF). H. Wang and X. Tong are grateful to China Scholarship Council for a PhD scholarship

References

[1] M. Arenz, V. Stamenkovic, B. Blizanac, K. Mayrhofer, N. Markovic, P. Ross, J. Catal., 232 (2005) 402-410.

[2] M.R. Gennero de Chialvo, G.C. Luque, A.C. Chialvo, ChemistrySelect, 3 (2018) 9768-9772.

[3] M.A. Scibioh, S.-K. Kim, E.A. Cho, T.-H. Lim, S.-A. Hong, H.Y. HaAppl. Catal., 84 (2008) 773-782.

[4] C. Lamy, S. Rousseau, E. Belgsir, C. Coutanceau, J.-M. Léger, Electrochim. Acta, 49 (2004) 3901-3908.

[5] P.S. Fernández, C.A. Martins, M.E. Martins, G.A. CamaraElectrochim. Acta, 112 (2013) 686-691.

[6] J. Kim, J. Lee, Y. Tak, J. Power Sources, 192 (2009) 674-678.

[7] R.H. Crabtree, John Wiley & Sons, 2010.

[8] S. Ramachandran, U. Stimming, Energy Environ. Sci., 8 (2015) 3313-3324.

[9] P.J. Kulesza, I.S. Pieta, I.A. Rutkowska, A. Wadas, D. Marks, K. Klak, L. Stobinski, J.A. Cox, Electrochim. Acta, 110 (2013) 474-483.

[10] J.-M. Léger, S. Rousseau, C. Coutanceau, F. Hahn, C. Lamy, Electrochim. Acta, 50 (2005) 5118-5125.

[11] M. Heinen, Z. Jusys, R. Behm, J. Phys. Chem. C, 114 (2010) 9850-9864.

[12] J. Torrero, F.J. Pérez-Alonso, M.A. Peña, C. Domínguez, A.O. Al-Youbi, S.A. Al-Thabaiti, S.N. Basahel, A.A. Alshehri, S. Rojas, ChemElectroChem, 3 (2016) 1072-1083.

[13] H. Wang, Z. Jusys, R. Behm, J. Phys. Chem. B, 108 (2004) 19413-19424.

[14] R. Kavanagh, X.M. Cao, W.F. Lin, C. Hardacre, P. Hu, Angew. Chem. Int. Ed., 51 (2012) 1572-1575.

[15] Z.-F. Xu, Y. Wang, J. Phys. Chem. C, 115 (2011) 20565-20571.

[16] J.-M. Jin, T. Sheng, X. Lin, R. Kavanagh, P. Hamer, P. Hu, C. Hardacre, A. Martinez-Bonastre, J. Sharman, D. Thompsett, Phys. Chem. Chem. Phys., 16 (2014) 9432-9440.

[17] Y. Wang, Y. Mi, N. Redmon, J. Holiday, J. Phys. Chem. C, 114 (2009) 317-326.

[18] Q. Wang, G. Sun, L. Jiang, Q. Xin, S. Sun, Y. Jiang, S. Chen, Z. Jusys, R. Behm, Phys. Chem. Chem. Phys., 9 (2007), 2686-2696.

[19] V. Comignani, J. M. Sieben, M. D. Sanchez, M. E. Duarte, Int. J. Hydrogen Energy, 42 (2017) 24785-24796.

[20] A. O. Neto, R. R. Dias, M. M. Tusi, M. Linardi, E. V. Spinacé, J. Power Sources, 166 (2007) 87-91.

[21] P. Chandran, D. Puthusseri, S. Ramaprabhu, Int. J. Hydrogen Energy, 44 (2019) 4951-4961.

[22] J. E. Thomas, A. R. Bonesi, M. S. Moreno, A. Visintin, A. M. Castro Luna, W. E. Triaca, Int. J. Hydrogen Energy, 35 (2010) 11681-11686.

[23] A.O. Neto, M. Giz, J. Perez, E. Ticianelli, E. Gonzalez, J. Electrochem. Soc., 149 (2002) A272-A279.

[24] K. Ding, Y. Zhao, L. Liu, Y. Cao, Q. Wang, H. Gu, X. Yan, Z. Guo, Int. J. Hydrogen Energy, 39 (2014) 17622-17633.

[25] R. Rizo, D. Sebastián, M.J. Lázaro, E. Pastor, Appl Catal B., 200 (2017) 246-254.

[26] S. García-Rodríguez, F. Somodi, I. Borbáth, J.L. Margitfalvi, M.A. Peña, J.L.G. Fierro, S. Rojas, Appl Catal B., 91 (2009) 83-91.

[27] X. W. Teng, A. Mendez-Vilas (Ed.), Spain, 2013, pp. 473-484.

[28] P. Wang, Y. Wen, S. Yin, N. Wang, P.Shen, Int. J. Hydrogen Energy, 42 (2017) 24689-24696.

[29] S. Yin, P. Wang, J. Lu, Y. Wen, P. Shen, Int. J. Hydrogen Energy, 42 (2017) 22805-22813.

[30] S. Y. Shen, T. S. Zhao, J. B. Xu, Int. J. Hydrogen Energy, 53 (2010) 12911-12917.

[31] E. P. Leão, M. J. Giz, G. A. Camara, G. Maia, Electrochim. Acta, 56 (2011) 1337-1343.

[32] I. YoungáCha, J. KeeáLee, S. JongáYoo, J. Mater. Chem. A., 3 (2015) 17130-17134.

[33] A. Barranco, A. Borras, A. R. Gonzalez-Elipe, A. Palmero, Prog. Mater Sci., 76 (2016) 59-153.

[34] A. Tselev, A. Gorbunov, W. Pompe, Rev. Sci. Instrum., 72 (2001) 2665-2672.

[35] P. Bommersbach, M. Chaker, M. Mohamedi, D. Guay, J. Phys. Chem. C, 112 (2008) 14672-14681.

[36] V.-L. Nguyen, M. Ohtaki, V. N. Ngo, M.-T. Cao, M. Nogami, Adv. Nat. Sci: Nanosci. Nanotechnol., 3 (2012) 025005.

[37] Y. Zhang, M. Janyasupab, C. W. Liu, X. Li, J. Xu, C. Liu, Adv. Funct. Mater., 22 (2012) 3570-3575.

[38] K. Kinoshita, D. Ferrier, P. Stonehart, Electrochim. Acta, 23 (1978) 45-54.

[39] T. Schmidt, H. Gasteiger, G. Stäb, P. Urban, D. Kolb, R. Behm, J. Electrochem. Soc., 145 (1998). 2354-2358.

[40] M. Łukaszewski, H. Siwek, A. Czerwiński, Electrochim. Acta, 52 (2007) 4560-4565.

[41] R. Oliveira, M. Santos, L. Bulhoes, E. Pereira, J. Electroanal. Chem., 569 (2004) 233-240.

[42] S. Trasatti, O. Petrii, Pure Appl. Chem., 63 (1991) 711-734.

[43] R. Woods, in A. J. Bard, (Eds.), Marcel Dekker, Inc., New York 1976, vol. 9. pp. 1

[44] G.y. Jarzabek, Z. Borkowska, Electrochim. Acta, 42 (1997) 2915-2918.

[45] A. Czerwinski, J. Sobkowski, Anal. Lett., 17 (1984) 2175-2181.

[46] M. Łukaszewski, M. Soszko, A. Czerwiński, Int. J. Electrochem. Sci, 11 (2016) 4442-4469.

[47] E. Antolini, Appl Catal B., 74 (2007) 337-350.

[48] J. Jiang, A. Kucernak, J. Electroanal. Chem., 543 (2003) 187-199.

[49] R. Gómez, A. Rodes, J. Perez, J. Feliu, A. Aldaz, Surf. Sci., 344 (1995) 85-97.

[50] S.S. Gupta, J. Datta, J. Electroanal. Chem., 594 (2006) 65-72.

[51] J. De Souza, S. Queiroz, K. Bergamaski, E. Gonzalez, F. Nart, J. Phys. Chem. B, 106 (2002) 9825-9830.

[52] F. Lima, E. Gonzalez, Electrochim. Acta, 53 (2008) 2963-2971.

[53] L. Rao, Y.-X. Jiang, B.-W. Zhang, Y.-R. Cai, S.-G. Sun, Phys. Chem. Chem. Phys., 16 (2014) 13662-13671.

[54] A. Calderón-Cárdenas, J.E. Ortiz-Restrepo, N.D. Mancilla-Valencia, G.A. J. Braz. Chem. Soc., 25 (2014) 1391-1398.

[55] J. Bai, X. Xiao, Y.-Y. Xue, J.-X. Jiang, J.-H. Zeng, X. Li, Y. Chen, ACS Appl. Mater. Interfaces, 50 (2018) 19755-19763.

[56] H.A. Gasteiger, N. Marković, P.N. Ross Jr, E.J. Cairns, Electrochim. Acta, 39 (1994) 1825-1832.

[57] F. Maillard, G.-Q. Lu, A. Wieckowski, U. Stimming, J. Phys. Chem. B, 109 (2005) 16230-16243.

[58] T.H. Yu, T. Hofmann, Y. Sha, B.V. Merinov, D.J. Myers, C. Heske, W.A. Goddard III, J. Phys. Chem. C, 117 (2013) 26598-26607.

[59] K.-W. Park, J.-H. Choi, B.-K. Kwon, S.-A. Lee, Y.-E. Sung, H.-Y. Ha, S.-A. Hong, H. Kim, A. Wieckowski, J. Phys. Chem. B, 106 (2002) 1869-1877.

[60] K. Bergamaski, E.R. Gonzalez, F.C. Nart, Electrochim. Acta, 53 (2008) 4396-4406.

[61] V.R. Stamenkovic, B.S. Mun, M. Arenz, K.J. Mayrhofer, C.A. Lucas, G. Wang, P.N. Ross, N.M. Markovic, Nat. Mater., 6 (2007) 241-247.

[62] M.A. Rigsby, W.-P. Zhou, A. Lewera, H.T. Duong, P.S. Bagus, W. Jaegermann, R. Hunger, A. Wieckowski, J. Phys. Chem. C, 112 (2008) 15595-15601.

Supporting Information

X-Ray photoelectron spectroscopy (XPS) characterization:

Measurements were conducted with a VG Escalab 220i-XL set with an Al Kα source (1486.6 eV). The anode was operated at 10 kV and 20 mA. The pass energy of the analyzer was fixed at 20 eV. All samples were analyzed with a spot size of 250 x 1000 μm located nearby in the center of the sample. Survey spectra ranging from 0 to 1300 eV were first obtained, and subsequently higher resolution multiplex scan spectra (Pt 4f, Rh 3d, O 1s, and C 1s core levels) were acquired. Quantification of the elements was accomplished with CasaXPS software (Casa Software Ltd.) by fitting the core level spectra after a Shirley background removal. The C 1s core level peak at 284.6 eV, stemming from hydrocarbon contaminants at the surface, was employed as an internal reference. All spectra have been recalibrated with reference to the C 1s core level peak of fortuitous carbon contamination. Using the CasaXPS software, the Pt and Rh surface concentratio is estimated by integrating the raw area of the Pt 4f (Rh 3d) and related to its relative intensity factor (RSF).

X-Ray photoelectron spectroscopy (XPS) results:

X-ray photoelectron spectroscopy (XPS) is a spectroscopic technique for characterizing the elemental composition, electronic structure and chemical environment of the elements on the material surface. The typical survey spectrum of nanocatalysts Pt_xRh_{100-x} alloy (Figure S6.1) displayed the presence of Pt, Rh, C, and O elements. The deposition process is conducted in a closed chamber under inert atmosphere that is Helium. In addition, before that deposition, the chamber is vacuumed with a pressure of 4×10^{-5} Torr (*Experimental section, 2.1. Catalysts preparation*). All these ensure that samples are not contaminated by oxygen during the growth process. Thus, the partial oxidation of the sample occurred as a result of post-exposure in air. The [Pt]/[Rh] ratio estimated from was 16.4, 13, 4.2 and 1.1 for $Pt_{90}Rh_{10}$, $Pt_{75}Rh_{25}$, $Pt_{50}Rh_{50}$, and $Pt_{25}Rh_{75}$, respectively. The core level XPS profile of Pt 4f spectra (Figure S6.2) exhibits one doublet Pt $4f_{7/2}$ and Pt $4f_{5/2}$, located at ca 70.6~71.3eV and 73.3~74.7 eV with the typical spin-energy separation of ca. 3.3 eV. The 3.3 eV binding energy (*BE*) difference between the Pt $4f_{7/2}$ and Pt $4f_{5/2}$is in accordance with Pt being in a metallic state. [1]. The Rh 3d core level region was similarly made by one doublet of Rh $3d_{5/2}$ and Rh $3d_{3/2}$, located at ca. 307.1~307.5eV and 311.8~312.2 eV corresponding to metallic Rh [2].

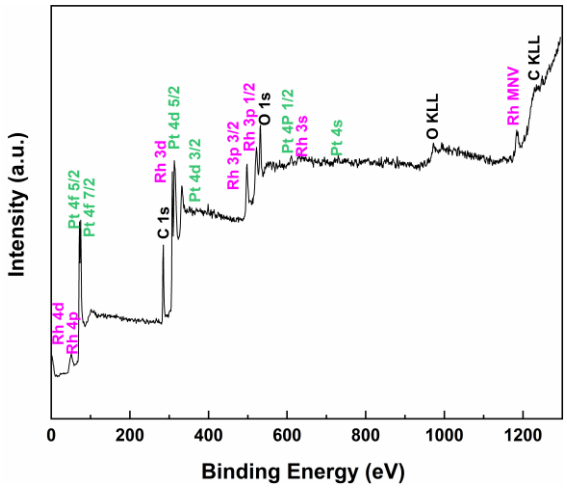

Figure S6.1 **Typical XPS surveys scan of the CBPLD synthesized Pt_xRh_{100-x} samples onto carbon paper substrate.**

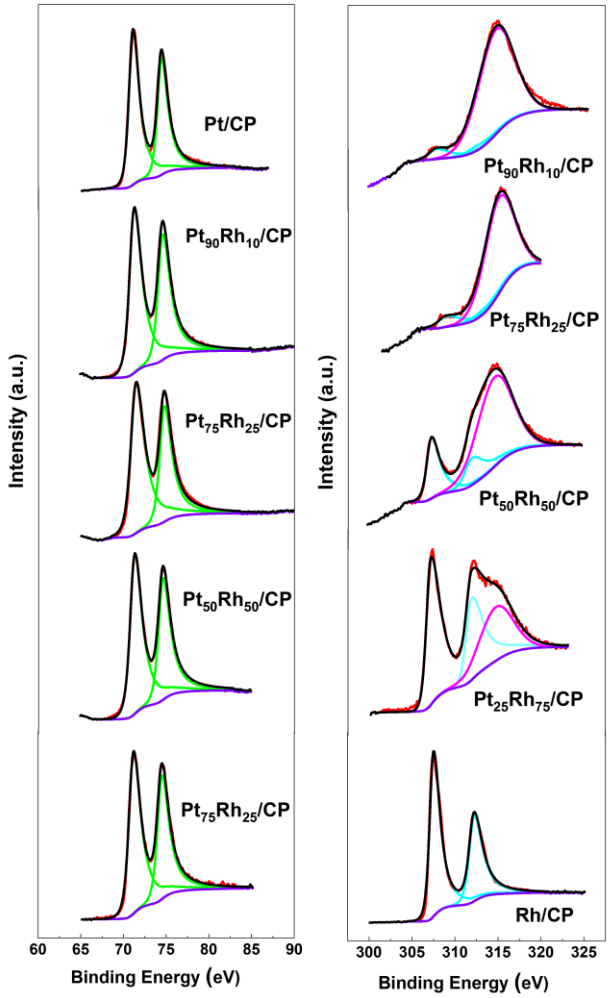

Figure S6.2 **High-resolution XPS profiles of the CBPLD synthesized Pt_xRh_{100-x} samples onto carbon paper substrate. (Left) Pt 4f core-level and (right) Rh 3d core-level.**

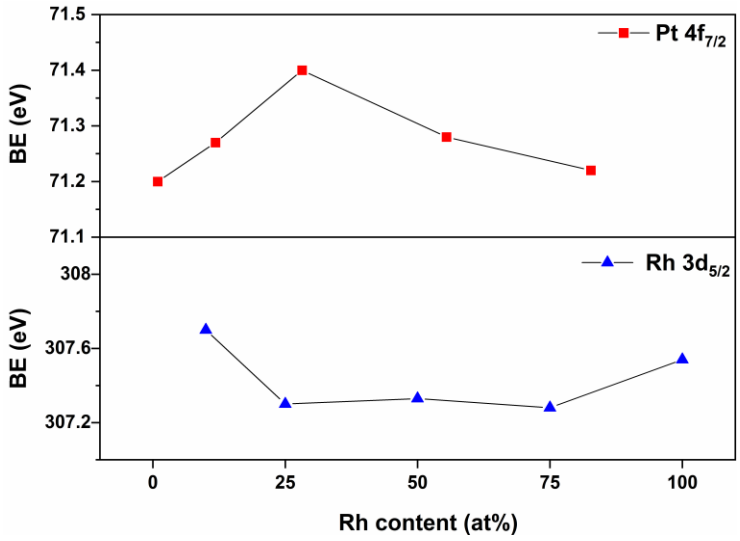

Figure S6.3 Binding energies (BEs) of the Pt $4f_{7/2}$ and Rh $3d_{5/2}$ as function of the Rh content.

Figure S6.3 reveals that as the Rh content increased from 0 to 25 at. %, the Pt $4f_{7/2}$ peak shifted by 0.20 eV to *BE*s, and then shifted back to lower *BE*s for Rh content higher than 25 at%. In the other hands, from 10 to 25 at% of Rh, the *BE* of the Rh $3d_{5/2}$ peak moved significantly by about 0.6 eV to lower *BE*s, leveled off and then shifted to higher *BE*s for a Rh content higher than 75 at%. These electronic modifications of the Pt *5d*-band (electron withdrawing effect) can be caused by the presence of Rh in the alloy [3-4], which will weaken the interaction between CO and the Pt surface and consequently accelerates the CO electrooxidation kinetics on Pt-Rh based catalysts.

References

[1] Wagner, C. D.; Riggs, W. M.; Davis,L. E.; Moulder, J. F. Handbook of X-ray Photoelectronic Spectroscopy; Perkin-Elmer Corp: Eden Prairie, MN, 1979.

[2] M.J. Jacinto, O.H.C.F. Santos, R. Landers, P.K. Kiyohara, L.M. Rossi, Appl. Catal. B: Environ.,90 (2009) 688-692.

[3] F. H. B. Lima and E. R. Gonzalez, Electrochim. Acta, 53 (2008) 2963-2971.

[4] V. Del Colle, J. Souza-Garcia, G. Tremiliosi-Filho, E. Herrero, and J. M Feliu, Phys. Chem. Chem. Phys., 13 (2011) 12163-12172.

7 CONCLUSIONS, LIMINATIONS AND PERSPECTIVES

This chapter is to sort out the summary of the research described in this thesis, limitations and the prospects for future research.

7.1 Conclusions

The state of the art of DEFCs technology cannot be commercialized in a short-term due to the sluggish anodic reaction, which has high overpotential and slow reaction kinetics. This thesis is dedicated to desgin the bi- an ternary Pt based catalysts with enhanced electrocatalytic activities towards EOR.

In this thesis, we synthesized template-free and bindless ternary layer-by-layer catalysts $RhPtSnO_2$ and co-deposited Pt_xRh_{100-x}/CP alloys by means of PLD and CBPLD technique at room temperature. We comprehensively studied the effect of Rh thickness (the number of laser pulses of Rh, $N_{lp, Rh}$) and the atomic ratio of Pt and Rh on EOR in binary and ternary catalysts. Moreover, we discovered the synergistic effect between the three constituents in the ternary electrocatalysts $RhPtSnO_2$ and a reaction mechanism was proposed based on the electrochemical analysis results. The general conclusions associated with the work described above are presented in this chapter.

Firstly, we investigate the influence of the number of laser pulses of rhodium ($N_{lp, Rh}$) on the morphology, electronic structure and electron transfer properties towards CO oxidation. We synthesized carbon paper supported Rh thin films with various numbers of laser pulses $N_{lp, Rh}$, ($N_{lp, Rh}$ = 5000,10000,20000 and 50000) via PLD. The SEM showed lower $N_{lp, Rh}$ formed smooth film, whereas higher N_{lp} yielded to highly porous structure. The XRD results indicated the Rh particle sizes were smaller when the $N_{lp, Rh}$ were lower and vice versa. The XPS demonstrated that both metallic Rh and Rh^{3+} were present at the surface of four catalysts, and the amount of metallic Rh (at%) increased along with the $N_{lp, Rh}$. Besides, the $N_{lp, Rh}$ has a remarkabe influence on electrochemical activity. The anodic stripping voltammetry showed the catalyst with higher $N_{lp, Rh}$ had a good CO oxidation performance. The catalyst Rh_{50} ($N_{lp, Rh}$ = 50000) exhibited the highest electroactive surface area (27.90 cm^2 *vs* 1.20 cm^2 of Pt), the lowest onset potential of CO electrooxidation (0.47 V *vs* 0.60 V Pt), and a net charge corresponding to electrooxidation of the CO adlayer of 424 µC cm^{-2} (*vs* 358 µC cm^{-2} of Pt).

Then, we study the influence of $N_{lp, Rh}$ on Pt- and Pt-SnO_2- based catalysts towards ethanol oxidation reaction (EOR) in acidic medium. Meanwhile, we also reveal the role of SnO_2 and Rh

in Pt-based catalysts on the electrooxidation of ethanol. We used PLD to deposit Rh, Pt and SnO_2 onto carbon paper (CP) layer by layer. The SEM illustrated that Rh, Pt and SnO_2 were layered deposited. The XRD showed the particle size of Pt became smaller in $PtSnO_2$- and PtRh-based catalysts, but the corresponding lattice parameter *a* and interplanar *d*-spacing d_{hkl} became bigger, and the 2θ shifted negatively. This trend was more obvious in ternary $RhPtSnO_2$ catalysts when increasing the $N_{lp,\ Rh}$, which implied that there was strong interaction between SnO_2(Rh) and Pt. The shift of the core level of SnO_2, Rh and Pt in XPS verified the strong metal-support interaction (SMSI) between them. The XPS also revealed that Sn was in Sn^{4+} state, Pt and Rh were in metallic states. The linear sweep voltammetry (LSV), chronoamperometry (CA) and CO stripping voltammetry results demonstrated that catalysts with higher $N_{lp,\ Rh}$ on the surface had worse performance in LSV and CA, but better CO oxidation performance. Conversely, the ternary catalyst Rh_5PtSnO_2/CP with moderate amount of Rh ($N_{lp,\ Rh}$ = 5000) had the best performance in terms of the lowest onset potential, highest current yield and durability, which can be respectively ascribed to the addition of SnO_2 (bi-functional mechanism) and the supply of Rh (electronic effect).

Next, we study the effect of the substrate carbon nanotubes CNTs in above-mentioned catalysts towards EOR. We grow CNTs on Ni/CP via chemical vapor deposition (CVD). Subsequently we deposited SnO_2, Pt and Rh on CNT layer by layer. Different with the CP supported catalysts with lamellar stacking characteristic; these CNT-supported catalysts were in cluster distribution. The SEM showed they were like clumps of corals or cauliflowers. Similar XRD and XPS results were observed with previous CP-supported catalysts, as well as the LSV, CA and CO stripping. But the CNT supported catalysts had better electrochemical behavior than the corresponding CP supported catalysts, especially the ternary Rh_5PtSnO_2/CNT, which had an unsurpassed performance with the lowest onset potential and highest current yield.

Finally, we focus on the effect of structure on EOR. We use CBPLD synthesize co-deposited PtRh with various atomic ratios of Pt: Rh (9:1, 3:1, 1:1, 1:3). The SEM, EDX and TEM results showed the bimetallic Pt_xRh_{100-x} catalysts were shrub-like and Pt and Rh nanoparticles were homogeneously dispersed on the carbon paper substrate with the average particle size less than 6 nm. The positive 2θ shift of Pt(111) and the shrink of *a* and d_{hkl} in XRD indicated Pt and Rh were alloyed. The XPS results revealed both Pt and Rh were in metallic state. The LSV, CA and CO stripping results manifested the added Rh remarkably enhanced the CO tolerance and the catalytic activity towards EOR, and the optimal atomic ratio of Pt: Rh was 3:1.

We propose a EOR mechanism on the ternary catalyst $Rh_5/Pt/SnO_2$ (Figure 7.1). The specific role for each constituent of PLD-synthesized catalysts on the ethanol electrooxidation pathway was summarized as followed: Pt was selected for ethanol chemisorption; SnO_2 provided OH species at lower potentials to removal of CO poisoning species, while Rh accounted for the C-C bond cleavage. In CBPLD-made catalysts Pt_xRh_{100-x}/CP, the role of Rh was not only to break the C-C bond, but also to active water for offering oxygen-containing species.

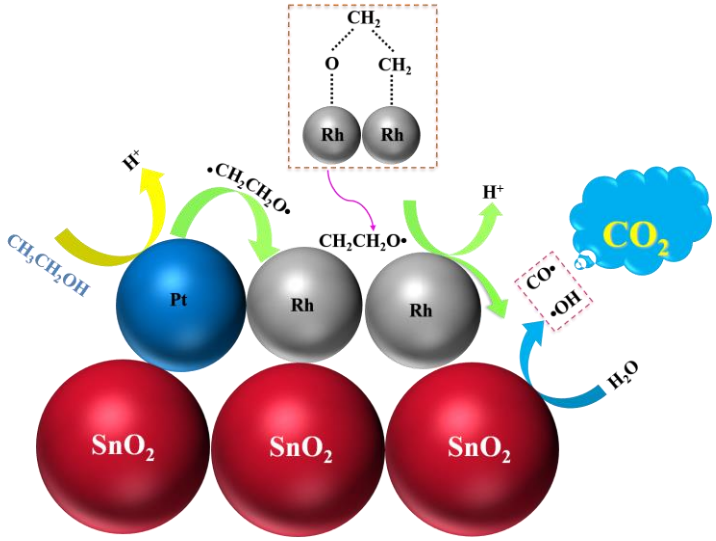

Figure 7.1 The possible EOR mechanism on the ternary catalyst $Rh_5/Pt/SnO_2$

The collected results were summarized as follows:

(1) Rh with higher N_{lp} has a bigger particle size and better CO oxidation capability.

(2) The promoter Rh and SnO_2 in the vicinity of Pt sites could provide a high activity for ethanol electrooxidation and better tolerance towards poisoning species due to synergistic effect of **bi-functional mechanism** and **electronic effect (ligand effect)**.

(3) The activity of the above catalysts for EOR decreased in the order of **co-deposited CP supported catalysts** ($Pt_{75}Rh_{25}$ > $Pt_{50}Rh_{50}$ > $Pt_{90}Rh_{10}$ > $Pt_{25}Rh_{75}$) > **layer-by-layer deposited CNT supported catalysts** ($Rh_5/Pt/SnO_2$ > Pt/SnO_2 > $Rh_{10}/Pt/SnO_2$ > $Rh_{20}/Pt/SnO_2$ > Rh_5/Pt > $Rh_{50}/Pt/SnO_2$ > Pt) > **layer-by-layer deposited CP supported catalysts.**

(4) **SnO_2** based catalysts > **CeO_2** based catalysts > **MnO_2** based catalysts > **TiO_2** based catalysts.

(5) In Pt_xRh_{100-x} alloys, lower content of Rh cannot generate enough oxygen-containing species at lower potentials, resulting in Pt poisoned. Also, there are possibly not enough Rh sites to effectively break the C-C bond, which leads to a low catalytic activity. While too much Rh will inhibit Pt active sites for further ethanol dehydrogenation. With a moderate ratio of Pt and Rh

(3:1), Rh modifies the electronic structure of Pt, making a temperate bonding energy between Rh and ethanol and CO-like species, which facilitates disintegrating ethanol.

Several other catalysts have been also considered during this project, and the list of these catalysts are summarized in Table 7.1

Table 7.1 List of the catalysts studied during this project

Synthetic Method	Substrate		Catalysts	LSV			CA	CO stripping	
				j_{pa} (mA cm^{-2})	E_{pa} (V)	E_{onset}	j_{ss} (mA m^{-2})	E_{onset} (V)	E_{pCO}(V)
PLD	CP	**Pt**	Pt	9.55	0.64	0.54	1.66	0.60	0.63
		Rh_n	Rh_5	0	-	-	0	0.40	0.62
			Rh_{10}	0	-	-	0	0.46	0.53
			Rh_{20}	0	-	-	0	0.47	0.49
			Rh_{50}	0	-	-	0	0.48	0.51
		Rh_n/Pt	Rh_5/Pt	11.77	0.65	0.48	4.94	0.53	0.57
			Rh_{10}/Pt	12.86	0.65	0.47	5.23	0.48	0.55
		SnO_2-based	Pt/SnO_2	19.06	0.66	0.46	6.07	**0.14**	0.51
			Rh_5/Pt/SnO_2	**21.53**	0.65	0.43	6.98	**0.17**	0.50
			Rh_{10}/Pt/SnO_2	17.05	0.65	0.46	6.12	0.23	0.60
			Rh_{20}/Pt/SnO_2	17.99	0.66	0.47	5.49	0.32	0.57
			Rh_{50}/Pt/SnO_2	13.05	0.66	0.51	3.64	0.45	0.55
		CeO_2-based	Pt/CeO_2	15.32	0.64	0.45	6.03	0.23	0.58
			Rh_5/Pt/CeO_2	14.48	0.62	0.43	5.30	0.50	0.58
			Rh_{10}/Pt/CeO_2	16.20	0.62	0.40	8.07	0.47	0.52
			Rh_{20}/Pt/CeO_2	14.80	0.65	0.46	5.60	0.49	0.60
			Rh_{50}/Pt/CeO_2	10.12	0.64	0.52	5.44	0.51	0.60
		TiO_2-based	Pt/TiO_2	15.13	0.66	0.48	7.51	0.28	0.60
			Rh_5 /Pt/TiO_2	14.70	0.66	0.48	5.59	0.53	0.63
			Rh_{10}/Pt/TiO_2	12.04	0.65	0.49	5.61	0.50	0.59
		MnO_2-based	Pt/MnO_2	13.97	0.66	0.48	5.84	0.58	0.60
			Rh_5/Pt/MnO_2	14.20	0.66	0.48	7.47	0.49	0.63
			Rh_{10}/Pt/MnO_2	10.94	0.65	0.53	4.62	0.47	0.55
	CNT	**Pt**	Pt	18.87	0.68	0.40	7.12	0.57	0.67
		Rh_n	Rh_5	0	0	0	0	0.49	0.55
			Rh_{10}	0	0	0	0	0.46	0.53
		Rh_n/Pt	Rh_5/Pt	21.34	0.65	0.23	11.59	0.57	0.62

			Rh_{10}/Pt	21.38	0.66	0.33	10.11	0.55	0.65
		SnO_2-based	Pt/SnO_2	23.16	0.67	0.16	12.74	0.19	0.61
			Rh_5/Pt/SnO_2	**27.77**	0.66	0.16	15.83	**0.17**	0.59
		CeO_2-based	Pt/CeO_2	23.43	0.67	0.34	12.96	0.60	0.66
			Rh_{10}/Pt/CeO_2	28.73	0.67	0.34	14.20	0.54	0.65
		TiO_2-based	Pt/TiO_2	11.40	0.65	0.42	4.84	0.51	0.67
			Rh_5 /Pt/TiO_2	18.23	0.66	0.38	5.89	0.50	0.66
		MnO_2-based	Pt/MnO_2	22.11	0.67	0.38	6.51	0.21	0.64
			Rh_5/Pt/MnO_2	25.14	0.66	0.38	6.58	0.31	0.62
CB-PLD	CP	**Pt_xRh_{100-x}**	$Pt_{90}Rh_{10}$	35.80	0.71	0.16	20.13	0.30	0.64
			$Pt_{75}Rh_{25}$	**42.63**	**0.68**	**0.15**	**21.17**	**0.16**	**0.53**
			$Pt_{50}Rh_{50}$	37.66	0.70	0.15	19.91	0.28	0.62
			$Pt_{25}Rh_{75}$	30.90	0.72	0.18	16.58	0.49	0.64

7.2 Limitations

Although we successfully design, synthesize and study the catalysts and excellent electrochemical performances are obtained, there are still some unfinished works and limitations we need to work on, such as what exactly the products are during the EOR, whether the selectivity of CO_2 is increased or not with the addition of SnO_2 and Rh to Pt, whether these anode catalysts will work well in the DEFC system.

7.3 Perspectives

The limitations of this research point towards topics to be addressed in the future. It can be started from three aspects:

(1) Synthesis of Pt_3Rh/MO_x catalysts. We will continue to synthesize co-deposited Pt_3Rh on metal oxides (SnO_2, CeO_2) with CP or CNT as substrate. Meanwhile, we will co-deposited Pt_3Rh on other metal oxides (*e.g.*, WO_x, RuO_x, and TaO_x) to find the most suitable metal oxides for ethanol oxidation.

(2) By means of *in-situ* FTIR and DEMS techniques, we will identify the reaction intermediates, products and quantify the amount of CO_2 generated during the EOR in binary and ternary catalysts.

(3) Performance examination. Study the performance and durability of the binary and ternary catalysts in membraneless microfluidic DEFC systems recently developed in our laboratory.

(4) Although the amount of Rh used in this thesis is very small, numerical modeling based on ab initio quantum atomistic methods (density functional theory) or classical methods (molecular dynamics) will be helpful to design and discover new noble metal-free multifunctional composites for ethanol electrocatalysis.

8 APPENDX I — RÉSUMÉ

8.1 Introduction

L'énergie joue un rôle crucial dans le développement économique et social. De nos jours, la demande mondiale d'énergie augmente de façon exponentielle en raison de l'expansion rapide de l'économie et de la croissance démographique continue. Alors que le système énergétique actuel est fortement dépendant des énergies fossiles (charbon, pétrole et gaz naturel), qui dominent environ 80% de la consommation mondiale d'énergie [1]. Il est rapporté que d'ici 2050, les approvisionnements en pétrole et en gaz ne seront probablement pas en mesure de répondre à la demande mondiale d'énergie [2]. Face à l'épuisement des combustibles fossiles, à la détérioration de l'environnement et à la demande d'énergie sans cesse croissante, il est d'une importance capitale d'explorer les sources d'énergie propres, renouvelables et durables et de créer un avenir meilleur pour les générations à venir. De nombreuses alternatives ont été étudiées, telles que l'énergie solaire, l'hydroélectricité, la marée, l'énergie éolienne, l'énergie nucléaire, la chaleur terrestre et les piles à combustible. Parmi ces ressources, les piles à combustible sont considérées comme l'énergie la plus prometteuse et une stratégie clé pour le développement énergétique durable en raison de leurs caractéristiques attrayantes: rendement élevé, absence de pollution et conditions de fonctionnement ambiantes.

Les piles à combustible sont présentes comme une technologie alternative hautement efficace et respectueuse de l'environnement pour la production d'énergie décentralisée. Les piles à combustible présentent les caractéristiques suivantes: (i) Propre. Les piles à combustible n'ont pratiquement aucune émission de polluants, les produits sont l'eau, la chaleur et le CO_2. (ii) Sans bruit. Il n'y a pas de pièces mobiles dans une pile à combustible, ce qui la rend plus silencieuse. (iii) Flexibilité du carburant. Les carburants peuvent être obtenus à partir de sources naturelles ou organiques à faible indice de carbone. (iv) Bonne fiabilité. La qualité de l'énergie fournie ne se dégrade pas avec le temps. (v) Haut rendement. Les piles à combustible ne sont pas limitées par la limite du cycle de Carnot. L'efficacité de conversion des piles à combustible peut atteindre 80% vs ICE 40%. (vi) Large plage d'application. La puissance fournie par les piles à combustible peut aller de 1 W à 1 MW. (vii) Densité d'énergie plus élevée et temps de décharge plus long.

Il est généralement admis que le PEMFC avec hydrogène comme carburant est l'une des technologies les plus prometteuses, mais H_2 n'est pas le carburant principal en raison de son coût élevé, de ses complications de stockage et de ses exigences de qualité rigoureuses. Bien

que le méthanol [3], l'acide formique [4], le formaldéhyde [5] ces carburants liquides semblent particulièrement pratiques, l'éthanol est plus attractif en raison des aspects suivants:

(i) Moins toxique.

(ii) Facilité de transport grâce à un point d'ébullition relativement plus élevé [6].

(iii) Perméabilité inférieure à celle du méthanol [7] (en raison de sa chaîne carbonée plus longue [8]).

(iv) Densité de puissance élevée due à l'électrooxydation complète de l'éthanol avec transfert de charge à 12 électrons [9] (8,01 kWh kg^{-1}, méthanol 6,1 kWh kg^{-1} [10], essence 12,89 kWh kg^{-1} [11]).

(v) Renouvelable. L'éthanol peut être facilement obtenu en grandes quantités à partir de la biomasse par fermentation d'une matière première contenant de la cellulose issue de l'agriculture (par exemple blé, maïs ou paille, canne à sucre, etc.) [12]. La production mondiale de bioéthanol a fortement augmenté, passant de 13,2 milliards de gallons en 2013 à 28,6 milliards de gallons en 2019 [13].

(vi) Compatible avec l'infrastructure de stockage et de livraison existante.

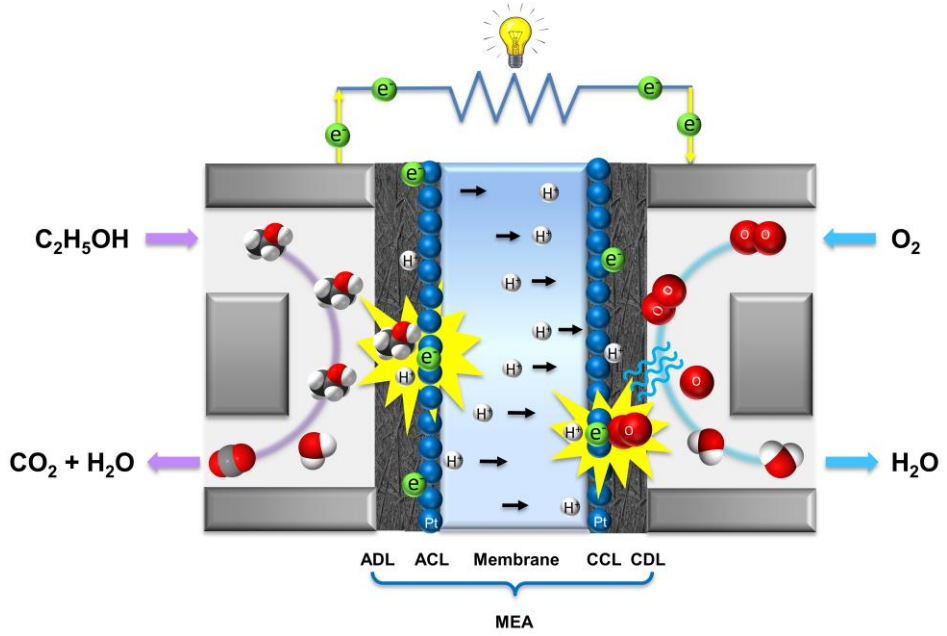

Figure 8.1 Principe de fonctionnement d'une DEFC acidique.

Les composants du DEFC et le principe de fonctionnement sont clairement illustrés dans la Figure 8.1. En théorie, l'éthanol est fourni à travers le champ d'écoulement anodique et est transféré de la couche de diffusion anodique (CDA) à la couche catalytique anodique (CCA), où l'éthanol est complètement oxydé en dioxyde de carbone et génère simultanément des protons

et des électrons. Ensuite, les électrons produits traversent le circuit électrique (charge), et les protons migrent à travers la membrane conductrice de protons vers la cathode. L'O_2 est acheminé à travers le champ d'écoulement cathodique et est transféré de la couche de diffusion cathodique (CDC) à la couche catalytique cathodique (CCC). En fin de compte, les électrons et les protons réagissent avec l'O_2 à la cathode, où se déroule la réaction de réduction de l'oxygène.

La réaction d'oxydation électrochimique globale de l'éthanol peut être exprimée comme suit:

$$\boldsymbol{C_2H_5OH + 3O_2 \rightarrow 2\,CO_2 + 3\,H_2O\left(\Delta E^{o}_{eq} = 1.145\,V\,vs.SHE\right)} \qquad \text{Eq (8.1)}$$

En réalité, l'éthanol est incomplètement oxydé en acétaldéhyde (AAL) et en acide acétique (AA) avec respectivement 2 et 4 transferts d'électrons. Parce que le Pt a du mal à cliver la liaison C-C de l'éthanol. En outre, le Pt est très susceptible d'être empoisonné par les intermédiaires fortement adsorbés tels que CO_{ad} et $CH_{x,\,ad}$. De plus, le coût élevé du platine est un autre facteur qui entrave la production à grande échelle de DEFC. En outre, la durabilité des matériaux d'électrode est critique.

Pour résoudre les problèmes mentionnés ci-dessus auxquels sont confrontés les DEFCs, il est nécessaire de développer un catalyseur qui peut fortement améliorer l'activité vis-à-vis de la ROE et la sélectivité en CO_2. Des efforts considérables ont été consacrés à l'exploration des bi- et tri- catalyseurs en combinant le Pt avec les métaux ou métaux de transition bon marché pour obtenir des catalyseurs.

Le mécanisme bifonctionnel (Figure 8.2). Le métal ajouté à proximité des nanoparticules de Pt peut dissocier l'eau à des potentiels inférieurs (0.4–0.6 V vs RHE, inférieurs à Pt 0.8 V vs RHE) et fournir des espèces oxygénées (OH_{ad}) pour atténuer les intermédiaires toxiques (CH_x et CO_{ad}) et libérer les sites actifs Pt en conséquence.

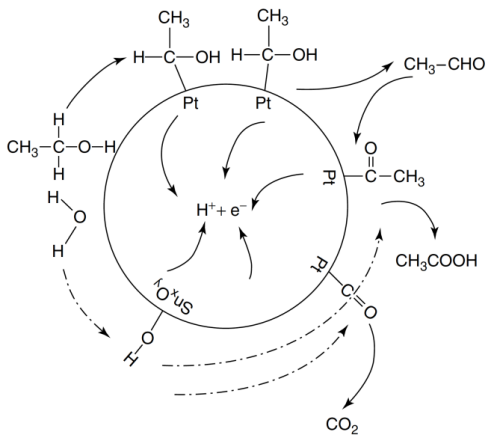

Figure 8.2 **Mécanisme propose pour l'électrooxydation de l'éthanol sur le catalyseur Pt–Sn/C [14].**

(2) L'interaction électronique avec le métal ajouté (Figure 8.3) modifie la structure électronique du Pt et provoque-le rétrogradage du centre de la bande *d* de Pt, ce qui peut diminuer l'énergie de liaison entre le CO et le Pt, ce qui réduit l'empoisonnement au CO sur Pt.

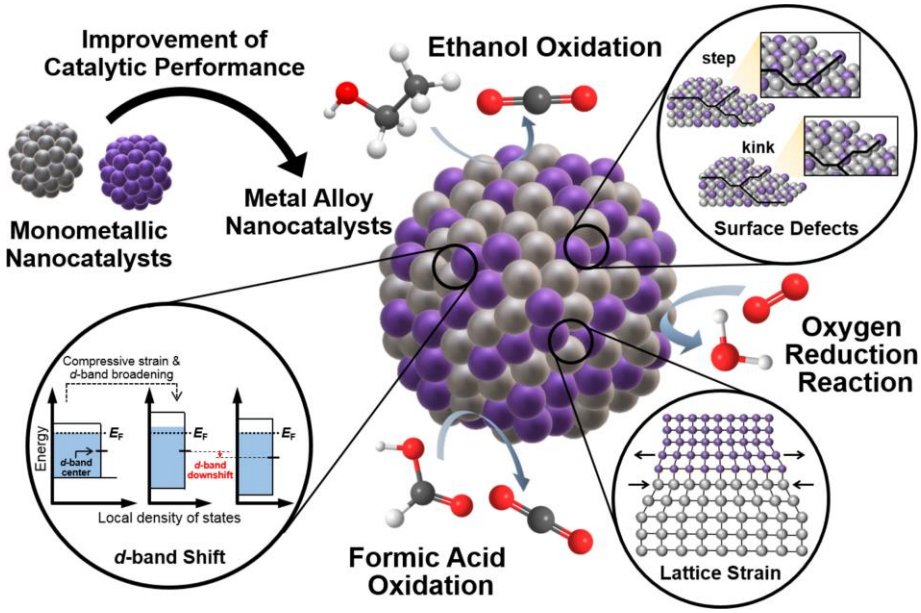

Figure 8.3 **Illustration du décalage de la bande *d* et des défauts de surface de l'alliage métallique pour l'amélioration de l'activité électrochimique [15].**

Jusqu'à présent, les catalyseurs binaires de PtSn, $PtSnO_2$ et Pt Ru ont été considérés comme les catalyseurs les plus efficaces pour la ROE [16-19], délivrant un courant faradique d'oxydation de l'éthanol plus élevé que le Pt pur. Malheureusement, le courant élevé contribue principalement au rendement élevé du produit d'oxydation incomplet AA. Ou plutôt, il a été trouvé que les catalyseurs PtSn [20-22], $PtSnO_2$ [23] et PtRu [22, 24-25] interrompent le clivage de la liaison C-C, et la sélectivité envers le CO_2 est encore faible.

Récemment, le rhodium a attiré une attention intensive en raison de son grand potentiel de scission de la liaison C-C pendant la ROE. Comme illustré dans le diagramme ci-dessous (Figure 8.4a), une configuration oxamétallacyclique à cinq membres du cycle s'est formée sur la surface Rh pendant la dissociation de l'éthanol, ce qui peut séparer efficacement la liaison C-C. Alors que η^2-CH_3CHO (Figure 8.4b) est préféré sur la surface Pt ou Pd [26-28], que la liaison C-C peut à peine être coupée.

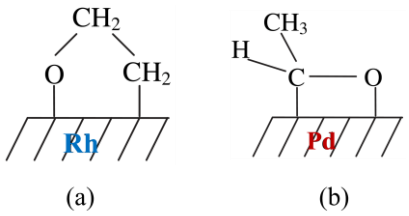

Figure 8.4 **Schematic diagram of an oxametallacyclic structure formed on Rh (111) surface during ethanol dissociation (a) and η^2–CH_3CHO formed on Pd (111) surface [26]**

Sur la base des principes ci-dessus, nous nous consacrons à la conception, à la recherche et au développement d'une série de catalyseurs ternaires $RhPtMO_2$ (M = Sn, Ce, Mn et Ti) et de catalyseurs binaires Pt_xRh_{100-x} à haute activité vers la ROE. Ces catalyseurs sont fabriqués par les méthodes de dépôt laser pulsé (PLD) (Figure 8.5a et b) et d'ablation laser à flux croisés (CBPLD) (Figure 8.5c), respectivement. Dans ce projet, nous avons considéré deux types de substrats, le papier carbone (PC) et les nanotubes de carbone (NTCs).

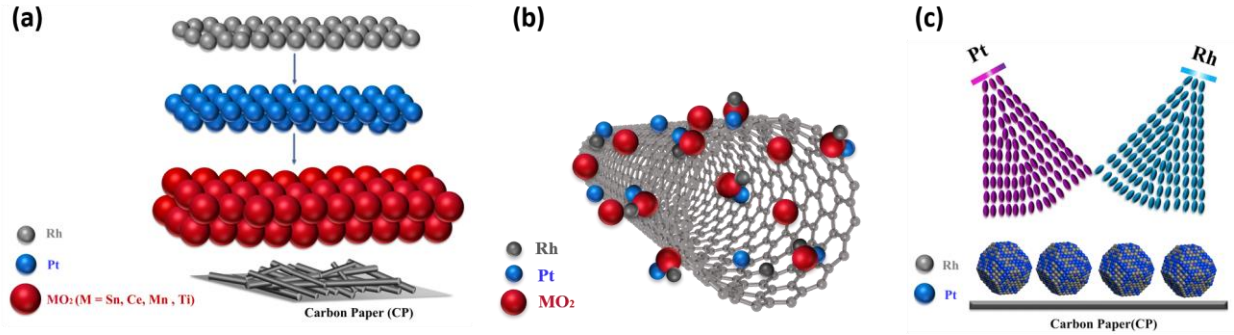

Figure 8.5 **(a et b) Les catalyseurs déposés couche par couche ont été fabriqués par le procédé de PLD et (c) les catalyseurs co-déposés ont été synthétisés par la technologie CBPLD.**

8.2 Les objectifs de la thèse

Ma thèse porte sur la conception et la fabrication de catalyseurs ternaires nanostructurés sans liant supportés par PC (TNCs) Rh-Pt-MO_2 (M = Sn, Ce, Mn et Ti) et l'alliage Pt_xRh_{100-x} pour les applications DEFC. L'objectif principal de cette étude est d'explorer l'effet de la quantité de Rh, les architectures des catalyseurs et le rôle de l'oxyde métallique et du Rh sur les performances

de la ROE. Cette thèse offrira une compréhension fondamentale de la coopération et de la division du travail des composants métalliques dans l'électrooxydation de l'éthanol, ainsi qu'une nouvelle méthodologie pour bien contrôler la morphologie et le rapport des constituants dans les catalyseurs bimétalliques.

Afin d'atteindre l'objectif principal, nous nous engageons dans les sous-objectifs suivants:

(1) Étude de l'influence du nombre d'impulsions laser (N_{lp}) et par là de l'effet de l'épaisseur de la couche Rh sur l'oxydation électrochimique du CO.
(2) Étudier le rôle de Pt, SnO_2 et Rh dans les catalyseurs $RhPtSnO_2$ supportés par du papier carbone ainsi que l'étude de l'effet de l'épaisseur de la couche Rh sur l'électrooxydation du CO et de l'éthanol.
(3) Étudier les propriétés catalytiques de support des nanotubes de carbone dans les catalyseurs à base de Pt et $PtSnO_2$ sur l'électrooxydation de l'éthanol.
(4) Étudier l'effet du rapport atomique du PtRh dans les catalyseurs Pt_xRh_{100-x} synthétisés par CBPLD sur l'ROE.

8.3 L'organisation de la thèse

Cette thèse se compose de 7 chapitres comprenant le résumé et les références. L'organisation de la thèse est listée ci-dessous:

Le chapitre 1 présente tout d'abord dans les grandes lignes le contexte et la motivation de la recherche sur les DEFC acides. Une revue détaillée de la littérature sur l'état de la recherche sur les DEFC à base de Pt est présentée.

Le chapitre 2 présente la méthodologie de cette thèse, y compris le schéma expérimental, les méthodes et les procédures. Une introduction détaillée sur diverses techniques de caractérisation physico-chimique et électrochimique et les paramètres expérimentaux correspondants sont également donnés dans ce chapitre.

Les chapitres 3 à 6 font état de quatre articles.

Le chapitre 7 résume les résultats et propose des orientations de recherche futures pour ce projet.

8.4 Conclusions

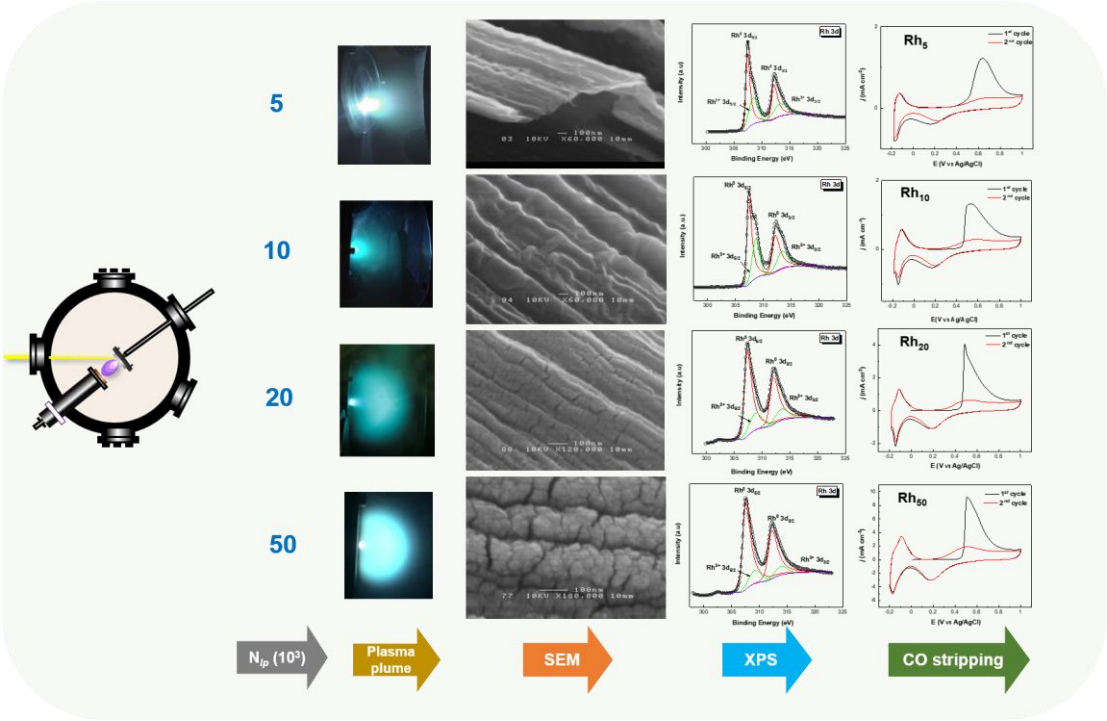

Figure 8.6 Le résumé graphique.

Premièrement, nous étudions l'influence du nombre d'impulsions laser (N_{lp}) du rhodium sur la morphologie, la structure électronique et les performances électrochimiques. Nous avons synthétisé de minces films de Rh supportés par du papier carbone avec différents nombres d'impulsions laser $N_{lp, Rh}$ (5000, 10000, 20000 et 50000) par la méthode de dépôt laser pulsé (PLD). La microscopie électronique à balayage (MEB) a montré qu'une N_{lp} plus faible produisait un film lisse, tandis qu'une N_{lp} plus élevée donnait une structure poreuse. La diffraction des rayons X (DRX) a indiqué que les tailles de particules de Rh étaient plus petites lorsque N_{lp} du Rh était plus faible, et vice versa. La spectroscopie photoélectronique aux rayons X (SPX) a démontré que les Rh^{3+} et Rh^0 étaient présents à la surface de tous les catalyseurs, et la quantité de Rh métallique (at%) a augmenté avec le N_{lp}. En outre, le $N_{lp, Rh}$ a une influence remarquable sur l'activité électrochimique. En effet, la voltammétrie de décapage anodique a montré que le catalyseur avec un N_{lp} plus élevé de Rh démontrait une bonne performance d'oxydation du CO. On constate que le film Rh déposé avec le $N_{lp, Rh}$ = 50000 présente la plus grande surface électroactive (27.90 cm^2 *vs* 1.20 cm^2 of Pt), le potentiel d'apparition le plus bas de l'électrooxydation du CO (0.47 V *vs* 0.60 V Pt), et une charge nette correspondant à l'électrooxydation de la couche de CO de 424 µC cm^{-2} (*vs* 358 µC cm^{-2} of Pt).

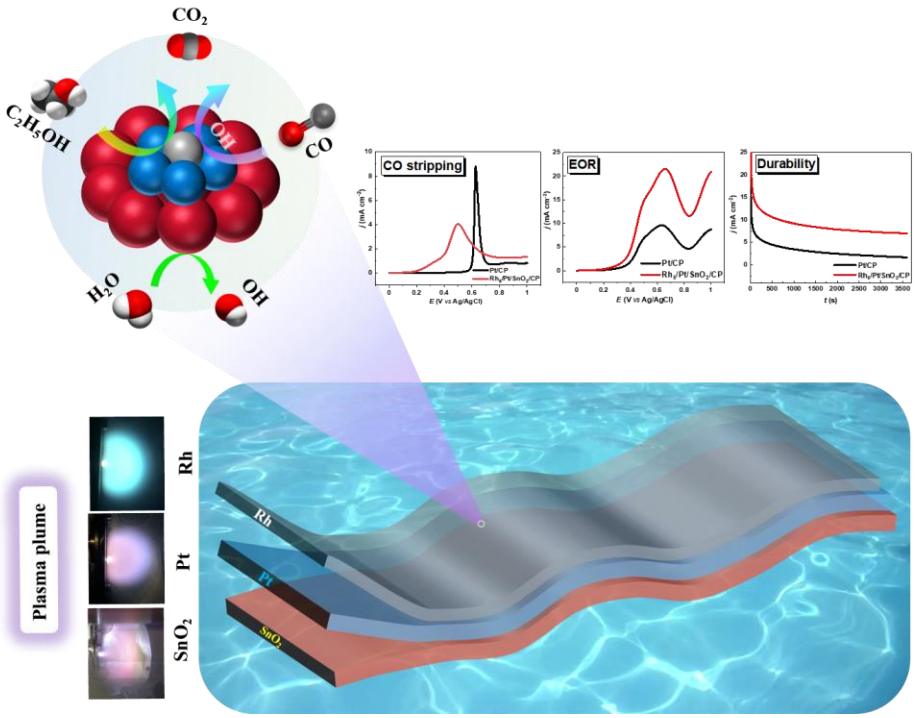

Figure 8.7 Le résumé graphique.

Secondement, nous étudions l'influence du N_{lp} de Rh sur les catalyseurs à base de Pt et Pt-SnO_2 vers la ROE en milieu acide. Parallèlement, nous révélons également le rôle de SnO_2 et Rh dans les catalyseurs à base de Pt sur l'électrooxydation de l'éthanol. Nous avons utilisé la PLD pour déposer le Rh, Pt et SnO_2 sur du papier carbone (PC) couche par couche. Le MEB a montré que Rh, Pt et SnO_2 étaient déposés. La DRX a montré que la taille des particules de Pt est devenue plus petite dans les catalyseurs à base de $PtSnO_2$ et PtRh, mais le paramètres de maille *a* et la distance interréticulaire d_{hkl} correspondant sont devenus plus grands, et le 2θ de Pt (111) s'est déplacé négativement. Cette tendance était plus évidente dans les catalyseurs ternaires $RhPtSnO_2$ lors de l'augmentation du N_{lp} du Rh, ce qui impliquait qu'il y avait une forte interaction entre le SnO_2 (Rh) et le Pt. Le changement du niveau de base de SnO_2, Rh et Pt dans SPX a démontré la forte interaction métal-support (SMSI) entre eux. Le SPX a également révélé que Sn était à l'état Sn^{4+}, Pt et Rh étaient à l'état métallique. Les résultats électrochimiques ont démontré que les catalyseurs avec un N_{lp} plus élevé de Rh avaient de moins bonnes performances en voltammétrie linéaire à balayage (LSV) et en chronoampérométrie (CA), mais un meilleur comportement à l'oxydation du CO. À l'inverse, le catalyseur Rh_5PtSnO_2/CP avec une quantité modérée de Rh ($N_{lp,\,Rh}$ = 5000) avait les meilleures performances en termes de potentiel d'apparition le plus bas, de rendement de courant et de

durabilité les plus élevés, qui peuvent être respectivement attribués à l'ajout de SnO_2 (mécanisme bifonctionnel) et à l'apport de Rh (effet électronique).

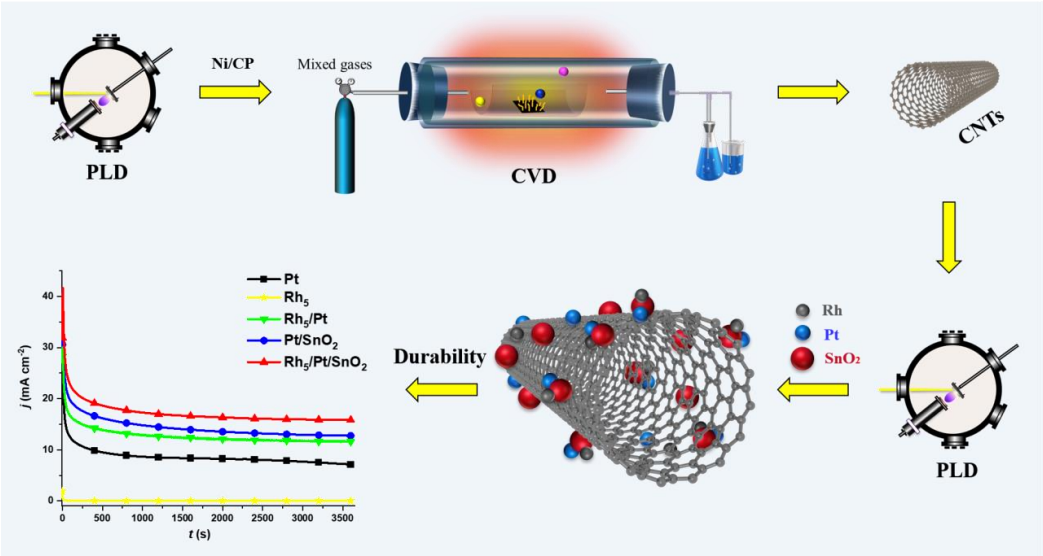

Figure 8.8 Le résumé graphique.

Ensuite, nous étudions l'effet du substrat (nanotubes de carbone NTCs) dans les catalyseurs susmentionnés vers la ROE. Nous synthétisons des TNCs sur Ni/PC par dépôt chimique en phase vapeur (CVD). Par la suite, nous avons déposé SnO_2, Pt et Rh couche par couche sur les TNCs. À la différence des catalyseurs supportés par le PC avec une caractéristique d'empilement lamellaire, ces catalyseurs supportés par les TNCs étaient en distribution groupée. Le MEB a montré qu'ils étaient comme des touffes de coraux ou de chou-fleur. Des DRX et SPX similaires ont été observés avec les précédents catalyseurs supportés par PC, ainsi qu'avec les LSV, CA et la voltammétrie de décapage du CO. Cependant, le catalyseur supporté par les TNCs présentait un meilleur comportement électrochimique que les catalyseurs correspondants supportés par le PC, en particulier le catalyseur Rh_5PtSnO_2/CNT avait une performance inégalée avec un potentiel d'apparition le plus bas et une densité de courant la plus élevée.

Enfin, nous nous sommes intéressés aux binaires Pt_xRh_{100-x}. Nous utilisons la CBPLD pour synthétiser des PtRh co-déposés avec divers rapports atomiques de Pt:Rh (9:1, 3:1, 1:1, 1:3). Les résultats MEB, spectroscopie de rayons X à dispersion d'énergie (EDX) et MET ont montré que les catalyseurs bimétalliques Pt_xRh_{100-x} étaient en forme d'arbuste et que les nanoparticules de Pt et Rh étaient dispersées de manière homogène sur le substrat en papier carbone avec une taille moyenne de particules inférieure à 6 nm. Le décalage positif 2θ de Pt (111) et la

contraction de *a* et d_{hkl} dans DRX ont indiqué que Pt et Rh étaient alliés. Le SPX a également révélé que le Pt et le Rh étaient sous forme métallique. Les résultats LSV, CA et la voltammétrie de décapage du CO ont montré que la présence du Rh ajouté a considérablement amélioré la tolérance envers le CO et l'activité catalytique envers la ROE avec un rapport atomique optimal Pt : Rh était de 3:1.

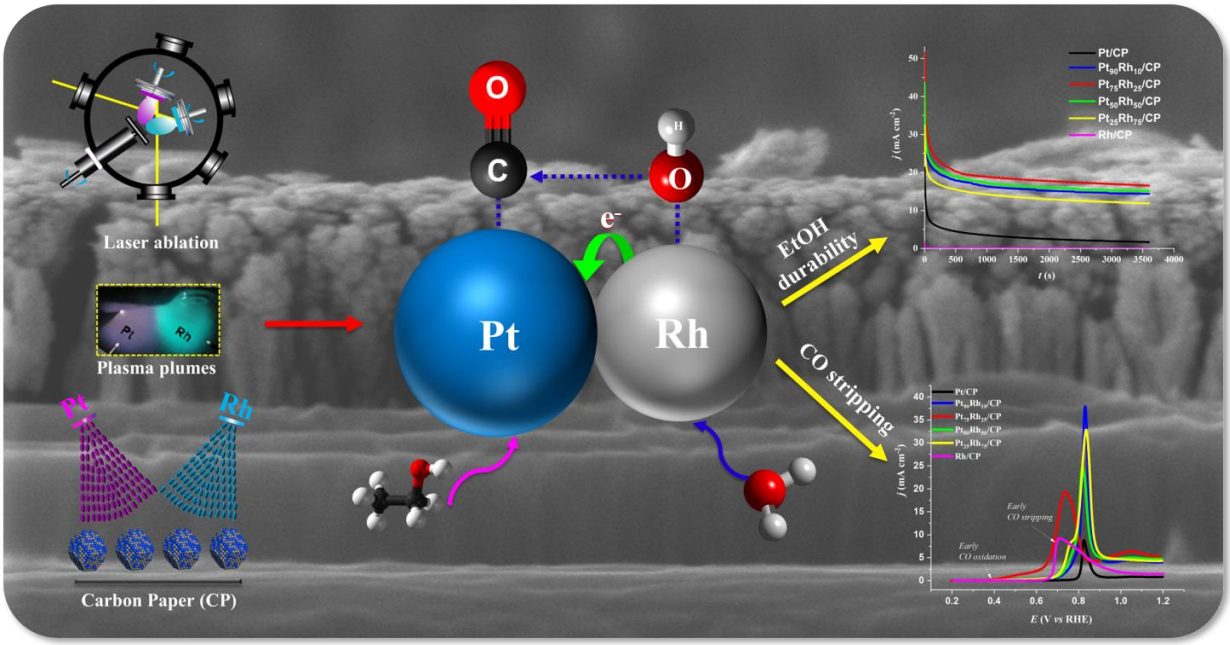

Figure 8.9 Le résumé graphique.

Nous proposons un mécanisme de la ROE sur le catalyseur ternaire $Rh_5/Pt/SnO_2$ (Figure 8.10). Le rôle spécifique de chaque constituant des catalyseurs synthétisés par PLD dans la voie d'électrooxydation de l'éthanol a été résumé comme suit: le Pt a été sélectionné pour la chimisorption de l'éthanol; le SnO_2 a fourni des espèces OH à des potentiels plus faibles d'élimination des espèces empoisonnantes le CO, tandis que le Rh représentait le clivage de la liaison C-C. Dans les catalyseurs Pt_xRh_{100-x}/CP fabriqués par CBPLD, le rôle de Rh n'était pas seulement de rompre la liaison C-C, mais aussi de produire de l'eau active pour offrir des espèces contenant de l'oxygène.

Sommairement

(1) Un film de Rh synthétisé avec un N_{lp} plus élevé contient une plus grande taille de particule et démontre une meilleure capacité d'oxydation du CO.

(2) Les promoteurs Rh et SnO_2 à proximité des sites de Pt fournissent fournir une activité élevée pour l'électrooxydation de l'éthanol et une meilleure tolérance envers les espèces

empoisonnées en raison de l'effet synergique du mécanisme bifonctionnel et de l'effet électronique.

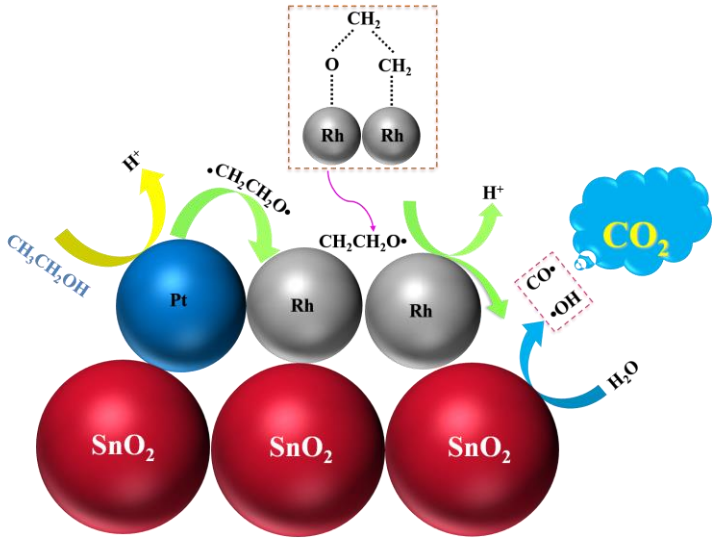

Figure 8.10 Proposition de mécanisme de la ROE sur le catalyseur ternaire $Rh_5/Pt/SnO_2$.

(3) L'activité des catalyseurs ci-dessus pour la ROE a diminué dans l'ordre des catalyseurs : **co-déposés** ($Pt_{75}Rh_{25}$ > $Pt_{50}Rh_{50}$ > $Pt_{90}Rh_{10}$ > $Pt_{25}Rh_{75}$) > **catalyseurs supportés par les NTCs déposés couche par couche** ($Rh_5/Pt/SnO_2$ > Pt/SnO_2 > $Rh_{10}/Pt/SnO_2$ > $Rh_{20}/Pt/SnO_2$ > Rh_5/Pt > $Rh_{50}/Pt/SnO_2$ > Pt > Rh) > **catalyseurs supportés par le PC couche par couche**.

(4) Catalyseurs à base de **SnO_2** > Catalyseurs à base de **CeO_2** > Catalyseurs à base de **MnO_2** > Catalyseurs à base de **TiO_2**.

(5) Dans l'alliage Pt_xRh_{100-x}, une teneur plus faible en Rh ne peut pas générer suffisamment d'espèces contenant de l'oxygène à des potentiels inférieurs, ce qui entraîne un empoisonnement du Pt. En outre, il n'y a peut-être pas assez de sites Rh pour rompre efficacement la liaison C-C, ce qui conduit à une faible activité catalytique. Alors qu'une teneur riche en Rh riche inhibera les sites actifs de Pt pour une déshydrogénation supplémentaire de l'éthanol. Cependant, avec un rapport modéré de Pt et Rh (3:1), le Rh modifie la structure électronique du Pt, créant une énergie de liaison tempérée entre le Rh et éthanol et les espèces de types CO, ce qui facilite la décomposition de l'éthanol.

Plusieurs autres catalyseurs ont également été envisagés au cours de ce projet, et le liste de ces catalyseurs est résumée dans le Tableau 8.1.

Tableau 8.1 Liste des catalyseurs étudiés lors de ce projet

Méthode de synthèse	Substrat		Catalyseurs	LSV			CA	CO stripping	
				j_{pa} (mA cm^{-2})	E_{pa} (V)	E_{onset}	j_{ss} (mA m^{-2})	E_{onset} (V)	E_{pCO}(V)
PLD	PC	**Pt**	Pt	9.55	0.64	0.54	1.66	0.60	0.63
		Rh_n	Rh_5	0	-	-	0	0.40	0.62
			Rh_{10}	0	-	-	0	0.46	0.53
			Rh_{20}	0	-	-	0	0.47	0.49
			Rh_{50}	0	-	-	0	0.48	0.51
		Rh_n/Pt	Rh_5/Pt	11.77	0.65	0.48	4.94	0.53	0.57
			Rh_{10}/Pt	12.86	0.65	0.47	5.23	0.48	0.55
		SnO_2-based	Pt/SnO_2	19.06	0.66	0.46	6.07	**0.14**	0.51
			Rh_5/Pt/SnO_2	**21.53**	**0.65**	0.43	6.98	**0.17**	0.50
			Rh_{10}/Pt/SnO_2	17.05	0.65	0.46	6.12	0.23	0.60
			Rh_{20}/Pt/SnO_2	17.99	0.66	0.47	5.49	0.32	0.57
			Rh_{50}/Pt/SnO_2	13.05	0.66	0.51	3.64	0.45	0.55
		CeO_2-based	Pt/CeO_2	15.32	0.64	0.45	6.03	0.23	0.58
			Rh_5/Pt/CeO_2	14.48	0.62	0.43	5.30	0.50	0.58
			Rh_{10}/Pt/CeO_2	16.20	0.62	0.40	8.07	0.47	0.52
			Rh_{20}/Pt/CeO_2	14.80	0.65	0.46	5.60	0.49	0.60
			Rh_{50}/Pt/CeO_2	10.12	0.64	0.52	5.44	0.51	0.60
		TiO_2-based	Pt/TiO_2	15.13	0.66	0.48	7.51	0.28	0.60
			Rh_5 /Pt/TiO_2	14.70	0.66	0.48	5.59	0.53	0.63
			Rh_{10}/Pt/TiO_2	12.04	0.65	0.49	5.61	0.50	0.59
		MnO_2-based	Pt/MnO_2	13.97	0.66	0.48	5.84	0.58	0.60
			Rh_5/Pt/MnO_2	14.20	0.66	0.48	7.47	0.49	0.63
			Rh_{10}/Pt/MnO_2	10.94	0.65	0.53	4.62	0.47	0.55
	TNC	**Pt**	Pt	18.87	0.68	0.40	7.12	0.57	0.67
		Rh_n	Rh_5	0	0	0	0	0.49	0.55
			Rh_{10}	0	0	0	0	0.46	0.53
		Rh_n/Pt	Rh_5/Pt	21.34	0.65	0.23	11.59	0.52	0.62

			Rh_{10}/Pt	21.38	0.66	0.33	10.11	0.55	0.65
		SnO_2-based	Pt/SnO_2	23.16	0.67	0.16	12.74	0.19	0.61
			Rh_5/Pt/SnO_2	**27.77**	0.66	0.16	15.83	**0.17**	0.59
		CeO_2-based	Pt/CeO_2	23.43	0.67	0.34	12.96	0.60	0.66
			Rh_{10}/Pt/CeO_2	28.73	0.67	0.34	14.20	0.54	0.65
		TiO_2-based	Pt/TiO_2	11.40	0.65	0.42	4.84	0.51	0.67
			Rh_5 /Pt/TiO_2	18.23	0.66	0.38	5.89	0.50	0.66
		MnO_2-based	Pt/MnO_2	22.11	0.67	0.38	6.51	0.21	0.64
			Rh_5/Pt/MnO_2	25.14	0.66	0.38	6.58	0.31	0.62
CB-PLD	PC	**Pt_xRh_{100-x}**	$Pt_{90}Rh_{10}$	35.80	0.71	0.16	20.13	0.30	0.64
			$Pt_{75}Rh_{25}$	**42.63**	**0.68**	**0.15**	**21.17**	**0.16**	**0.53**
			$Pt_{50}Rh_{50}$	37.66	0.70	0.15	19.91	0.28	0.62
			$Pt_{25}Rh_{75}$	30.90	0.72	0.18	16.58	0.49	0.64

8.5 Bibliographie

[1] B. Dudley, BP Statistical Review, London, UK, accessed Aug, 6 (2018) 2018.

[2] P.P. Edwards, V.L. Kuznetsov, W.I. David, N.P. Brandon, Energy Policy, 36 (2008) 4356-4362.

[3] W. Zhou, B. Zhou, W. Li, Z. Zhou, S. Song, G. Sun, Q. Xin, S. Douvartzides, M. Goula, P. Tsiakaras, J. Power Sources, 126 (2004) 16-22.

[4] X. Yu, P.G. Pickup, J. Power Sources, 182 (2008) 124-132.

[5] V. Selvaraj, M. Alagar, K.S. Kumar, Appl. Catal. B, 75 (2007) 129-138.

[6] W. Du, Q. Wang, D. Saxner, N.A. Deskins, D. Su, J.E. Krzanowski, A.I. Frenkel, J. Am. Chem. Soc., 133 (2011) 15172-15183.

[7] J. Wang, S. Wasmus, R. Savinell, J. Electrochem. Soc., 142 (1995) 4218-4224.

[8] S. Song, W. Zhou, Z. liang, R. Cai, G. Sun, Q. Xin, V. Stergiopoulos and P. Tsiakaras, Appl. Catal. B: Environ, 55 (2005) 65.

[9] L.B. Lave, W.M. Griffin, H. MacLean, Sci. Technol., 18 (2001) 73-78.

[10] C. Lamy, A. Lima, V. LeRhun, F. Delime, C. Coutanceau, J.-M. Léger, J. Power Sources, 105 (2002) 283-296.

[11] R. Schulz, J. Huot, G. Liang, S. Boily, G. Lalande, M. Denis, J. Dodelet, Mater. Sci. Eng. A, 267 (1999) 240-245.

[12] C. Lamy, C. Coutanceau, J.M. Leger, Catalysis for sustainable energy production, (2009) 1.

[13] G. Sorda, M. Banse, C. Kemfert, Energy Policy, 38 (2010) 6977-6988.

[14] S. Song, W. Zhou, Z. Zhou, L. Jiang, G. Sun, Q. Xin, V. Leontidis, S. Kontou, P. Tsiakaras, Int. J. Hydrogen Energy, 30 (2005) 995-1001.

[15] M. Kim, C. Lee, S.M. Ko, J.-M. Nam, J. Solid State Chem., 270 (2019) 295-303.

[16] W. Zhou, B. Zhou, W. Li, Z. Zhou, S. Song, G. Sun, Q. Xin, S. Douvartzides, M. Goula, P. Tsiakaras, J. Power Sources, 126 (2004) 16-22.

[17] E. Antolini, J. Power Sources, 170 (2007) 1-12.

[18] Y. Wang, S. Zou, W.-B. Cai, Catalysts, 5 (2015) 1507-1534.

[19] Z.W. Chia, J.Y. Lee, Encyclopedia of Inorganic Chemistry, (2006).

[20] F. Vigier, C. Coutanceau, A. Perrard, E. Belgsir, C. Lamy, J Appl Electrochem, 34 (2004) 439-446.

[21] C. Lamy, S. Rousseau, E. Belgsir, C. Coutanceau, J.-M. Léger, Electrochim. Acta, 49 (2004) 3901-3908.

[22] H. Wang, Z. Jusys, R. Behm, J. Power Sources, 154 (2006) 351-359.

[23] W. Du, G. Yang, E. Wong, N.A. Deskins, A.I. Frenkel, D. Su, X. Teng, J. Am. Chem. Soc., 136 (2014) 10862-10865.

[24] Q. Wang, G. Sun, L. Jiang, Q. Xin, S. Sun, Y. Jiang, S. Chen, Z. Jusys, R. Behm, Phys. Chem. Chem. Phys., 9 (2007) 2686-2696.

[25] L. Colmenares, H. Wang, Z. Jusys, L. Jiang, S. Yan, G. Sun, R. Behm, Electrochim. Acta, 52 (2006) 221-233.

[26] M. Mavrikakis, D. Doren, M. Barteau, J. Phys. Chem. B, 102 (1998) 394-399.

[27] E. Vesselli, A. Baraldi, G. Comelli, S. Lizzit, R. Rosei, Chemphyschem, 5 (2004) 1133-1140.

[28] P.Y. Sheng, A. Yee, G. Bowmaker, H. Idriss, J. Catal., 208 (2002) 393-403.

9 APPENDIX II

Publications during the Ph.D.

1. **Haixia Wang**, Shuhui Sun, Mohamed Mohamedi, Plasma Synthesized Tri-Layered Rhodium−Platinum−Tin Oxide Nanoscale with Enhanced Tolerance to CO-Poisoning and High Electroactivity for Ethanol Oxidation, Energy Technol., 9(2021)2000949.
2. **Haixia Wang**, Shuhui Sun, Mohamed Mohamedi, Synthesis of free-standing ternary Rh-Pt-SnO2-carbon nanotubes nanostructures as highly active and robust catalyst for ethanol oxidation, RSC Adv., 10 (2020), 45149.
3. **Haixia Wang**, Shuhui Sun, Mohamed Mohamedi, Study on the influence of the thickness of nanostructured rhodium films toward electrooxidation of adsorbed carbon monoxide, *SN Applied Sciences*, 2 (2020), 1.
4. **Haixia Wang**, Xin Tong, Shuhui Sun, Mohamed Mohamedi, Nanostructured shrub-like bimetallic Pt_xRh_{100-x} alloys grown on carbon paper for the oxidative removal of adsorbed carbon monoxide for ethanol fuel cells reaction, *Electrochim. Acta*, 355 (2020), 136823.
5. Amel Tabet Aoul, **Haixia Wang**, Youling Wang, Mohamed Mohamedi, 3D Porous Sphere-Like Aggregates of Bimetallic PtRh Nanoparticles Grown onto Carbon Nanotubes: Efficient and Durable Catalyst for the Ethanol Oxidation Reaction, *J. Electrochem. Soc.*, 164 (2017), F685.
6. Naser Mohammadi, Chahrazed Benabid, **Haixia Wang**, Juan Carlos Abrego-Martinez, Youling Wang, Mohamed Mohamedi, Three-dimensional Pt catalyst on TiO_2 Structures: Synthesis, Characterization and Optimal Morphology for Efficient Ethanol Electrooxidation in Acidic Medium, (2020). doi.org/10.1002/elsa.202000020

Contributions to the international conferences during the Ph.D.

2018.10 presented the *international conference on advanced materials and processes for environment, energy and health* (iCAMP) 2018, Montreal, Canada (*Oral*).

2018.07 presented at *the international conference on energy, materials and photonics* (EMP 2018), 2018, Montreal, Canada (*Oral*).

2017.10 presented at the *1st annual Symposium of Centre québécois sur les matériaux fonctionnels (CQMF)*, 2017, Sherbrooke, Canada (*Best Poster Award*).

2016.11 presented at the *Materials Research Society (MRS)*, 2016, Boston, USA (*Poster*).

2016.05 presented at the *Advanced Materials Annual Conference*, 2016, Montreal, Canada (Poster).